AN INVESTIGATION OF P-WAVE SCATTERING IN THE CRUST AND UPPER MANTLE USING TRAVEL-TIME FLUCTUATIONS AND ARRAY SIGNAL COHERENCE

by

Samuel Bakare Ojo

Department of Geophysics

Submitted in partial fulfillment
of the requirements for the degree of
Doctor of Philosophy

Faculty of Graduate Studies
The University of Western Ontario
London, Ontario
March, 1981.

© Samuel Bakare Ojo 1981.

THE UNIVERSITY OF WESTERN ONTARIO - FACULTY OF GRADUATE STUDIES

C E R T I F I C A T E O F E X A M I N A T I O N

Chief Advisor

R.F. Mereu

Examining Board

Advisory Committee

C. Mansinha

A. Hayatsu

C. Mansinha

C. Keen

The thesis by

Samuel Bakare Ojo

entitled

An Investigation of P-Wave Scattering in the Crust and Upper Mantle using Travel-time Fluctuations and Array Signal Coherence

is accepted in

partial fulfillment of the

requirements of the degree of

Doctor of Philosophy

Date April 27, 1981

M.E. Flat

Chairman of Examining Board

ABSTRACT

The propagation of P-waves through models of the Earth's crust and upper mantle with slightly random, lateral inhomogeneities superimposed on one composed of layers with vertical velocity gradients was investigated. The maximum deviation of velocity from a mean value at a given depth, and a correlation distance derived from a two-dimensional smoothing filter were two parameters used to vary the amplitude and size of the velocity anomalies. The resulting models show short discontinuous reflectors scattered about at various depths throughout the models, and are thus in agreement with many deep seismic reflection experiments.

On the other hand, numerical experiments using ray-tracing techniques showed that the effect of the lateral and vertical velocity anomalies is to scatter the energy, and break up the continuous travel-time lines from vertical gradient models into travel-time segments with different slopes similar to those observed in many long range seismic refraction experiments, and to those resulting from layering effects in the media. The travel-time segments produced an apparent intermediate layer at depths which could be correlated to the correlation distance.

In a similar manner, the effect of the velocity anomalies in the upper mantle models is to cause several arrivals of distinctly different slowness (dT/dA) to be observed over very short distances similar to observations obtained from a number of array studies, thereby suggesting that it might not always be necessary to invoke major discontinuities in the upper mantle to explain these rapid variations in slowness and travel-time observations.

On the basis of some long-range refraction data from the 1979 COCRUST experiment in southern Manitoba and Saskatchewan, a random model was produced for the crust of that region, and showed that the optimum correlation distance and r.m.s. velocity fluctuation that best describe the travel-time fluctuations are 5 km and 1% respectively.

A method was also developed to extract the information about the scattering characteristics of different P-wave travel paths from the ratio of the incoherent energy to the total incident energy of the signal recorded at an array station. It is based on the assumption that if a ray passes through a homogeneous earth, the energy arriving at an array station should be relatively coherent, whereas if the ray encounters lateral and vertical inhomogeneities, its energy will be incoherent and much more complex.

A series of coherence measurements were made on more than 300 earthquake recordings (distance 15 -36 , azimuth 0^0 -360^0 ; and distance 40^0 -67^0 , azimuth 0^0 -130^0) at the

Gauribidanur medium aperture (25 km) seismic array (GBA) in southern India, and over 65 earthquake recordings (distance 12°~30°, azimuth 165 -285) at the Yellowknife seismic array (YKA) in western Canada.

The analyses showed that there is relatively more heterogeneity for the continental upper mantle region around India than for the corresponding oceanic structure, with the structure above 400 km tending to be more complex than the structure below that depth. The YKA analyses showed that the upper mantle structure under the north-western part of the North American continent could be progressively more heterogeneous with depth between 400 km and 750 km.

ACKNOWLEDGEMENTS

I sincerely wish to thank my supervisor, Dr. R.F. Mereu for his constant interest, guidance, and encouragement throughout the course of this study. I would also like to thank Dr. A.E. Beck, Head of the Department of Geophysics, whose initial encouragement made it possible for me to come and study here.

I am grateful to Dr. Z. Hajnal of the University of Saskatchewan who supplied the data of the 1979 COCRUST refraction experiment before our copy of the tapes was ready. The encouragement of the members of staff of the Department of Geophysics is also gratefully acknowledged.

Special thanks are also due to my parents for their encouragement and support. Finally, I express my sincere gratitute to my wife, Iyabo Ojo for her constant support and encouragement, and for her secretarial help at various stages of this study.

Financial assistance was provided by a Federal Government of Nigeria Scholarship, a study fellowship from the Ahmadu Bello University, Zaria, Nigeria, a Special University Scholarship from the University of Western Ontario during my last two terms, and the National Science and Engineering Research Council of Canada (NSERC) grant No A-1793.

TABLE OF CONTENTS

	Page
CERTIFICATE OF EXAMINATION	ii
ABSTRACT	iii
ACKNOWLEDGEMENTS	iv
TABLE OF CONTENTS.....	vii
LIST OF TABLES	xi
LIST OF FIGURES	xii
LIST OF ABBREVIATIONS AND SYMBOLS	xxi
CHAPTER 1 INTRODUCTION	1
1.1 Introduction	1
1.2 Background from Previous Studies	2
1.3 Outline of Thesis	4
CHAPTER 2 P-WAVE SCATTERING THROUGH A CRUST WITH RANDOM INHOMOGENEITIES	6
2.1 Introduction	6
2.2 Development of the Numerical Experiments .	10
2.3 Determining the Characteristics of Numerical Models	18
2.3.1 The Ray Tracing Procedure and Computer Programs	23
2.4 General Travel-time Response of Numerical Models.....	32
CHAPTER 3 A SCATTERING MODEL FOR THE 1979 COCRUST REFRACTION DATA	52

3.1 Introduction 52
3.2 The Refraction Survey 53
3.3 The Travel Time Data 55
3.4 A Random Velocity Model for the Travel Time Data 66
3.5 Extremal Inversion of Travel Time Data.... 84
3.5.1 Velocity-depth Bounds for the Cocrust Refraction Data 88
CHAPTER 4 P-WAVE SCATTERING THROUGH AN UPPER MANTLE WITH RANDOM INHOMOGENEITIES 100
4.1 Velocity Structure of the Upper Mantle ... 100
4.2 Results from Experiments for the Upper Mantle 112
4.3 Apparent Velocity Model 123
CHAPTER 5 ARRAY SIGNAL COHERENCE AND ITS RELATIONSHIP TO P-WAVE SCATTERING..... 131
5.1 Rationale 131
5.2 Theoretical Considerations 133
5.3 Data Analysis Procedure 145
5.4 Tests with Synthetic Data 149
5.4.1 Additional Tests with Nth Rooth Beam Forming..... 153
CHAPTER 6 PRELIMINARY ASSESSMENT OF COHERENCE MEASUREMENTS ON GBA AND YKA .DATA..... 158
6.1 Objective and Rationale 158
6.2 The Gauribidanur Seismic Array 164
6.3 The Yellowknife Seismic Array 166
6.4 Analyses and Correction of the Data 168

6.5 Effects of Signal Complexity 173
6.6 Effects of Signal Frequency 185
6.7 Effects of Focal Depth 197
6.8 Summary 202
CHAPTER 7 INTERPRETATION OF FROM GBA AND YKA 204
7.1 Introduction 204
7.2 Results - GBA 205
7.2.1 The Himalayan Region 208
7.2.2 The Java Trench 212
7.2.3 The Mid-Indian Ocean Ridge..... 215
7.2.4 The Hindukush Region 219
7.3 Lower Mantle Data from GBA 222
7.4 Results - YKA 224
7.4.1 The California Region 227
7.4.2 The Alaska Peninsula 230
7.5 Discussion 233
CHAPTER 8 DISCUSSION AND CONCLUSIONS 239
8.1 Mineralogical Considerations for Velocity Fluctuations..... 239
8.2 Suggestions for Further Work 245
8.3 Conclusions 246

* * *

APPENDIX A
A.1 Listings of the ray tracing computer program for flat earth model 252
A.2 Listings of the ray tracing computer program for spherical earth model 265

APPENDIX B A simplified tau method for the inversion of slowness data (by R.F. Mereu)..... 277

APPENDIX C

C.1 GBA data for complexity factor, spectral ratio, and scattered energy data 281

C.2 YKA data for complexity factor, spectral ratio and scattered energy data 287

REFERENCES 289

VITA 304

LIST OF TABLES

Table	Description	Page
2.1	Main computational steps in ray tracing program.	30
3.1	Least-squares and apparent velocities and intercept times.	63
3.2	Velocities and depths for random model.	74
5.1	Main steps in computing scattered energy from array data.	146

LIST OF FIGURES

Figure	Description	Page
2.1	Line drawing composite showing the structure and reflections picked for lines 1, 1A, and 2 (after Smithson et al., 1970).	8
2.2	Starting velocity model with smooth lateral variation superimposed on a velocity gradient.	12
2.3	Velocity contour plot of model shown in Figure 2.2 contour interval is 0.025 km/s.	15
2.4	Velocity contour plot similar to Figure 2.3 for a different set of random numbers.	17
2.5	Velocity contour plot similar to Figure 2.3 for a correlation distance of 5 km.	20
2.6	Velocity contour plot similar to Figure 2.3 for a maximum velocity perturbation of 0.19 km/s.	22
2.7	Ray-tracing configuration for flat earth model.	25
2.8	Ray-tracing configuration for spherical earth model.	27
2.9	(a) Simple crustal earth model, and (b) comparison of ray-tracing travel time with standard ray theory (Bullen, 1963) travel times for model in (a).	33
2.10	Travel-time plot and ray diagram for homogeneous crustal model.	35
2.11	Travel-time plot and ray diagram for heterogeneous crustal model.	37
2.12	A comparison of travel-time plots and least-squares regression velocities for a model with (a) correlation distance of 5 km, (b) correlation distance of 15 km.	38
2.13	Variation of depth to apparent discontinuity as a function of correlation distance. Maximum velocity perturbation is 0.13 km/s.	40
2.14	Variation of depth to apparent discontinuity as	

	a function of correlation distance. Maximum velocity perturbation is 0.19 km/s.	41
2.15	Travel-time residuals for a model with r.m.s. velocity fluctuation of (a) 0.05 km/s (b) 0.075 km/s.	43
2.16	Travel-time residuals for the same model as Figure 2.15 with r.m.s. velocity fluctuation of (a) 0.10 km/s, (b) 0.15 km/s.	44
2.17	Two examples of Travel-time plot for a model with correlation distance of 5 km, and maximum velocity fluctuation of 0.13 km/s.	46
2.18	Two examples of travel-time plot for a model with correlation distance of 10 km, and maximum velocity fluctuation of 0.13 km/s.	47
2.19	Two examples of travel-time plot for a model with correlation distance of 15 km, and maximum velocity fluctuation of 0.13 km/s.	48
2.20	Two examples of travel-time plot for a model with correlation distance of 5 km, and maximum velocity fluctuation of 0.19 km/s.	49
2.21	Two examples of travel-time plot for a model with correlation distance of 10 km, and maximum velocity fluctuation of 0.19 km/s.	50
2.22	Two examples of travel-time plot for a model with correlation distance of 15 km, and maximum velocity fluctuation of 0.19 km/s.	51
3.1	Simplified map showing locations of the seismic refraction lines (after Hajnal, 1980).	54
3.2	Vertical component refraction record section from northern shots 9 and 13 showing least-squares fits to first arrival times. The records have been normalized to the maximum amplitude in each trace and the normalizing factors are shown at the top of each trace. The station numbers are shown at the bottom of each trace.	57
3.3	Vertical component refraction section from southern shots 10-12.	58
3.4	Vertical component refraction section from northern shots 14 and 17.	59
3.5	Vertical component refraction section from southern shots 15-18.	60

3.6	Vertical component refraction section from western shots 19 and 20.	61
3.7	Reduced travel-time distance plot for the section of Figure 3.3 showing a possible break in travel-time segment.	67
3.8	Two layered-earth models derived from the 1977 refraction data (after Green et al., 1980).	68
3.9	Refraction section showing the travel times (stars) obtained from the best fit random model shown in Figure 3.10.	72
3.10	Best-fit random model for the section of Figure 3.9.	73
3.11	As for Figure 3.9 with "shot point" shifted 50 km to the south.	76
3.12	Travel times for the equivalent homogeneous model of Figure 3.10.	78
3.13	(a) Travel-time residuals of first arrival times for Line B(N-S). The residuals are relative to the least- squares regression line of the first arrival times. (b) Travel-time residuals for best-fit model with r.m.s. velocity fluctuation of 0.06 km/s.	81
3.14	Travel-time residuals for model with r.m.s. fluctuation (a) 0.10 km/s, (b) 0.15 km/s.	82
3.15	Best-fit travel times (stars) of random model for Line A(N-S).	83
3.16	Best-fit random model for Line A(N-S).	85
3.17	Travel-time residuals for (a) Line A(N-S), (b) best-fit random model.	86
3.18	Tau bounds obtained from (a) the combined data of Line A, (b) for Line B(N-S), and (c) for Line B(S-N).	92
3.19	Velocity-depth extremal bounds (unbroken lines) obtained from the tau bounds of Figure 3.18(a) compared with a layer solution (broken lines) for Line A. The layer solution is after Hajnal (1980).	93
3.20	Velocity-depth bounds and layer solution for Line B(N-S).	94
3.21	Velocity-depth bounds and layer solution for	

	Line B(S-N).	95
3.22	Velocity-depth bounds for Line B(N-S) superimposed by the best-fit random model (broken lines).	97
3.23	Velocity-depth bounds for Line A superimposed by the best-fit random model (broken lines).	98
4.1	The Jeffreys (1939) model	102
4.2	The Gutenberg (1959) low-velocity medel.	103
4.3	The Herrin et al. (1968) model.	105
4.4	The Green and Hales (1968) model.	106
4.5	The Johnson (1969) model.	107
4.6	The Helmberger and Wiggins (1971) HWNE model.	108
4.7	The Simpson et al. (1974) SMAK I model.	109
4.8	The Mereu et al. (1974) SMAK II model.	110
4.9	The Ram Datt (1981) model.	111
4.10	Simple upper-mantle starting model for the numerical experiments.	113
4.11	Travel-time curve for the model shown in Figure 4.10 by conventional ray theory (unbroken line), and by ray tracing (crosses).	114
4.12	Ray geometry for starting model.	115
4.13	Ray geometry for model with smoothed lateral inhomogeneities superimposed on the basic model of Figure 4.10.	117
4.14	Travel-time and slowness results for the model shown in Figure 4.13.	118
4.15	Travel-time and slowness results similar to that shown in Figure 4.14, but for a different set of random numbers.	119
4.16	Travel-time and slowness data observed at Warramunga array (WRA) for northeastern Australia (after Simpson et al., 1974).	120
4.17	Travel-time and slowness data observed at Yellowknife array (YKA) for the Alaska Peninsula (after Ram et al., 1978).	122

4.18 Tau-data for the travel-time results shown in Figure 4.14. A curve for the basic model of Figure 4.10 (unbroken line), is also shown for comparison. 124

4.19 Tau data for travel-time results of Figure 4.15. 125

4.20 Tau data computed from the results of Simpson et al. (1974) compared with values for the J-B and Herrin tables. 126

4.21 Tau data computed from the results of Ram et al. (1978) compared with values for the J-B and Herrin tables. 127

4.22 Apparent velocity-depth envelope for the travel-time data of Figure 4.13 compared with the SMAK II model (Mereu et al. 1974), the RMW-2 model (Ram et al., 1978) and the Ram Datt model (Ram Datt, 1981). 129

5.1 (a) Synthetic array data without noise using GBA array configuration and single wavelet. (b) Adaptive processed solutions (SR is the sampling rate, V and AZ are the given apparent velocity and azimuth used to form the beam (SRB)). 135

5.2 (a) Synthetic array data using three separate wavelets with same apparent velocity and azimuth. (b) Adaptive processed solutions. 140

5.3 (a) Synthetic array data using three separate wavelets with different apparent velocity and azimuth. (b) Adaptive processed solutions. 141

5.4 (a) Same as Figure 5.3(a), (b) Adaptive processed solutions and beam (SRBMX) formed by velocity and azimuth sweep. 143

5.5 (a) Synthetic array data with no noise. (b) Synthetic data with 20% of total trace energy comprised of random noise. (c) Synthetic data with 60% of total trace energy comprised of random noise. 151

5.6 A measure of the effectiveness of noise correction for different noise levels. Noise residuals are deviation of $E_T / (N.E_{av})$ from unity. 152

5.7 Predicted incoherent or scattered energy versus true incoherent energy in synthetic data. 154

5.8 A comparison of the coherence results for Nth root processing. 156

6.1 Epicentral map for earthquakes (GBA) used in the upper mantle study around India. Concentric circles denote epicentral distances of 20°, 40°, 60°, and 80° from inner to outer circle. The azimuth distributions of events are: 1. Himalayan region (0°-90°), 2. Java trench (90°-180°), 3. Mid-Indian oceanic ridge (180°-280°), and 4. Hindukush region (280°-360°). The select Hindukush events used for the focal depth study in Section 6.7 are identified by "H". 161

6.2 Epicentral map for earthquakes recorded at the YKA. Concentric circles denote epicentral distances of 20°, 40°, and 60° from inner to outer circle. The azimuth distributions of events are: 1. California region (165°-265°), 2. Alaska Peninsula (265°-285°). 163

6.3 Configuration of the Gauribidanur medium aperture seismic array (GBA) (after Mowat and Burch, 1964). 165

6.4 Configuration of the Yellowknife medium aperture seismic array (YKA) (after Weichert, 1975). 167

6.5 Two array record sections from GBA illustrating the polarity reversal of station B9 for the record section on the right. 172

6.6 a,b,c and d. Examples of record sections from GBA to illustrate the relationship between simple signals and scattered energy. The adaptive processed solutions of the sections (after Ram and Mereu, 1977) are also shown for comparison. (a) Complexity factor (F_C) is 1.4; scattered energy (S.E.) is 12% (b) F_C = 1.7; S.E. = 7% 175

6.7 a,b,c, and d: Examples of record sections from GBA to illustrate the relationship between complex signals and scattered energy. The adaptive processed solutions of the records (after Ram and Mereu, 1977) are also shown for comparison (a) Complexity factor (F_C) is 9.0; Scattered energy (S.E.) is 9% (b) F_C = 4.3; S.E. = 7% (c) F_C= 3.8; S.E. = 49% (d) F_C= 6.7; S.E. = 54% 181

6.8 Scattered energy versus distance for NTS events. 186

6.9	Some typical beams and their corresponding relative amplitude for NTS events recorded at YKA.	188
6.10a	Some typical beams and their corresponding relative amplitude for NTS events recorded at YKA.	189
6.10b	Some typical beams and their corresponding relative spectra for events recorded at YKA from the California region.	190
6.10c	Some typical beams and their corresponding relative amplitude spectra for events recorded at GBA from the Himalayan region.	191
6.10d	Typical beams and relative amplitude spectra for events recorded at GBA from the Java trench.	192
6.10e	Typical beams and relative amplitude spectra for events recorded at GBA from the Mid-Indian ocean.	193
6.10f	Typical beams and relative amplitude spectra for events recorded at GBA from the Hindukush region.	194
6.11	Scattered energy versus spectral ratio for the NTS events.	196
6.12	Scattered energy versus focal depth for select Hindukush events.	199
6.13	Spectral ratio versus focal depth for select Hindukush events.	200
6.14	Observed slowness versus focal depth for select Hindukush events. The slowness values were taken from the study of Ram and Mereu (1977).	201
7.1	Observed scattered energy as a function of the azimuthal distribution of events.	207
7.2	Signal spectral ratio versus azimuth of events.	209
7.3	Observed scattered energy versus signal spectral ratio.	210
7.4	Observed scattered energy as a function of the epicentral distance of the events. The line parallel to the distance axis is used to emphasize the observed trend.	211
7.5	Observed scattered energy versus signal	

	spectral ratio.	213
7.6	Observed scattered energy as a function of the epicentral distance of the events. The line parallel to the distance axis emphasizes the observed trend.	214
7.7	Observed scattered energy versus signal spectral ratio.	216
7.8	Observed scattered energy versus epicentral distance of events.	217
7.9	Observed scattered energy versus signal spectral ratio.	220
7.10	Observed scattered energy versus epicentral distance of events.	221
7.11	Observed scattered energy versus epicentral distance excluding the select Hindukush events and events with spectral ratio greater than 0.4.	223
7.12	Observed scattered energy versus epicentral distance for upper and lower mantle data. The line parallel to the distance axis emphasizes the differences in scattered energy between upper mantle data (15°-35°) and lower mantle data (40°-67°).	225
7.13	Observed scattered energy versus epicentral distance for upper and lower mantle data. The line parallel to the distance axis emphasizes the difference between upper mantle data (15 -36°) and lower mantle data (45°-65°).	226
7.14	Observed scattered energy versus signal spectral ratio.	228
7.15	Observed scattered energy versus epicentral distance.	229
7.16	Observed scattered energy versus signal spectral ratio.	231
7.17	Observed scattered energy versus epicentral distance.	232
8.1	Velocity versus plagioclase composition calculated from aggregate theory. Crosses represent Voigt and Reuss averages. Dots refer to observed velocities in plagioclase rocks at 1.5 kb (after Christensen, 1965).	242

8.2 (a) Diagram showing proportions of principal minerals in a series of igneous rocks ranging from granite to dunite. (b) Variation of calculated velocity with composition for the same sequence of rocks as in (a). Dots refer to observed velocities at 1.5 kb for rocks approximating the mineral composition in (a) ranging from granite to dunite (after Christensen, 1965). 243

LIST OF ABBREVIATIONS AND SYMBOLS

ABBREVIATIONS	DESCRIPTIONS
BARC	Bhabha Atomic Research Centre
CDC	Control Data Corporation
COCRUST	Consortium for Crustal Reconnaissance Using Seismic Techniques
CPU	Central Processing Unit
DEG	Degrees
$dT/d\Delta$	Slowness
E_{av}	Average energy from all array channels
E_B	Beam energy
E_T	TAP energy
EMR	Energy, Mines and Resources
F_c	Complexity factor
FFT	Fast Fourier Transform
FM	Frequency Modulated
GBA	Gauribidanur Medium Aperture ($\sim$25 Km) Seismic Array (India)
HF	Higher frequency band
JB	Jeffreys-Bullen Earth Model (1939)
L	Correlation distance
LASA	Large Aperture (200 Km) Seismic Array (U.S.A.)
LF	Lower frequency band
LVZ	Low Velocity Zone
NORSAR	Norwegian Seismic Array (Norway)

NTS	Nevada Test Site
P	Compressional wave
p	Ray parameter
P_g	P-phase from upper crust
P^*	P-phase from lower crust
P_n	P-phase from just below the Moho
Q	Attenuation quality factor
r.m.s.	Root mean square
SBLUE	Summation of blue line seismometers output (ΣB)
SRB	Summation of red and blue lines
SRBM	Summation of red and blue line maximum from velocity and azimuth sweep
SRED	Summation of red line seismometers output; (ΣR)
TAP	Time Averaged Product $\Sigma R x \Sigma B$
TAPMX	Time Averaged Product Maximum from velocity and azimuth sweep
UKAEA	United Kingdom Atomic Energy Authority
UWO	University of Western Ontario
WRA	Warramunga Medium Aperture Seismic Array (Australia)
YKA	Yellowknife Medium Aperture Seismic Array (Canada)

SYMBOLS	DESCRIPTIONS
Δ	Epicentral distance
ΔV	Velocity fluctuation
>	Greater than

$<$	Less than
Σ	Summation
τ	Time Delay Function

CHAPTER 1

INTRODUCTION

1.1 INTRODUCTION

One of the advantages of using more than just the first arrival times of P waves in the analysis of seismic data is the fact that in travelling between the source and the receiver, the basic waveform of the signal becomes significantly altered in character, preserving a wealth of information about the structures encountered along its travel path. This information may, in theory, be extracted with suitable and appropriate techniques. By the same token, one of the major problems of observational seismology is the correct interpretation of the large amount of details often observed in seismic record sections. The problem is often complicated by the fact that, as with most geophysical problems, no unique solution is possible and one must be content with a solution that is consistent with presently available data.

Part of the complexity in recorded signals is caused by noise generated by the recording system, but advances in instrumentation and data processing techniques have eliminated this problem to a large degree. By far the greatest cause of signal complexity is, therefore, due to

various scattering processes in different regions of the Earth's interior during transmission of the signal from the source to the receiver. This problem has been the subject of investigation by many workers, and the diversity of both the approach and the interpretation of the cause is testimony of the complexity of the problem.

1.2 BACKGROUND FROM PREVIOUS STUDIES

P-wave scattering studies were not very widespread until relatively recently for a good reason. The major disadvantage of using conventional single station seismograms for studying the scattering phenomenon is that details of other arrivals apart from the main seismic phases (e.g. P, PP, e.t.c.) are often completely lost in the maze of arrivals. Since scattered waves generally arrive at a receiver simultaneously from a range of different directions with different apparent velocities (King et al., 1975), it was not until the advent of array networks that a reliable estimate of the slownesses and azimuths of the various contributions became possible.

It was apparent for a long time that certain arrivals could sometimes be recognized on seismic records which were not accounted for in the Jeffreys-Bullen (JB) tables or travel-time curves, and it was clear from their travel times that these were none of the regular phases. One of the earliest interpretation of the coherent signals between P and 60 seconds after PP was by Nguye-Hai in 1963 who

interpreted them as topside or underside reflections from upper mantle discontinuities (King et al., 1975). This is the so-called P_dP hypothesis (d is the depth of the discontinuity) which was subsequently used by many others to explain various coda arrivals (see for example, Bolt et al., 1968; Husebye and Madariaga, 1970; Davies et al., 1971; Gutowski and Kanasewich, 1974). However, Wright and Muirhead (1969), and Wright (1972) showed from array studies that the observed travel times and slownesses of these precursors were inconsistent with the P_dP hypothesis, and suggested an interpretation involving asymmetric reflection at distances near 20 degrees from the source or recording station.

Cleary et al. (1975), on the other hand, suggested that the travel times and slownesses of body wave coda which follow P and the precursors to PP were consistent with scattering by random inhomogeneities in the crust and uppermost mantle. This interpretation was also applied to precursors to PKP (Wright, 1975), and precursors to PKPPKP (Haddon et al., 1977). Precursors to PKPPKP were also interpreted as a result of scattering at various depths in the mantle (Doornbos and Vlaar, 1973; Doornbos, 1975). Alternative interpretations of P signal complexity include those of Aki (1969), Aki and Chouet (1973) who interpreted coda waves from small local earthquakes as backscattering from numerous heterogeneities distributed uniformly in the crust; and Douglas, Marshall and Corbishley (1971), Douglas

et al. (1973), and Barley (1977) who interpreted signal complexity as the result of differential attenuation or absorption; the effect of attenuation of the direct P signal relative to the later arrivals.

One other important manifestation of P-wave scattering in seismic data which has been the subject of more recent investigations is the relatively large amount of small-scale fluctuations in seismic parameters such as travel times and amplitudes. These fluctuations which are significantly larger than the corresponding measurement errors (Dahle et al., 1975) were explained by modelling the crust and upper mantle as a Chernov (Chernov, 1960) random medium (Aki,1973; Capon, 1974; Christoffersson, 1975; Berteussen et al., 1975, 1977).

1.3 OUTLINE OF THESIS

With the above background in mind, the prime objectives of the present study are: (1) to investigate how small-scale fluctuations in travel-time, amplitude, and slowness measurements may be accounted for by P-wave scattering in the crust and upper mantle, and (2) to investigate the relationship between P-wave scattering along the signal travel path, and upper mantle heterogeneity. Accordingly, a random media method of modelling the crust and upper mantle was adopted for the first part, and a coherence method was developed for the second part.

In Chapter 2, numerical experiments are developed to test and predict the observed behaviour of travel-time data for crustal models. A ray tracing program which was written to produce travel-time curves for various two-dimensional random models is also described (see also Mereu and Ojo, 1980). In Chapter 3, the results and observations of Chapter 2 are applied to some refraction data from a long-range experiment in southern Manitoba and Saskatchewan. Chapter 4 discusses the numerical experiments of Chapter 2 as they apply to the upper mantle. In Chapter 5, a coherence method of determining the relative scattered energy in a signal by using array record sections is developed. The factors that affect the efficiency of the method are also investigated with synthetic data in Chapter 5, and with real data in Chapter 6. In order to relate the measured scattered energy to the P-wave scattering characteristics of the signal ray paths, over 340 earthquake recordings from Gauribidanur array (GBA) in India for earthquakes in the distance range 15-35 degrees and 40-70 degrees, and Yellowknife array (YKA) in Canada for the distance range 12-30 degrees were analyzed. The earthquake data had been used in a previous study (Ram and Mereu, 1977), and were divided according to four seismic zones for GBA data, and two seismic zones for YKA data. The results of these analyses are described in Chapter 7 (see also Ojo and Mereu, 1980). A summary of the major findings of this work is given in Chapter 8.

CHAPTER 2

P-WAVE SCATTERING THROUGH A CRUST WITH RANDOM INHOMOGENEITIES

2.1 INTRODUCTION

When large-scale, deep seismic refraction experiments for crustal studies were started more than three decades ago, interpretation of the data was often based on the two or three-layered model in which the velocity in each layer was asssumed to be constant. On this basis several intra-crustal discontinuities, including the Conrad discontinuity which ostensibly separates two regions with boundary velocities from 6.0-6.6 to 6.8-7.2 km/s and depth ranging from about 10 to 20 km, have been widely reported in the literature (Hodgson, 1953; Katz, 1955; Bolt et al., 1958; Hales and Sacks, 1958; Doyle et al., 1959; Press, 1960; Woollard, 1959; Berry and West, 1966 and others.) However, neither the Conrad discontinuity nor any of the other intra-crustal discontinuities are consistent in their occurrence, velocity, or depth on a world wide basis (see for example Steinhart and Woollard, 1961, Table 1).

More recently detailed crustal investigations based not only on the refraction method, but also the reflection method, the dynamic characteristics of seismic record

sections, and geological evidence have shown that this simple layered model does not adequately explain all the data observed. Most workers therefore accept that there are shortcomings in this simple interpretation, and that it is unlikely that intra-crustal discontinuities are continuous over the large distances covered in seismic refraction surveys.

When, for instance, the results from deep seismic crustal reflection experiments are compared with those of refraction experiments (see for example Mair and Lyons, 1976; Berry and Mair, 1980), two relatively different pictures of the crust emerge in general. The reflection experiments (see for example Figure 2.1; or Cumming and Chandra, 1975; or the Cocorp data, Smithson et al., 1979) show that, (i) apart from the sedimentary layers near the surface, very few sub-surface discontinuities including the Moho are continuous, and (ii) the observed reflector segments are numerous and are scattered about at various depths through the section. On the other hand, because of the basic assumption inherent in the refraction method, the various observed travel-time lines (see Figures 3.2-3.6 in Chapter 3) are associated with various layers within the Earth. Simple earth models thus have a two layered crust separated by the Conrad discontinuity, this being based on the observation of P_g and P* branches. More complex models may have several layers with gradients including low velocity ones and lateral structures to explain the

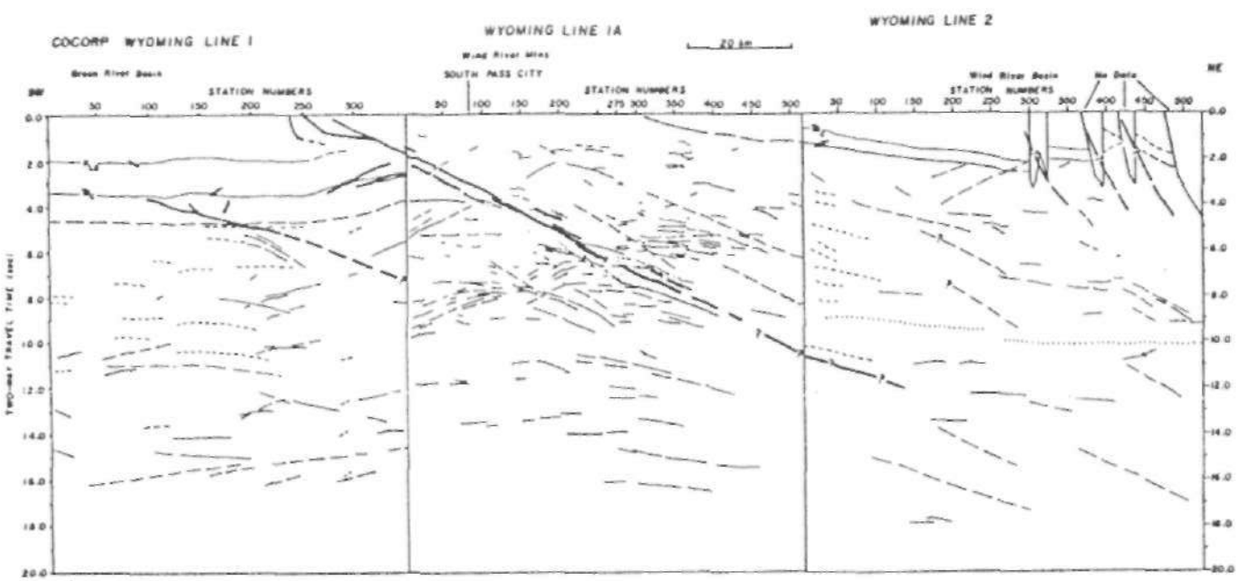


Figure 2.1: Line drawing composite showing the structure and reflections picked for lines 1, 1A, and 2 (after Smithson et al., 1979).

complexity of many sections.

It is well known that refraction experiments do not have the resolving capabilities of reflection experiments, and that structures derived from them tend to be much more simple. This, however, only partially explains the two results, and although some of the observed features of the record section are accounted for by such simple models numerous inconsistences remain particularly concerning the erratic behaviour of amplitudes which sometimes vary by an order of magnitude over only a few kilometers, and are frequently not associated with any theoretical travel-time line predicted by the model. A detailed review of the problems of interpreting crustal data was given by James and Steinhart (1966). Part of the problem obviously stems from the fact that the crust and mantle are heterogeneous media. Indeed, the other extreme of the conventional layered model approach is to assume that the seismic structure of the crust and upper mantle is so complex that it behaves as a medium with random inhomogeneities (see for example Nikolajev and Tregub, 1970).

In recent years considerable progress was made in using the Chernov random media theory (Chernov, 1960) to explain travel-time and amplitude anomalies (Aki, 1973; Capon, 1974; and Berteussen et al., 1975). The Chernov theory is based on a statistical description of the medium in terms of the mean square of fractional fluctuation of velocity, the correlation distance, and the linear extent of the

inhomogeneous region. The correlation distance is defined as the distance between two points at which the velocity fluctuations become uncorrelated. There is evidence from some of these studies that a correlation distance of 10 to 15 km exist under the LASA and NORSAR arrays, and in the paper of Berteussen et al. it was shown that 50% to 60% of the variance of time and amplitude anomalies at NORSAR could be explained by random media theory. Aki et al. (1976, 1977) also found from three-dimensional earth modelling studies that the lower limit of true r.m.s. velocity fluctuations in the lithosphere under these arrays is about 3%. A similar value was obtained for upper mantle structure beneath the United States (Romanowicz, 1979). How such fluctuations affect the travel-time lines is the subject of this chapter.

2.2 DEVELOPMENT OF THE NUMERICAL EXPERIMENTS

In spite of the uncertainties in the interpretation of detailed structures from refraction data, there still remains the broad agreement from numerous such experiments that large vertical velocity gradients exist within the crust as well as the upper mantle (see for example Mereu et al., 1977). If this is the case then it would not be realistic to model the crust as a random medium in the vertical direction in the same manner that it is modelled in the horizontal direction. A reasonable picture of the real Earth would therefore have a simple deterministic character

in the vertical direction with a certain degree of randomness superimposed on it in both the horizontal and vertical direction. The vertical velocity gradients can be associated with high pressure physical effect, and the lateral variations with compositional changes in the various rock types.

With the above in mind, numerical models were generated using the following equation (Mereu and Ojo, 1980).

$$V_{ij} = U_j + \Delta V_{ij} \quad , \qquad (2\text{-}1)$$

i and j are, respectively, the horizontal (distance) and vertical (depth) location of the point with velocity V_{ij}.

where $\Delta V_{ij} = K\ (A_{ij} * F_{ij})$ (2-2)

Here V_{ij}= the discrete two dimensional array of velocities used in the model

U_j = the discrete vertical velocity values for a given simple spherically symmetric earth model.

ΔV_{ij}= the lateral variations in velocity.

A_{ij}= a two-dimensional array of random numbers.

F_{ij}= a simple smoothing filter of dimensions L x L

K = a scaling factor such that the maximum value of the smoothed random numbers is equal to ΔV_{max} where ΔV_{max} is the maximum variation which the velocity will be allowed to have at any depth.

K and L are two parameters that affect the amplitude and size of the velocity anomalies respectively. Figure 2.2 illustrates a hypothetical starting model (U_j) with the

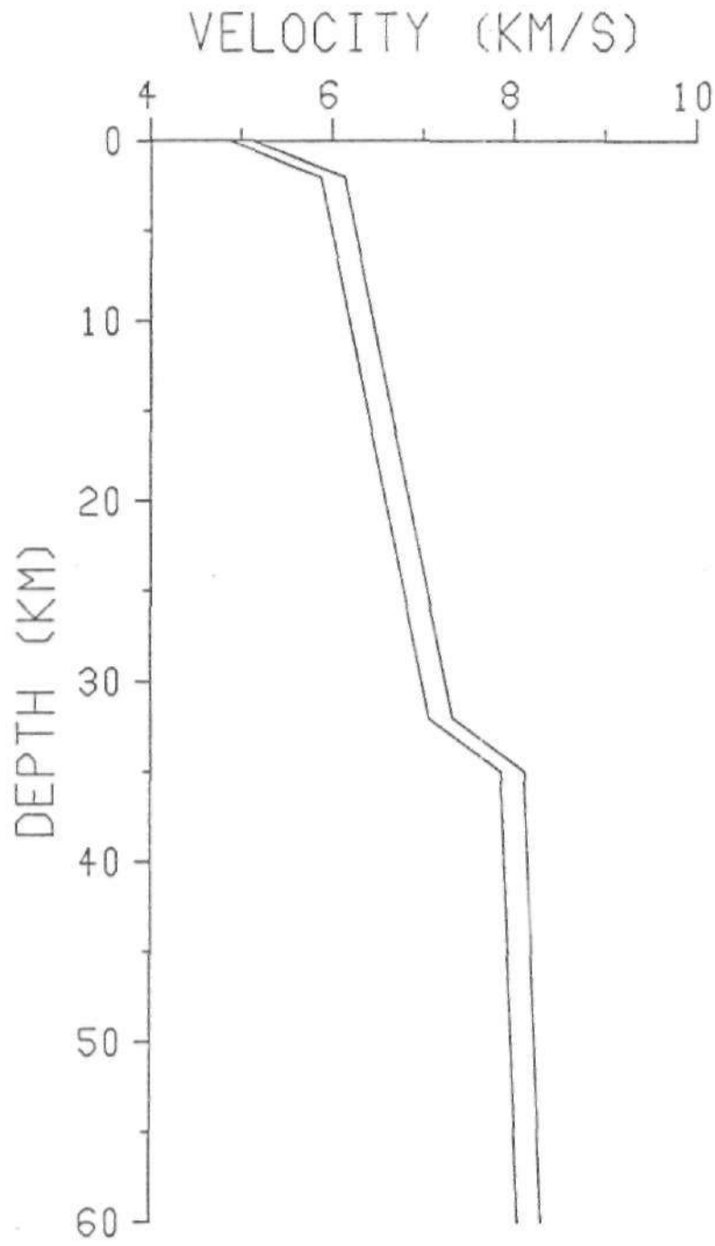


Figure 2.2: Starting velocity model with smooth lateral variation superimposed on a velocity gradient.

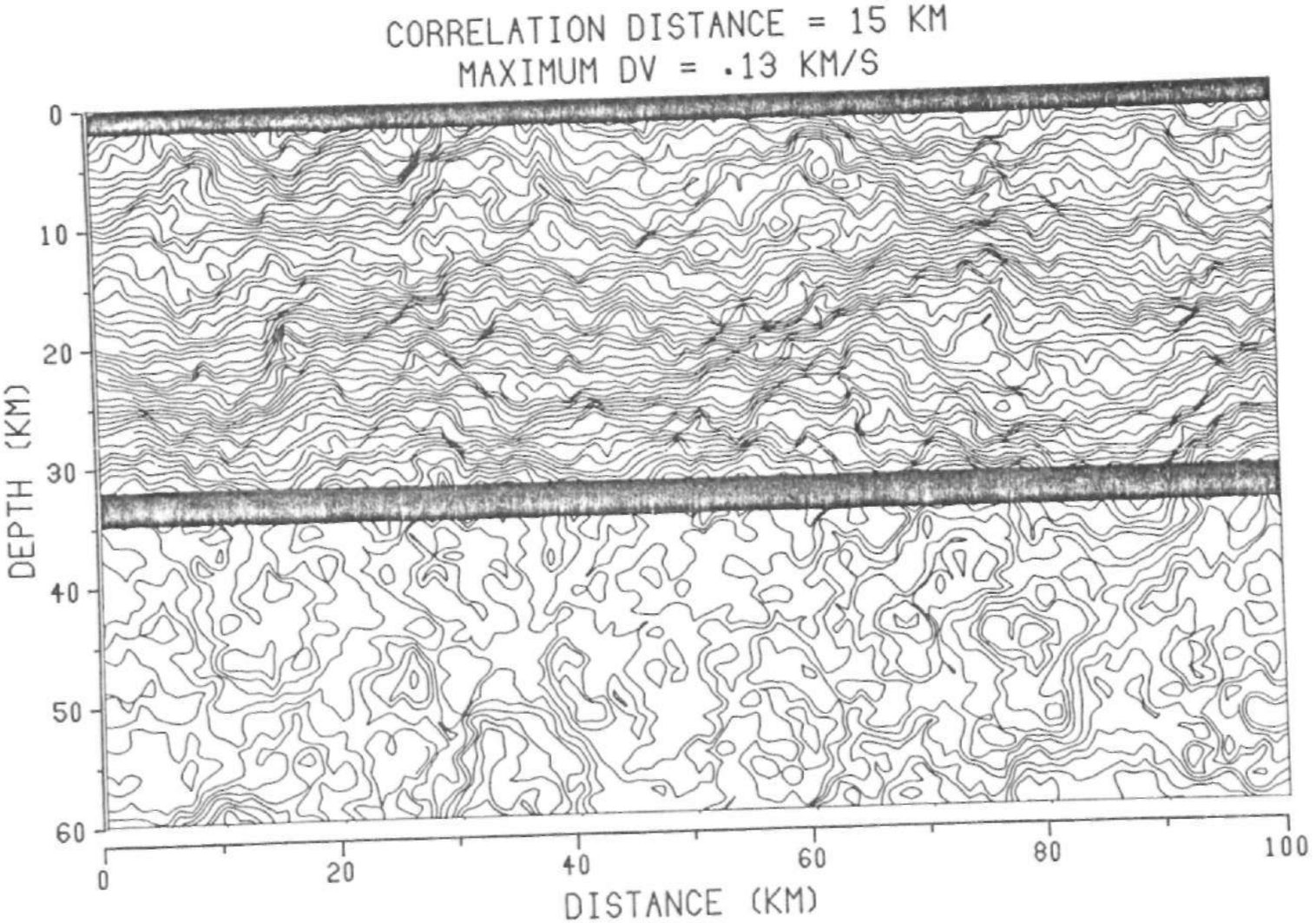
parallel lines showing the maximum variation allowed at each level. In all the models used K was chosen so that only small values of ΔV_{max} (i.e. 0.26 km/s or less) were generated. This value corresponded to a maximum root mean square (r.m.s.) fluctuation in velocity of about 2.5% for the models. Figure 2.3 is a velocity contour plot of the final model, and shows how the velocity varies with horizontal distance and depth. It is interesting to note that if a reflection experiment were done over an earth depicted by the model of Figure 2.3, reflectors with relatively small slopes would probably be detected at locations where the velocity contour lines are close together. There will therefore be numerous short reflectors distributed at various depths throughout the model, and the overall appearance of Figure 2.3 will be similar to the record sections obtained from near vertical reflection crustal experiments.

Figure 2.4 is a velocity contour plot of a different model similar to that of Figure 2.3, but derived from a different suit of random numbers. In this manner, different models can be generated with the same controlling parameters of U_j and ΔV_{max} so that the characteristics determined for these parameters may be statistically significant.

One important point to note about the model concerns the parameter L. It is defined as the correlation distance, and the corresponding correlation function is defined as the two dimensional autocorrelation function of the smoothing

Figure 2.4: Velocity contour plot similar to Figure 2.3 for a different set of random numbers.

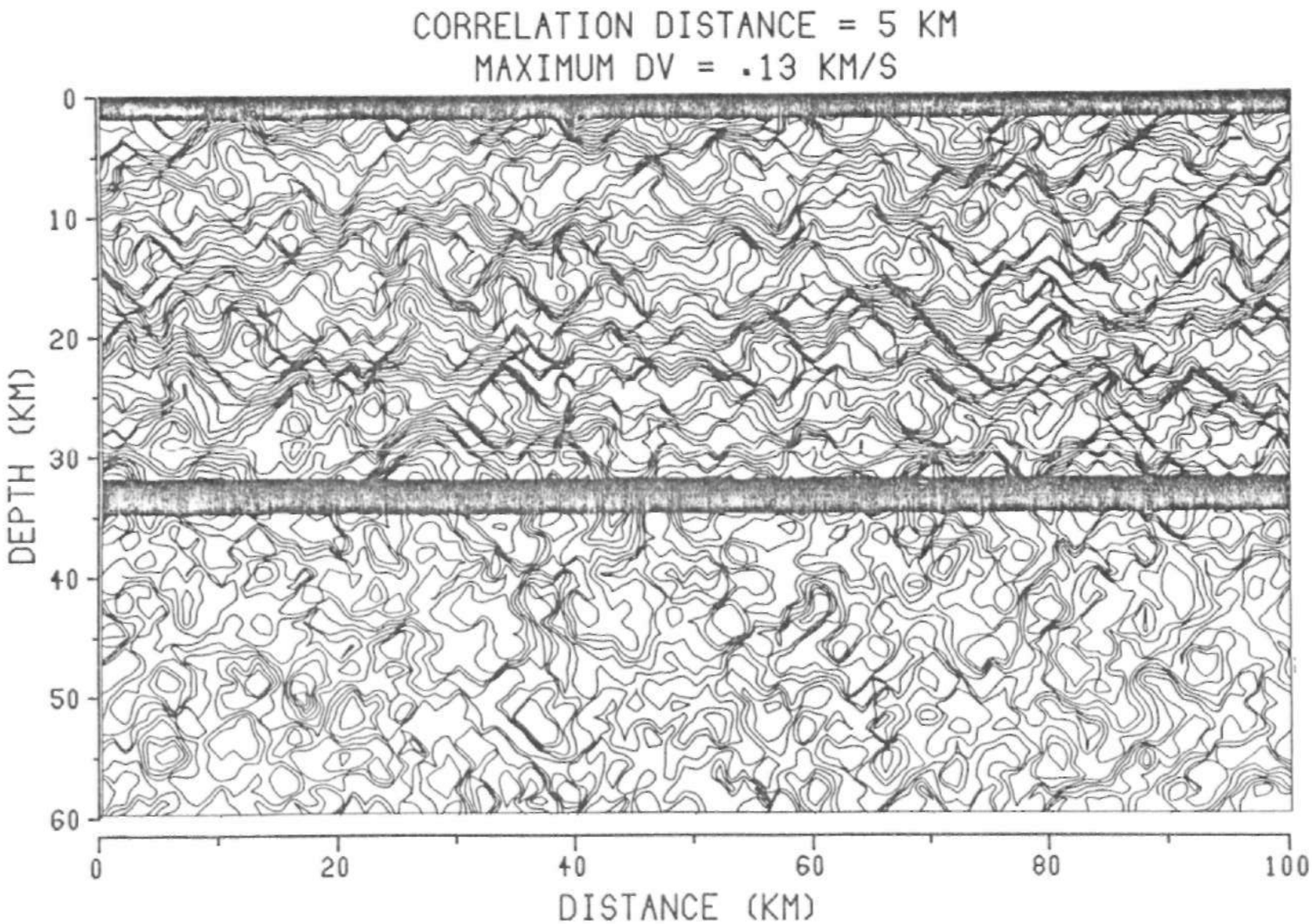
Figure 2.3: Velocity contour plot of model shown in Figure 2.2. Contour interval is 0.025 km/s. The two bands at the top and middle of the plot were caused by a large concentration of contours due to high velocity gradients at those depths in the model.

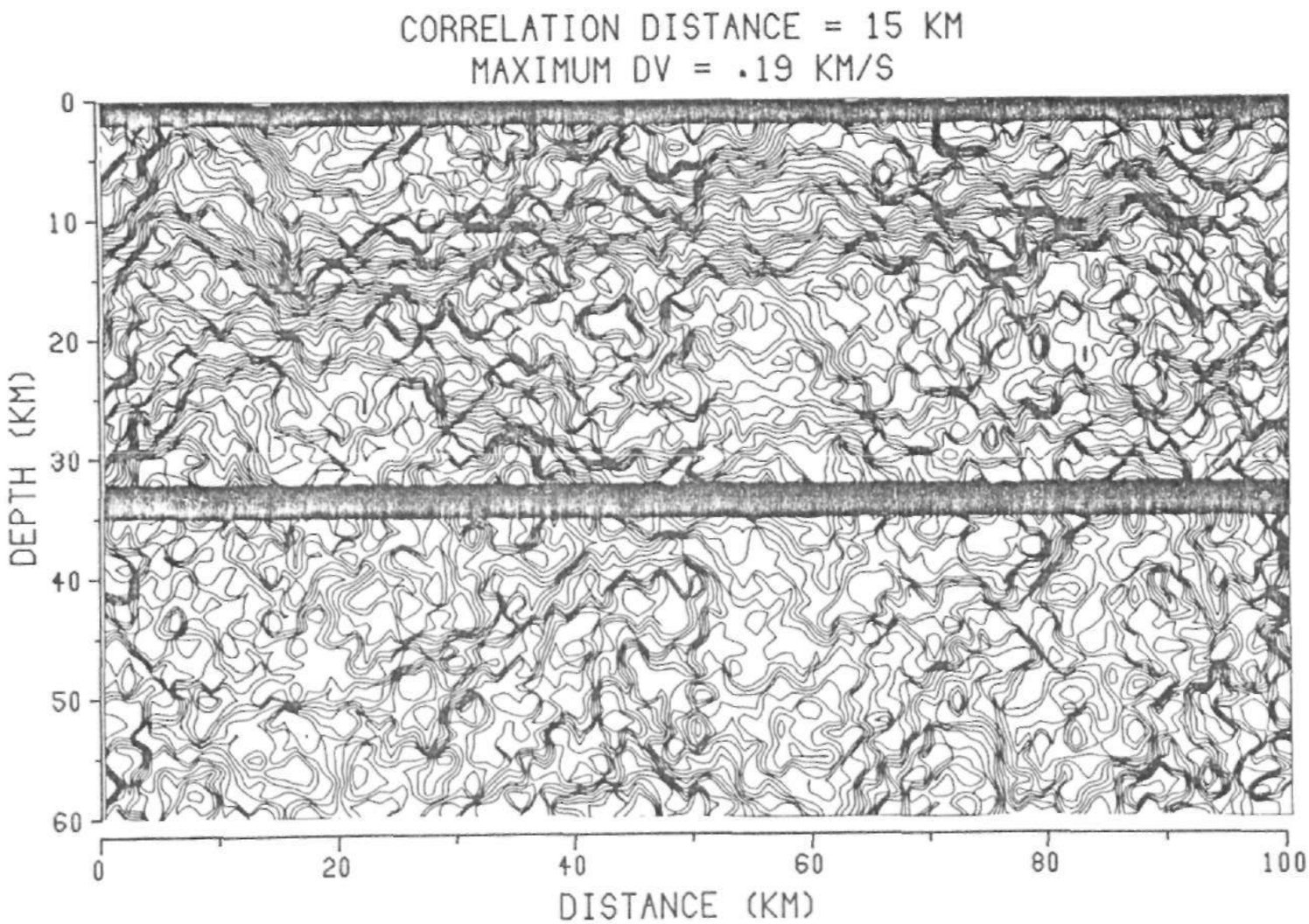

CORRELATION DISTANCE = 15 KM
MAXIMUM DV = .13 KM/S
DEPTH (KM)
0
10
20
30
40
50
60
0
20
40
60
80
100
DISTANCE (KM)

filter F_{ij}. Such a function is triangular in shape (for example, the autocorrelation of (1,1,1) is (1,2,3,2,1)), and is similar in form to the Gaussian function used in the Chernov random media theory. It is well known that the autocorrelation function of a set of completely random numbers is a delta function, whereas the autocorrelation function of the filtered numbers will have the same form as the filter's autocorrelation function (Robinson, 1967b). It therefore follows that by smoothing the set of random numbers with F_{ij}, the size of the observed structure is determined by L. Figure 2.5 and Figure 2.6 illustrate the effect on the model of changing the quantities L and ΔV_{max} respectively. It will be noted that while the layering effect appears to be enhanced by decreasing L (Figure 2.5), or increasing ΔV_{max} (Figure 2.6), the continuity of the layers are greatly reduced by so doing, thereby contributing to the overall picture of short reflectors interspersed by transparent zones.

2.3 DETERMINING THE CHARACTERISTICS OF NUMERICAL MODELS

One of the most powerful ways of determining the complete response of a medium to a point source is through the use of a finite difference approach (Kelly et al., 1976; Alterman and Karal, 1968). Such a method is capable of predicting all transmissions, reflections, diffractions and wave conversions. In other words it should be possible to determine the complete scattered field of energy at any


CORRELATION DISTANCE = 5 KM
MAXIMUM DV = .13 KM/S
DEPTH (KM)
0
10
20
30
40
50
60
0
20
40
60
80
100
DISTANCE (KM)


CORRELATION DISTANCE = 15 KM
MAXIMUM DV = .19 KM/S
DEPTH (KM)
0
10
20
30
40
50
60
0
20
40
60
80
100
DISTANCE (KM)

particular point and at anytime. However, its major limitation is the fact that the computing cost and core requirements on a large-size computer rapidly become excessive as the number of grid points used increases. Kelly et al. (1976) used 140 x 100 and 250 x 100 grid mesh with a grid spacing of 20 ft in their models. They found that the approximate central processing unit (CPU) time for an average model with traces of length 0.6 to 0.8 seconds was 8 minutes. By comparison, our typical crustal models were 220 x 60 km, and the size of the upper mantle models were at least 3000 x 1000 km. It would therefore have required excessive computer time, core requirements, and cost to solve such a problem adequately with the finite difference approach. This method was not used here for that reason, and in its place, travel-time curves were obtained with the ray theory using a method similar to that described by Gebrande (1976). This restricted meaningful solutions to only those cases where the correlation distances were much longer than the wavelength of typical short period waves, and to the first arrival energy.

2.3.1 THE RAY TRACING PROCEDURE AND COMPUTER PROGRAMS

Ray tracing methods can be divided into two broad categories. The first category traces rays between two specified end points (see for example Julian and Gubbins, 1977; Pereyra et. al., 1980), and in the second the starting point and direction of the ray at the source are

specified (e.g. Jackson, 1970; Gebrande, 1976). Although both methods have adaptations for use in inhomogeneous media, the latter method was preferred because it would allow a study of the focussing and de-focussing effects of local velocity gradients in the models. The method we have used traces rays through a rectangular or spherical two-dimensional grid of points representing a cross-section of the earth, where each point of the grid corresponds to a given spatial location with a sampled velocity. The calculation of ray paths and travel times were based on Snell's Law, and the equations used are those for a continuously changing velocity model with discontinuities being treated as transition zones with steep velocity gradients. In general, therefore, the ray path is an arc of a circle with a radius of curvature equal to (Telford et al., 1976 p. 274; Gebrande, 1976),

$$\rho = V/(|\text{grad } V|.\sin\alpha) \qquad (2\text{-}3)$$

where V is the velocity, grad V is the velocity gradient and α is the angle between the direction of the ray and the velocity gradient at the starting point of the ray. If the velocity is piece-wise constant the radius of curvature will also be constant, and one can proceed along a ray from one point to another by following the curvature through a very small angular increment $\Delta\phi$ corresponding to a small arc $\rho\Delta\phi$ (Figure 2.7).

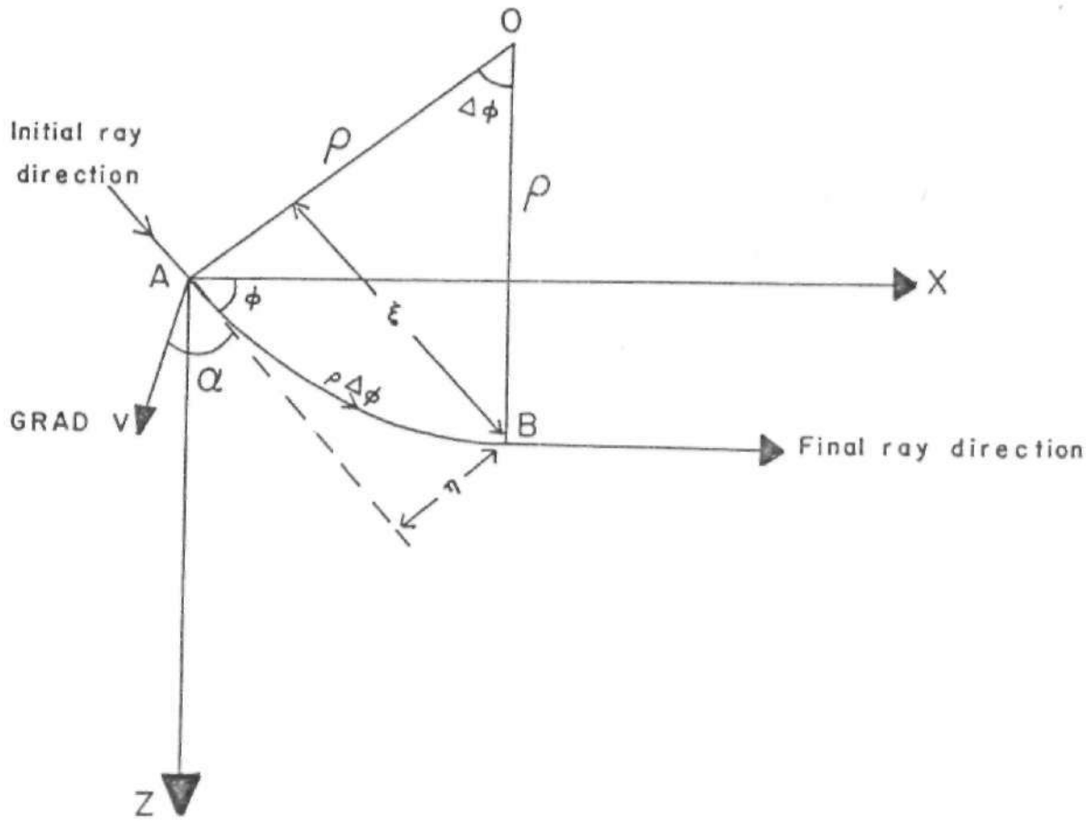


Figure 2.7: Ray-tracing configuration for flat earth model.

The computational procedure then consisted of determining at the point corresponding to the seismic source (for instance point A in Figure 2.7) the velocity gradient (grad V), the angle (α), and the radius of curvature (ρ). The new point (B) which is reached by bending the ray through the small arc $\rho\Delta\phi$ was determined by moving a distance

$$\xi = \rho \sin \Delta\phi \tag{2-4}$$

in the direction of the ray and,

$$\eta = \rho(1-\cos \Delta\phi) \tag{2-5}$$

in a direction normal to the ray. The coordinates of the new points (X_B, Z_B) with respect to the old point (X_A, Z_A) is then given by

$$X_B = X_A + \xi \cos \phi + \eta \sin \phi \tag{2-6}$$

$$Z_B = Z_A + \xi \sin \phi - \eta \cos \phi \tag{2-7}$$

where ϕ is the angle the ray makes with the x-axis.

Alternatively for a spherical earth model the polar coordinates of A is (R_A, θ_A), and the coordinate of the new point B can be computed from the geometry of the configuration (Figure 2.8), i.e.

$$R_B = [R_A^2+4\rho^2\sin^2(\Delta\phi/2)-4R_A\rho\sin(\Delta\phi/2)\cos(i+\Delta\phi/2)]^{\frac{1}{2}} \tag{2-8}$$

Now since

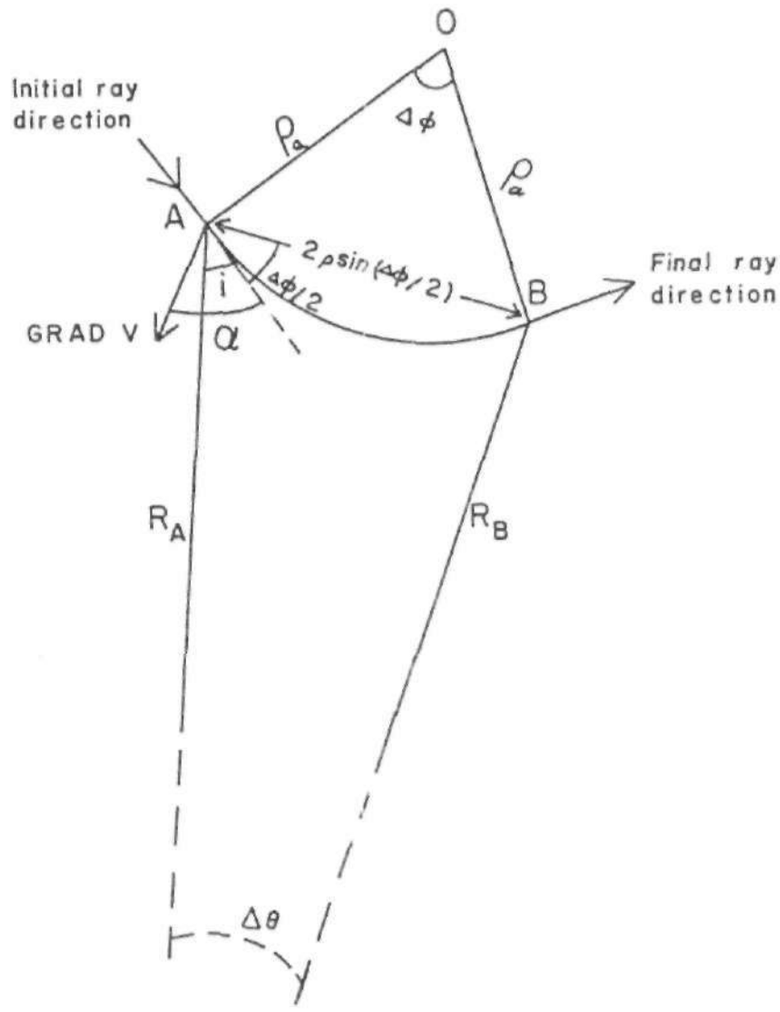


Figure 2.8: Ray-tracing configuration for spherical earth model.

$$AB/\sin(\Delta\theta) = R_B/\sin(\Delta\phi/2 + i) \tag{2-9}$$

$$\Delta\theta = \sin^{-1}\left[\frac{2\rho \sin(\Delta\phi/2).\sin(\Delta\phi/2 + i)}{R_B}\right] \tag{2-10}$$

and

$$\theta_B = \theta_A + \Delta\theta \tag{2-11}$$

The travel-time from point A to point B is (Gebrande, 1976),

$$\Delta t = \frac{1}{|\text{grad } V|}\left[\text{Arctanh}(\cos\alpha) - \text{Arctanh}(\cos(\alpha+\Delta\phi))\right] \tag{2-12}$$

At the new point B a new initial ray direction was found, and a new velocity gradient was determined by interpolation. By successively repeating the process the ray paths could be traced step-by-step from their source to the earth's surface.

In the special case when grad V=0 or $\sin(\alpha)=0$, the ray path is not curved but straight, $\Delta\phi$ must therefore be set to zero and ξ fixed to a small value. Then

$$\Delta t = \xi/V \tag{2-13}$$

for grad V = 0, or

$$\Delta t = \frac{1}{|\text{grad } V|} \ln(V_B/V_A) \tag{2-14}$$

for $\sin(\alpha) = 0$.

Other points to be noted regarding computational procedure are the signs of ρ, η and $\Delta\phi$. The radius of curvature is a signed quantity and is positive if the centre of curvature is located to the left side relative to the direction of the ray, and vice-versa. Similarly, a positive sign of indicates an anti-clockwise curvature of the ray. The sign of $\Delta\phi$ must be chosen to be identical with that of ρ.

Because the incremental value $\Delta\phi$ was chosen arbitrarily small, the ray path would, in general, not terminate at the earth's surface. When the ray therefore penetrated the earth's surface by a distance greater than a pre-set small value, the last point was abandoned, and the incremental value reduced. This process was then repeated until the ray terminated at the earth's surface to within the pre-set value.

Two computer programs were written in Fortran IV for a two-dimensional flat earth model and a spherical earth model according to the equations described in the last section. Table 2-1 summarizes the various computational steps in the computer program, and the program lists are given in Appendix A. In step 5 of Table 2-1, the variation of velocity and velocity gradient within any cell made up of four neighbouring grid points were assumed to be linear within the cell, and were interpolated from the values of the four neighbouring grid points. This approximation was found to be sufficiently accurate provided the grid size was not too large; typical values were 1 km for the flat earth

TABLE 2-1

MAIN COMPUTATIONAL STEPS IN RAY TRACING PROGRAM

1. Read from disc file grid parameters, e.g. area (LX by LZ), grid size (HX by HZ); and fix incremental arc length (ARC=$\rho\Delta\phi$) as a fraction of the grid interval.

2. Read from cards initial starting coordinates of ray, initial angle of incidence, maximum angle of incidence to be investigated, and incremental value; compute ray parameter.

3. Read velocity data from disc file, and compute corresponding spacial coordinates.

4. Compute horizontal (or tangential) component, and vertical (or radial) component of velocity gradient, and the resultant velocity gradient at each grid point (GRADV).

5. Locate position of ray head with respect to the origin, and determine the velocity and the magnitude, and direction of the velocity gradient (GRADV) at this point. Compute the angle between GRADV and the direction of the ray path (ANGI).

TABLE 2-1 Continued

6. Compute the radius of curvature of the ray path (RHO), and the incremental angle (DELPHI); project ray through arc, and compute the new coordinates of the ray path.

7. Check to ensure that ray has not penetrated the earth's surface, and compute the piece-wise time (DELT), and the total time (T) to new point.

8. Compute new ray direction and repeat steps 5 to 7 until ray penetrates the earth's surface.

9. When ray penetrates the earth's surface, terminate the ray within specified distance of the surface, and compute the total time (T), the total distance (AND), the reduced travel-time (RTM), and slowness (SL).

10. Change the angle of incidence, and repeat steps 2 to 9.

11. Output results onto line-printer, and plotter if desired.

model and 5 km for the spherical earth model.

When the program was applied to uniform spherically symmetric earth models as a check, the results obtained were found to agree very closely to that predicted by conventional spherical ray theory (Bullen, 1963). An example is shown in Figure 2.9. It should be noted that the procedure described above works best in the absence of sharp discontinuities.

All computations were performed on a Control Data Corporation (CDC) Cyber 73 computer at the University of Western Ontario. The computer has 96K words of Central Memory and 125K words of Extended Core Storage. The travel times of a typical crustal model for rays separated by 0.5 degrees of incident angle required an average of 37K words of memory and 4 minutes CPU time. For the average upper mantle model, the equivalent values are 25K words of memory and 10 minutes CPU time. The upper mantle model required less core memory because more disc facilities were used to cut down on the core requirements.

2.4 GENERAL TRAVEL-TIME RESPONSE OF NUMERICAL MODELS

The starting velocity model which was the basis of all our numerical experiments is shown in Figure 2.2. Two relatively large velocity gradients were incorporated in this starting model based on evidence, in the literature, from numerous seismic refraction experiments (see for

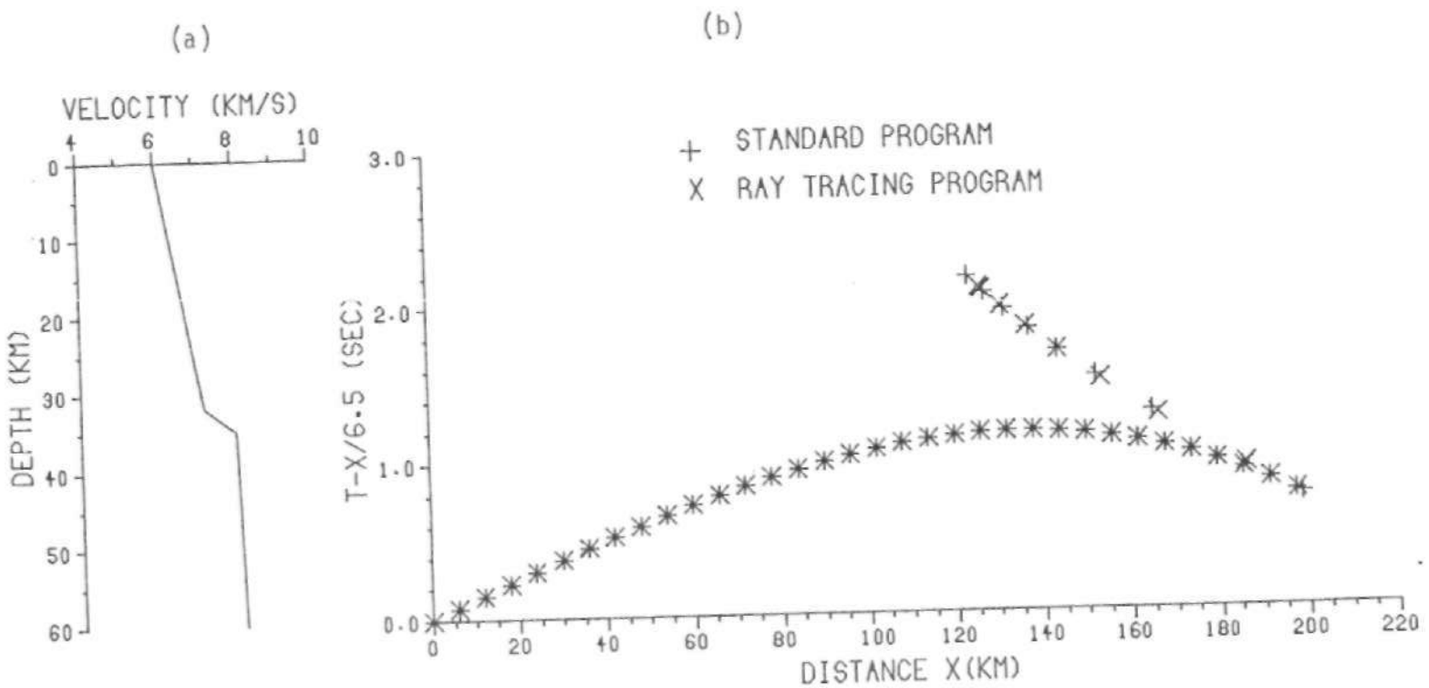


Figure 2.9: (a) Simple crustal earth model, and (b) comparison of ray-tracing travel times with standard ray theory (Bullen, 1963) travel times for model in (a).

example Berry and Fuchs, 1973). The first steep gradient from 5.0 - 6.0 km/s in the top 2 km is based on the general knowledge that velocities of about 3.0 - 5.0 km/s are characteristic for the sedimentary, or metamorphic rocks which cover the consolidated crust. The thickness of this layer is very variable and an arbitrary value of 2 km was chosen for the model. The second steep gradient from 7.2 - 8.0 km/s at a depth of 32 km is associated with the Moho discontinuity, and one of the strongest evidence for this is the large amplitude retrograde reflection branch which is commonly observed on seismograms in the distance range 120-200 km. Apart from these two regions the crust was assumed to contain no velocity discontinuities, and to have a gentle linear gradient from the earth's surface to the M-discontinuity.

If there were no lateral heterogeneities (i.e. $\Delta V_{ij} = 0.0$), the travel-time curve of such a model would be a smooth continuous curve. Figure 2.10 shows the travel-time points and ray paths for a number of rays, separated by equal intervals of incident angle, emanating from a surface point source which were traced step by step through the laterally homogeneous model. The rays were not plotted near the shot point because the density of rays at this point tended to smear the plot. For this reason also, travel-time points for the first 10-15 km of distance representing the top layer with the high velocity-gradient were not plotted in all the subsequent plots. It will be noted in Figure

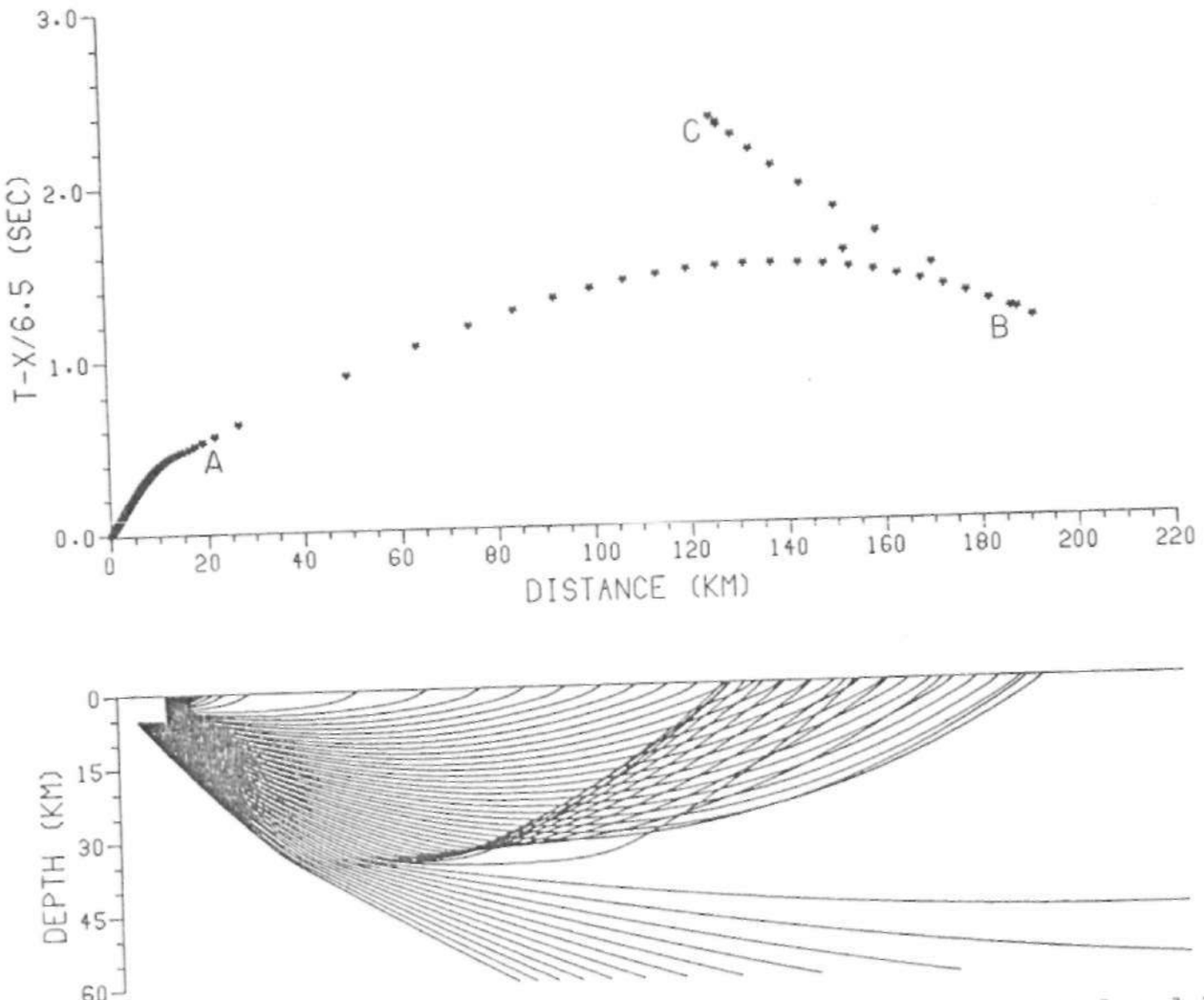


Figure 2.10: Travel-time plot and ray diagram for homogeneous crustal model.

2.10 that apart from the first 20 km, and the ends of the branches AB and BC where the points are highly concentrated, all the other points increase in concentration progressively along the forward branch, and the retrograde branch. Since areas of large concentration of points on the curve indicate large amplitude arrivals and vice-versa, the travel-time curve predicts that there should be no erratic variation in first arrival amplitudes for a laterally homogeneous earth.

Figure 2.11 shows the travel-time plot and ray paths through a model with velocity perturbations such that ΔV_{max} was 0.13 km/s (maximum r.m.s. velocity fluctuation was 1%), and the correlation distance was 15 km. An examination of this figure shows that the smooth continuous nature of the curve for the homogeneous model has disappeared, and in its place is a travel-time curve which can clearly be broken up into different line segments. Furthermore, amplitude variations now appear along the line segments indicated by the concentration of the travel-time points at certain distances along the profile.

Figure 2.12 is an example of two of the travel-time plots obtained for a series of models using different combinations of ΔV_{max} and L. The apparent velocities computed from linear least-squares fit to the points of the resulting line segments are also shown in the figure. Attention is particularly drawn to the apparent velocities and intercept times of the second line segments of the travel times which show an apparent rise when the

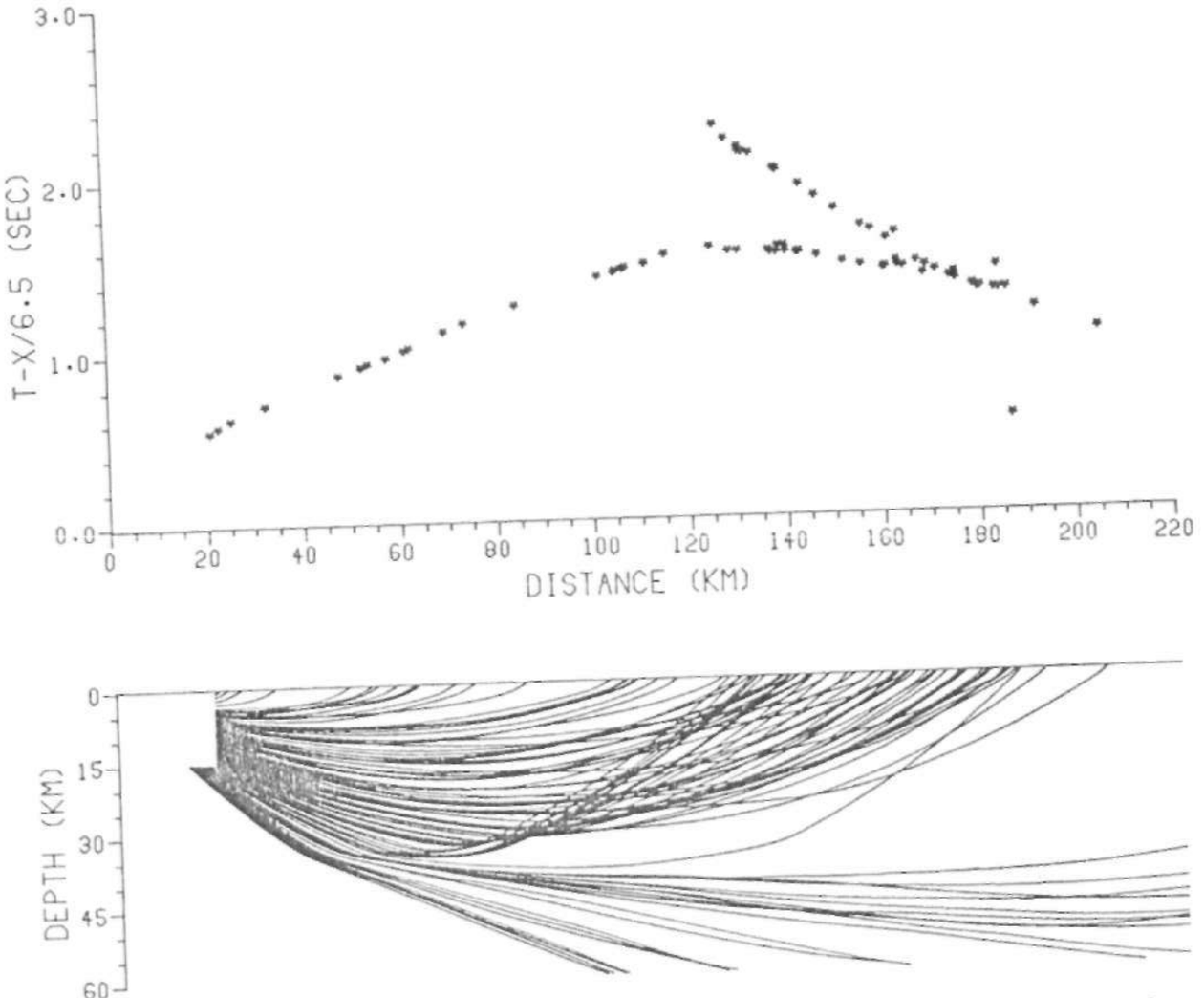
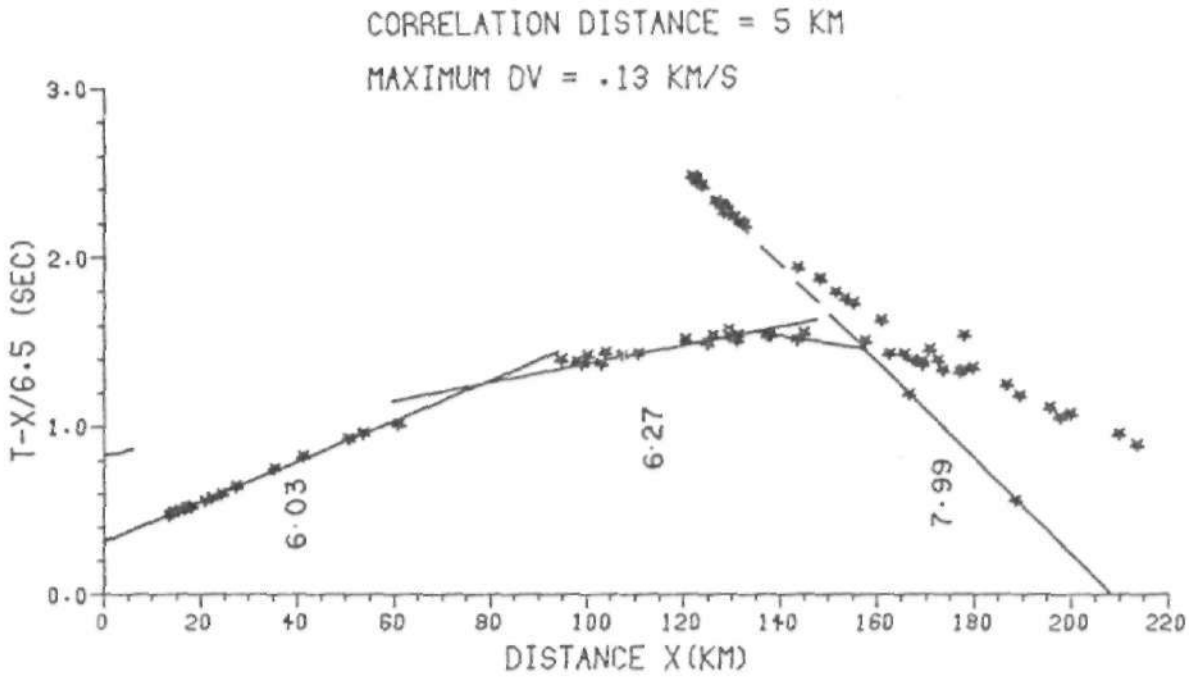


Figure 2.11: Travel-time plot and ray diagram for heterogeneous crustal model.

(a)



(b)

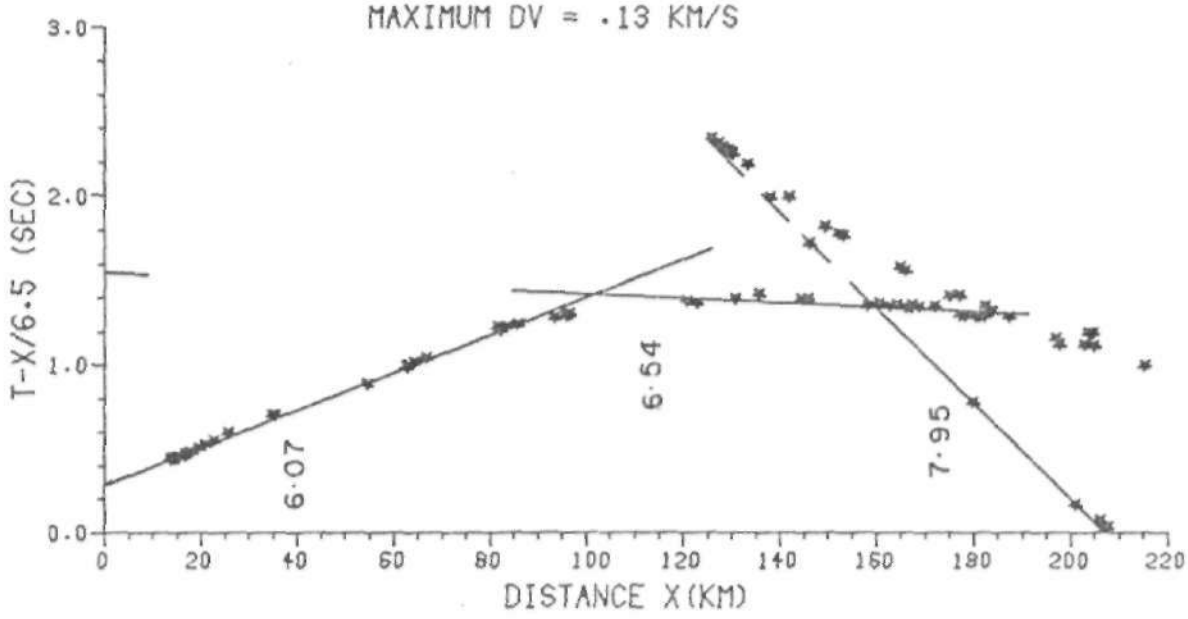


Figure 2.12: A comparison of travel-time plots and least-squares regression velocities for a model with (a) correlation distance of 5 km, (b) correlation distance of 15 km.

correlation distance L was increased. Some further illustrations will be found at the end of this chapter (Figures 2.17-2.24). An examination of the figures show the following main features (excluding the top layer).

(i) The travel-time curves are broken up into two or more line segments with variable apparent velocities and cross-over points. This suggests that one or more apparent discontinuities are present.

(ii) The average velocity of the different line segments depends on the number of apparent refractors in the layer, and the boundary velocities.

(iii) The first segment (P_g) has much less scatter on it than the second segment (P*).

(iv) If the breaks in the travel-time line are interpreted as resulting from intermediate discontinuities, their depths range in value from about 5 km to 14 km.

(v) No large retrograde reflection branch is observed with respect to these apparent discontinuities.

All the above features are typical of what is observed in practice. In addition, the P^* line appeared to be better defined when the correlation parameter L was increased, and the depth to the apparent intermediate discontinuities appeared to be dependent on this parameter. Figure 2.13 and Figure 2.14 show how the depth to the apparent intermediate

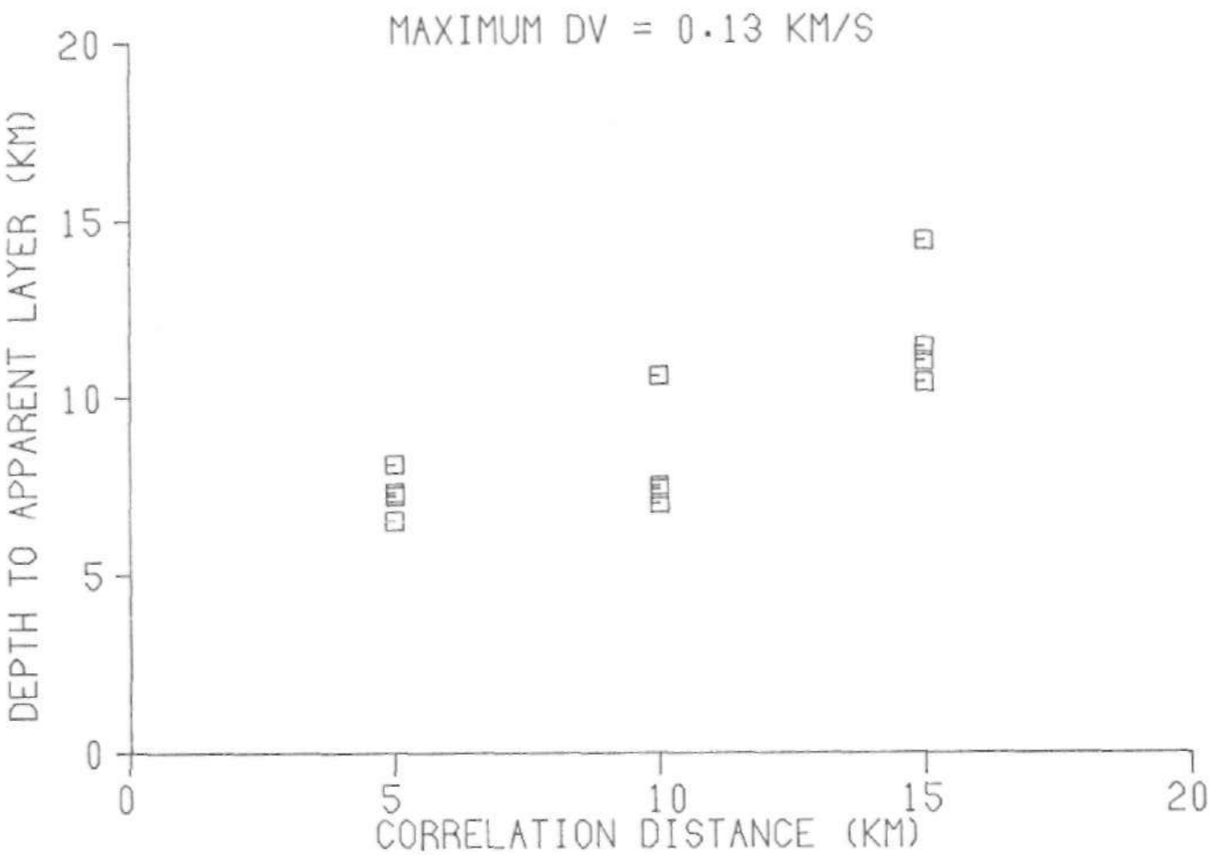


Figure 2.13: Variation of depth to apparent discontinuity as a function of correlation distance. Maximum velocity perturbation is 0.13 km/s. The points represent measurements from twelve different random models.

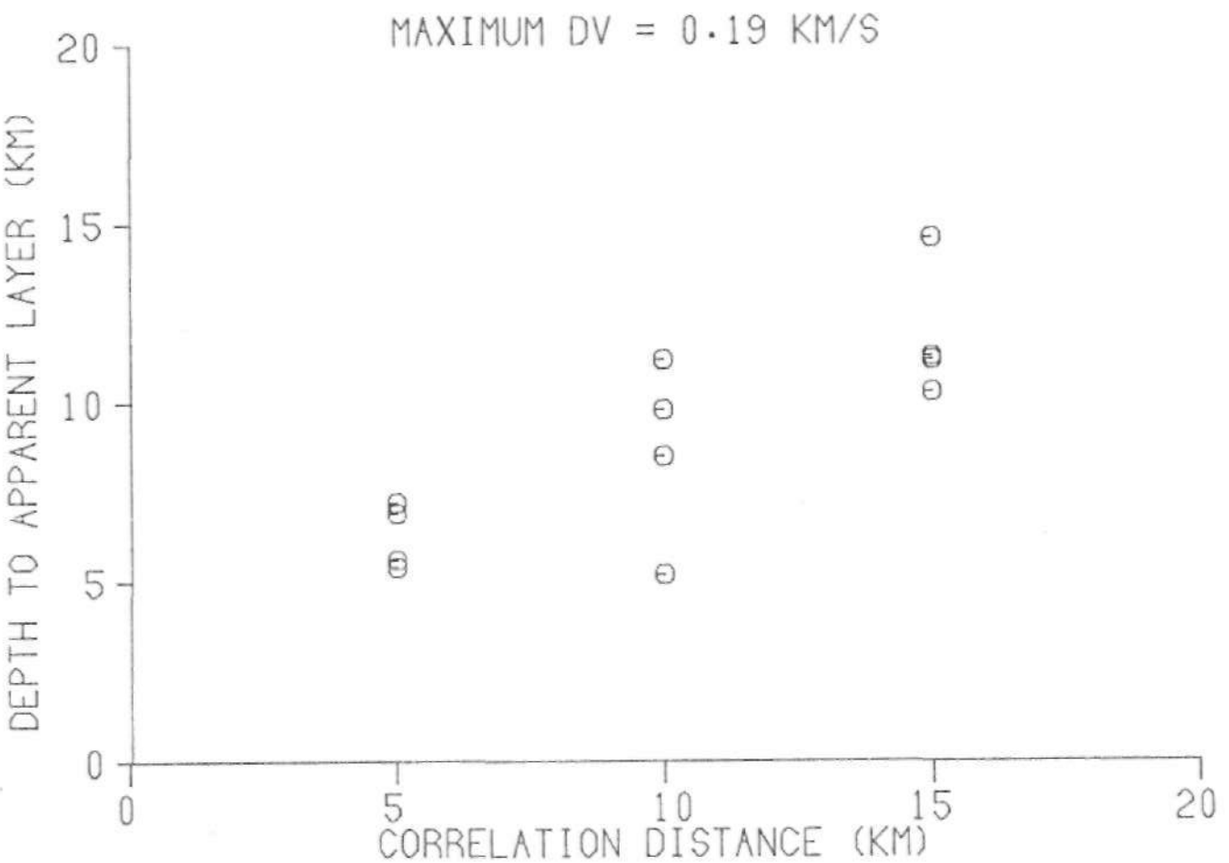


Figure 2.14: Variation of depth to apparent discontinuity as a function of correlation distance. Maximum velocity perturbation is 0.19 km/s. The points represent measurements from twelve different random models.

layer varies as a function of the correlation distance for two different ΔV values respectively. Four different models were generated for each of the three correlation distances 5, 10 and 15 km to check the repeatability of the results. The figures show, especially from L is 5 and 15 km, that the apparent depth to the intermediate discontinuity increases as L increases.

To illustrate the effect of changing the maximum velocity fluctuation that a model was allowed to have, travel-time residuals were computed for models in which L was kept constant, and the fluctuations were varied. The residuals were defined as the deviation of the travel times from the least-squares fit line corresponding to the relevant segment of the travel-time plot. The velocity fluctuations have been expressed as a r.m.s. variation because this is more representative of the model, since it describes the true velocity variation in the model for which it was determined. The figures show that the travel-time residuals do not change significantly for the P_g branch but increase progressively as the r.m.s. velocity fluctuation increases for the P* branch which is also consistent with the behaviour of real data. This approach will be used later (Chapter 3) to determine the amount of fluctuation that best describe the travel time fluctuations observed in a true refraction section. As mentioned earlier, these observations are very similar to those observed with real data, and a simple explanation for them is proposed here.

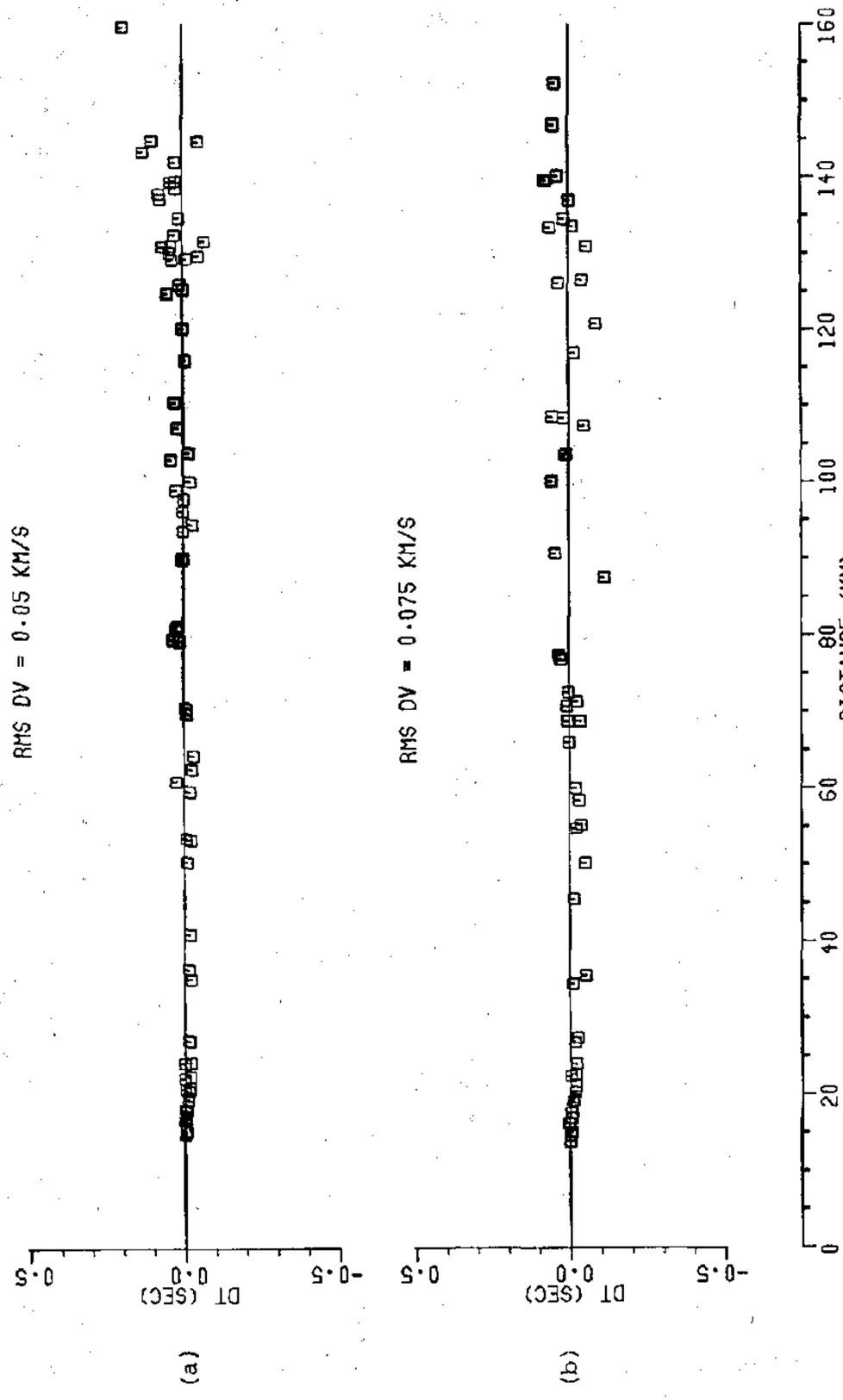


Figure 2.15: Travel-time residuals for a model with r.m.s. velocity fluctuation of (a) 0.05 km/s (b) 0.075 km/s.

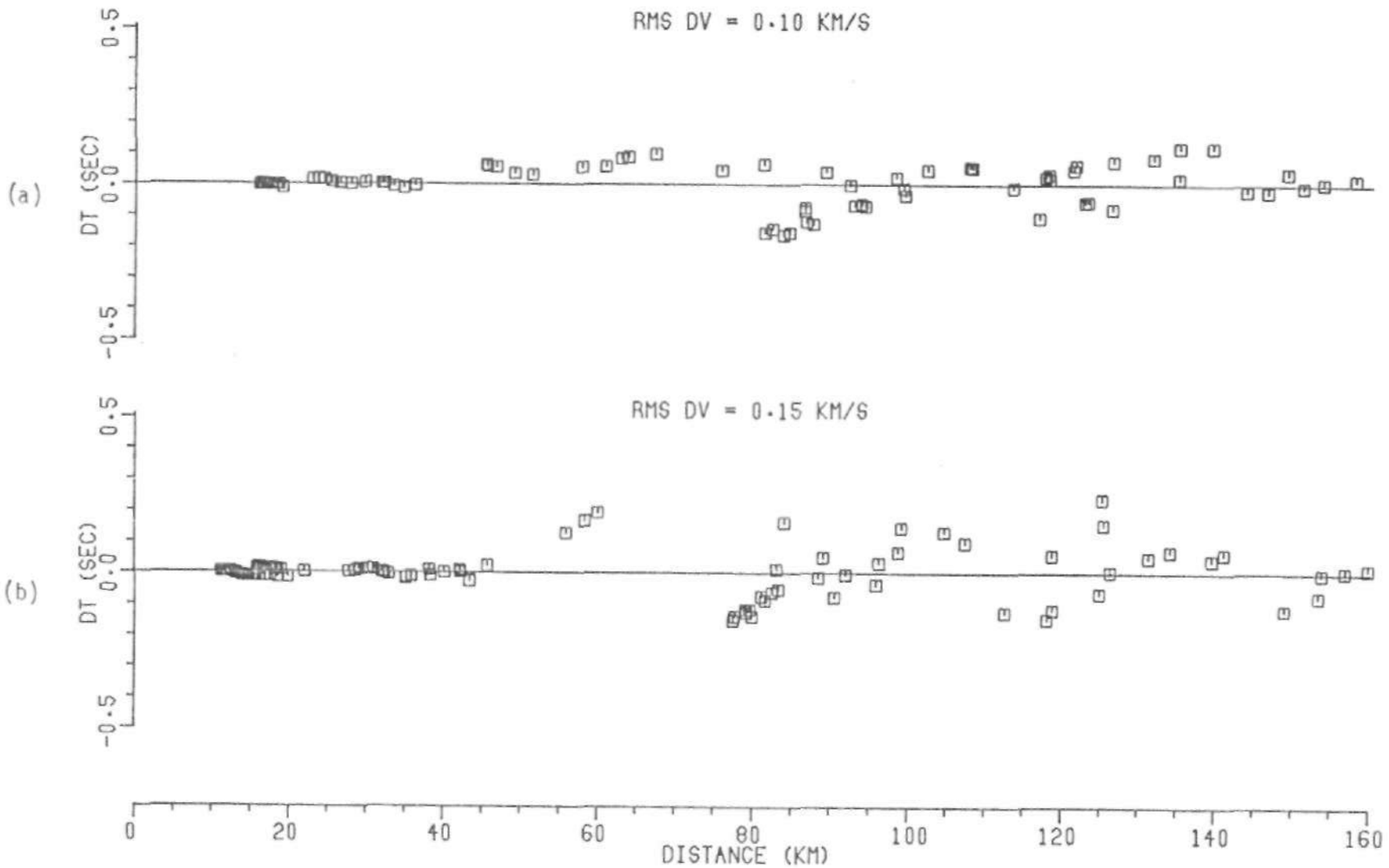


Figure 2.16: Travel-time residuals for the same model as Figure 2.15 with r.m.s. velocity fluctuation of (a) 0.10 km/s (b) 0.15 km/s.

The travel path t for a ray going from the source to a station can be considered to be made up of three components as follows:

$$t = d + h + u \qquad (2\text{-}15)$$

where d is the downgoing component, h is an approximately horizontal component, and u is the upgoing component. When the ray does not travel deep in the medium, d and u are small compared to h (see Figure 2.10 or 2.11). Since the component h tends to average out the effects of the lateral velocity variations very little scattering of the travel-time points would be expected for shallow paths such as P_g. As the ray penetrates deeper into the model, however, components d and u form a much more significant part of the total travel time. Since the upgoing component will be very sensitive to the correlation distance L, the scatter in the travel-time curve will tend to reflect variations in u and hence will be a function of L. In other words the lengths of the observed travel-time segments should be directly related to the correlation distance or the scale of the inhomogeneities present. Breaks will therefore occur in the travel-time curve when the upgoing portion u begins to sample a new correlation region of the medium, and the depth to the apparent discontinuity will in turn be directly related to the correlation distance.

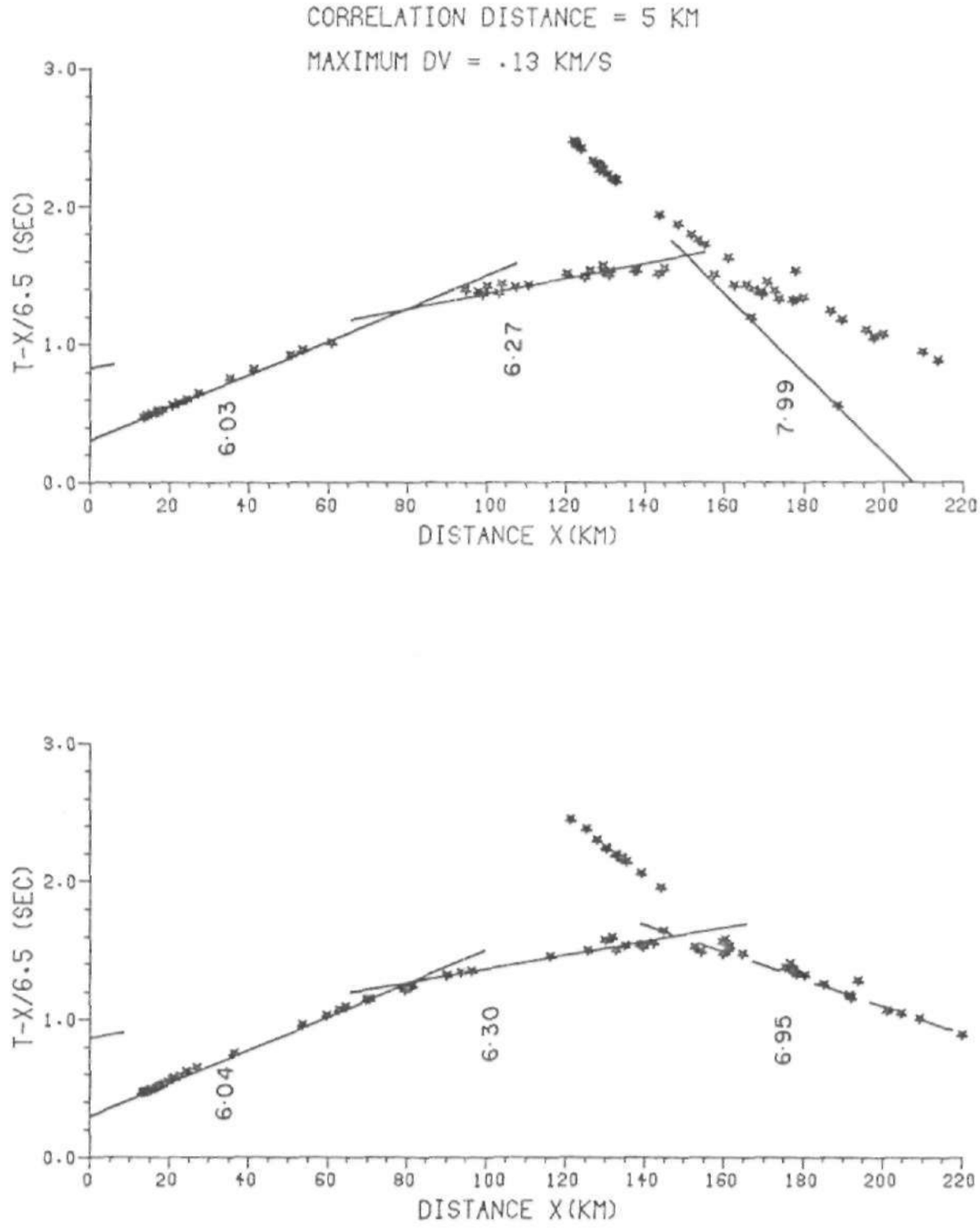


Figure 2.17: Two examples of travel-time plot for a model with correlation distance of 5 km, and maximum velocity fluctuation of 0.13 km/s.

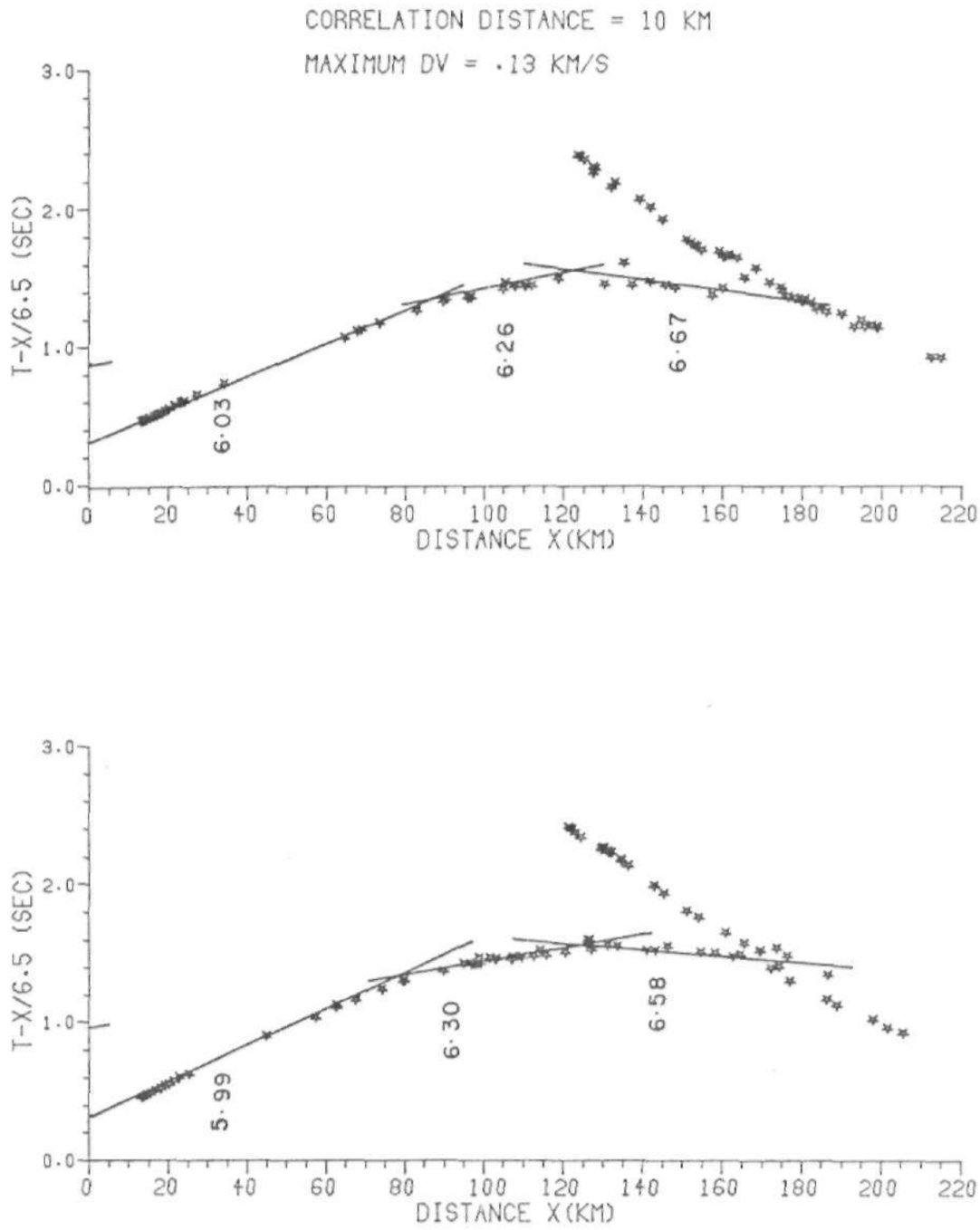


Figure 2.18: Two examples of travel-time plot for a model with correlatiCn distance of 10 km, and maximum velocity fluctuation of 0.13 km/s.

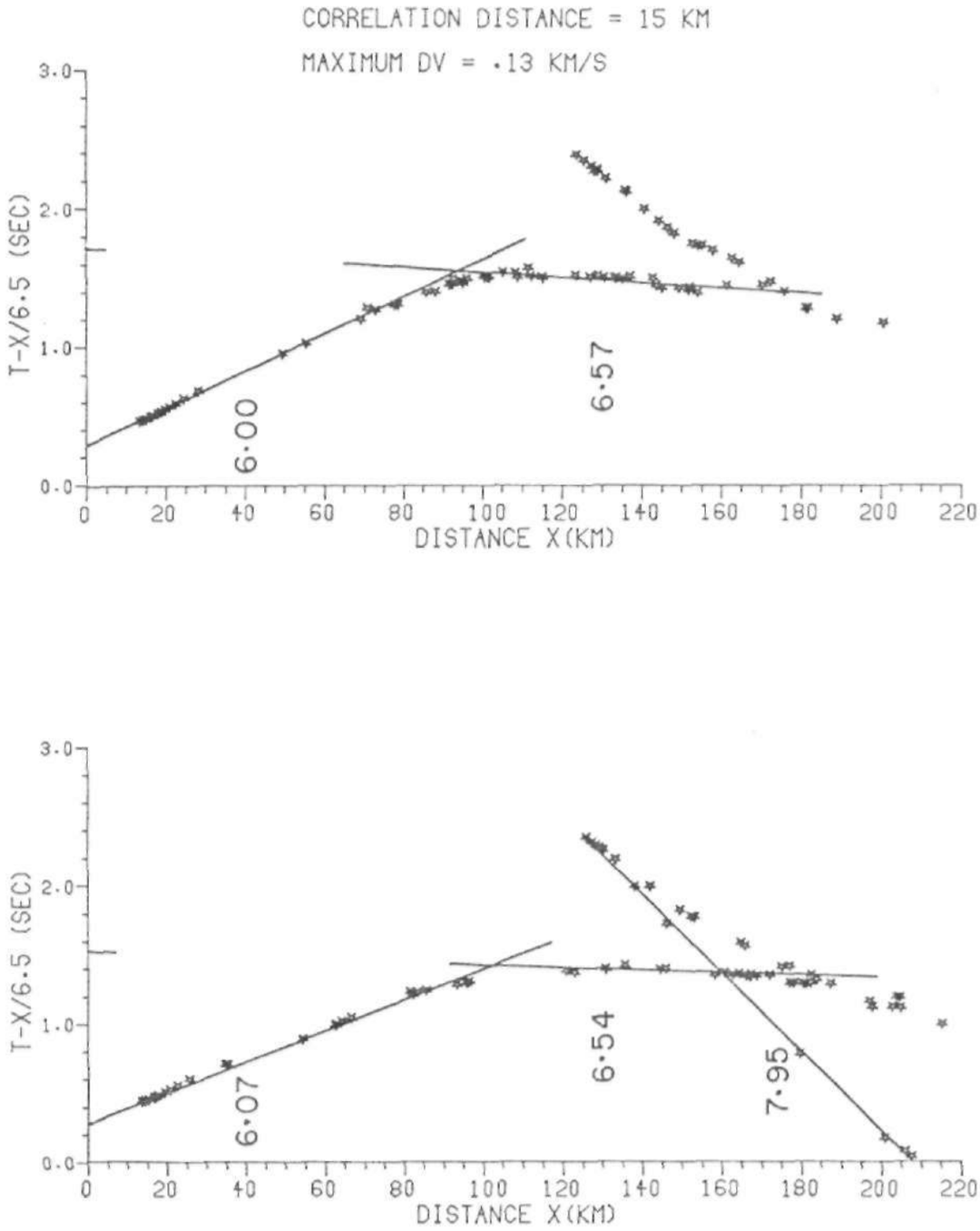


Figure 2.19: Two examples of travel-time plot for a model with correlation distance of 15 km, and maximum velocity fluctuation of 0.13 km/s.

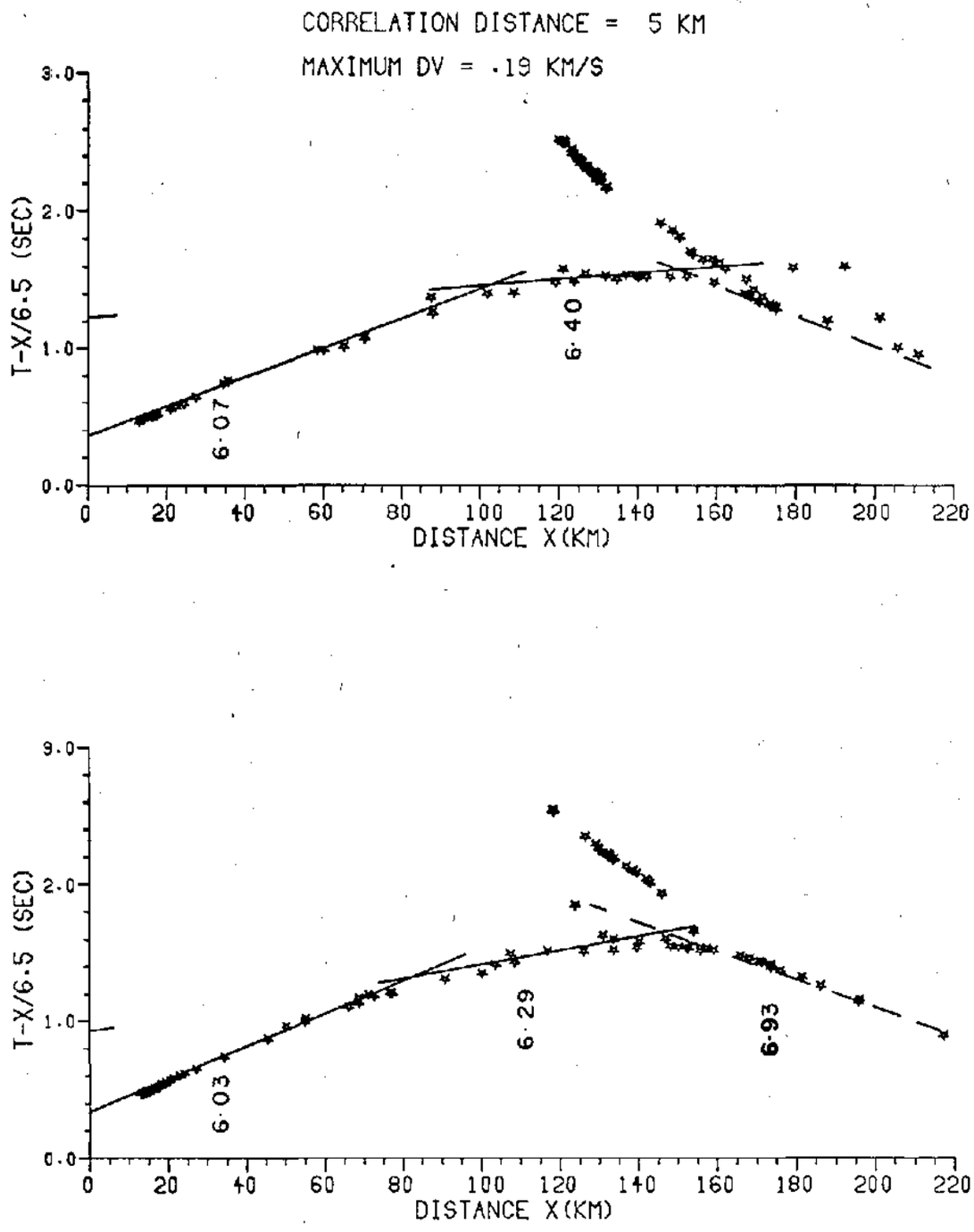


Figure 2.20: Two examples of travel-time plot for a model with correlation distance of 5 km, and maximum velocity fluctuation of 0.19 km/s.

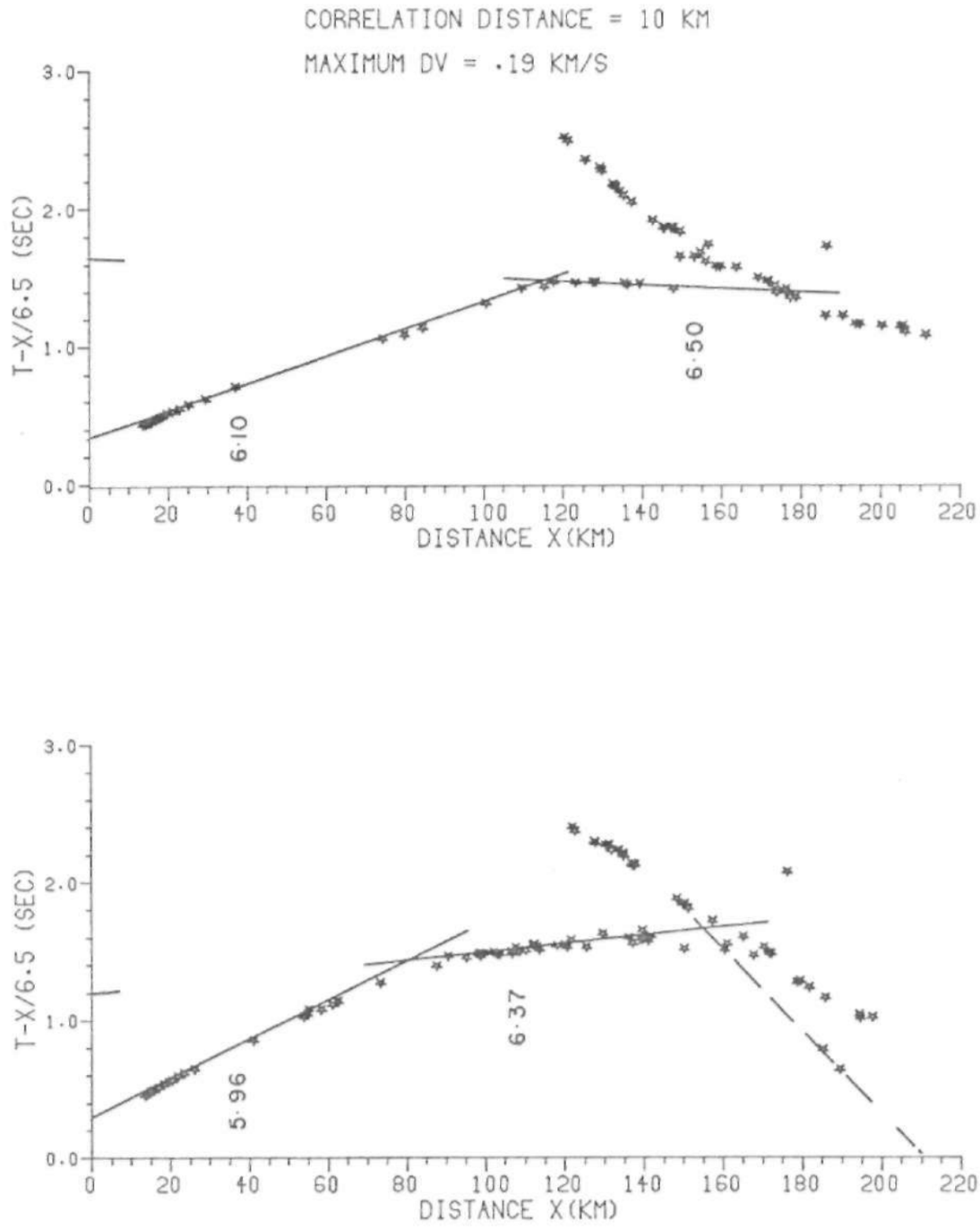


Figure 2.21: Two examples of travel-time plot for a model with correlation distance of 10 km, and maximum velocity fluctuation of 0.19 km/s.

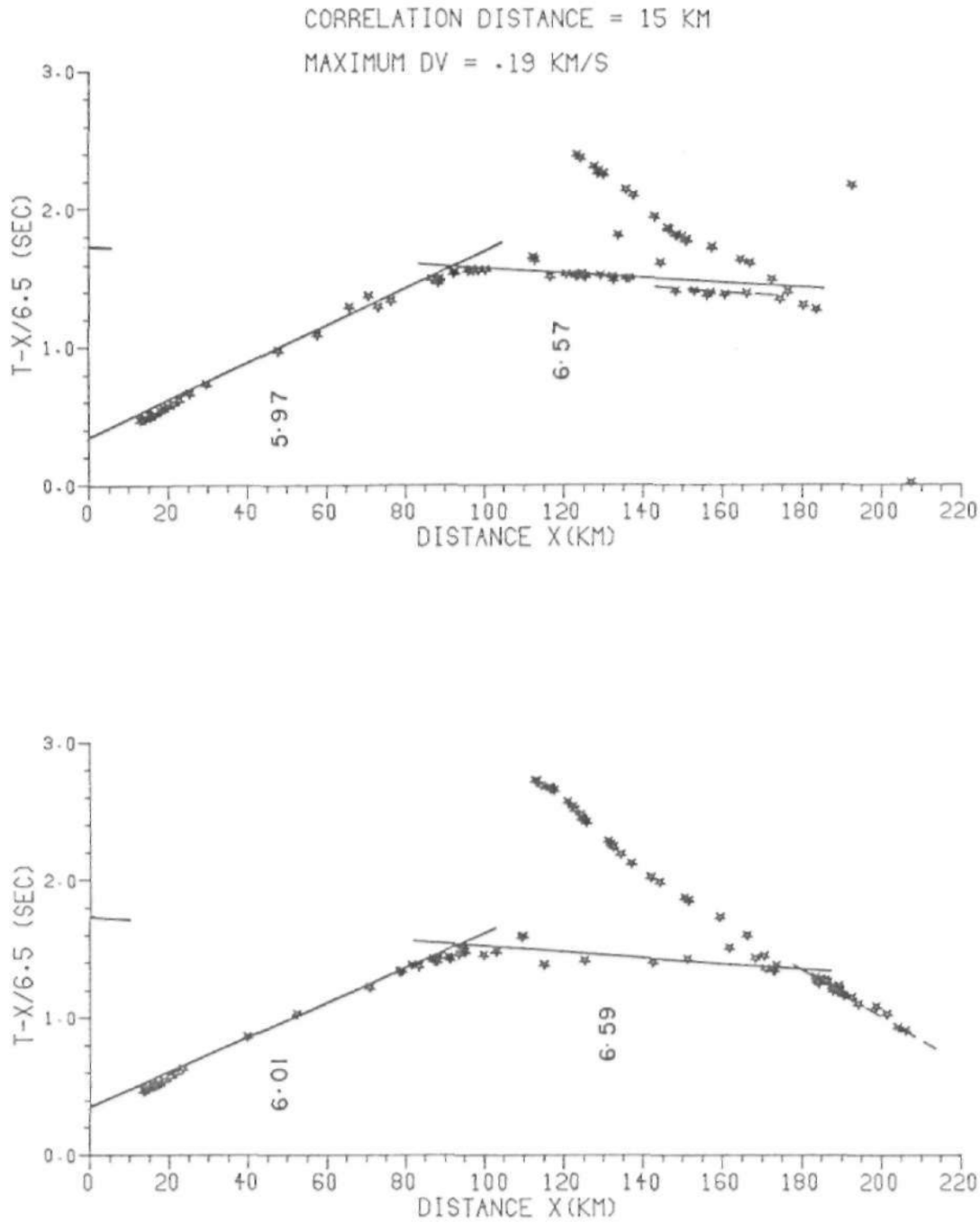


Figure 2.22: Two examples of travel-time plot for a model with correlation distance of 15 km, and maximum velocity fluctuation of 0.19 km/s.

CHAPTER 3

A SCATTERING MODEL FOR THE 1979 COCRUST REFRACTION DATA

3.1 INTRODUCTION

In August 1979, the University of Western Ontario participated in a cooperative seismic survey in the southern part of Manitoba and Saskatchewan. The experiment was organized by the Consortium for Crustal Reconnaissance Using Seismic Techniques (COCRUST) as a continuation of a program which was started in 1977 to study the crustal structure across the boundary of the Superior and Churchill tectonic Provinces in southern Canada. The rationale for the program and some of the initial results were discussed by Green and Stephenson (1978), Green, Cumming and Cedarwell (1979), Green et al. (1980), and Hajnal et al. (1980).

Our present interest is the application of the results of the numerical experiments discussed in Chapter 2 to some of the refraction data of the 1979 experiment. The considerable similarity between travel-time plots such as those in Figures 2.17 to 2.24 of Chapter 2, and those described for the 1977 experiment (Green et al., 1980; Figures 2 and 3) strongly indicates the relevance of this approach to the problem.

3.2 THE REFRACTION SURVEY

The field work was conducted during a two-week period in August 1979, including six days for travelling to and from the location. The general layout of the refraction lines are shown in Figure 3.1, and consists of two reversed profiles in the north-south direction (Lines A and B), and one unreversed profile in the east-west direction (Line C). Line A was located very close to the Superior Province boundary in Manitoba along an approximate longitude of 101 02'W while Line B was located in Saskatchewan within the Churchill Province along approximate longitude of 103 45'W. The approximate latitude of Line C is 49 40'N and it extended from Assiniboia in Saskatchewan to just east of Carlyle, also in Saskatchewan. The average separation between recording stations was about 8 km.

Instrumentation consisted of twelve recording systems provided by the Earth Physics Branch of the Department of Energy, Mines and Resources (EMR), and eight units provided by the Department of Geophysics, University of Western Ontario (UWO). The EMR units recorded digitally with one vertical and one horizontal component seismometers, while the UWO systems recorded frequency modulated (FM) analog signals with vertical component seismometers except for three units which recorded one vertical and two horizontal components seismometers. The UWO units also recorded a WWVB radio signal. All units were pre-programmed to switch the systems on at several specific shot times in the early

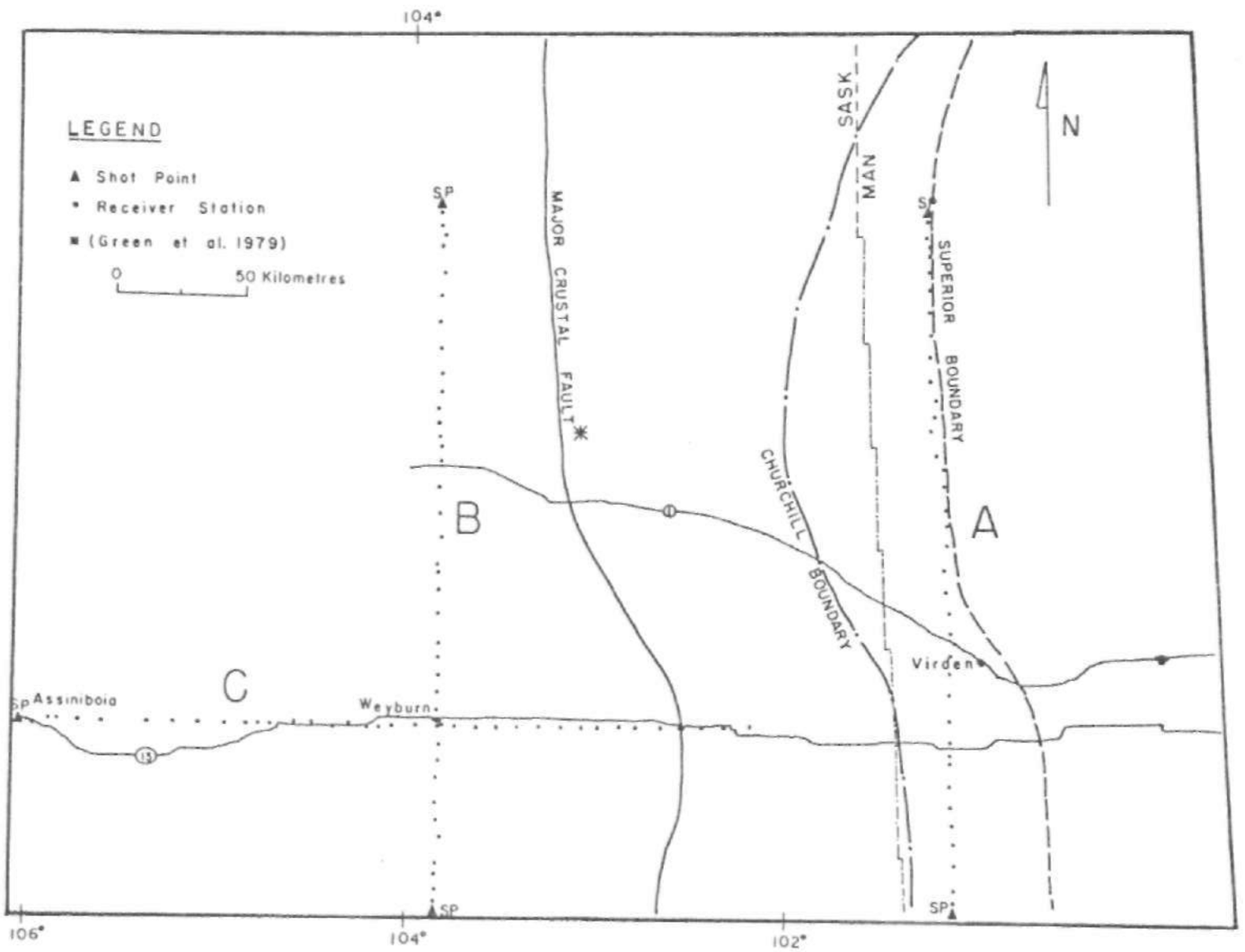


Figure 3.1: Simplified map showing locations of the seismic refraction lines (after Hajnal, 1980).

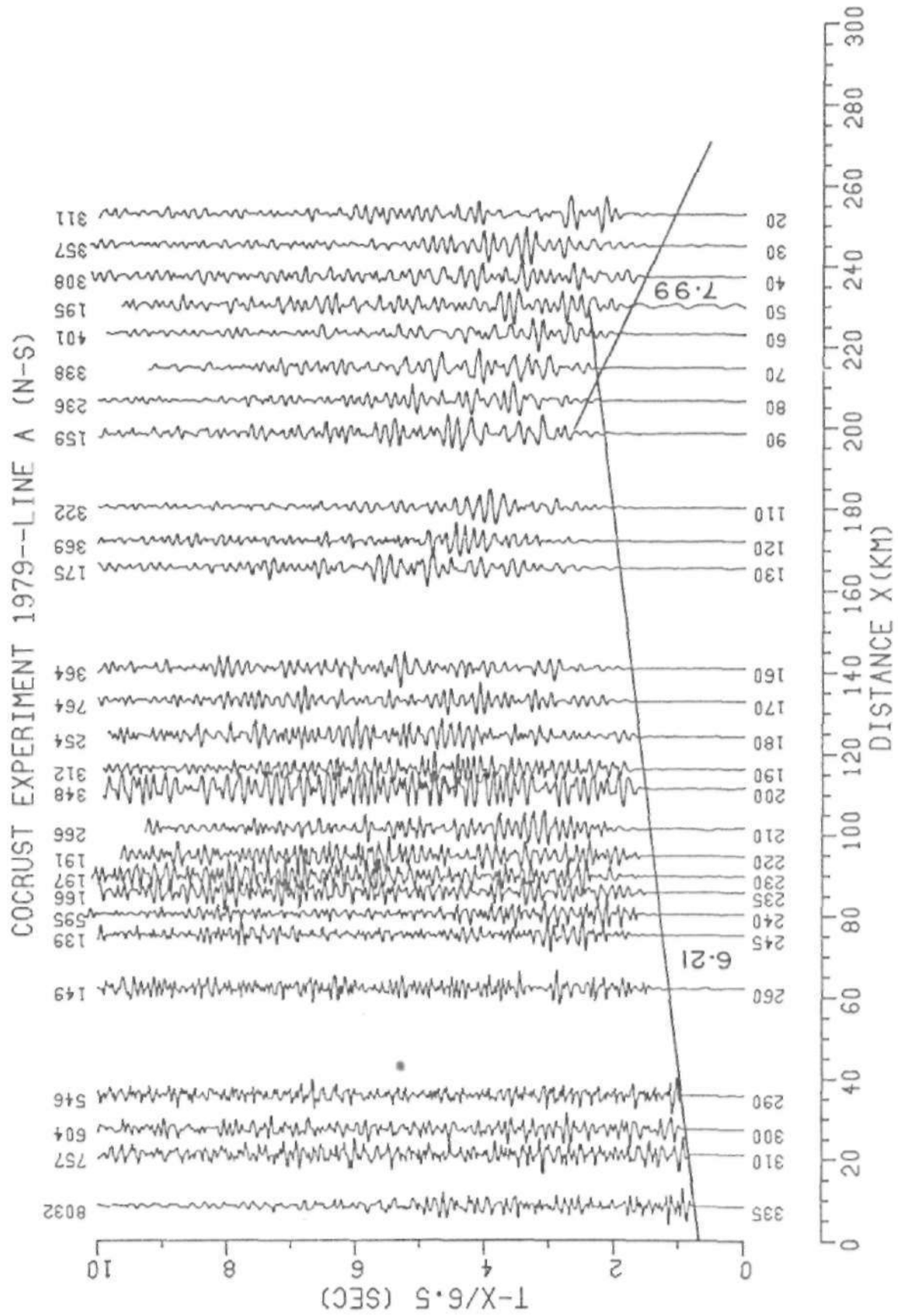
morning, and once in the evening for the east-west profile.

A minimum of two shots was fired at every shot point, and consisted of a small shot of 400 kg in two holes and a larger shot of 1200 kg in six holes. The procedure consisted of deploying the units at one-half of the line, the smaller shot was fired at the end closest to the receivers and the larger shot at the other end of the profile. The receivers were then moved to the other half of the profile, and the process repeated with the centre recorder being common to the two spreads. Further details on the logistics of the survey, stations and shot point locations, elevations, charge sizes and other pertinent information were discussed in a preliminary report (Hajnal, 1980).

3.3 THE TRAVEL TIME DATA

The refraction data were compiled on a digital tape in ten digital files. One file contains all the headers for each individual trace for a single line, and this is followed by the file that contains all the data traces for that specific line. The first three data samples contain the receiver number, shot number, and the component number.

The computer plots of the vertical component records are shown in Figures 3.2 to 3.6 on a reduced time scale, using a reducing velocity of 6.5 km/s. As the plots show, the records are, in general, of good quality and onset times


COCRUST EXPERIMENT 1979--LINE A (N-S)
T-X/6.5 (SEC)
DISTANCE X(KM)
7.99
6.21
311
357
308
195
401
338
236
159
322
369
175
364
764
254
312
348
266
191
197
166
595
139
149
546
604
757
8032
20
30
40
50
60
70
80
90
110
120
130
160
170
180
190
200
210
220
230
235
240
245
260
290
300
310
335

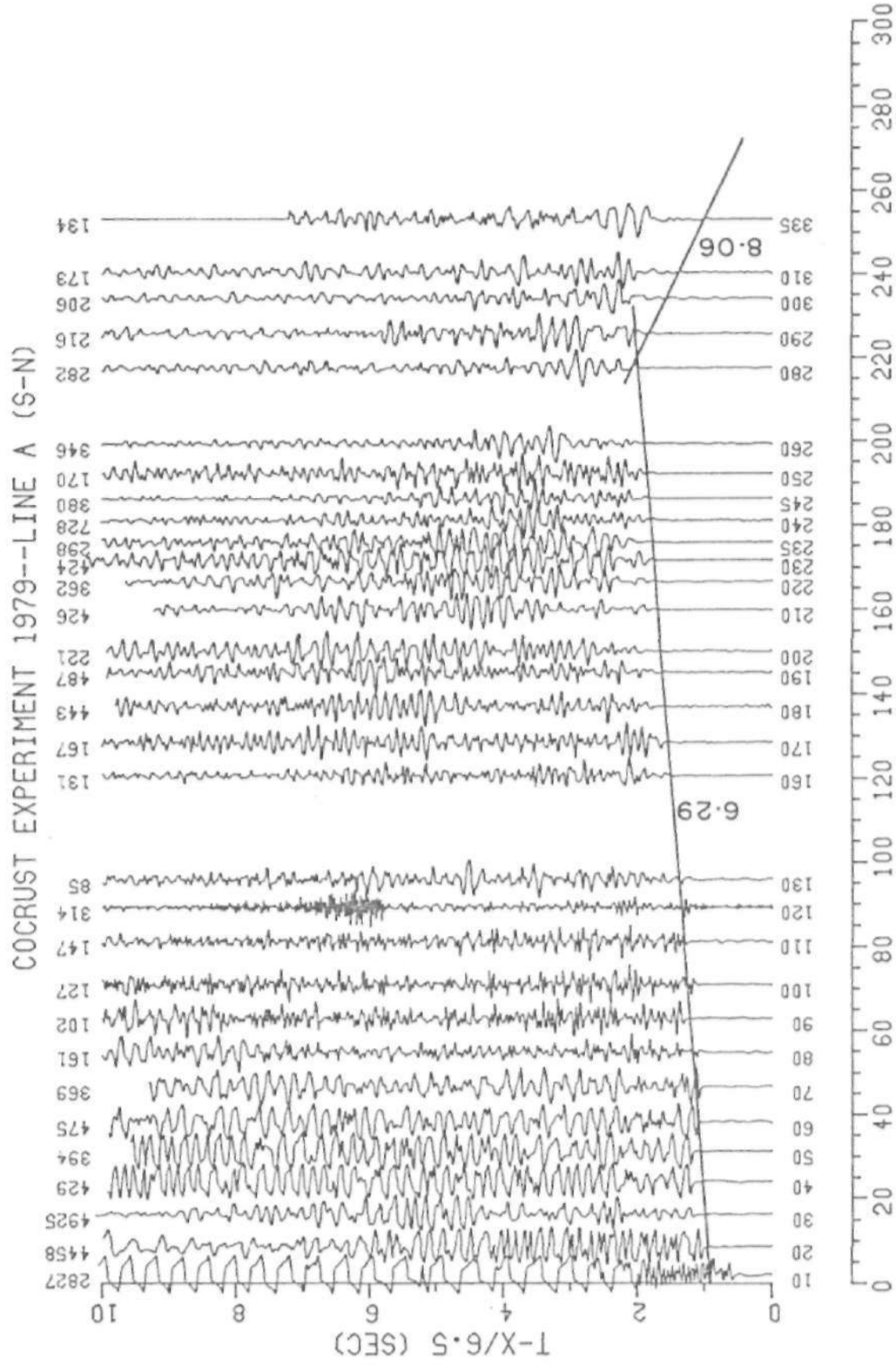


Figure 3.3: Vertical component refraction section from southern shots 10-12.

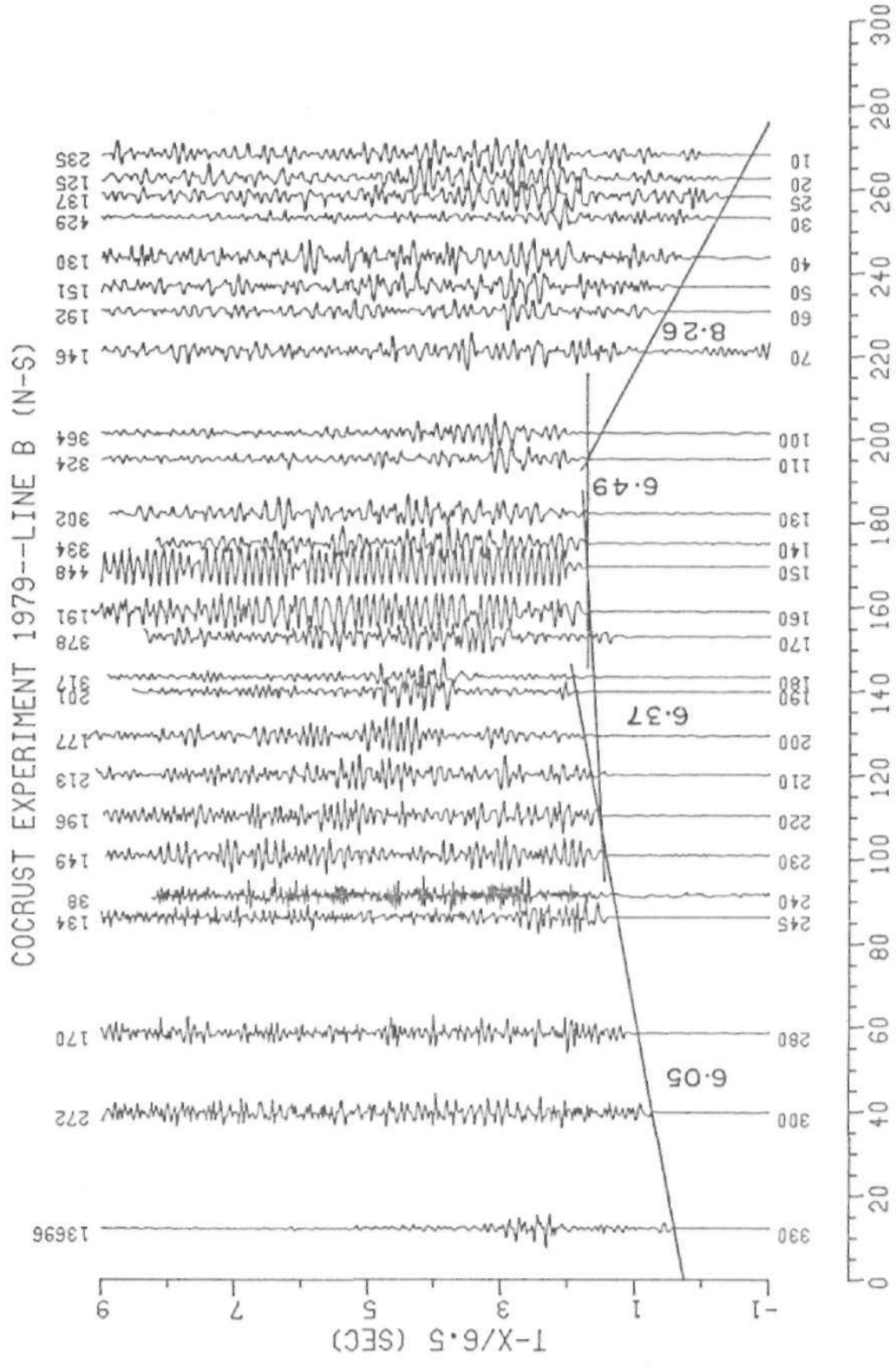


Figure 3.4: Vertical component refraction section from northern shots 14 and 17.

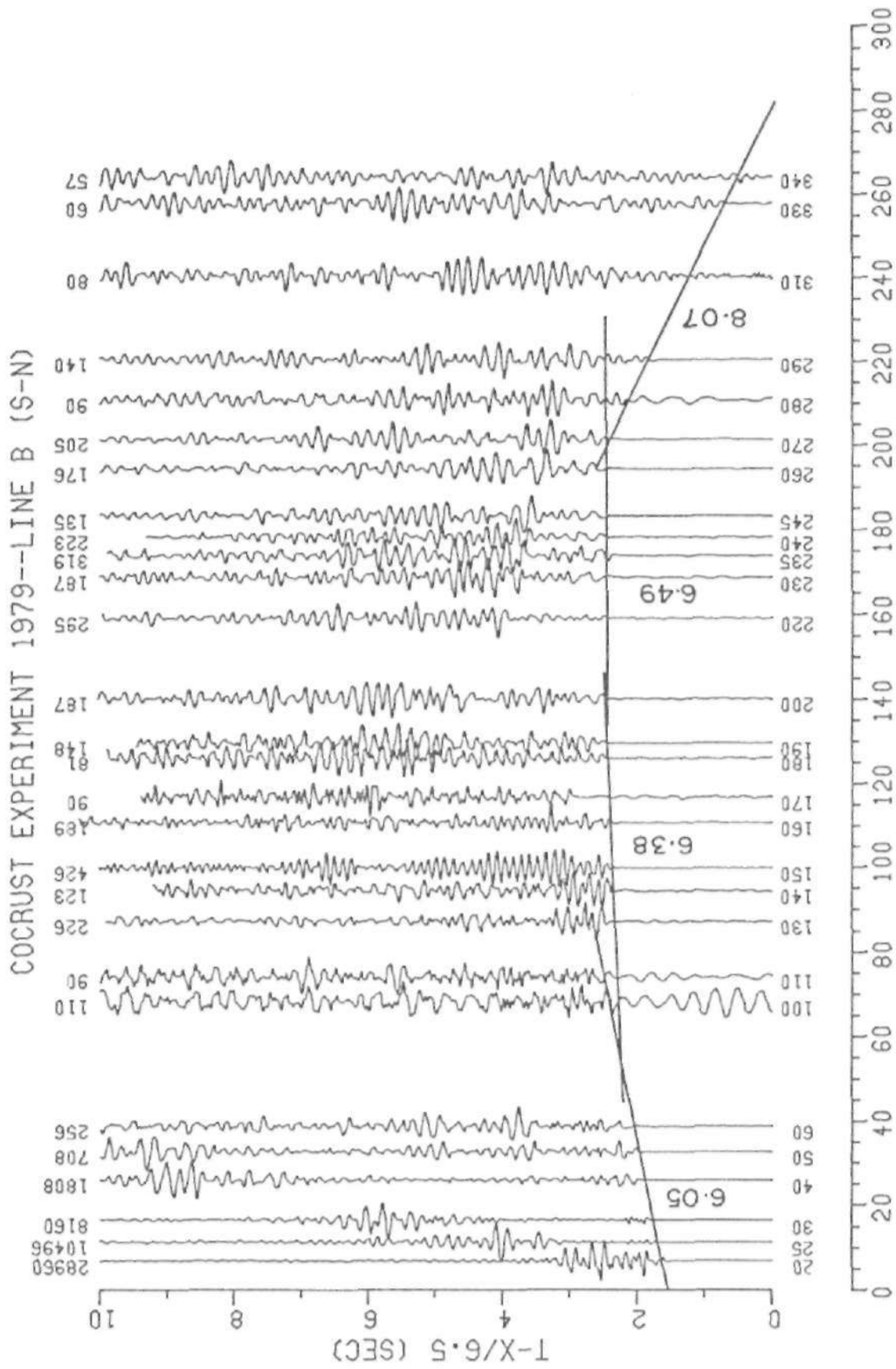


Figure 3.5: Vertical component refraction section from southern shots 15-18.

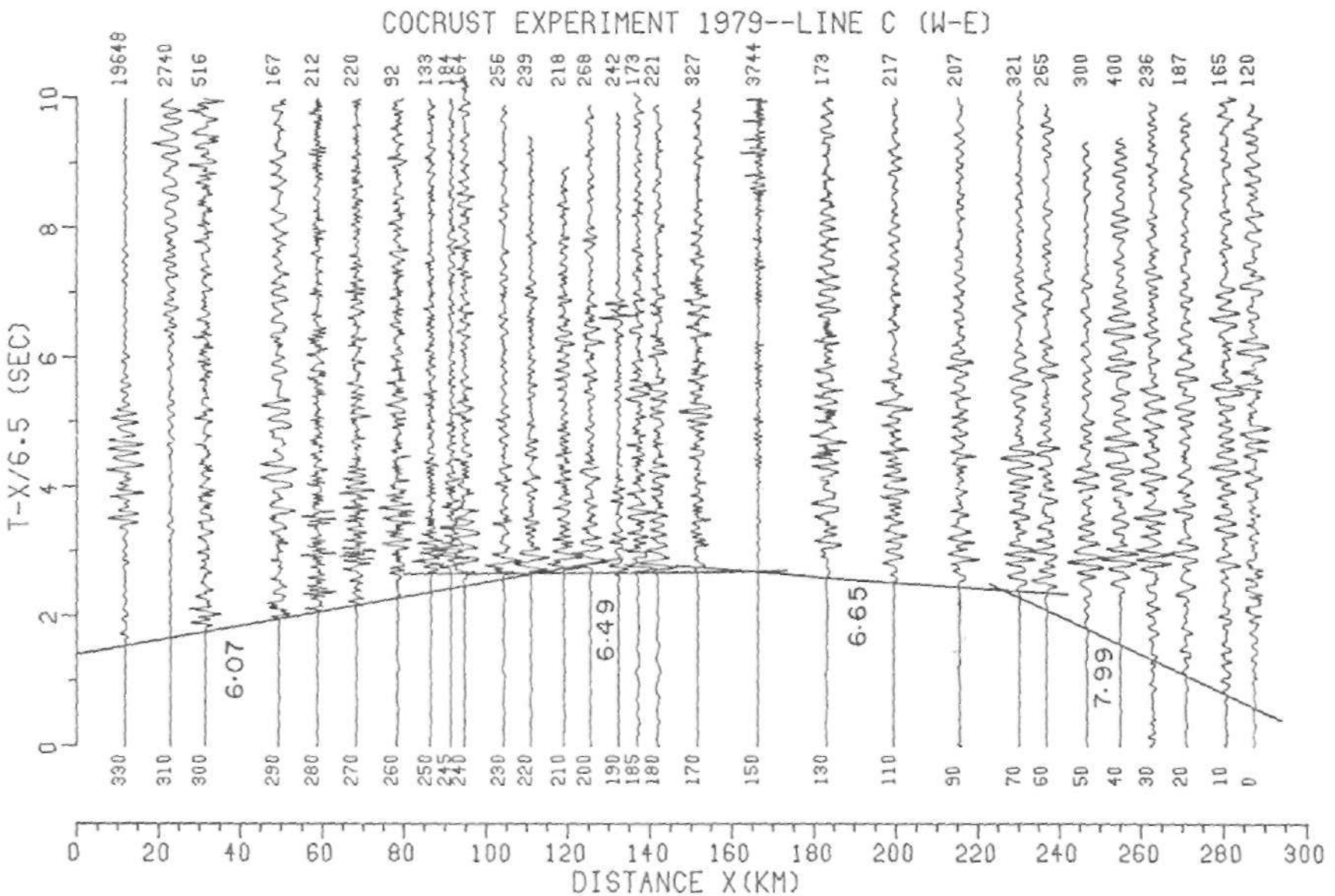


Figure 3.6: Vertical component refraction section from western shots 19 and 20.

could be determined for many of them with an accuracy of 0.02 seconds. However, a few of the traces (for example, Line C (W-E): traces 0-30; and Line B(S-N): traces 310-340) show very low signal-to-noise ratio, and onset time determinations may be in error by as much as 0.1 seconds or more. All the plots show some gaps between traces which were caused by recovery problems with some of the EMR digital magnetic cassette tapes. The uniformly high amplitudes of the first few records in the section of Figure 3.3 was caused by overloading of the UWO recorders. Each record was normalized to the maximum amplitude in the interval plotted, and the normalizing factors are shown at the top of the traces. It should be pointed out that these factors provide only a rough guide to the amplitude variation of the records since the two halves of each figure correspond to two different shots, and each half is made up of records from two different recording systems.

Also shown in the figures just described are the least-squares fit to the first arrival times, and the apparent velocities obtained from them. A summary of the apparent velocities and intercept times are given in Table 3-1(a-e). It will be noted that with the exception of Line A, the first arrivals to a distance of about 220 km can be fitted to two or three travel-time segments, but as Figures 3.2 and 3.3 show, the arrival times of Line A for a corresponding distance are best fitted to a single travel-time segment. Because of the relatively more scatter

TABLE 3-1

Least-squares and apparent velocities and intercept times

LINE A(N-S)

LAYER NUMBER	NUMBER OF RECORDS	RECORDS USED	LEAST-SQUARE APPARENT VELOCITIES (KM/S)	LEAST SQUARE INTERCEPT (SEC.)	CORRELATION COEFFICIENT	COMMENTS
			*3.62			
1						
2	21	80-335	6.21 ± 0.01	0.73 ± 0.04	1.0000	Reliable
3	6	20-70	7.99 ± 0.09	8.41 ± 0.33	0.9997	Reliable

LINE A(S-N)

			*3.62			
1						
2	23	10-260	6.29 ± 0.02	0.88 ± 0.05	0.9999	Reliable
3	5	280-335	8.06 ± 0.21	8.52 ± 0.75	0.9990	Reliable

* Determined from velocity logs (Hajnal, 1980)

TABLE 3-1 Contd.

LINE B(N-S)

LAYER NUMBER	NUMBER OF RECORDS	RECORDS USED	LEAST-SQUARE APPARENT VELOCITIES (KM/S)	LEAST SQUARE INTERCEPT (SEC.)	CORRELATION COEFFICIENT	COMMENTS
			*4.0			
1						
2	3	280-330	6.05 ± 0.06	0.27 ± 0.09	0.9999	Reliable
3	9	170-245	6.37 ± 0.05	1.14 ± 0.14	0.9998	Reliable
4	6	100-160	6.49 ± 0.02	1.69 ± 0.06	1.0000	Reliable
5	8	10-70	8.26 ± 0.11	3.22 ± 0.41	0.9994	Reliable

LINE B(S-N)

			*3.2			
1						
2	6	20-60	6.05 ± 0.07	1.57 ± 0.05	0.9997	Reliable
3	10	100-200	6.38 ± 0.13	2.09 ± 0.33	0.9985	Reliable
4	7	220-270	6.49 ± 0.06	2.36 ± 0.27	0.9998	Reliable
5	5	280-340	8.07 ± 0.34	8.44 ± 1.67	0.9973	Poor SNR

* Determined from velocity logs (Hajnal, 1980)

TABLE 3-1 Contd.

LINE C(W-E)

LAYER NUMBER	NUMBER OF RECORDS	RECORDS USED	LEAST-SQUARE APPARENT VELOCITIES (KM/S) *3.2	LEAST SQUARE INTERCEPT (SEC.)	CORRELATION COEFFICIENT	COMMENTS
1						
2	10	240-330	6.07 ± 0.06	1.40 ± 0.11	0.9996	Reliable
3	8	170-230	6.49 ± 0.05	2.62 ± 0.14	0.9999	Reliable
4	4	90-150	6.65 ± 0.09	3.24 ± 0.38	0.9998	Reliable
5	8	0-70	7.99 ± 0.43	8.79 ± 1.76	0.9913	Poor SNR

* Determined from velocity logs (Hajnal, 1980).

of the arrival times for Line A(S-N) in this distance range, and the gap in the records between 90 km and 120 km (Figure 3.3), an attempt was made to fit two regression lines to the data; but as Figure 3.7 shows this results in a lower apparent velocity for the later branch which might have been caused by lateral changes in the structure of this area. Since the gap in the section precludes a proper definition of the structure, and since it does not show up on the reversed profile, we consider that these arrival times should be treated as one travel time branch instead of two.

On the basis of the first arrival times, a layered-model analysis of both the present data and those from the 1977 experiment were given by Hajnal et al. (1980), and Green et al. (1980). It is therefore not our intention to repeat that aspect of the interpretation here, and the important findings of those studies can be summarized by Figure 3.8. It should be mentioned that the variation of apparent velocities and intercept times indicate considerable lateral heterogeneity beneath all the profiles, and a preliminary interpretation of some reflection data from the area (Green et al. 1980) showed that the crustal structure in the area is very complex.

3.4 A RANDOM VELOCITY MODEL FOR THE TRAVEL TIME DATA

The interpretation which follows is based on a model derived by using the principles developed in the last chapter. The aim was to determine the correlation distance

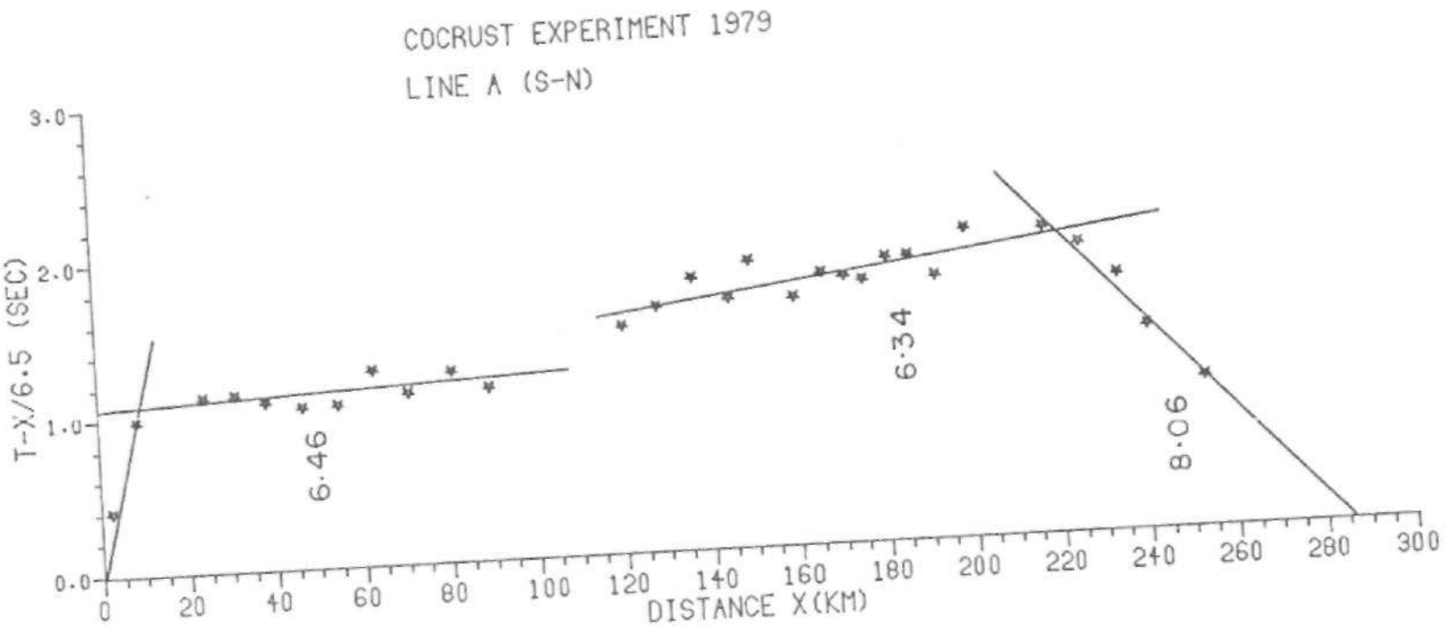


Figure 3.7: Reduced travel-time distance plot for the section of Fig. 3.3 showing a possible break in travel-time segment.

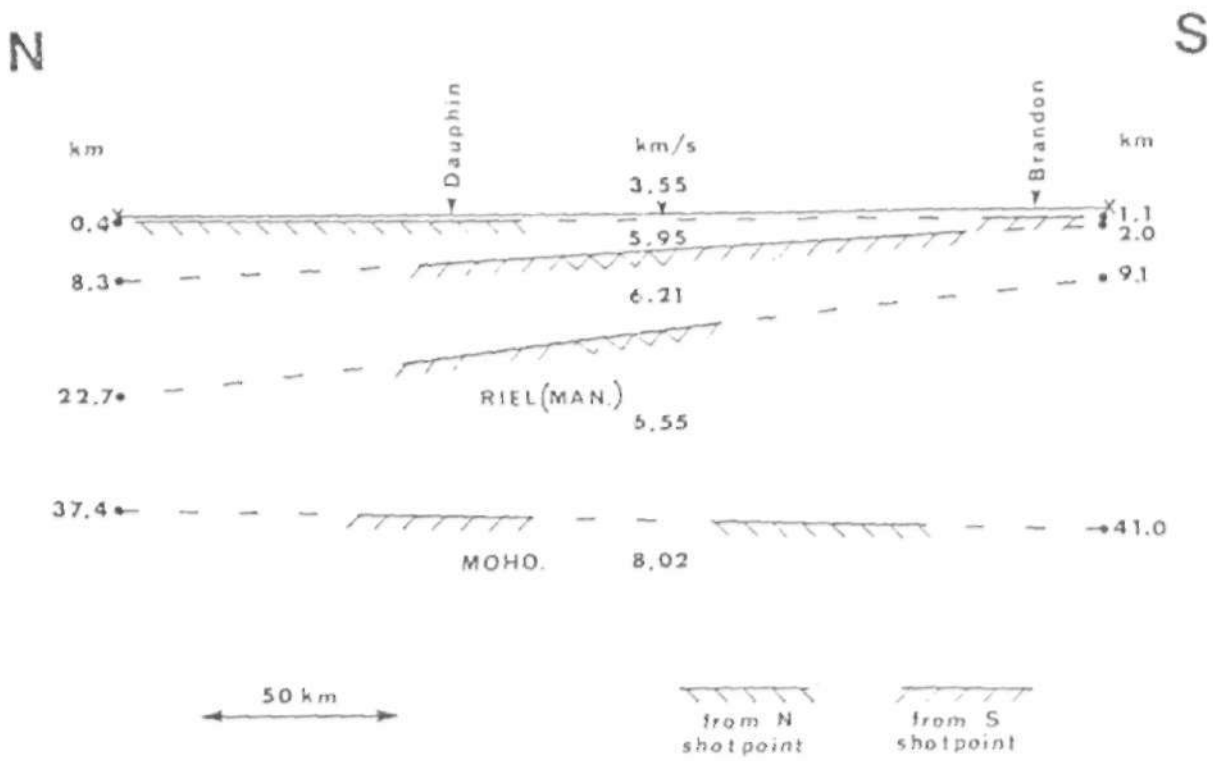


Figure 3.8: Two layered-earth models derived from the 1977 refraction data (after Green et al., 1980).

and the root-mean-square (r.m.s.) fluctuation in velocity which statistically predict the observed fluctuation in the travel time data and, to some extent, the amplitudes. Accordingly, the parameters which were varied include the depth to the Moho, the correlation distance, and the maximum fluctuation which the velocity was allowed to have at any depth. The velocities at the surface and the Moho boundary were fixed, and a linear gradient was assumed between the two boundary values. The surface velocities were obtained from velocity logs as reported by Hajnal (1980). Rays were traced through the model as described in Chapter 2, and the predicted travel times were compared with the observed travel times from the refraction survey. The model was then modified and the procedure was repeated until there was a satisfactory fit between the predicted and observed travel times.

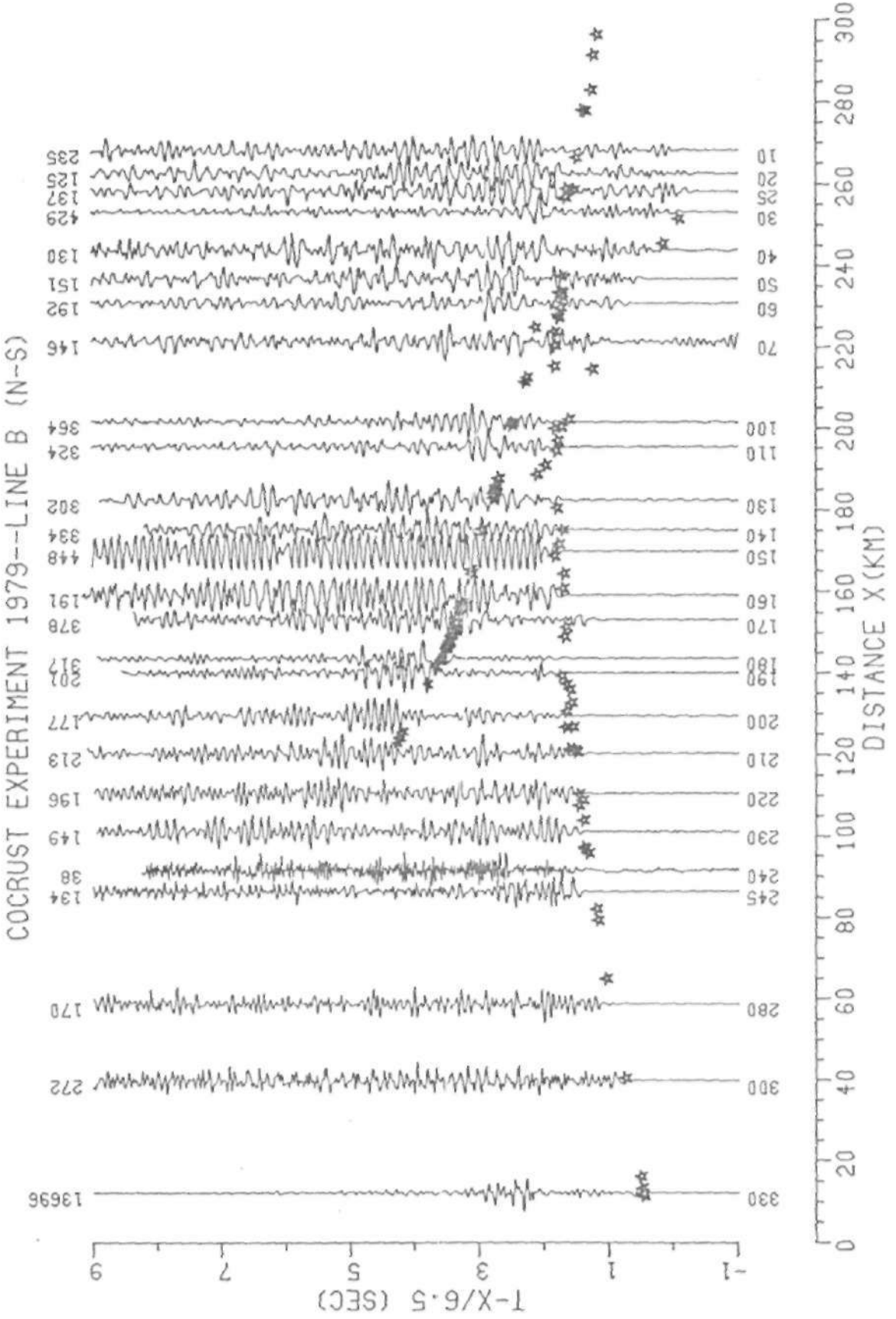
As the above clearly shows, the procedure was a trial and error process and was not only time-consuming, but was also expensive. For this reason it was decided that, since no big advantage would be gained by repeating the procedure for each and every one of the refraction lines, it would be more prudent to run all the tests on one of the better record sections. The record section shown in Figure 3.4 for Line B(N-S) was selected for two main reasons. Firstly, the onset times for all the traces except trace #70 were relatively quite distinct; and secondly, the retrograde reflection branch was fairly well defined in this section,

thus providing some additional constraint in the modelling. The gaps in the record section at distances less than 80 km were not considered a serious problem since it is fairly well known that the travel-time branch in this distance range is relatively well behaved.

Figure 3.9 shows the predicted reduced travel times (stars) that best fit the observed refraction section, and Figure 3.10 (Table 3-2a) shows the corresponding velocity model from which the travel times were obtained. The correlation distance was 5 km, and the maximum variation in velocity was 0.15 km/s. This corresponded to a mean r.m.s. fluctuation of 0.06 km/s or 1%.

The stars in Figure 3.9 represent travel times for rays which were separated by equal intervals of slowness (or ray parameter), and areas of large concentration of stars imply high amplitude arrivals, whereas areas of low concentration suggest low amplitude arrivals. We thus see that the random model predicts erratic large amplitudes for parts of the direct and retrograde branches, and low amplitudes for the other areas especially the P_n branch. It would be noted that the observed refraction section shows high amplitude arrivals for the retrograde branch. It was also found that in several trials with different models, the concentration of stars changed from model to model except with respect to the P_n branch for which low amplitude arrivals were constantly predicted. This is again consistent with the present data (and most refraction data) which show weak

Figure 3.9: Refraction section showing the travel times (stars) obtained from the best-fit random model shown in Figure 3.10.


COCRUST EXPERIMENT 1979--LINE B (N-S)
DISTANCE X(KM)
T-X/6.5 (SEC)

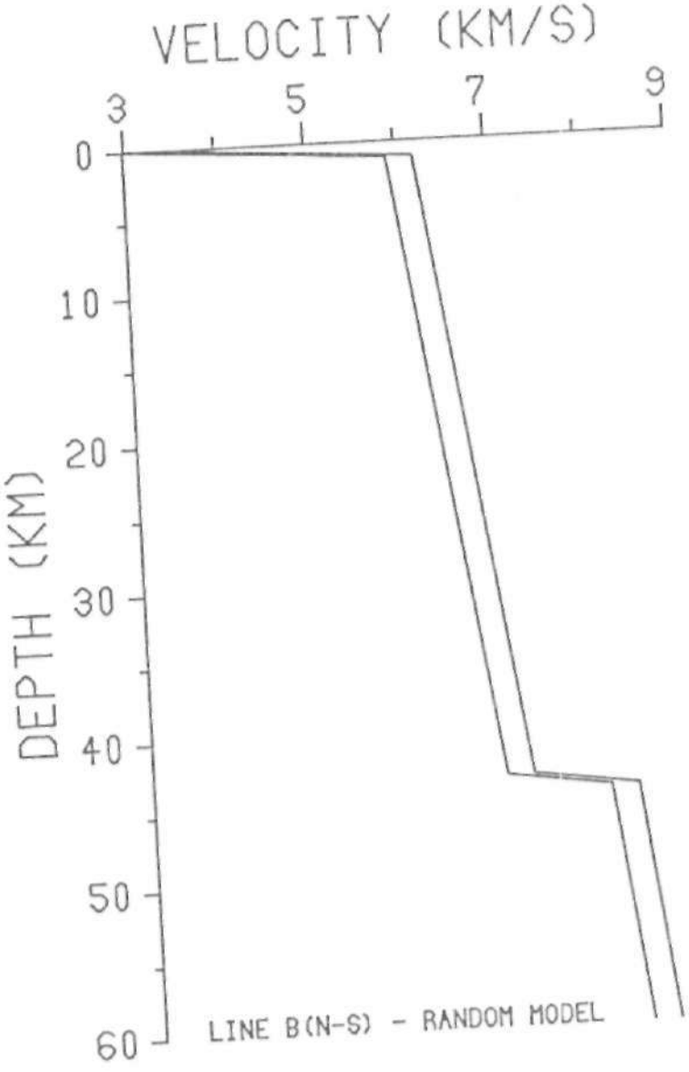


Figure 3.10: Best-fit random model for the section of Figure 3.9.

TABLE 3-2

Velocities and depths for random model

(a)

LINE B(N-S)

DEPTH (km)	VELOCITY (km/s)
0.0- 1.0	3.05-3.35
1.0-43.0	5.92-6.22
43.0-44.0	6.95-7.25
44.0-60.0	8.10-8.40
60.0-	8.45-8.75

(b)

LINE A(N-S)

DEPTH (km)	VELOCITY (km/s)
0.0- 3.0	3.45-3.75
3.0-43.0	6.07-6.37
43.0-45.0	6.65-6.95
45.0-60.0	7.85-8.15
60.0-	8.10-8.40

onsets for the P_n branches in all the sections.

It is instructive to observe what the effect of changing the shot point location would be on the amplitude variation. Figure 3.11 shows the predicted arrival times (stars) for the same model that produced the results shown in Figure 3.9, but with the starting point of the rays shifted 50 km to the south. A comparison of Figures 3.9 and 3.11 shows that large amplitude arrivals are predicted for various arrivals in the distance range 30-100 km in the latter figure whereas the former predicts low amplitude arrivals for this distance range. Furthermore, the predicted location of the large amplitude arrivals in the retrograde branch has shifted from about 145 km in the former figure to 165 km in the latter figure. It is therefore conceivable that a shot point location can be found for this model for which the retrograde branch will become very poorly defined.

Clee et al. (1974) observed a similar effect in travel-time sections obtained from a detailed reflection-refraction experiment conducted near Yellowknife, Northwest Territories, in Canada. Figures 3 and 4 of their paper show that two sections obtained from shot points which were separated by only 15 km produced remarkably different seismic sections. It therefore appears that the details observed on a seismic record section depends on the location of the shot point. One may thus explain, in this term, the absence of a retrograde branch in Line C (Figure 3.6), or

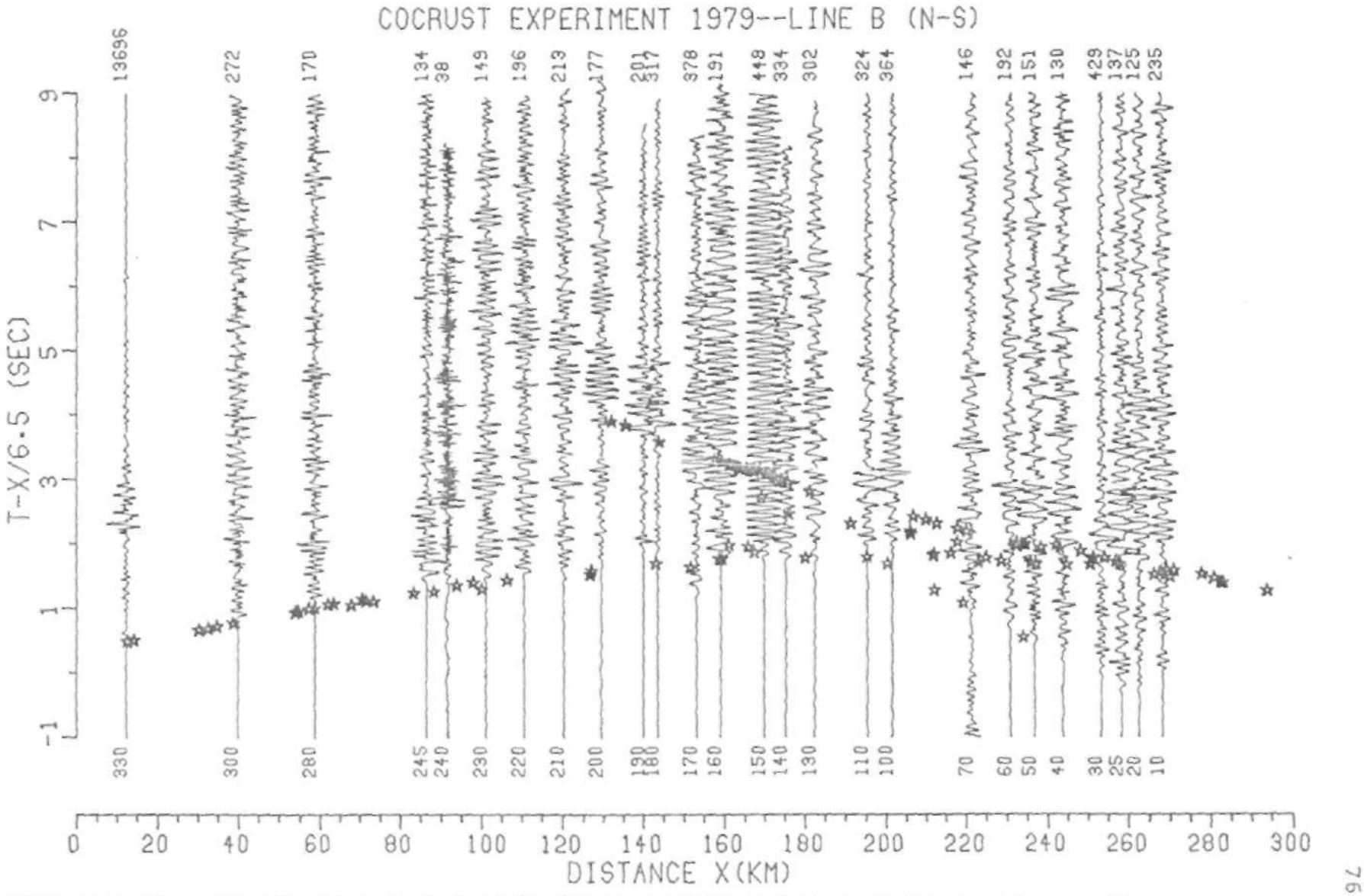


Figure 3.11: As for Figure 3.9 with "shot point" shifted 50 km to the south.

its poor definition in Line A (Figures 3.2 and 3.3), and the erratic behaviour of amplitudes along the record sections.

It is also interesting to observe the behaviour of the travel-time curve, in comparison with the above, when in the limiting case the velocity perturbation is allowed to approach the zero value, i.e. for the homogeneous case. Figure 3.12 shows the travel times for such a case. In contrast to the results for the heterogeneous case, Figure 3.12 predicts that amplitude should increase progressively along the forward branch and the retrograde branch. It was also noted that the travel times for the homogeneous model were slightly less. It follows therefore that an additional effect of the velocity perturbations in the heterogeneous case is to increase the mean path length of the rays.

When the correlation distance for the model of Figure 3.10 was increased to 10 km or 15 km, an equally good fit of the observed travel times were obtained upto about 200 km, but the P_n branch was not defined at all. Since a quantitative comparison of amplitudes is not possible from these results, it is difficult to draw any firm conclusions about the correlation distance that best describe the data. Intuitively, however, and from the results using the model with a correlation distance of 5 km and the homogeneous model, it is felt that a low value near 5 km rather than 10 km or 15 km is the more probable answer. This is supported by the results of the numerical experiments in Chapter 2 which showed that short correlation distances could be

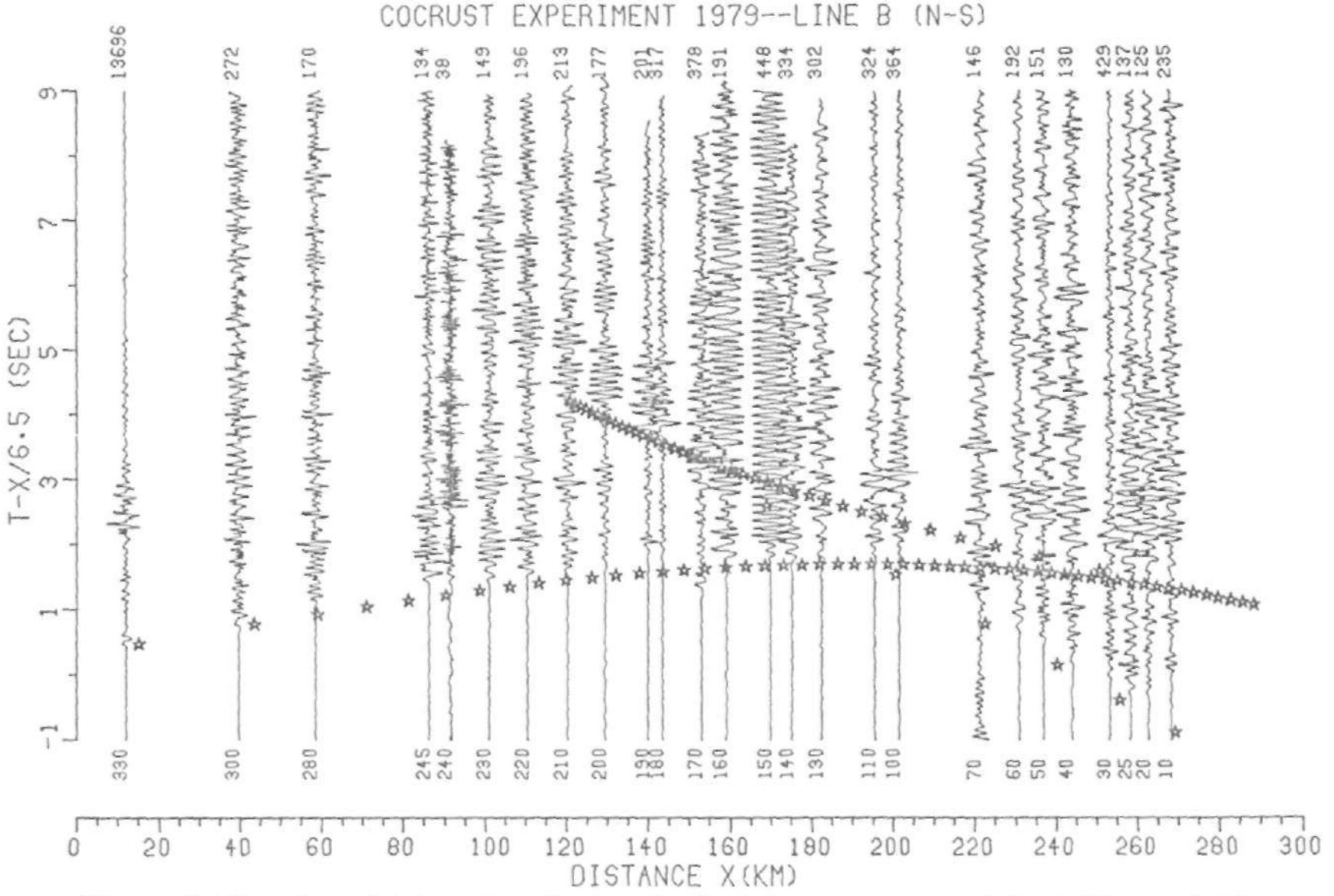
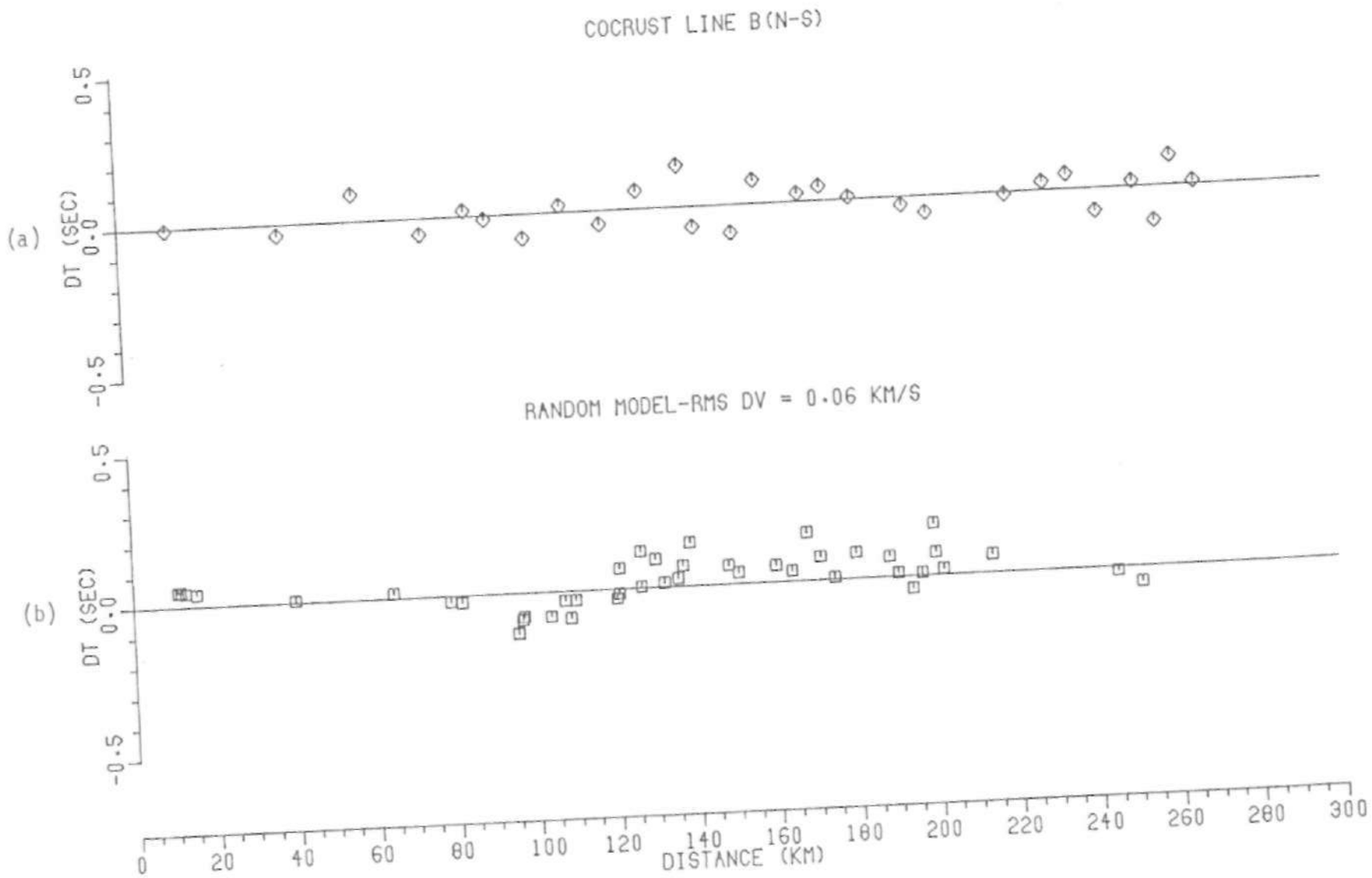


Figure 3.12: Travel times for the equivalent homogeneous model of Figure 3.10.

correlated with shallow apparent discontinuities; and as the results of Green et al. (1980) and Hajnal (1980) show, an interpretation of the least-squares apparent velocities and intercept times lead to some shallow apparent intermediate discontinuities.

In order to determine the r.m.s. fluctuation in velocity that best describe the observed travel time fluctuations, a series of travel-time curves were generated by varying the maximum velocity perturbation in Figure 3.10 and determining the corresponding mean r.m.s fluctuation of the whole model. For a better qualitative comparison with the observed data, the results were not plotted in the form shown in Figures 3.9 and 3.11, but as travel-time residuals relative to the least-square regression line of the first arrival times for the corresponding travel-time segment. Figure 3.13 shows a comparison of the residuals for the observed travel times and the random model which best fit the observed. As the figure shows, the residuals are comparable in magntiude. Figure 3.14 shows the result of increasing the r.m.s. velocity fluctuation to 0.10 km/s (or 1.5%) and 0.15 km/s (or 2.2%) respectively. It will clearly be noted that the residuals are now too large to satisfy the observed variation.

In order to ascertain that these parameters describe the whole of the crust under the study area, a similar model was computed for one of the travel time profiles of the other north-south line (Line A(N-S)) using the same


COCRUST LINE B(N-S)
(a)
DT (SEC)
0.5
0.0
-0.5
RANDOM MODEL-RMS DV = 0.06 KM/S
(b)
DT (SEC)
0.5
0.0
-0.5
0
20
40
60
80
100
120
140
160
180
200
220
240
260
280
300
DISTANCE (KM)

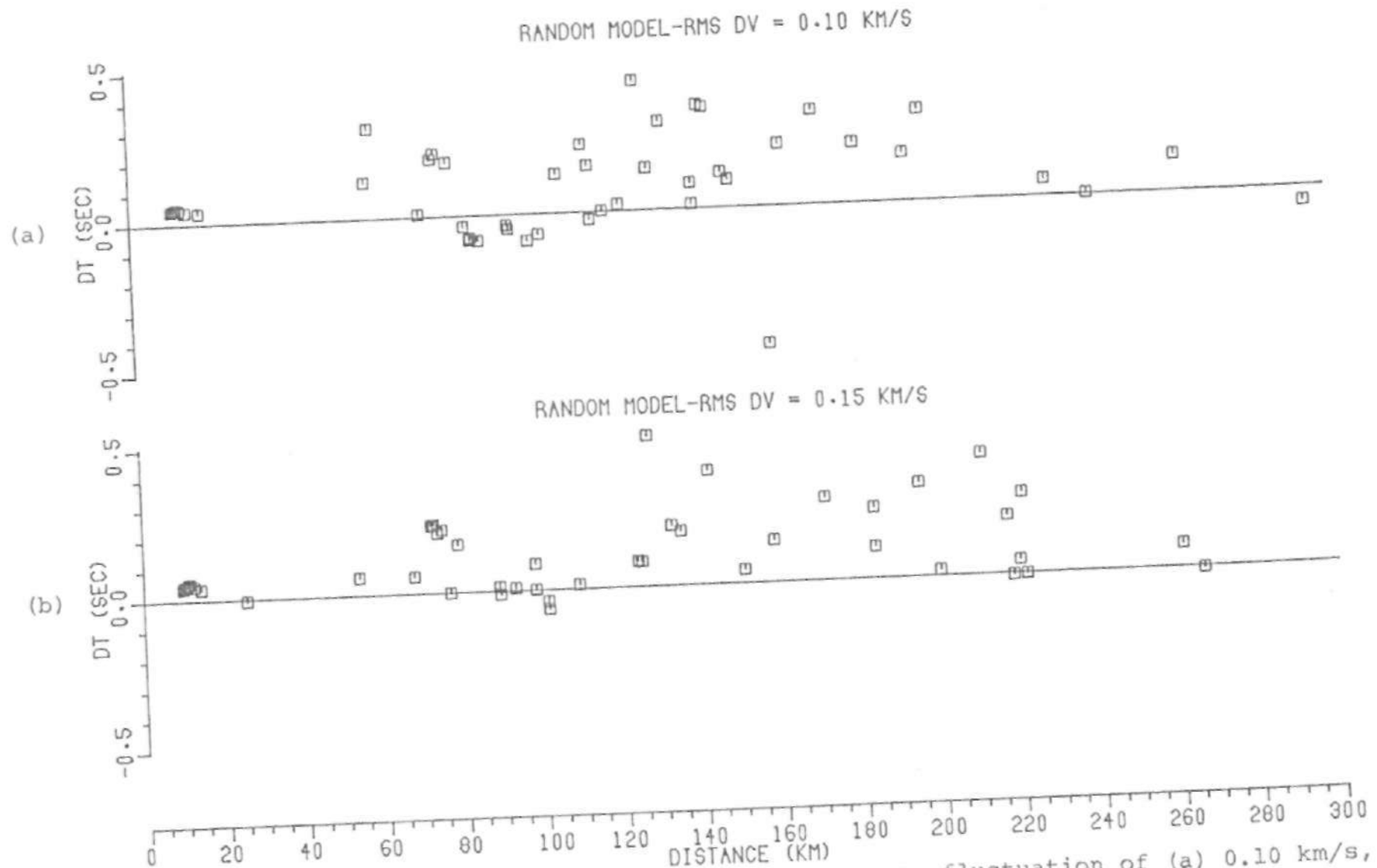


Figure 3.14: Travel-time residuals for model with r.m.s. fluctuation of (a) 0.10 km/s, (b) 0.15 km/s.

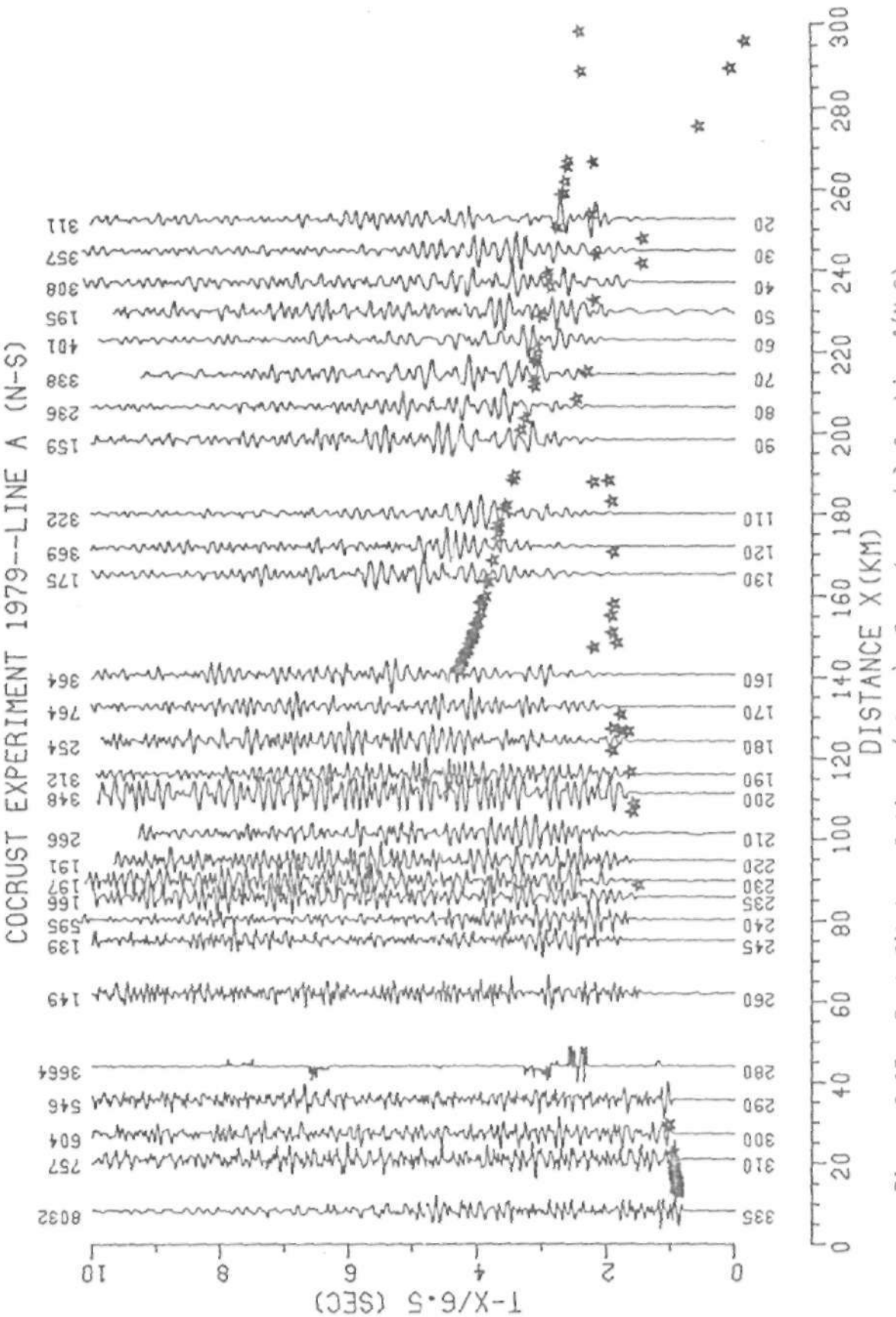


Figure 3.15: Best-fit travel times (stars) of random model for Line A(N-S).

correlation distance and r.m.s. velocity fluctuation that were determined earlier. Figure 3.15 shows the predicted travel times (stars) that fit the observed travel times, and Figure 3.16 (Table 3-2b) shows the the corresponding velocity model from which the travel times were obtained. A comparison of the travel-time residuals for Figure 3.15 is shown in Figure 3.17. One may thus conclude with some confidence that the travel-time and amplitude fluctuations for the crust of this area may be described by a random model with a correlation distance close to 5 km and a mean r.m.s. fluctuation in velocity of about 0.06 km/s or 1%.

3.5 EXTREMAL INVERSION OF TRAVEL TIME DATA

In recent years, emphasis has shifted from the conventional travel-time inversion technique in which layering is assumed in the crust, and a constant velocity is ascribed to the layers towards a model of the crust in which the velocity is allowed to vary continuously with depth. The aim is then to obtain extremal bounds on the possible velocity-depth distributions which fit the travel-time data. These bounds themselves do not represent suitable velocity profiles, nor do all velocity profiles which lie between the bounds (Kennett and Orcutt,1976). The approach however, recognizes the often stated fact that since only a finite data set is usually available, with observational errors, an infinite number of possible solutions to the inverse problem exist (Backus and Gilbert, 1968).

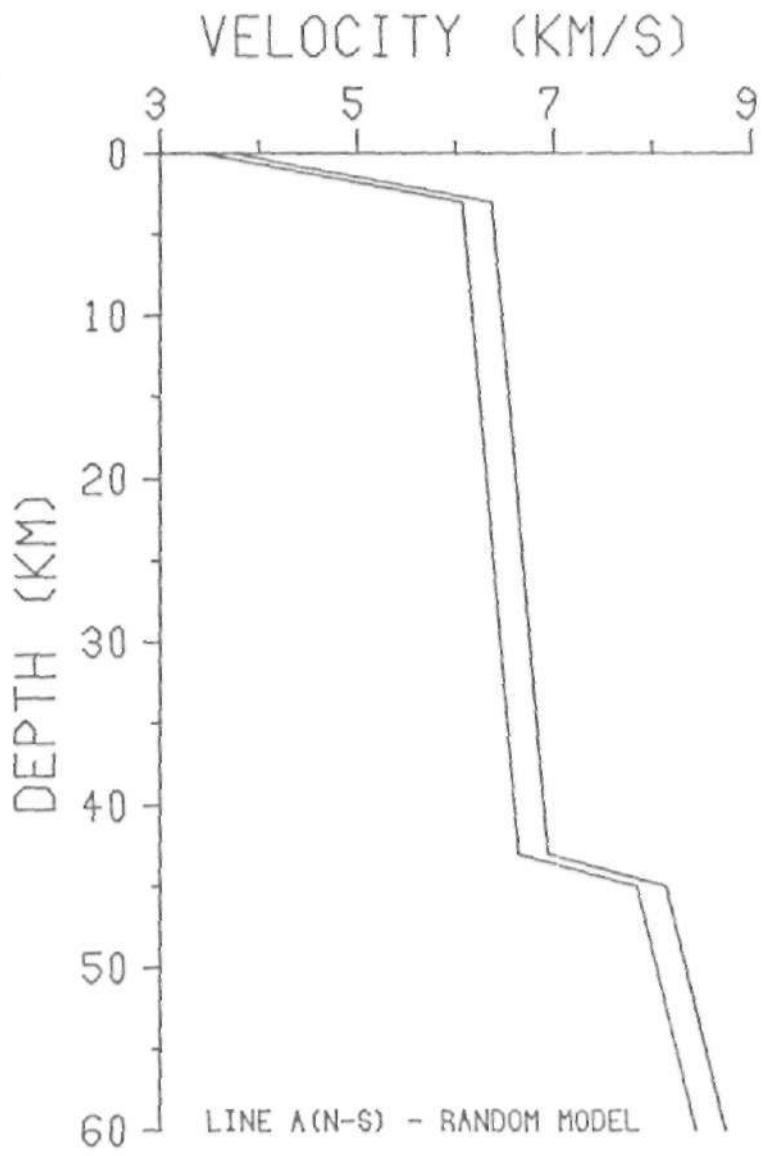


Figure 3.16: Best-fit rancom model for Line A(N-S).

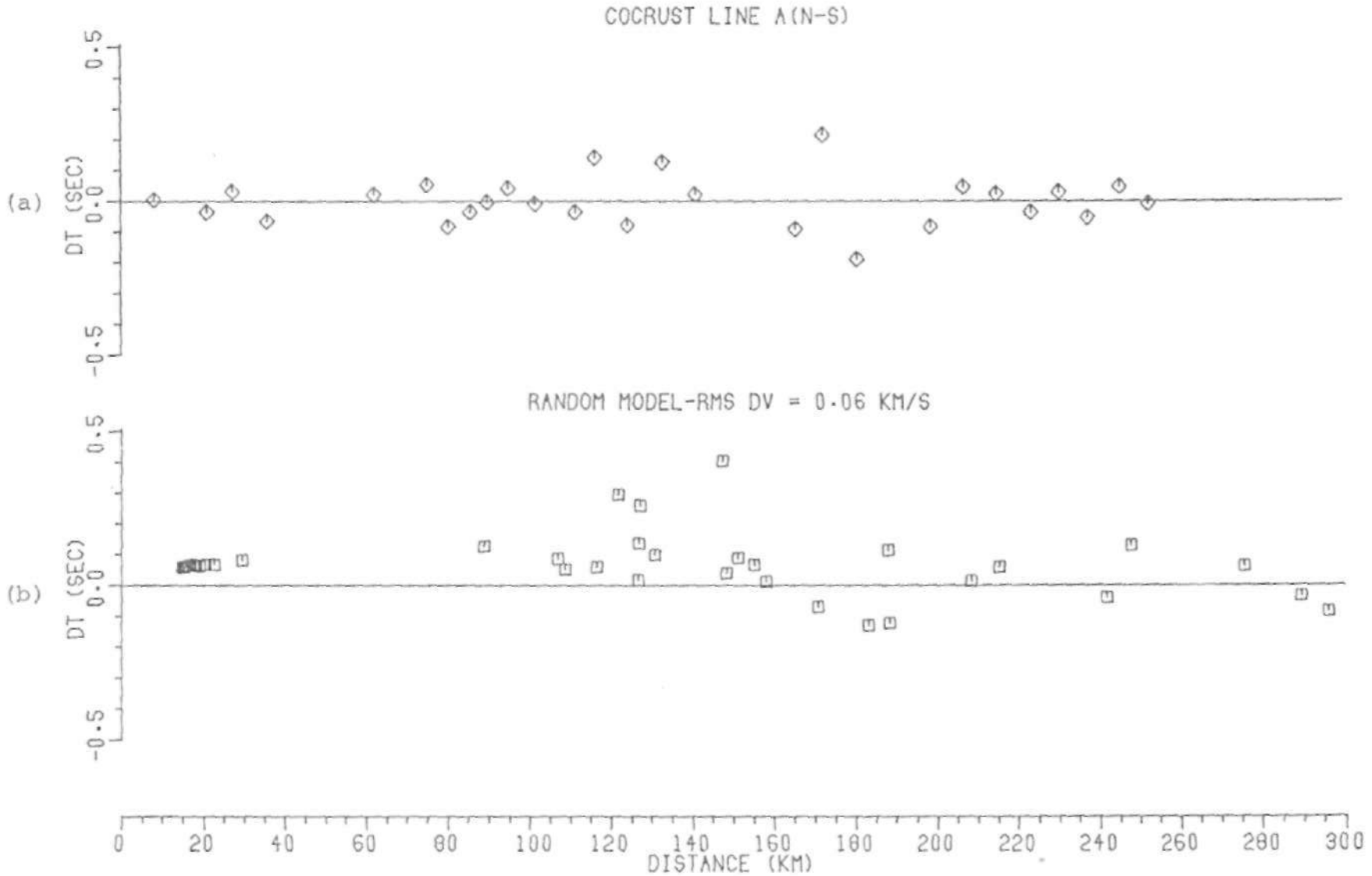


Figure 3.17: Travel-time residuals for (a) Line A(N-S), (b) best-fit random model.

Results of this approach to travel time inversion is modestly represented in the literature. McMechan and Wiggins (1972) introduced a method for the determination of the envelope of possible velocity models, by constructing in the ray parameter-distance (p-Δ) plane, an envelope around the data. The envelope was defined by the scatter of the data points, the uncertainties in the measurements, and various assumptions regarding the behaviour of the curve. Bessonova et al. (1974, 1976) described a method for deriving extremal bounds on possible velocity models from estimates of bounds on the function tau(p) defined by;

$$\tau(p) = T(p) - pX(p) \qquad (3\text{-}1)$$

where p is the ray parameter, T is the travel time, and X is the epicentral distance. They also discussed a practical method of estimating the function tau(p). Kennett (1976) compared the method of Bessonova et al. (1974) and the linearized inverse technique of Johnson and Gilbert (1972), which also used the function tau(p) in which iterative improvement is made to a trial model until it is in agreement with the data. Other studies which used the linear inversion technique include those of Kennett and Orcutt (1976); and Dorman and Jacobson (1980). Davies and Chapman (1975) applied the classical Herglotz-Wiechert method to obtain an envelope which contains all possible models by assuming that the data are from one branch of a travel-time curve. Jurkevics and Wiggins (1980) obtained their velocity-depth envelope from a family of p(x) (ray

parameter versus distance) functions consistent with the data, and Garmany et al. (1979) described a geometrical approach which provides extremal solution using linear programming.

3.5.1 VELOCITY-DEPTH BOUNDS FOR THE COCRUST REFRACTION DATA

The method that was used to obtain velocity-depth bounds for the present data was suggestesd by Dr. R.F. Mereu who also kindly supplied the computer subroutine. The method is a simplified tau inversion technique similar to that of Bessonova et al. (1974) in that it uses the function given by equation (3-1), and similar to the method of Garmany et al. (1979) in that it exploits to full advantage the geometrical nature of the problem. It eliminates the rather complicated mathematical approach of some of the other methods, and its major advantage is therefore its simplicity. Basically, it determines a set of minimum and maximum depths at which some computed velocities would occur for layers derived from a set of discrete slowness values, and minimum and maximum tau corresponding to each value of the slowness. A brief outline of the method and the necessary equations are given in Appendix B.

Tau is the delay time function, and represents the intercept on the time axis of a tangent to the travel-time curve at the point where the local slope is p (i.e. the apparent velocity equals 1/p). It may therefore be determined by numerical differentiation of the travel-time

curve to obtain p, followed by a direct substitution in equation (3-1). Johnson and Gilbert (1972), and Dorman and Jacobson (1980) have shown that errors in p generate only second-order errors in tau, which is one of the attractions of the function. The other major advantage is that tau is single-valued with respect to p, decreases monotonically with increasing p and is continuous except at values of p corresponding to the tops of any low-velocity zone at which points it has a negative jump.

Since the present data were occassionally sparse because of recovery problems with some of the records, it was decided that interpolation of the travel-time data and differentiation to obtain p would not be very suitable. Tau bounds were therefore determined by using the technique of Bessonova et al. (1974) from the knowledge that the function:

$$\tau(X,p_o) = T(x) - p_o X \qquad (3\text{-}2)$$

has a single stationary point which is a maximum for the generally direct, and a minimum for the generally receding branch of the travel-time curve; the extreme value of the function is tau for the ray parameter, p_o. As Kennett and Orcutt (1976) reported in their comparison of the two methods, the technique of Bessonova et al. (1974) appeared to have greater numerical stability.

The procedure then was to determine tau from the maxima or minima of reduced time (T-pX) versus distance plots for

trial values of p. From equation (3-1), one finds that for an error in travel time δT and distance δX for a particular ray parameter, p the error in $\tau(p)$ will be approximately,

$$\delta\tau = \delta T - p\delta X \qquad (3\text{-}3)$$

Since the error in distance is often very small, the error in tau is approximately the error in the travel time. The tau bounds may then be constructed with the estimated travel-time errors.

Preliminary determination of tau using only the first arrival times showed that an undesirable gap existed in the tau and p data which corresponded to the retrograde branch and parts of the P_n branch. In order to reduce the portion that would have to be interpolated to as small an area as possible, retrograde arrival times were determined for Line A(S-N), Line B(N-S), and Line B(S-N) where they could be identified. Since these arrivals are second or later arrivals, they were often obscured and it is estimated that some of the travel times for this branch could be in error by as much as 0.5 seconds. Similarly, the P_n branch was often defined poorly by very few arrival times, and the maxima of the reduced time versus distance plot was not very well defined. Errors in tau estimates for this branch could therefore also be as high as 0.5 seconds.

With the above in mind, tau bounds were constructed with a width of 0.5 seconds, except for p values greater than 0.15 s/km for which the width was 0.3 seconds to

reflect the relatively lower errors for the earlier part of the travel-time curve. The travel times for Line A(N-S) and its reverse profile Line A(S-N) were very similar, so the data were combined to give a single solution. The travel times of Line C(W-E) was not inverted because the gaps in the records between 140 km and 230 km, together with the large scatter of the travel times for the P_n branch due to poor signal-to-noise ratio meant that the tau estimates could not be determined satisfactorily.

Figure 3.18 (a), (b), and (c) show the tau(p) extremal bounds for Line A(combined), Line B(N-S), and Line B(S-N). The figures show that the tau(p) bounds are essentially similar except for values of p greater than about 0.155 s/km. This corresponds to apparent velocities less than 6.45 km/s which indicates that considerable lateral variation exists for the very shallow crust in this area. This was also reflected in the large fluctuation in the intercept times of the first branch of the travel-time curves (see Table 3-1, 3-2, and 3-3). The small jump in tau(p) between p equals 0.128 s/km and 0.133 s/km (Figure 3.18 b) corresponds to a change in tau estimates from the retrograde branch to the P_n branch, and is therefore probably not real. The tau bounds for Line A required interpolation in the interval of p between 0.143 and 0.156 s/km. Since none of the sections showed any marked jump in tau, no low velocity layer is associated with the crust in this area.

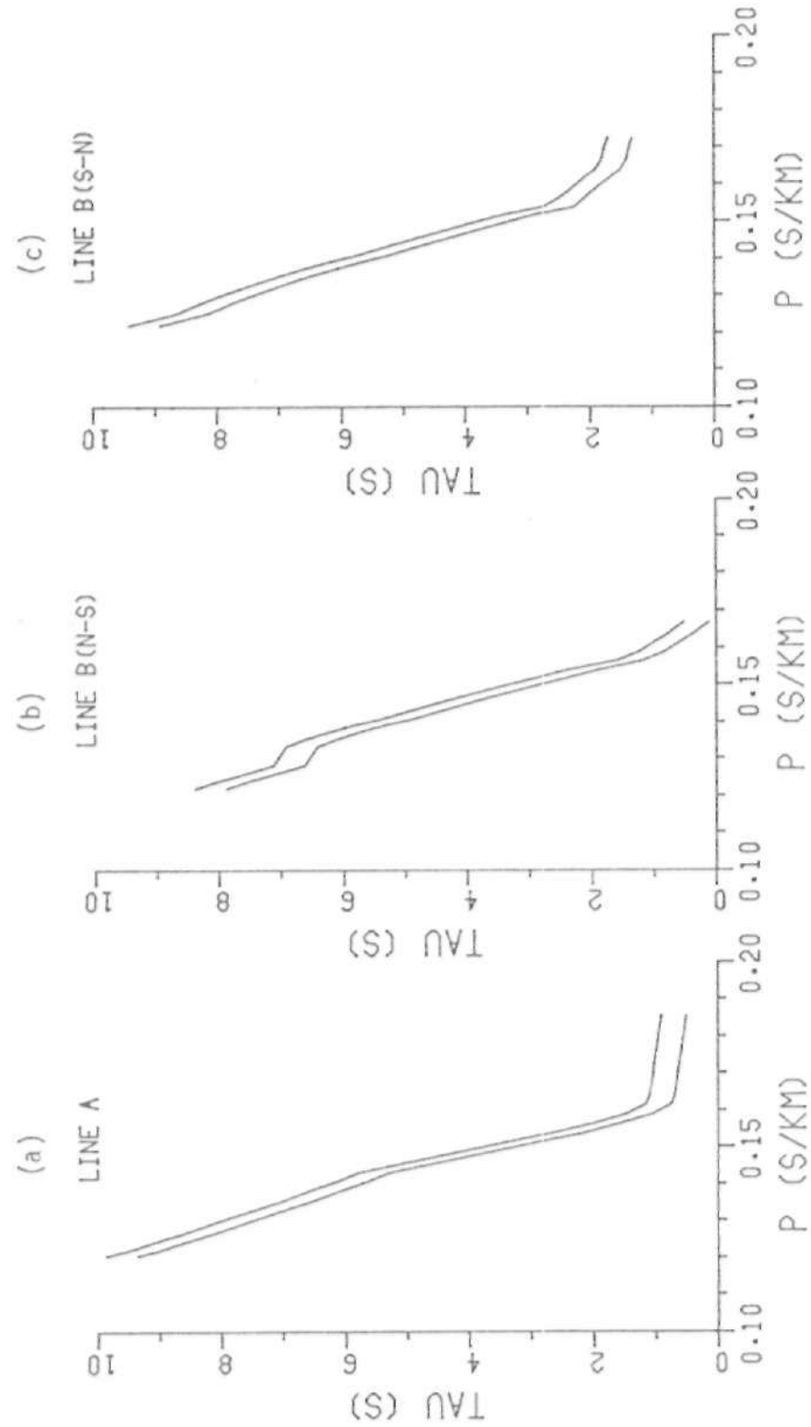


Figure 3.18: Tau bounds obtain from (a) the combined data of Line A, (b) for Line B(N-S), and (c) for Line B(S-N).

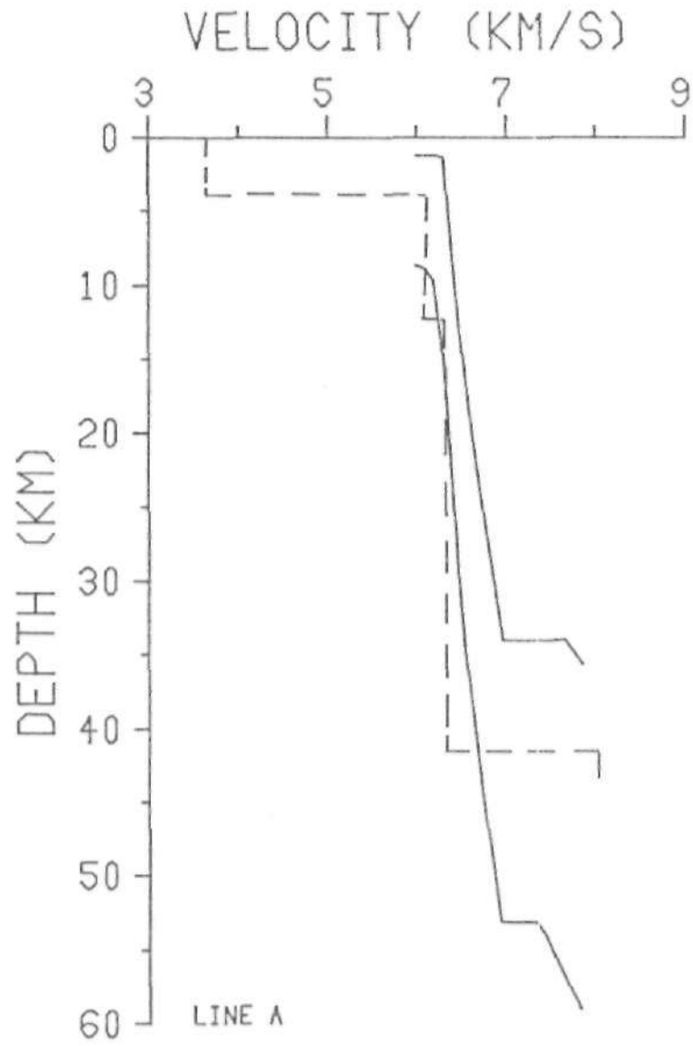


Figure 3.19: Velocity-depth extremal bounds (unbroken lines) obtained from the tau bounds of Figure 3.18(a) compared with a layer solution (broken lines) for Line A. The layer solution is after Hajnal (1980).

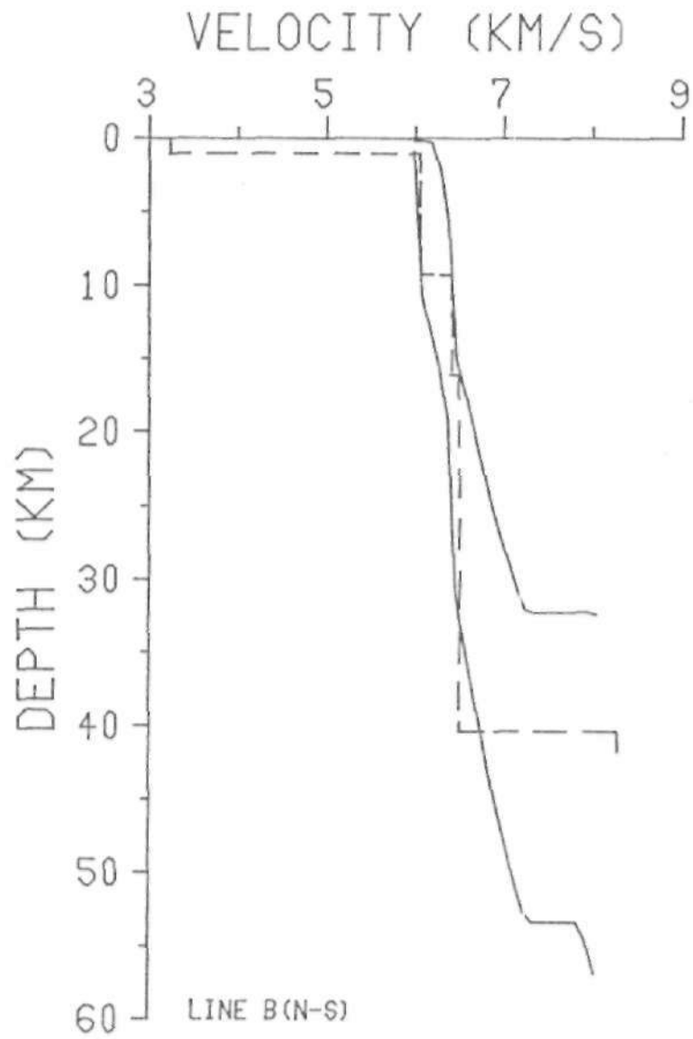


Figure 3.20: Velocity-depth bounds and layer solution for Line B(N-S).

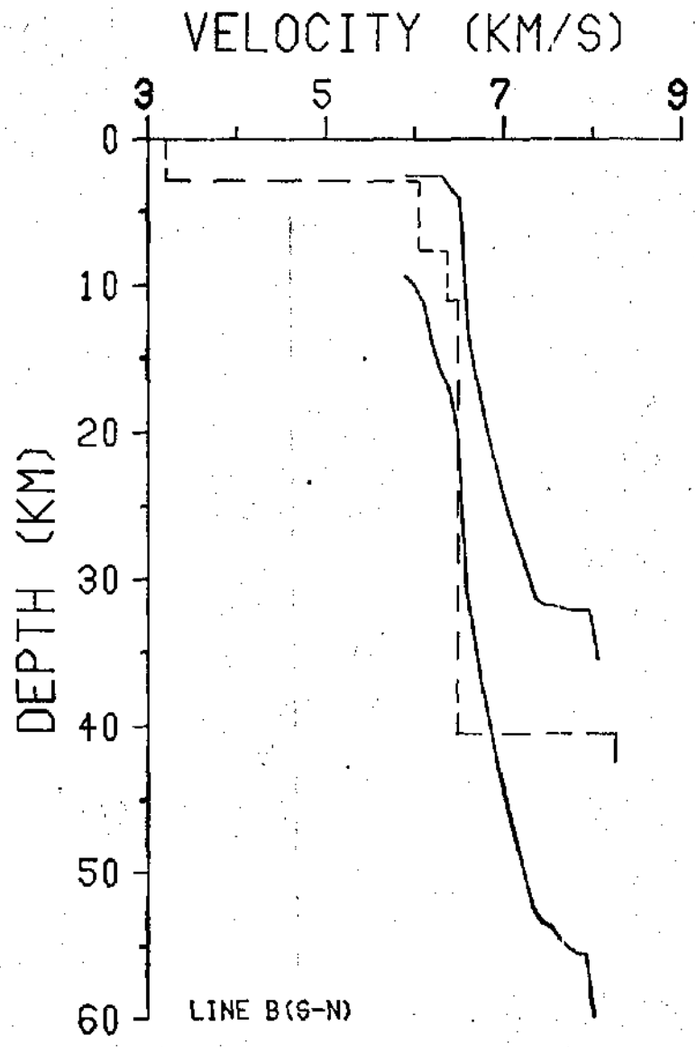


Figure 3.21: Velocity-depth bounds and layer solution for Line B(S-N).

Figures 3.19, 3.20, and 3.21 show velocity-depth bounds obtained from the tau-p curves with the layer solutions (dashed lines) of Hajnal (1980) superimposed for comparison. The bounds of velocities less than 6.0 km/s are not shown in the figures because the tau values in this region were extrapolated to zero for the surface velocity and cannot be meaningful. With the exception of Line A the layered solution appear, for the most part, to be well constrained by the velocity-depth extremal bounds. The large bounds for depths below 30 km is a reflection of the uncertainty in tau bounds for this region. The unusual behaviour of the velocity-depth bounds of Line A with respect to the layer solution might have been caused by an uncertainty in the tau bounds due to the relatively more interpolation required for this line. We, however, recall that the travel-time curve of this profile also behaved exceptionally, leading us to suspect that the problem with this profile may have its origin in the local crustal structure of this area. The fact that the profile lies along portions of the Superior Province boundary as delineated by Green et al. (1979) (see Figure 3.1) might be responsible for the anomalous behaviour. Additional investigation along this line of thought is planned for the future.

In Figures 3.22 and 3.23, a comparison of the velocity-depth bounds is made with the random velocity models of Figures 3.10 and 3.16. The figures again show that good agreement occurs for depths above 30 km,

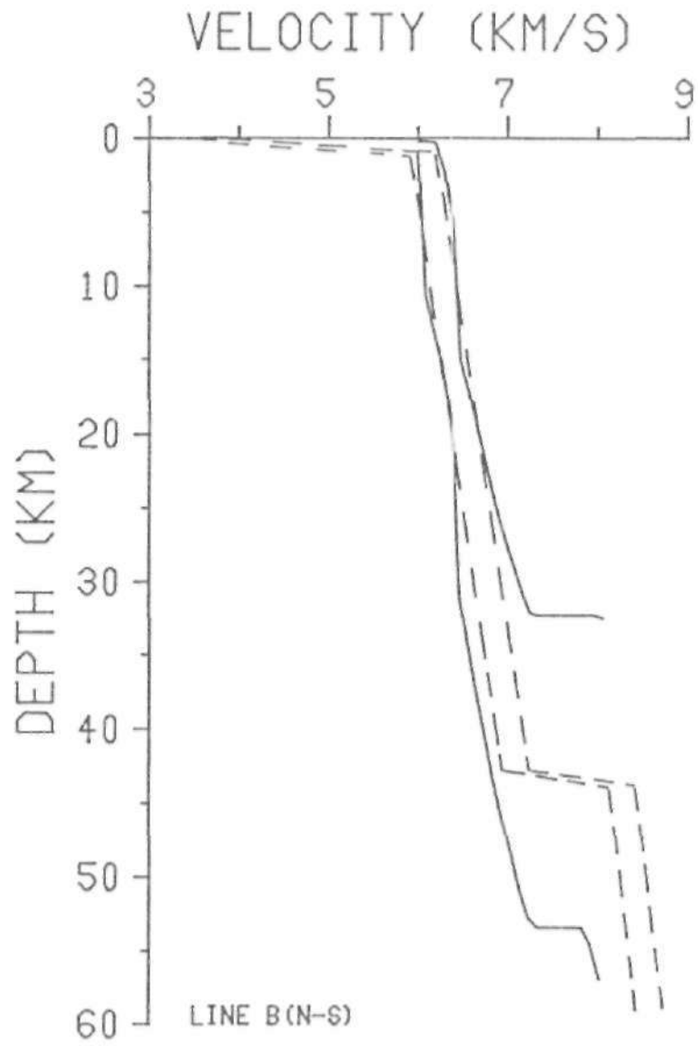


Figure 3.22: Velocity-depth bounds for Line B(N-S) superimposed by the best-fit random model (broken lines).

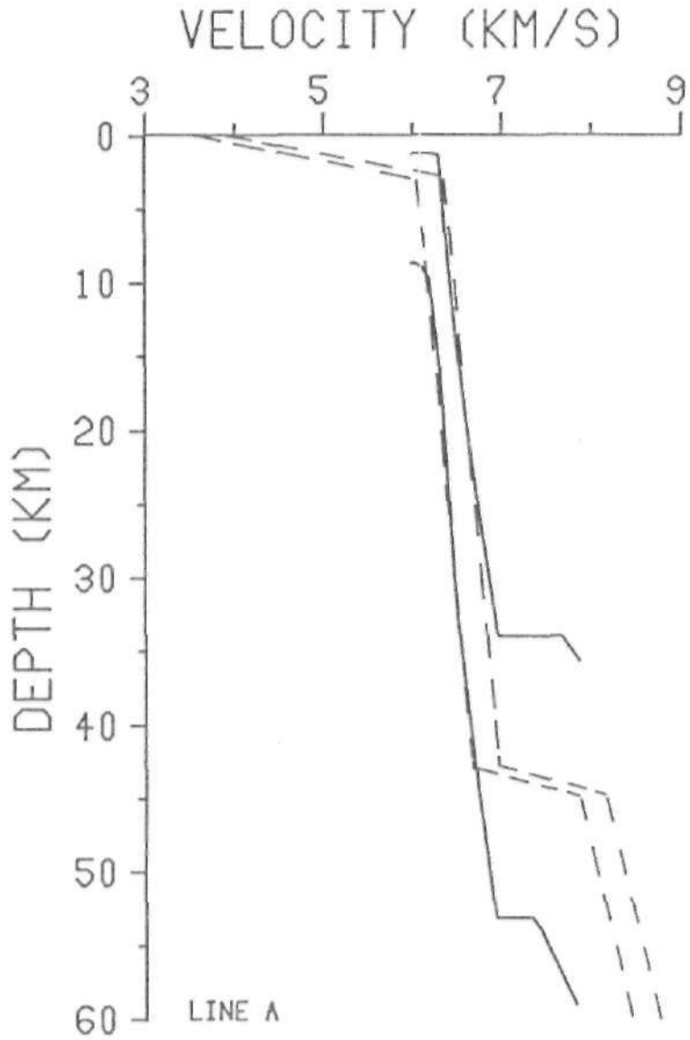


Figure 3.23: Velocity-depth bounds for Line A superimposed by the best-fit random model (broken lines).

corresponding to portions of the refraction sections from which relatively accurate tau bounds could be estimated. The similarity of the models above 30 km, and the relatively good fit of the travel times shown in Figures 3.9, 3.11, and 3.15 all suggest that the random model may be considered as a tightly constrained extremal solution of the data.

CHAPTER 4

P-WAVE SCATTERING THROUGH AN UPPER MANTLE WITH RANDOM INHOMOGENEITIES

4.1 VELOCITY STRUCTURE OF THE UPPER MANTLE

The upper mantle is another region of the Earth where a great deal of uncertainty and complexity exist. However, the considerable progress which has been made in determining body wave velocities in this region of the Earth's interior has, to some extent, enhanced our understanding of its properties. Because of the implications of the results of our numerical experiments to the interpretation of upper mantle travel times, a brief review of existing upper mantle velocity models and their travel-time curves is appropriate in providing a basis for comparison.

The large number of velocity models in the literature today, and the differences in detail between them is an indication that there are significant regional and lateral variations in structure of the upper mantle. Other reasons for these differences include limitations in the interpretation of the observed data caused by incomplete and inaccurate data, and the non-uniqueness of the geophysical inverse problem.

Two of the earliest models commonly referred to are those of Jeffreys (1939) and Gutenberg (1959). The velocity distributions in these models are similar in many respects except that the distribution of Jeffreys has a sharp velocity increase at a depth of 413 km (Figure 4.1c), whereas that of Gutenberg shows a low-velocity zone from just below the crust to a depth of 200 km (Figure 4.2c). The justification for Gutenberg's low-velocity zone was amplitude data from shallow focus earthquakes, which show a rapid decrease in amplitude with distance up to about 15 degrees where they suddenly become large, and thereafter decrease more slowly. The minor triplication around 20 degrees in Jeffreys' travel time curve (Figure 4.1b) is caused by the sharp velocity increase at 413 km depth and is absent in a later model by Jeffreys and Shimshoni (1966). There was, in later years, evidence from surface-wave dispersion studies in support of Gutenberg's low-velocity layer in some regions (Press, 1959, Takeuchi et al., 1959; Dorman et al., 1960); and there were also indications of two zones with rapid increase in shear velocity with depth between 350 to 450 km and 600 to 700 km (Anderson and Toksoz, 1963; Toksoz and Anderson, 1966; Toksoz et al., 1967).

Other gross earth models include those of Lehmann (1964) which explain the same general features as those in the Gutenberg model, and Herrin et al. (1968) which is an over-simplified model of the upper mantle adopted in order

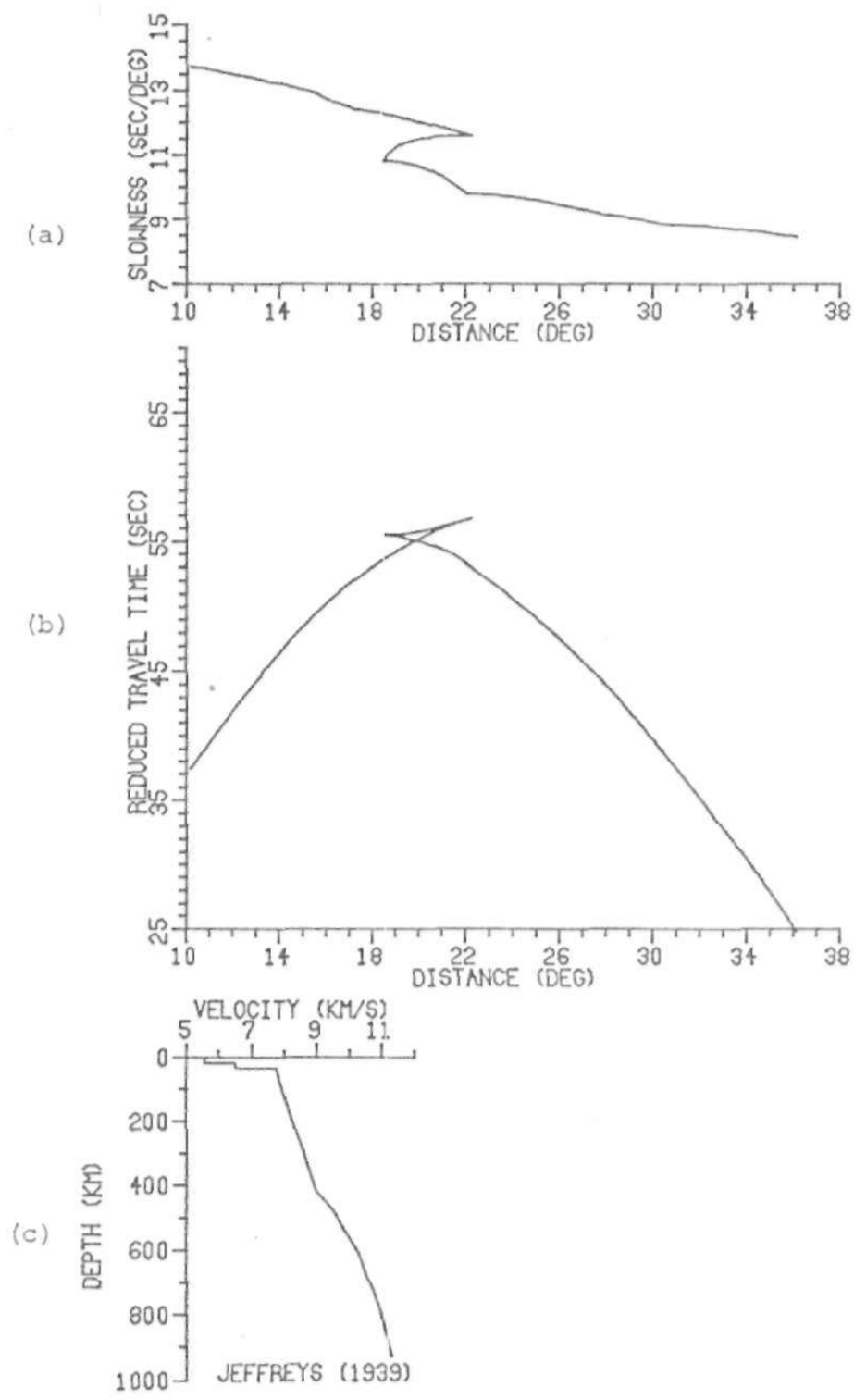


Figure 4.1: The Jeffreys (1939) model.

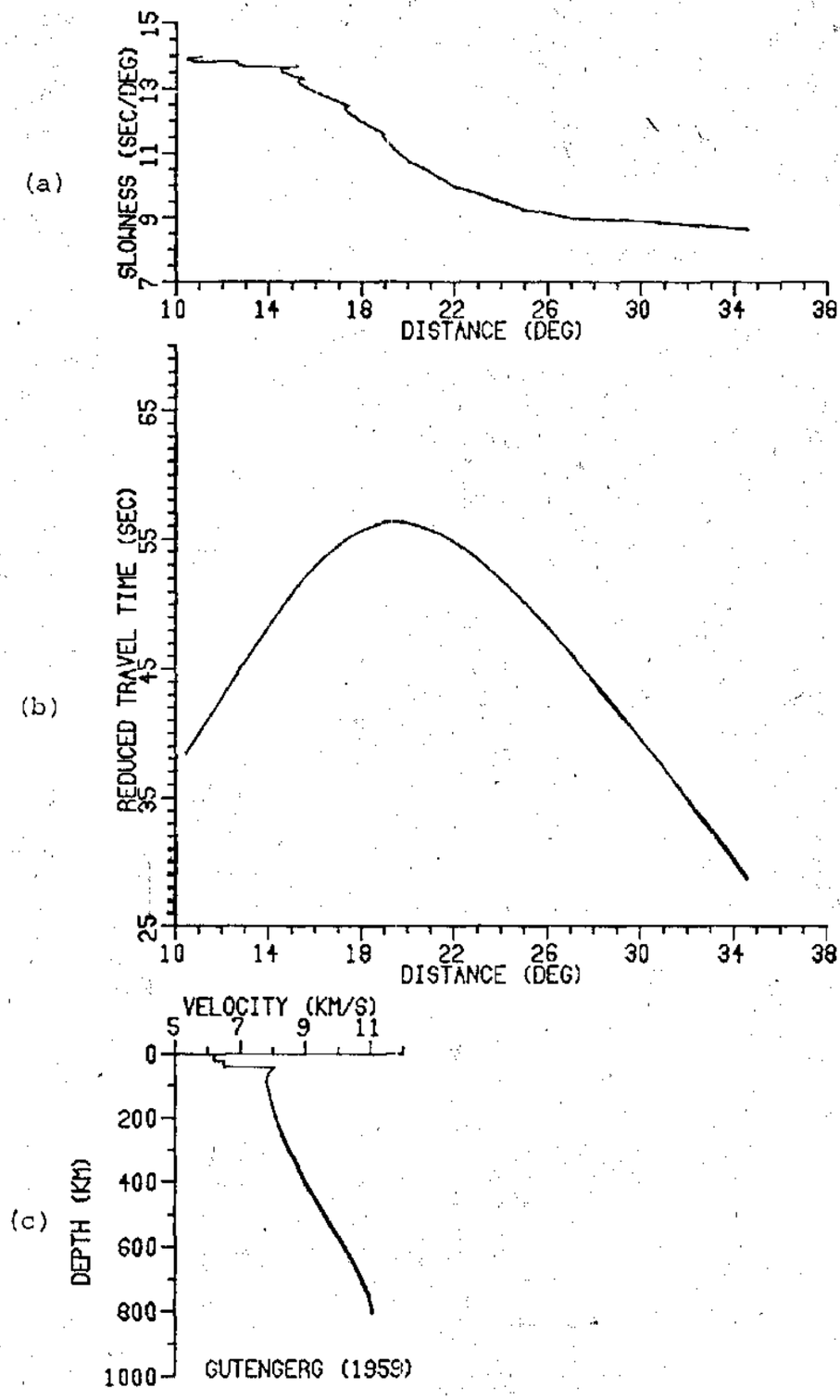


Figure 4.2: The Gutenberg (1959) low-velocity model.

to provide a standard for the investigation of regional variations in travel times (Figure 4.3).

The development of arrays in the late 1950's made it possible to determine $dT/d\Delta$ directly without having to smooth and numerically differentiate widely spaced data. This facilitated measurements for the first arrivals as well as for later arrivals which could then be included in the inversion of travel time data for more reliable results. Since then, a large number of studies have been done on the velocity structure of the earth's mantle, and comprehensive reviews may be found by Lehmann (1967), Julian and Anderson (1968), Hales (1972), and Simpson (1973). A summary of recent models include those of Niazi and Anderson (1965), Lukk and Nersesov (1965), Johnson (1967), Kanamori (1967), Green and Hales (1968), Lewis and Meyer (1968), Archambeau et al. (1969), Helmberger and Wiggins (1971), Wiggins and Helmberger (1973), Mass and Alexander (1974), Simpson et al. (1974), King and Calcagnile (1976), Dey-Sarkar and Wiggins (1976), Ram and Mereu (1977), Burdick and Helmberger (1978), Ram Datt (1981), and others.

While all these models also differ from one another in detail, most of them contain the same general features, i.e. discontinuities or large positive velocity gradients near depths of 400 km and 600 km (see for example Figures 4.4c, 4.5c and 4.8c); and a low-velocity zone at some depths in the upper-most mantle (Figures 4.5c and 4.6c). The presence of these transition zones implies that two major

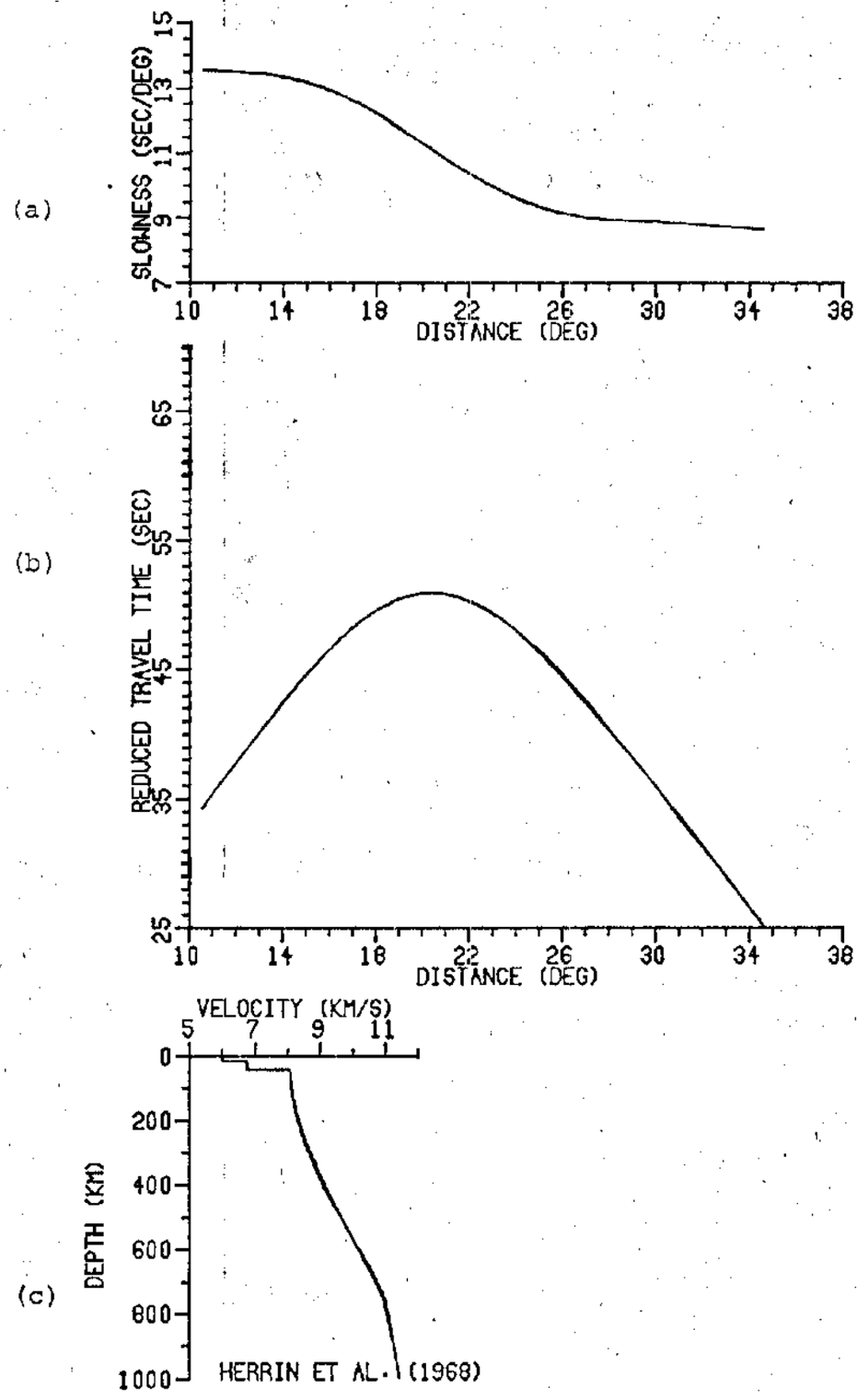


Figure 4.3: The Herrin et al. (1968) model.

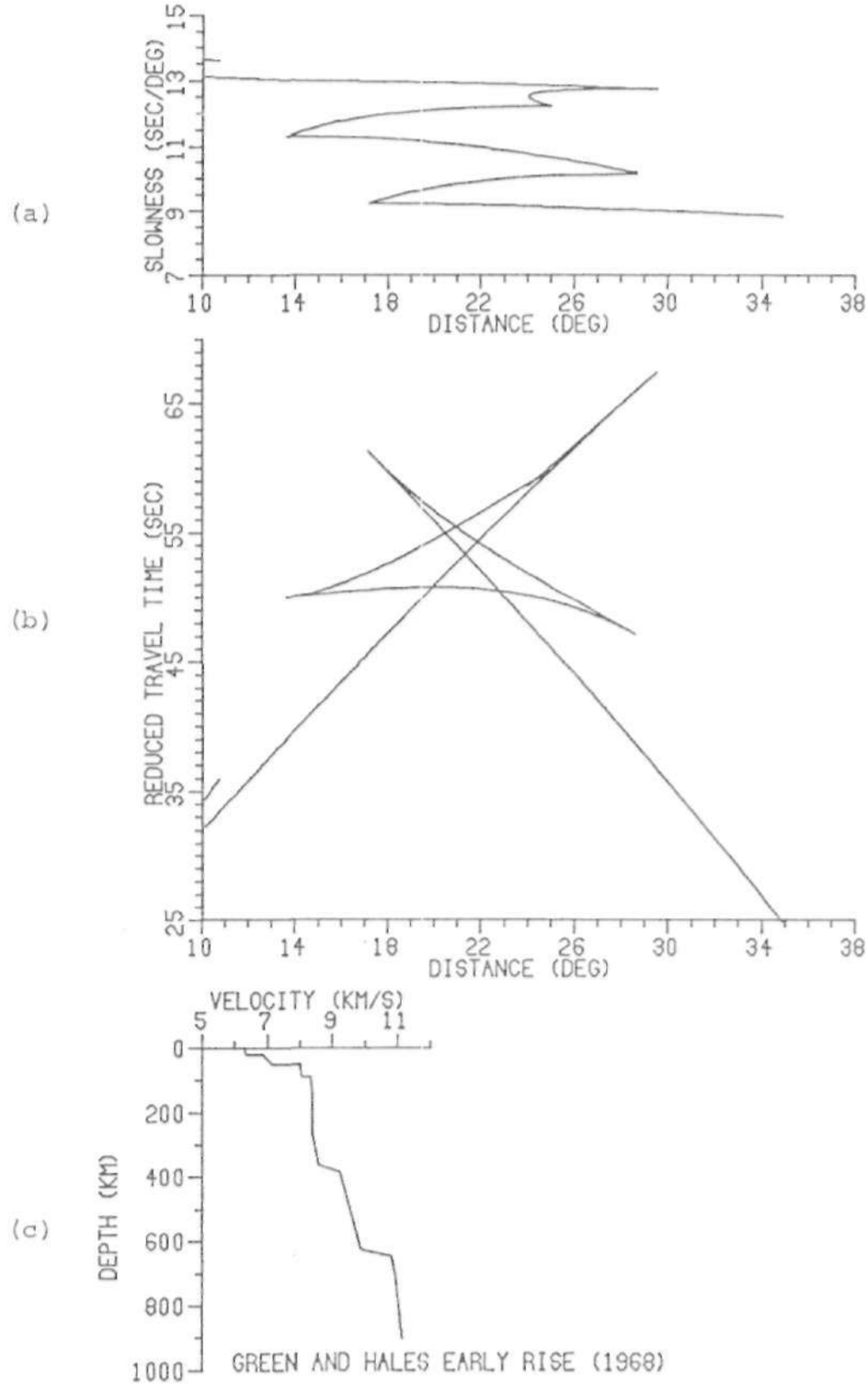


Figure 4.4: The Green & Hales (1968) model.

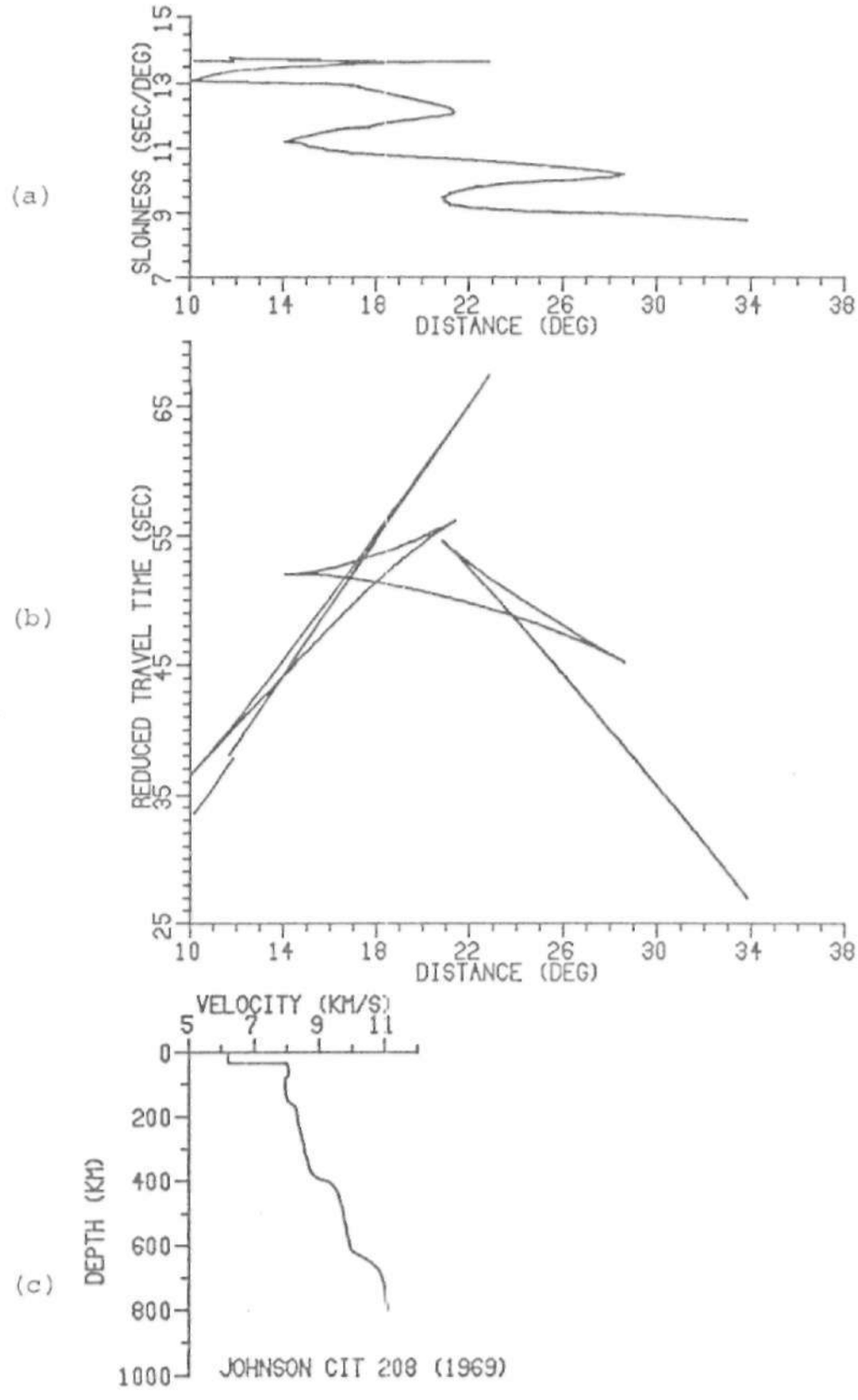


Figure 4.5: The Johnson (1969) model.

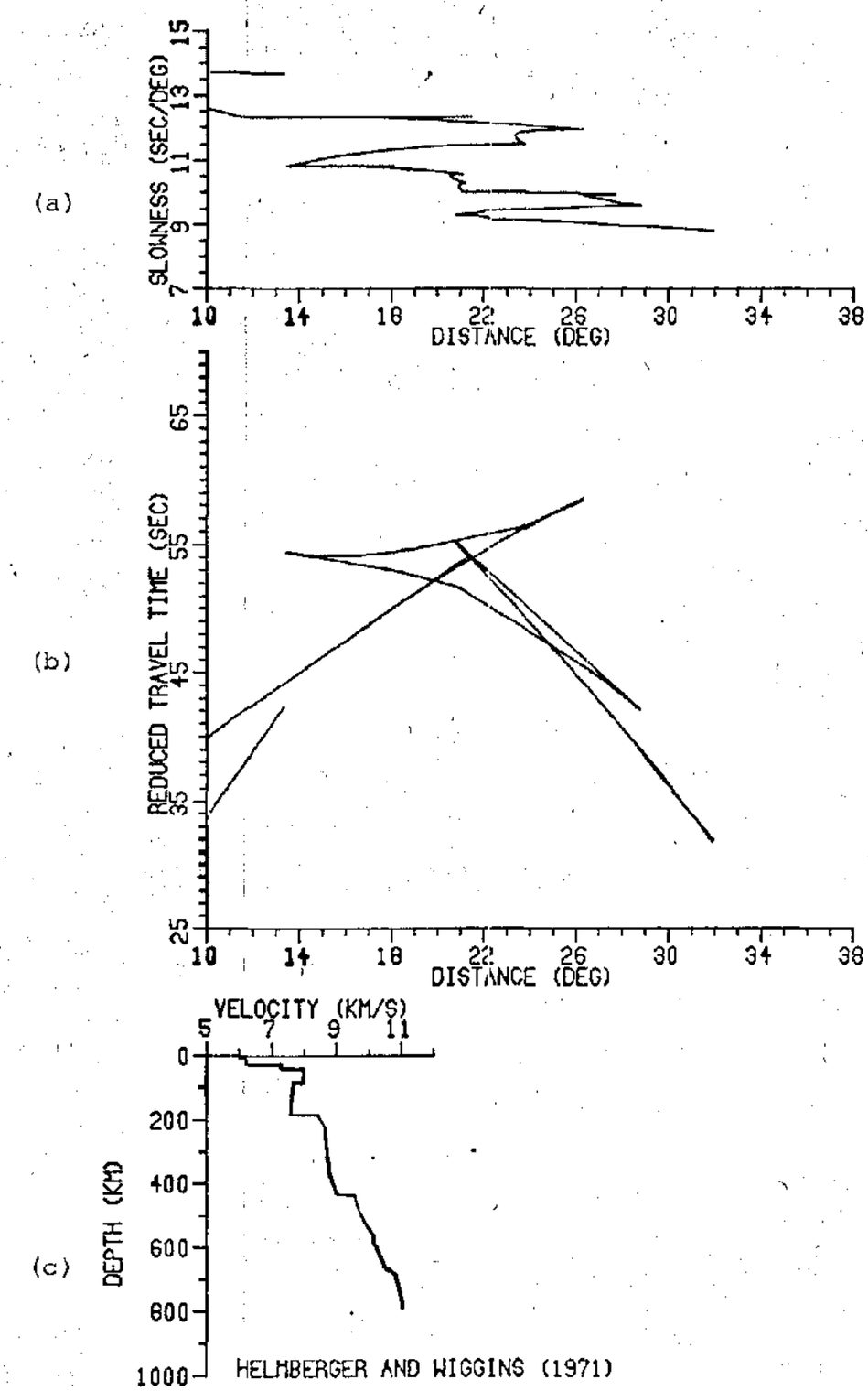


Figure 4.6: The Helmberger & Wiggins (1971) HWNE model.

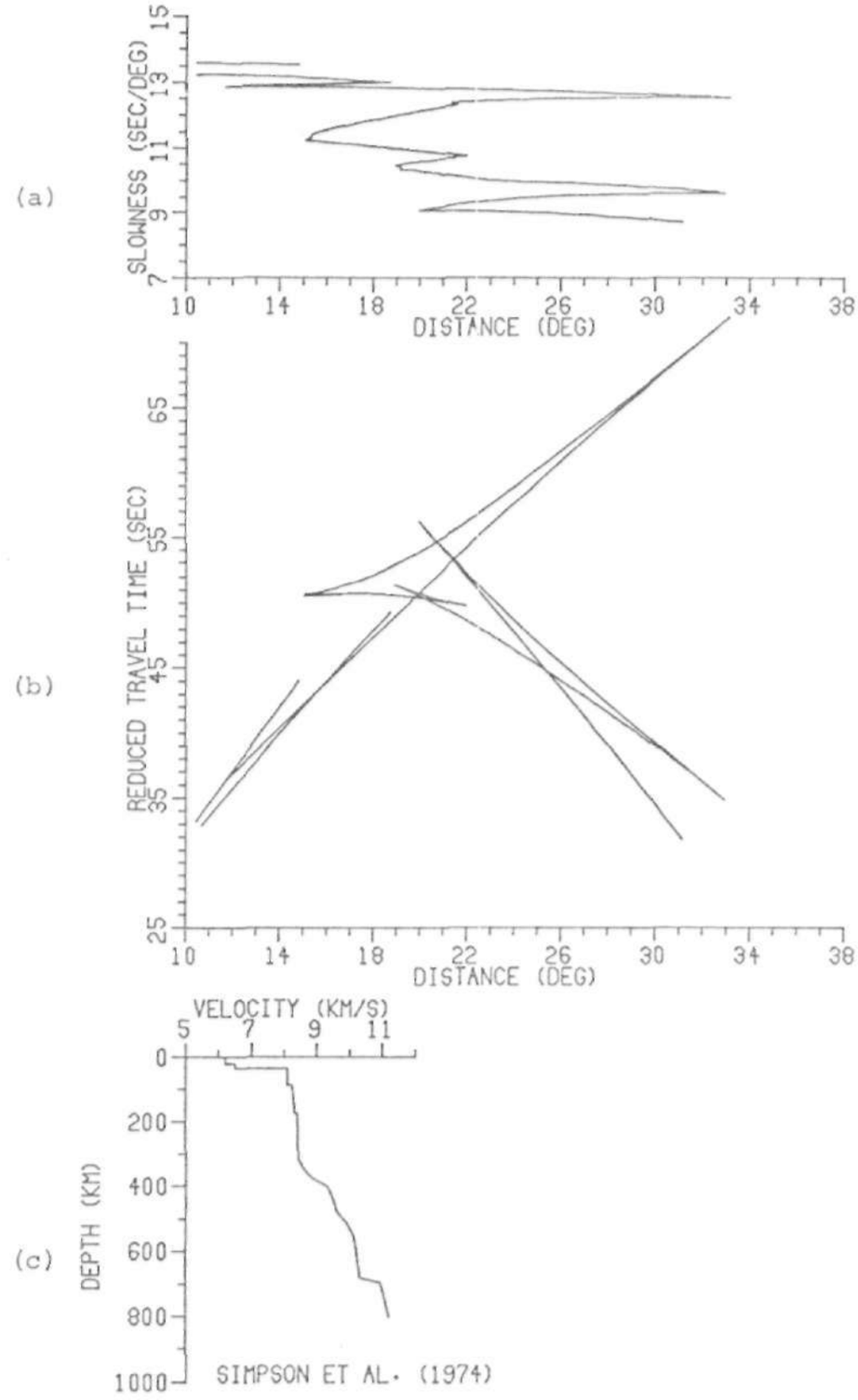


Figure 4.7: The Simpson et al. (1974) SMAK I model.

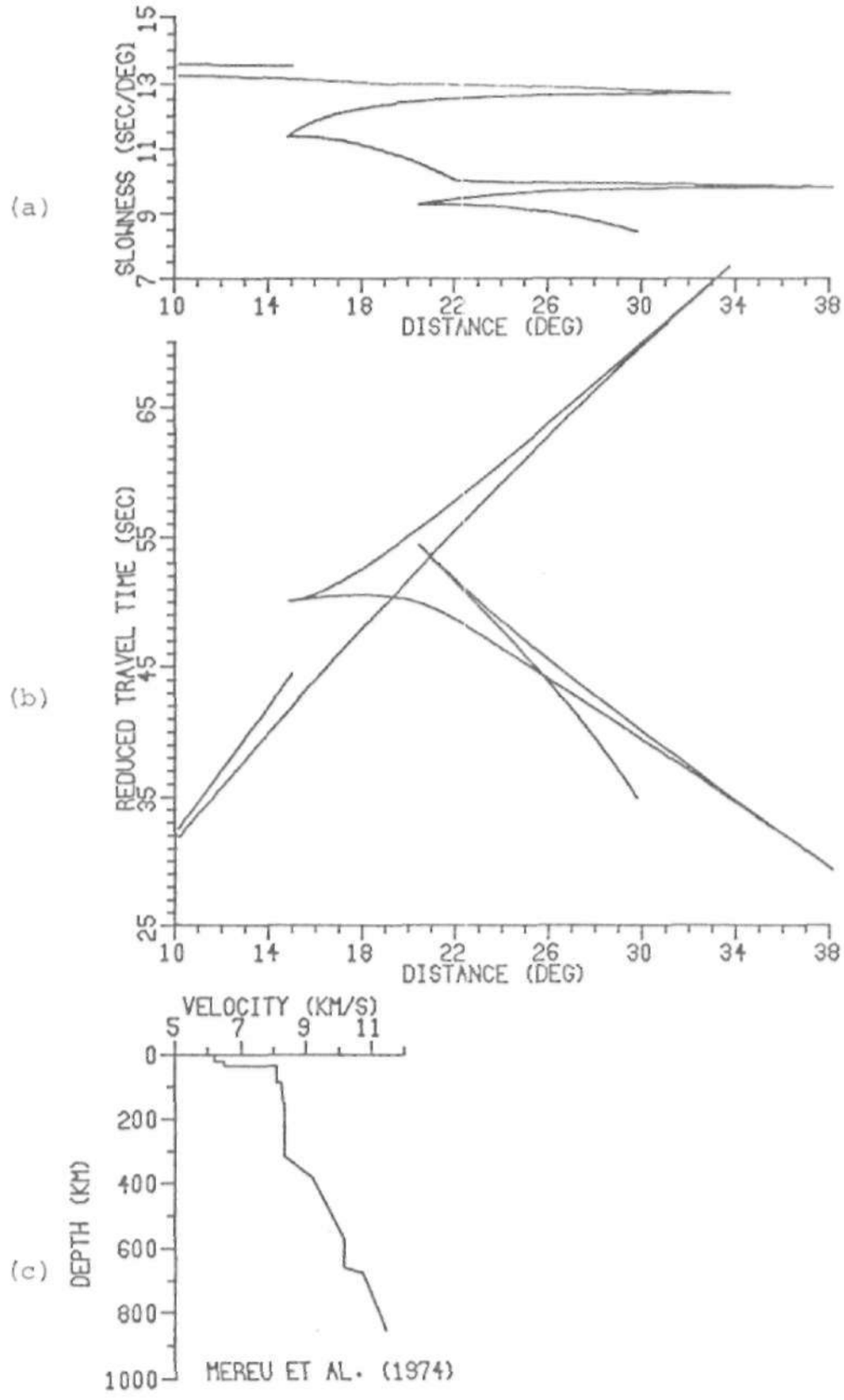


Figure 4.8: The Mereu et al. (1974) SMAK II model.

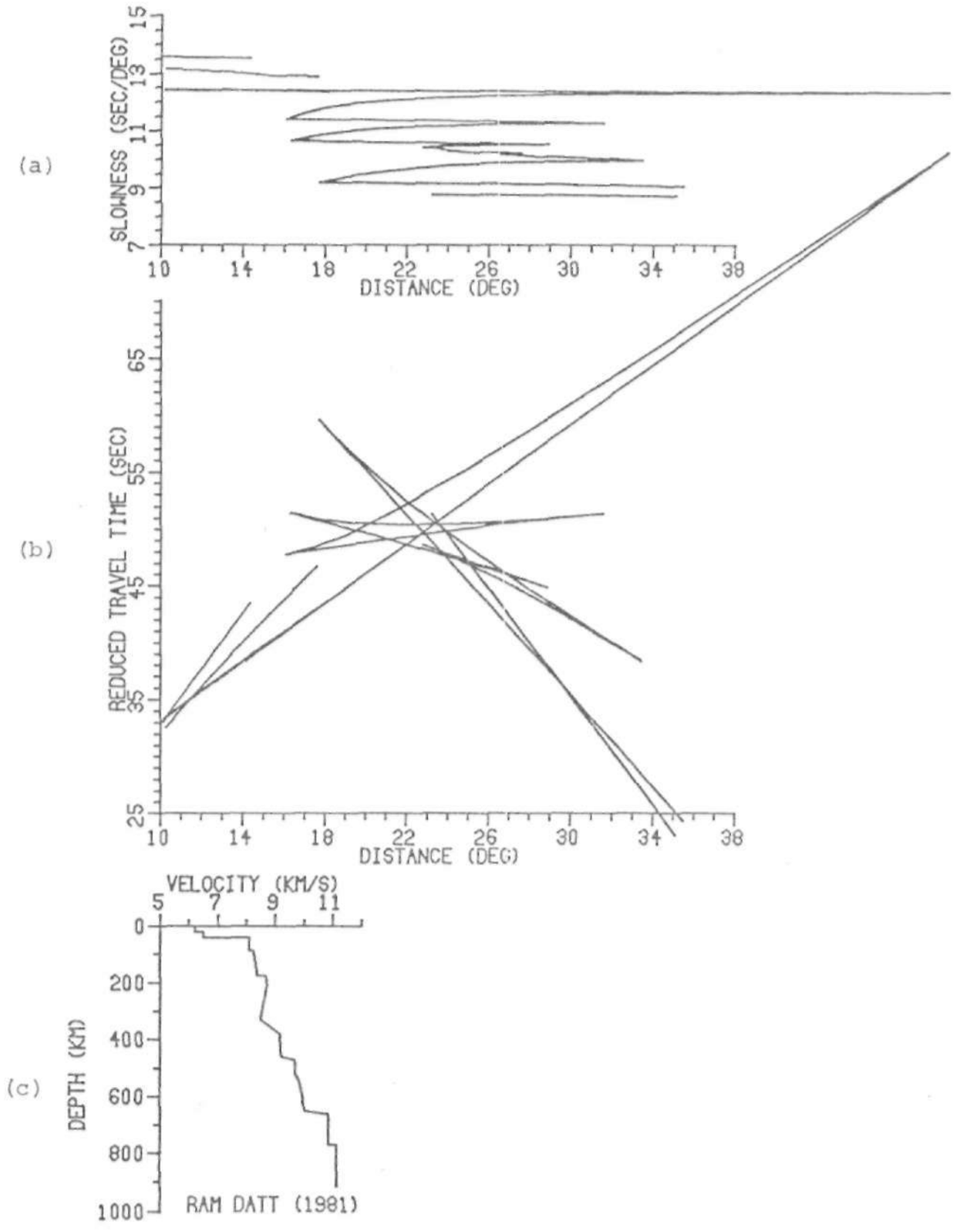


Figure 4.9: The Ram Datt (1981) model.

triplications should exist in the travel-time curve for distances less than 30 degrees as indicated in the examples shown in Figures 4.4b to 4.8b.

4.2 RESULTS FROM EXPERIMENTS FOR THE UPPER MANTLE

The numerical experiments for the upper mantle followed the same general procedure described in Chapter 2 for the crustal models. The basic starting velocity model is shown in Figure 4.10 and consists of the Herrin model (Herrin et al., 1968) for depths below 40 km. The top of the model was represented by a single-layered crust with a transition zone where the velocity increases from 6.75 to 8.0 km/s between depths of 30 and 35 km. The theoretical travel-time curve for such a model is a smooth continuous curve without any triplications or breaks, and is shown in Figure 4.11. The crosses in that figure represent travel times calculated for the model by the ray tracing program described in Section 2.3.1 of Chapter 2, whereas the continuous curve was derived from conventional ray theory (Bullen, 1963). As the figure indicates, agreement between the two is very good, and Figure 4.11 represents another check of the ray tracing procedure. Figure 4.12 shows ray paths that would be obtained for such a homogeneous model.

The basic model was then modified with random variations in velocity in the same manner as the crustal model of Figure 2.3. The maximum velocity perturbation was 0.2 km/s (or 0.07 km/s r.m.s.), and the correlation

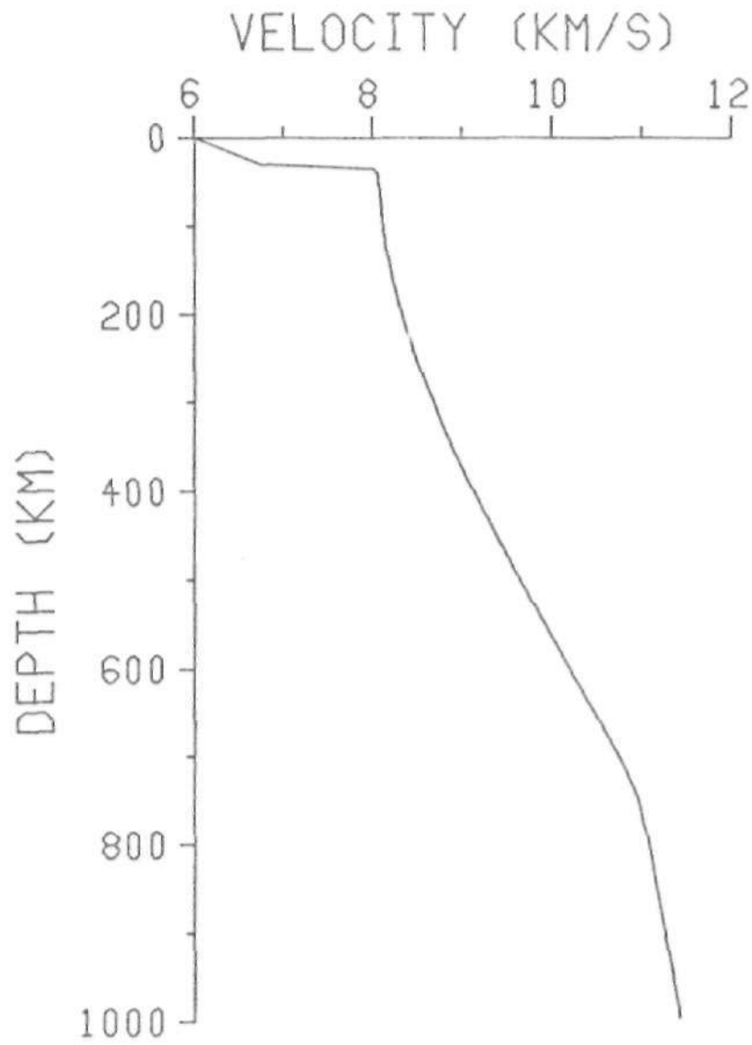


Figure 4.10: Simple upper-mantle starting model for the numerical experiments.

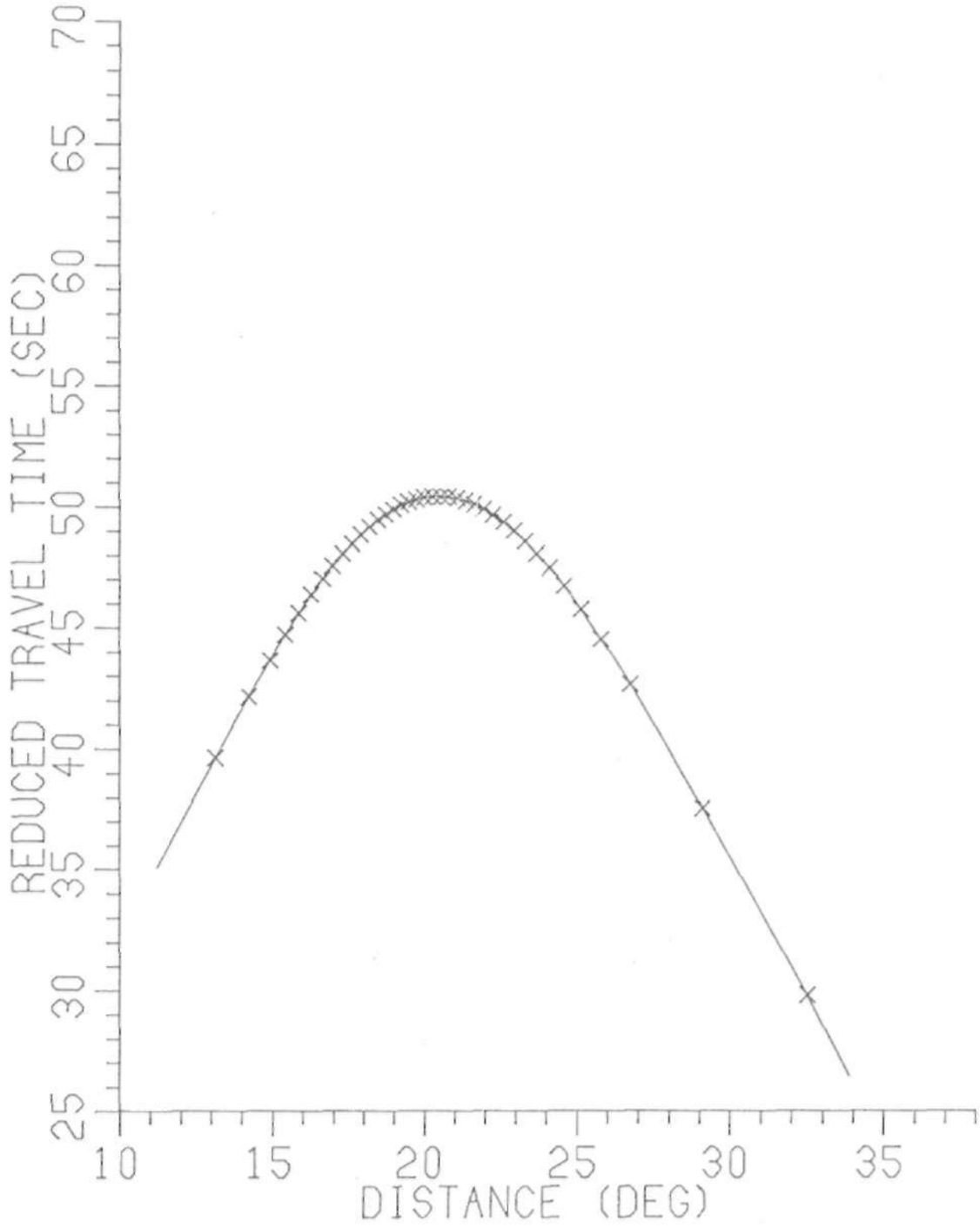


Figure 4.11: Travel-time curve for the model shown in Figure 4.10 by conventional ray theory (unbroken line), and by ray tracing (crosses).

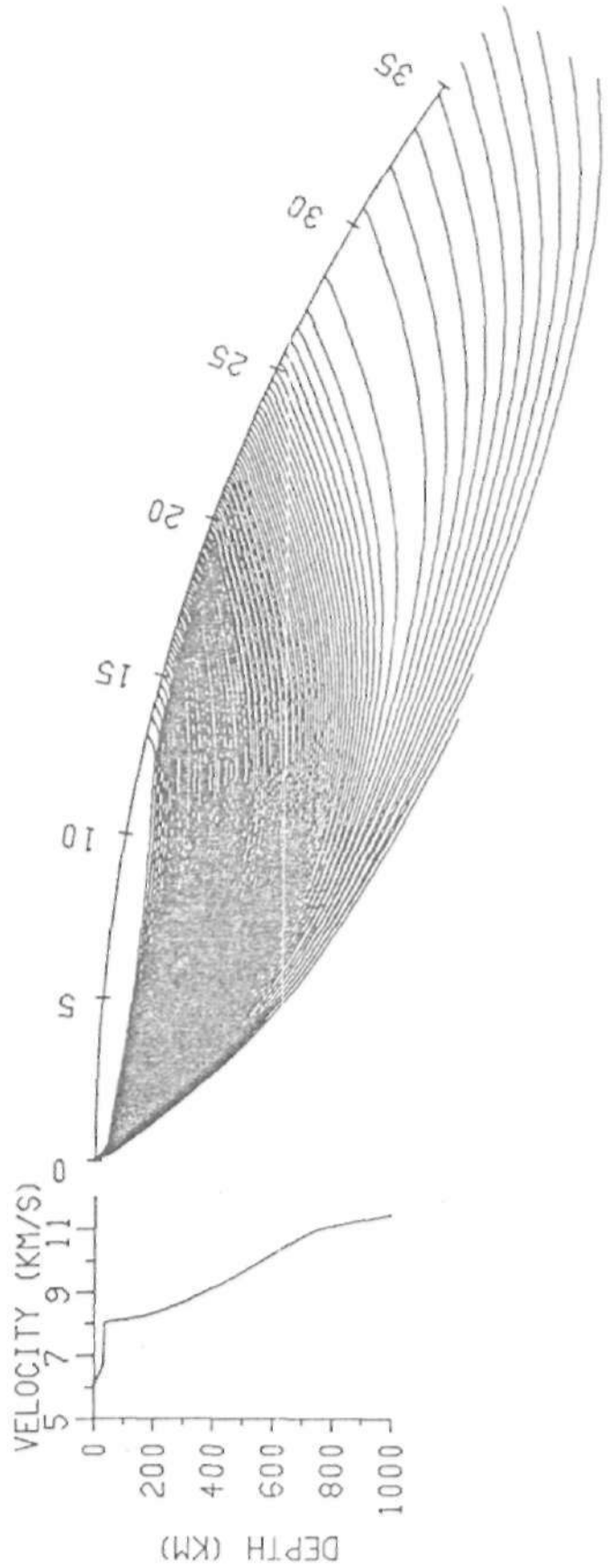


Figure 4.12: Ray geometry for starting model.

parameter was fixed at 15 km because this value is consistent with results from other upper mantle studies (e.g. Aki, 1973). The resulting ray path diagram for one of the models is shown in Figure 4.13. An examination of this figure reveals that the smooth predictable travel paths evident in Figure 4.12 has now been replaced by complicated paths which show many local retrograde patterns, and in some cases appeared to be affected by a channelling effect probably caused by small-scale, local negative gradients. The manner in which these features are translated on to a travel-time plot is shown in Figure 4.14 where the travel time of each ray has been plotted on a reduced time scale (reducing velocity is 10 km/s) as a short line. The slopes of the short line segments show the slowness ($dt/d\Delta$) for each arrival point.

Figure 4.14 predicts that as a result of multi-pathing, several arrivals of distinctly different $dt/d\Delta$ should be observed on any seismogram, and that rapid changes in $dt/d\Delta$ should be observed over very short distances. This is particularly true for the distance range 17 to 25 degrees, and was consistent when the experiment was repeated for a different set of random numbers (Figure 4.15). This pattern of points is very similar to the overall appearance of observations obtained from a number of array studies; e.g. Simpson et al. (1974), Ram and Mereu (1977), England et al. (1977), Ram et al. (1978), and Ram Datt (1981). An example from Simpson et al. (1974) is shown in Figure 4.16,

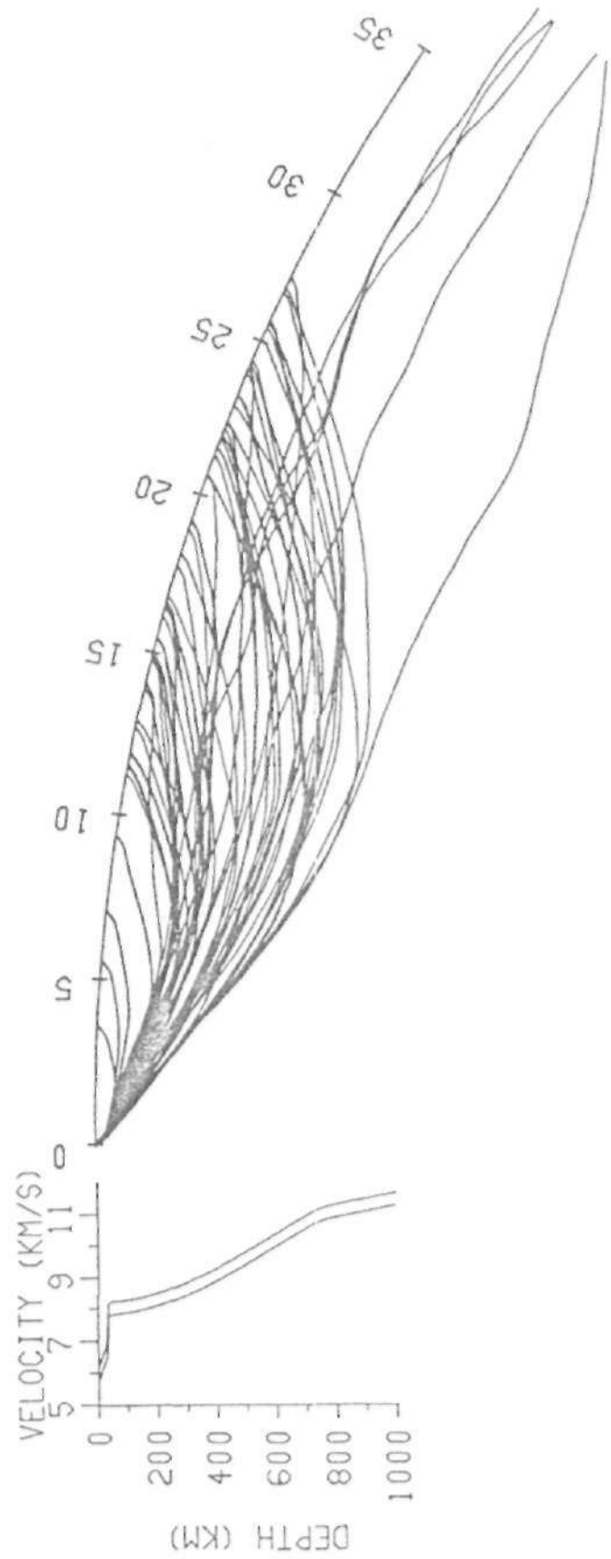


Figure 4.13: Ray geometry for model with smoothed lateral inhomogeneities superimposed on the basic model of Figure 4.10.

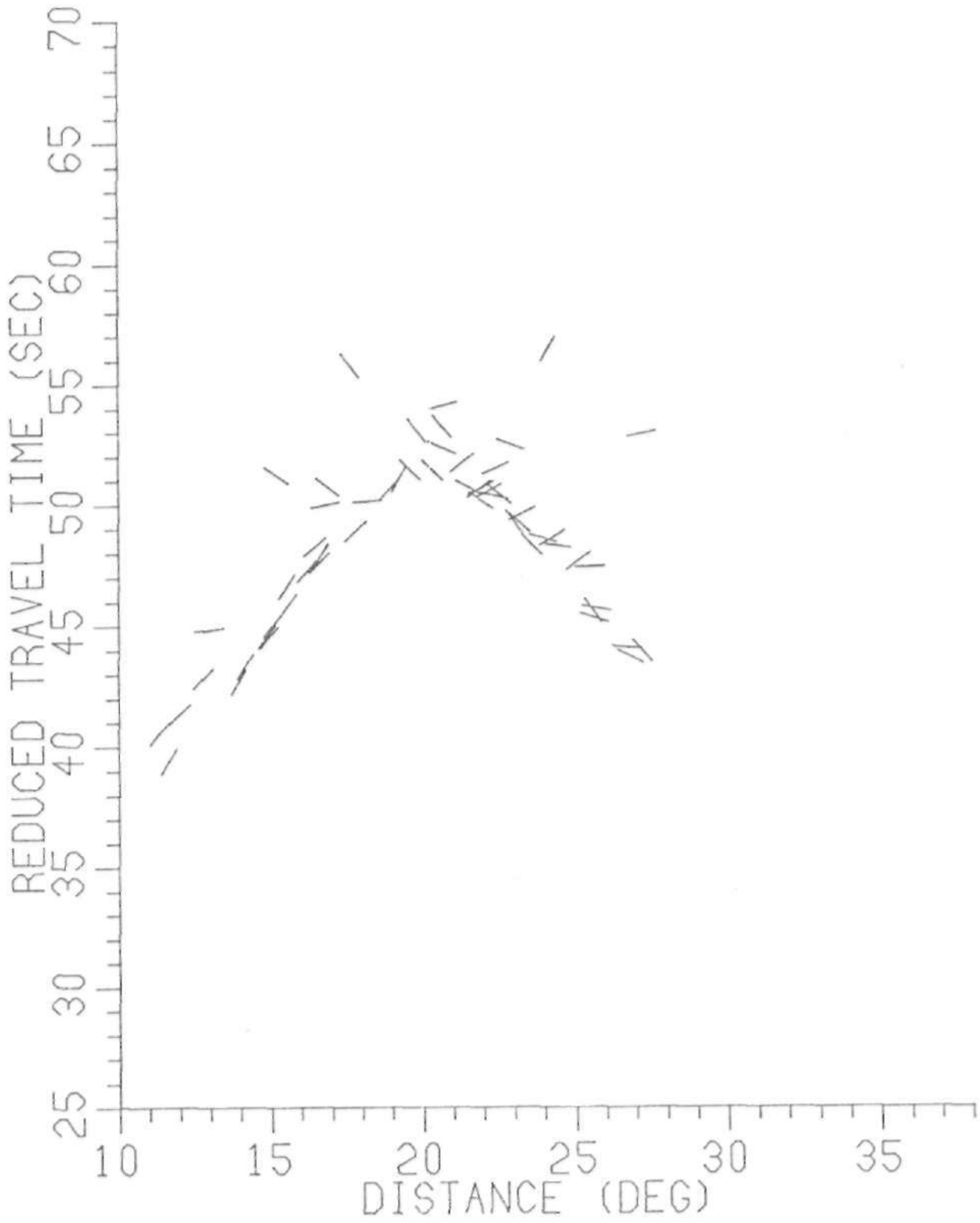


Figure 4.14: Travel-time and slowness results for the model shown in Figure 4.13.

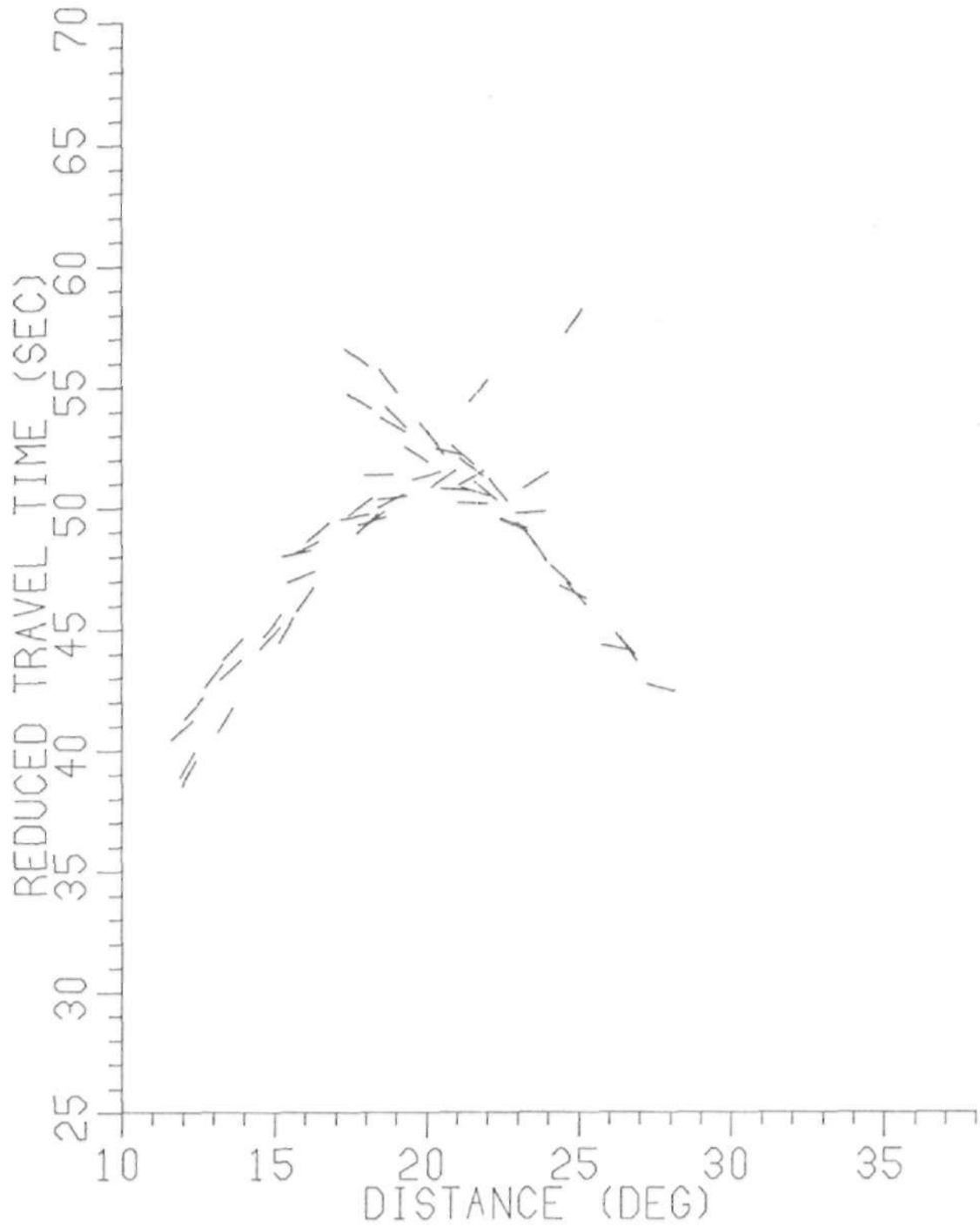


Figure 4.15: Travel-time and slowness results similar to that shown in Figure 4.14, but for a different set of random numbers.

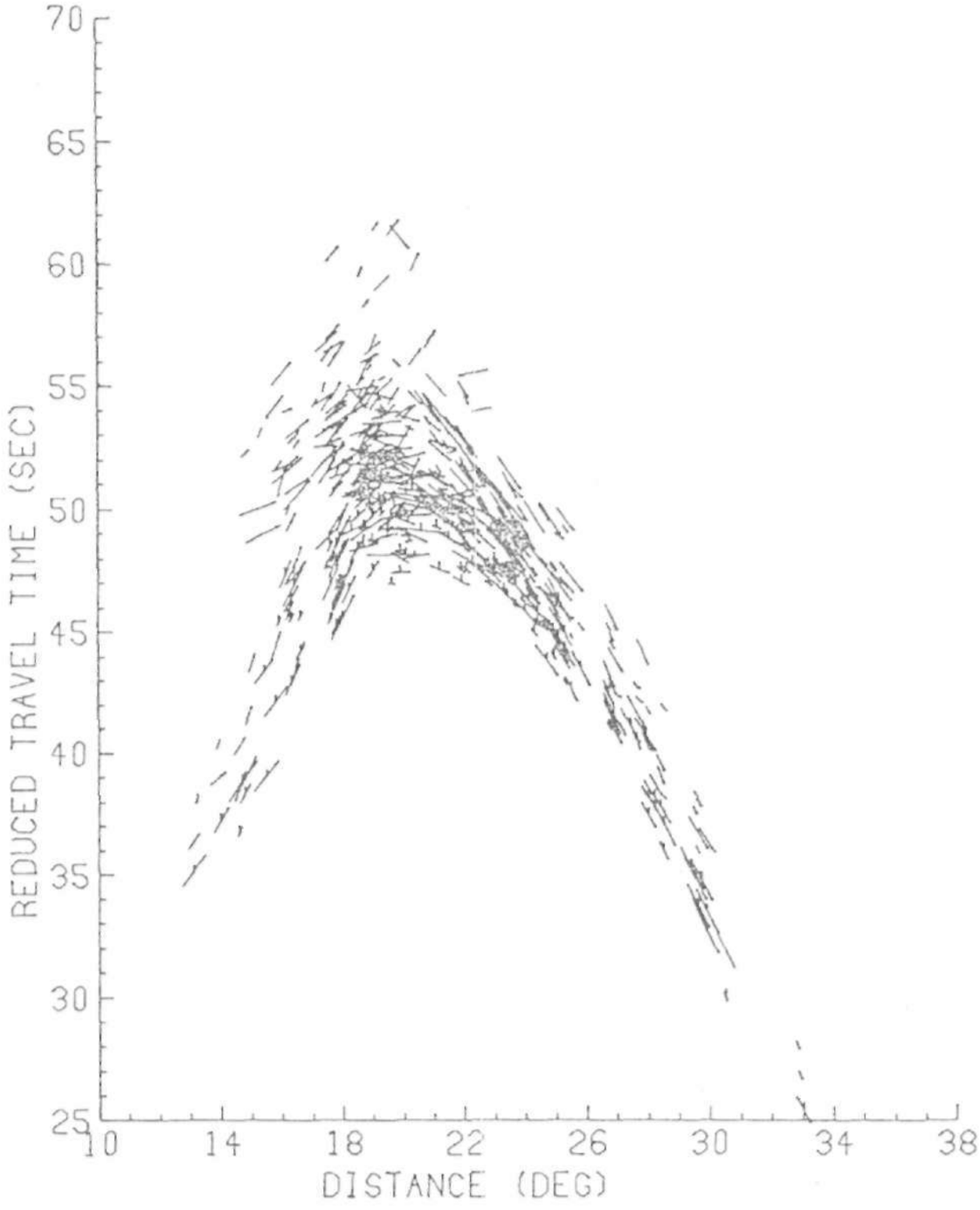


Figure 4.16: Travel-time and slowness data observed at Warramunga array (WRA) for northeastern Australia (after Simpson et al., 1974).

and another from Ram et al. (1978) is shown in Figure 4.17.

If one attributes the rapid changes in the slowness of the first arrivals to the effect of the discontinuities near 400 and 650 km, major triplications are introduced into the theoretical travel-time results such as indicated in Figures 4.5b-4.9b. Signal amplitudes should therefore be observable on the forward ends of the later-arrival branches. However, considerable difficulties have been encountered when attempts were made to identify these branches by following through the pattern of later-arrival $dt/d\Delta$ measurements. Green and Hales (1968) in their study of P-wave travel times in the central United States also found little evidence for the triplicated branches. Mereu et al. (1974) explained their absence by varying Q such that the values of Q above each of the two high velocity gradient zones were at least 50% less than the values just below the zones, and Ram Datt (1981) attempted to examine the extensions in terms of reflections produced by the underside of the discontinuities. However, the complexity of the Ram Datt (1981) model (Figure 4.9) does however suggest that a random media approach to the problem may provide an alternative explanation for the absence of the branches. In other words the branches are not observable because they do not exist, and the complex pattern of slowness observations is the direct result of scattering from lateral and vertical inhomogeneities as is shown in Figure 4.14 and Figure 4.15. This contention will be further illustrated by an inversion

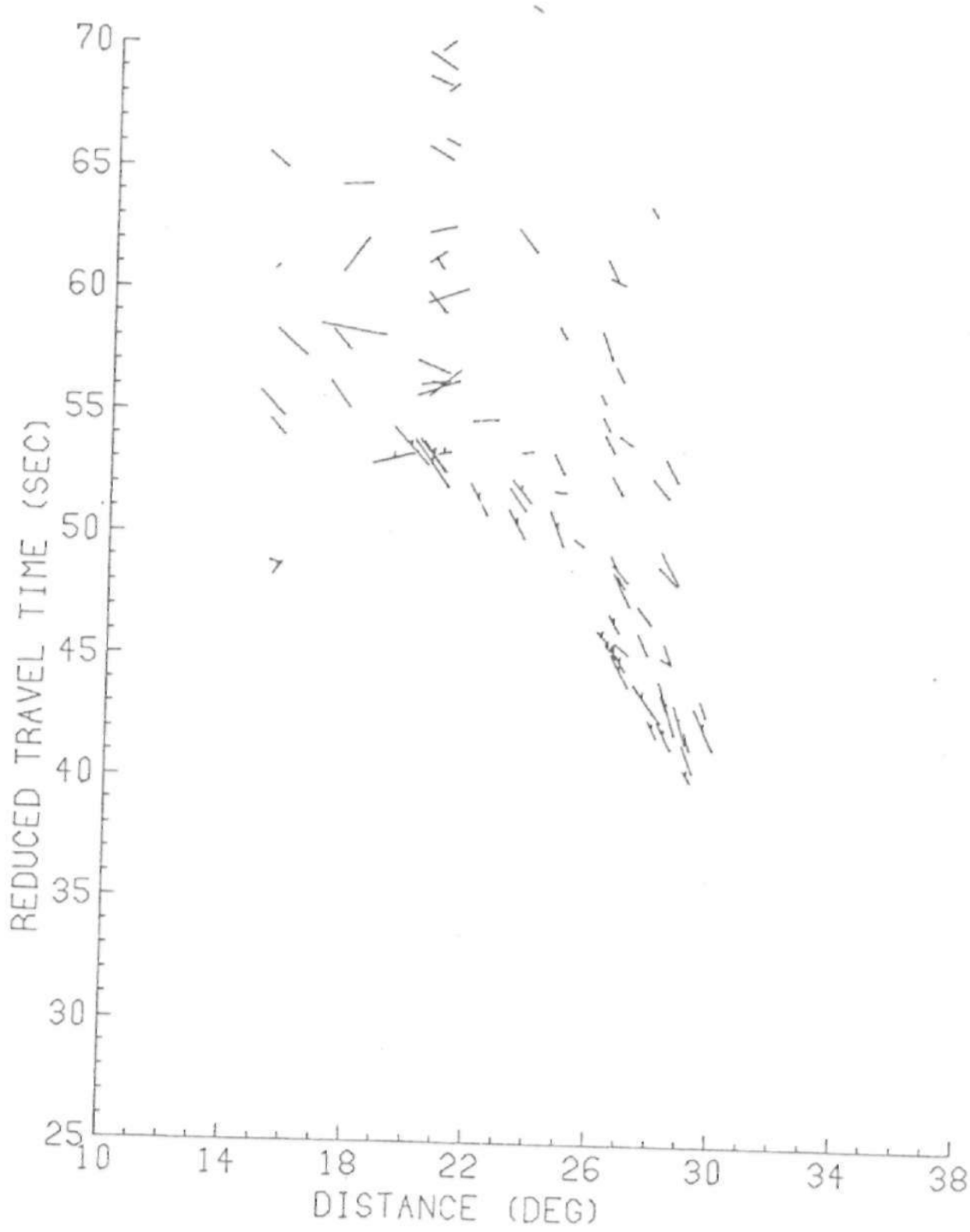


Figure 4.17: Travel-time and slowness data observed at Yellowknife array (YKA) for the Alaska Peninsula (after Ram et al., 1978).

of the synthesized travel-time and slowness data of Figure 4.14 to obtain a velocity-depth profile which will be compared with the models derived from the array data.

4.3 APPARENT VELOCITY MODEL

The procedure which was used here to obtain a velocity model for the synthesized data is the simplified tau inversion method described in Chapter 3. As was indicated in that chapter, the method is similar to other methods that define a velocity-depth envelope which bounds the range of earth structures consistent with the data (for example McMechan and Wiggins, 1972; Bessonova et al., 1974; Jurkevics and Wiggins, 1980). It determines a set of minimum and maximum depths at which some computed velocities would occur for layers derived from a set of discrete slowness values and minimum and maximum tau corresponding to each value of the slowness.

Figures 4.18 and 4.19 show τ-p plots for the two scattering models described earlier and, for comparison, Figures 4.20 and 4.21 show corresponding τ-p plots for the travel-time plots of Figures 4.16 and 4.17 from array studies in the Australia region (Simpson et al., 1974), and western Canada (Ram et al., 1978) respectively. As may be seen from these figures, the general shape of the plots are similar, and the scatter in the data is of comparable magnitude for the four cases especially when the results from the scattering models are compared with the

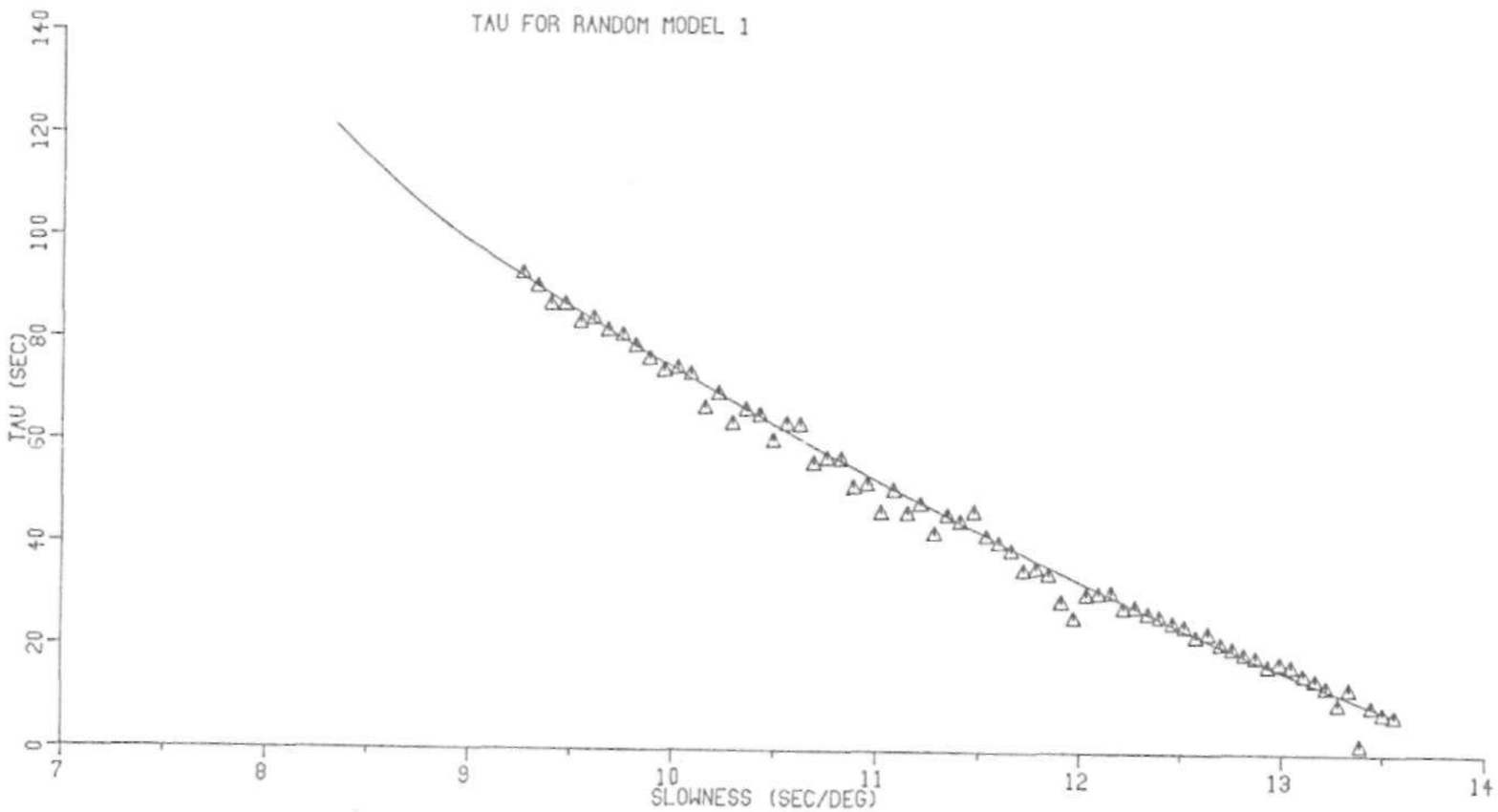


Figure 4.18: Tau data for the travel-time results shown in Figure 4.14. A curve for the basic model of Figure 4.10 (unbroken line) is also shown for comparison.

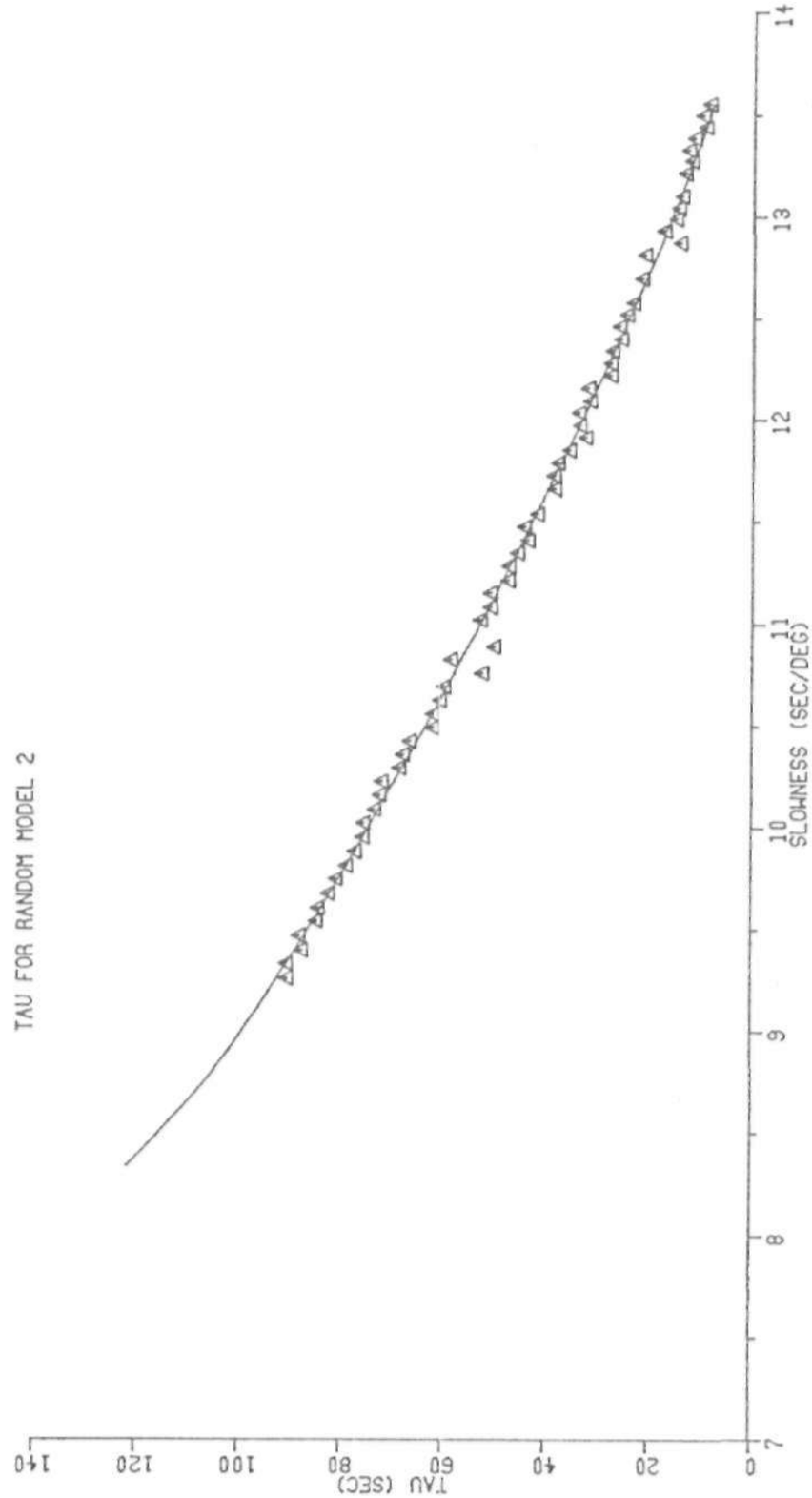


Figure 4.19: Tau data for travel-time results of Figure 4.15.

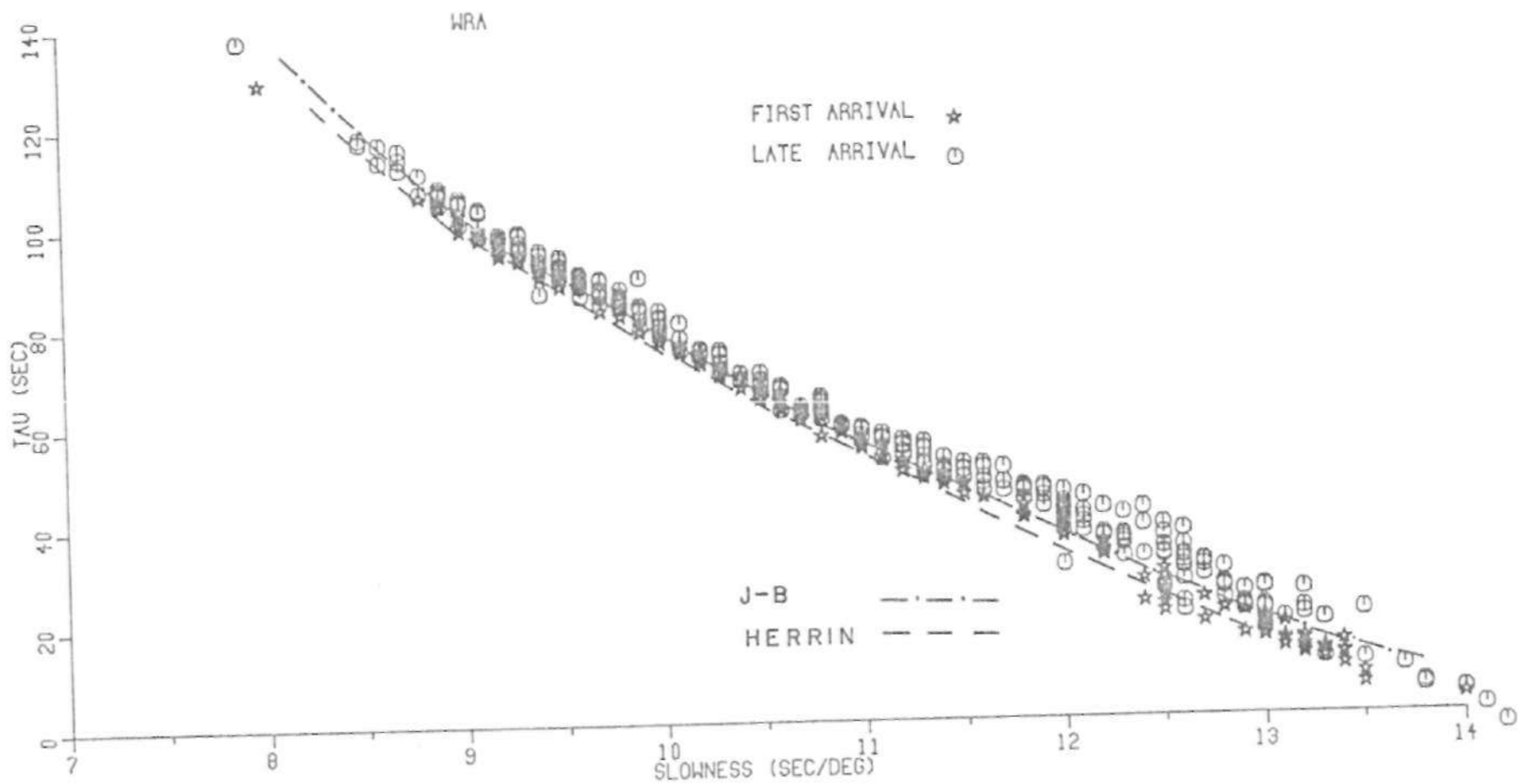


Figure 4.20: Tau data computed from the results of Simpson et al. (1974) compared with values for the J-B and Herrin tables.

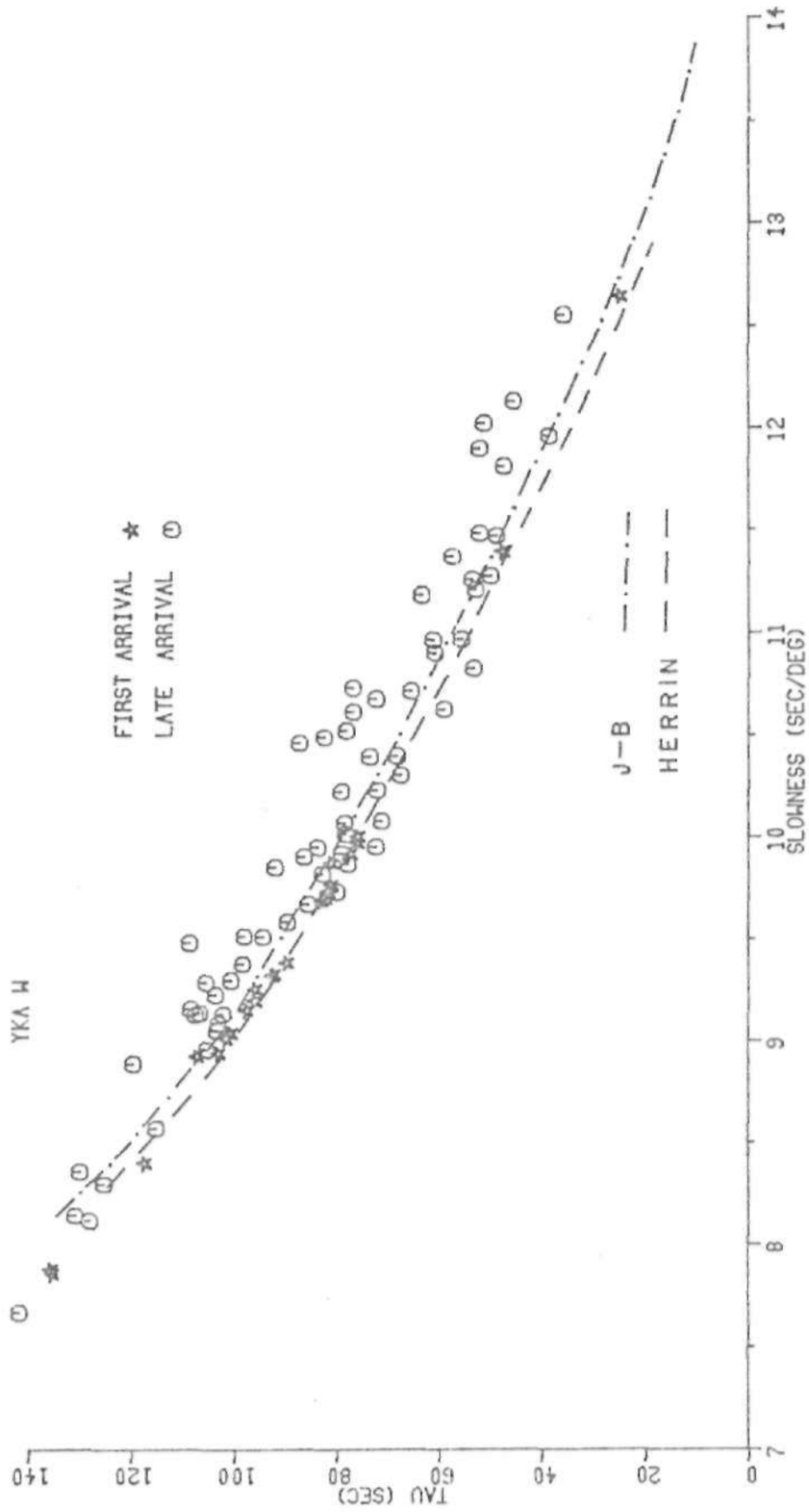


Figure 4.21: Tau data computed from the results of Ram et al. (1978) compared with values for the J-B and Herrin tables.

first-arrival array data. Also shown in Figures 4.18 and 4.19 are the τ-p curves for the corresponding homogeneous model (unbroken line), and further comparisons were made between the array data and the J-B and Herrin models (Figures 4.20 and 4.21). On the basis of comparisons between the scatter of points about the homogeneous τ-p curve in Figures 4.17 and 4.18 for the synthesized data, and the scatter of points about the J-B and Herrin curves (Figures 4.19 and 4.20) for the array data, it is concluded that the J-B model gives a better fit to the array data for the deeper upper mantle regions. The Herrin model appears to give a better fit for the uppermost mantle of these two regions.

The velocity-depth bounds obtained from the τ-p inversion of Figure 4.18, and the velocity structures obtained from the SMAK II model (Mereu et al., 1974), the RMW-2 model (Ram et al., 1978), and the Ram Datt model (1981) are compared in Figure 4.22. The Ram Datt model was also obtained for north of Australia. The figure shows that the velocity models derived from the array data are well bounded, for the most part, by the extremal model from the synthesized data. This indicates that the random model is, in general terms, a plausible upper mantle model. It will also be noted that the extremal velocity bounds show several velocity jumps, thereby predicting discontinuities where none, in fact, existed. The indication, therefore, is that it may not always be necessary to invoke velocity

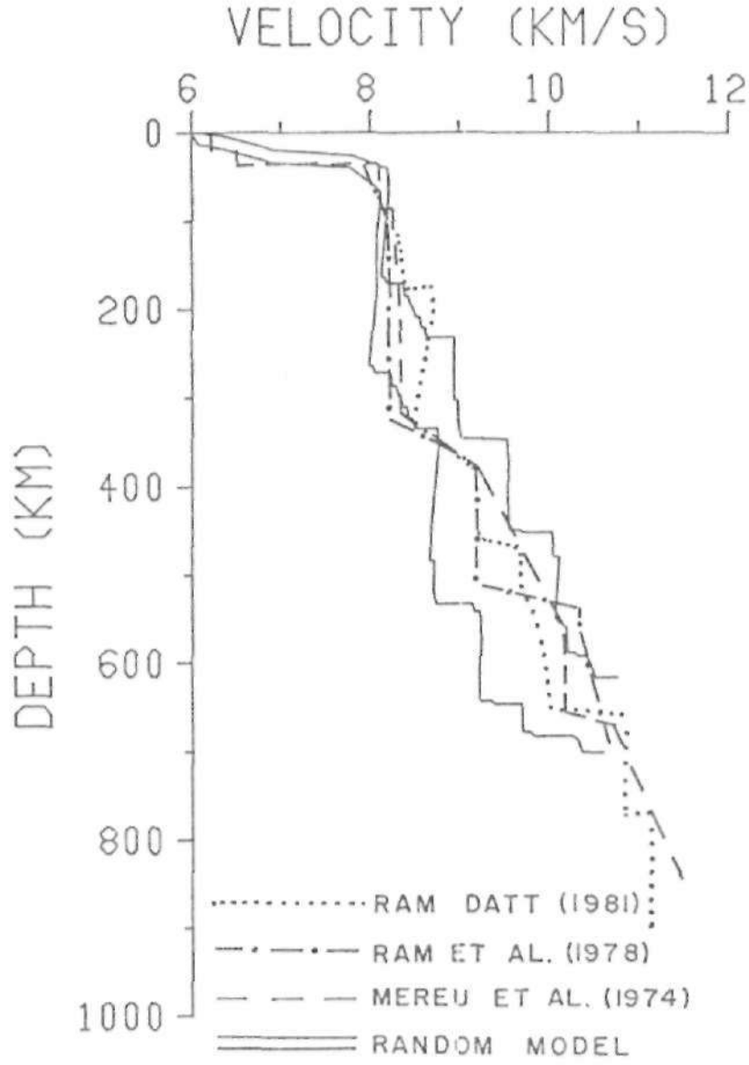


Figure 4.22: Apparent velocity-depth envelope for the travel-time data of Figure 4.13 compared with the SMAK II model (Mereu et al.,1974) RMW 2 model (Ram et al., 1978), and the Ram Datt model (Ram Datt, 1981).

discontinuities in the upper mantle to explain breaks in the travel-time curve or the rapid variations in $dT/d\Delta$ data from array studies.

CHAPTER 5

ARRAY SIGNAL COHERENCE AND ITS RELATIONSHIP TO P-WAVE SCATTERING

5.1 RATIONALE

If the assumption is valid, as evidence from travel-time, slowness, and amplitude anomalies seem to suggest, that various regions of the Earth are heterogeneous, the question arises as to whether more scattering takes place along certain travel paths as opposed to others. To investigate this further, use was made of the fact that when a ray path passes through a homogeneous earth, the energy that arrives at a seismic array will be relatively coherent and the complexity of the signal will depend mainly on the source function. However, when the ray path passes through both lateral and vertical inhomogeneities, much of the signal energy is scattered and arrives at the array as incoherent energy. The signal complexity in this case will therefore depend not only on the source function, but also on multipathing effects caused by the rapid changes in velocity gradient and on random scattering of the signal energy along the travel path. Since the individual P-wave recording at any seismic station must necessarily consist of both the coherent and incoherent

or scattered energy that arrive at the station, a separation of the incident energy into these two components should provide some information about the relative scattering properties along the travel path of the incident signal.

In this respect, the advantages of a seismic array over a single seismic station are of particular importance. Firstly, arrays make it possible to measure directly the slowness (or apparent velocity), and the azimuth of the signal. Secondly, by applying time delays to bring the signals into phase and summing the coherent outputs from each seismometer, an improvement in signal-to-noise ratio (SNR) is achieved. Since scattered waves generally arrive at a station simultaneously from a range of different directions with different apparent velocities (King et al., 1975), a reliable estimate of the slownesses and azimuths of the various contributions is only possible from this type of processing. Array signal processing techniques thus provide some attractive capabilities for the study of scattered waves.

Other techniques based on the complexity of P-wave signals have been employed, to some extent in the past, to study the variations in earth's structure, and source characteristics. Lambert et al.(1969) in a study of signals from the LONGSHOT explosion described a complexity factor (F_C) based on a time distribution of P energy in the signal. They found that F_C was distance dependent, and noted that average complexities should be interpreted carefully since

an average from near stations would be much different than an average from distant stations. They also pointed out that complexity is meaningful in studying several events only when these events are at approximately the same distance from the stations. Douglas et al. (1973) also studied the complexities, spectral ratios, and magnitudes of some explosion signals from different tectonic regions. They concluded that the complexity of P signals is caused when the direct P travels by a path of lower average Q relative to the later arrivals.

The major limitation of this complexity factor, however, is its inability to effectively discriminate between complexity generated at the source, and that generated by structure between the source and the station or under the station. This greatly restricts its application to earthquake signals which, as often as not, have complexity generated near the source region. The parameter which is developed in this chapter depends on the coherence of the signal, and appears to have that discriminating property.

5.2 THEORETICAL CONSIDERATIONS

A convenient way of separating the coherent energy from the scattered energy incident at the array is by the beam forming process (see for example Birtill and Whiteway, 1965). In its basic form, beam forming consists essentially of applying appropriate steering delays to the individual

channel of an array to correct for the non-vertical incidence of seismic energy, summing them and taking the mean to obtain the beam. The assumption is that the signal is coherent between stations and the noise random or incoherent. For medium aperture type arrays like the Yellowknife (YKA) in Canada, Gauribidanur (GBA) in India and Warramunga (WRA) in Australia, the inter-seismometer spacing of 2.5 km is such that these simple assumptions about the noise field are essentially valid.

Displayed in Figure 5.1a are a set of synthetic array data 16 seconds long generated with a single 3-second wavelet introduced across the array with an apparent azimuth of 191 degrees, and an apparent velocity of 8.0 km/s. The physical parameters of the array are those of GBA because some of the earthquake data later used in this study were recorded at that array. The array consists of two L-shaped arms (called blue and red lines) each containing ten short-period, 1-second vertical seismometers spaced at 2.5 km intervals.

The adaptive processed solutions obtained by a method originally described by Gangi and Fairborn (1968), and discussed by King et al. (1973), using the computer programs of Mereu and Ram (1975) are shown in Figure 5.1b. Each sampled point of the seismometer channels may be represented as

$$g_{ij} = s_{ij} + n_{ij}; \text{ where } i = 1...M; \; j = 1...K \qquad (5\text{-}1)$$

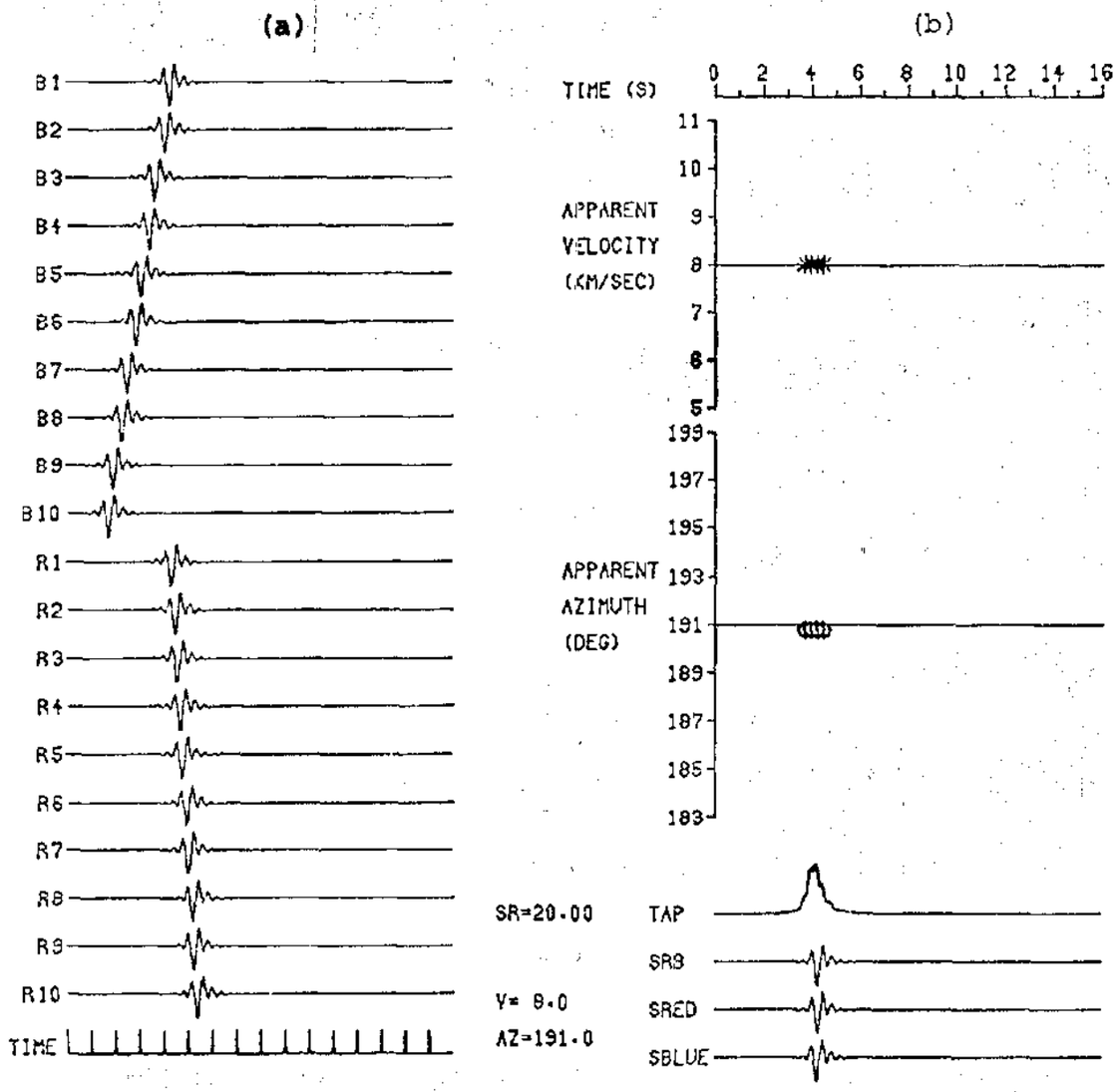


Figure 5.1: (a) Synthetic array data without noise using GBA array configuration and a single wavelet.
(b) Adaptive processed solutions (SR is the sampling rate, V and AZ are the given apparent velocity and azimuth used to form the beam (SRB)).

g_{ij} = the j-th sample of the output at the i-th seismometer

n_{ij} = the j-th sample of noise at the i-th seismometer.

s_j = the j-th sample of the signal.

M is the number of seismometers in the array, and K is the total number of sampled points per channel. The noise term consists of two components made up of random, and signal generated noise. The random part includes instrument generated noise, and wind noise which are stationary and independent of the presence of a signal. On the other hand, the signal generated noise arises as a result of incoherent energy caused by scattering along the travel path due to lateral, and vertical inhomogeneities.

Thus the beam is

$$F_j = \frac{1}{M}\sum_{i=1}^{M} g_{ij} = s_j + \frac{1}{M}\sum_{i=1}^{M} n_{ij} \quad (5\text{-}2)$$

It is therefore obvious that when noise is absent as in Figure 5.1a, the beam (SRB) is identical to each of the individual channels with the appropriate steering delay applied. The steering delays are calculated according to (see for example King et al.,1973)

$$t_i = \frac{R_i \cos(\phi - \theta_i)}{V} \quad (5\text{-}3)$$

where R_i and θ_i are the polar coordinates of the sites for

the i-th seismometer with respect to the cross-over point of the array; ϕ and V are the expected or given azimuth and apparent velocity respectively.

One other useful output from beam forming processing is the Time Averaged Product (TAP), and it represents the square root of the variation of the correlation coefficients for a fixed window-width (TAP window) moved along the partial sum outputs of the beam. It is obtained by taking the square root of the product of the sum of the red (SRED) and the sum of the blue (SBLUE) channels averaged over the TAP window (see Figure 5.1b).

When the signal is perfectly coherent across the array and the steering delays accurately determined, the energy of the beam (E_B) defined as the sum of the squared amplitude of the beam is equal to the energy of the individual channels or, more appropriately, the mean energy of all the individual channels (E_{av}) since as indicated earlier, SRB is now identical to the individual channels with appropriate delay applied.

Similarly, the beam of the red channels (SRED) and the beam of the blue channels (SBLUE) are identical to SRB and from equation (5-2)

$$R_j = B_j = F_j = s_j \qquad (5\text{-}4)$$

for the noise-free case, where R_j, B_j and F_j are the sampled

beam of the red, blue and total channels respectively. From the definition of TAP, we have that

$$T_j = \sqrt{A_j} = \left[\sum_{j}^{k} R_j . B_j \right]^{\frac{1}{2}}; \quad k = N + j - 1 \tag{5-5}$$

where N is the number of points in the TAP window. For example

$$\begin{aligned}
A_1 &= s_1^2 + s_2^2 + s_3^2 + \ldots \ldots + s_N^2 \\
A_2 &= \quad s_2^2 + s_3^2 + s_4^2 + \ldots + s_N^2 + s_{N+1}^2 \\
A_3 &= \quad\quad s_3^2 + s_4^2 + s_5^2 + \ldots . + s_{N+1}^2 + s_{N+2}^2 \\
A_4 &= \quad\quad\quad s_4^2 + s_5^2 + s_6^2 + \ldots . . + s_{N+2}^2 + s_{N+3}^2
\end{aligned} \tag{5-6}$$

etc.

If the energy as defined earlier is the sum of the squared amplitude trace, then the energy of the TAP trace is given by

$$\begin{aligned}
E_T &= \sum_{j=1}^{K} A_j \\
&= s_1^2 + 2s_2^2 + 3s_3^2 + \ldots + N.[s_N^2 + s_{N+1}^2 + \\
&\quad s_{N+2}^2 + \ldots + s_{K-N+1}^2] + \ldots + 2s_{K-1}^2 + s_K^2
\end{aligned} \tag{5-7}$$

From equation (5-7) we observe that when the end effects are avoided, the TAP energy is

$$E_T = N. \sum_{j=N}^{K-N+1} s_j^2 \qquad (5-8)$$

But Σs_j^2 is the energy of the individual channels, or E_{av}. Therefore the energy of the TAP is equal to the mean energy of the individual traces multiplied by the number of points in the TAP window.

From the preceding, it follows that when all the energy incident at the array is coherent, the ratio of the energy of the beam to the mean energy of all the individual traces equals unity; or the ratio of the TAP energy to the product of the mean energy of all individual traces and the number of points in the TAP window equals unity, i.e.

$$E_B/E_{av} = 1.0$$

and (5-9)

$$E_T/E_{av}.N = 1.0$$

Figure 5.2a and 5.2b illustrate another synthetic example in which three wavelets were introduced across the array of records representing a case with two additional arrivals coming in with the same apparent azimuth and velocity as the first arrival. Equation (5-9) would be found to be equally valid for this case.

Very few seismic signals, however, exhibit the simple configuration of these examples. A problem therefore arises when we have a complex signal with different parts of the

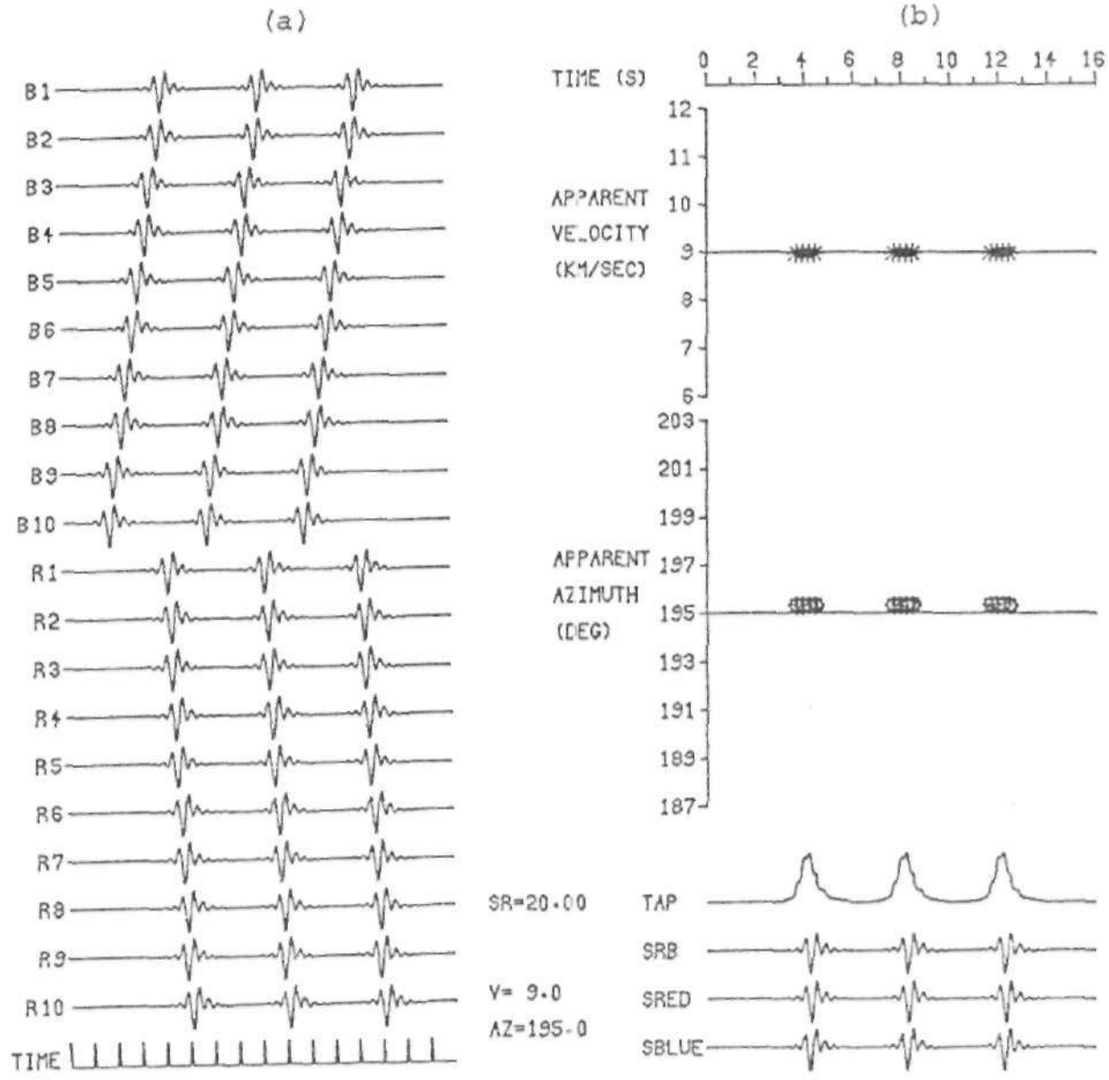


Figure 5.2: (a) Synthetic array data using three separate wavelets with same apparent velocity and azimuth.
(b) Adaptive processed solutions.

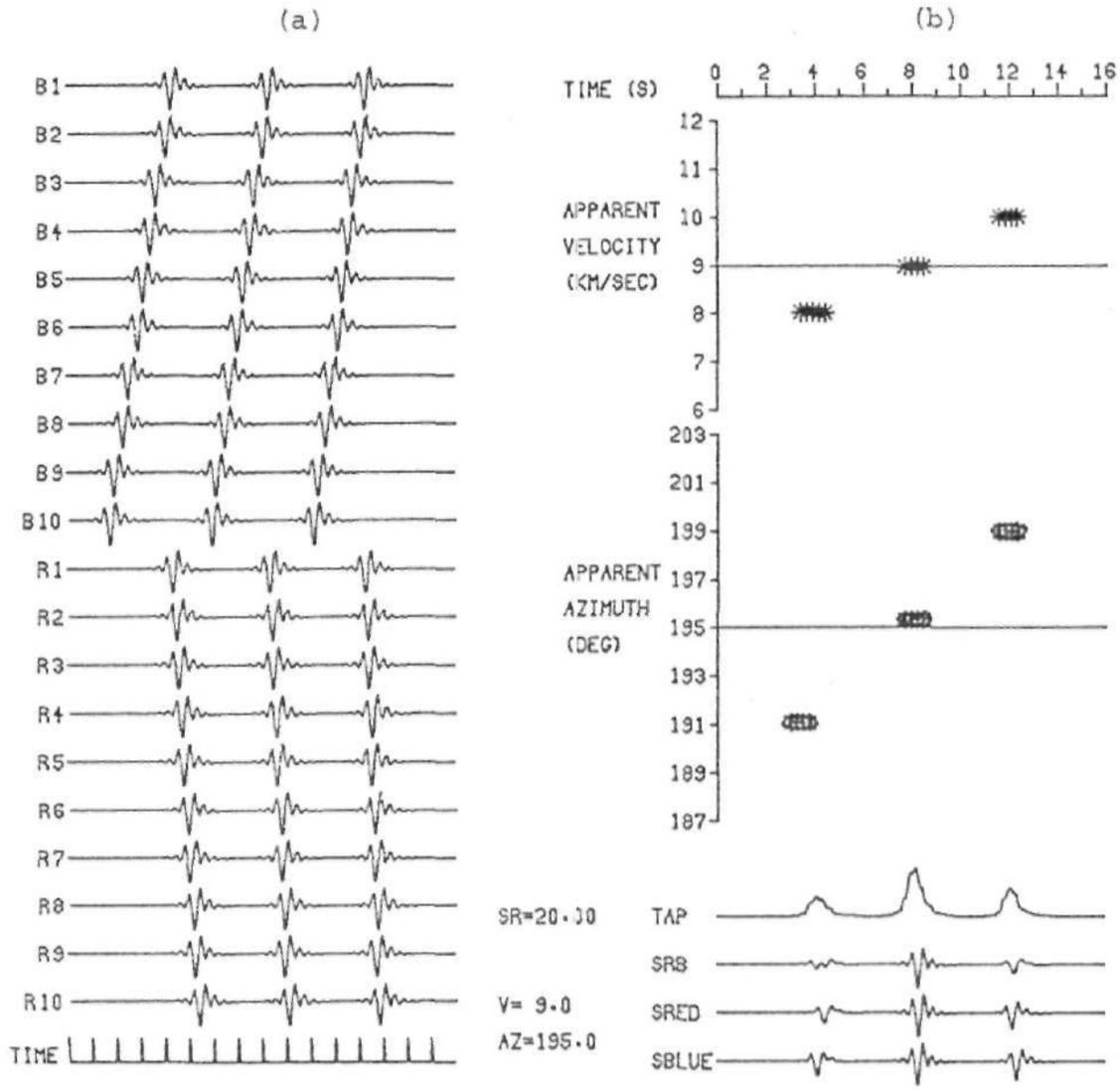


Figure 5.3: (a) Synthetic array data using three separate wavelets with different apparent velocity and azimuth.
(b) Adaptive processed solutions.

signal train arriving at the array with different apparent azimuths and velocities due to multipathing, coherent scattering and random scattering. The problem is illustrated in Figure 5.3, and arises because in the conventional beam forming and adaptive processing routine, the initial trial velocity and azimuth must be close to the true values, and the optimum beam formed is for one particular velocity and azimuth. Other coherent energies which arrive with different apparent velocities and azimuths have a degenerated beam, and appear incoherent. In Figure 5.3a for instance, the three arrivals have different apparent azimuths and velocities and only the central event with a velocity of 9 km/s, azimuth 195 degrees appears coherent in the beam and TAP traces. As can also be seen in Figure 5.3b, even the degenerated events have very good adaptive processed solutions, but in spite of the fact that the three arrivals are coherent, the established relations of equation (5-9) would not hold for this case.

To overcome this problem, the beam was formed in an iterative manner by using a range of apparent velocities and azimuths, and preserving the maximum value of the beam so formed for each point of the signal trace. In this manner, a good beam (SRBMX in Figure 5.4) was formed for coherent energies arriving at the array with different apparent azimuths and velocities, and all incoherent energies still remain degenerated in the beam. Equation (5-9) with SRBMX and TAPMX energies substituted for the SRB and TAP energies

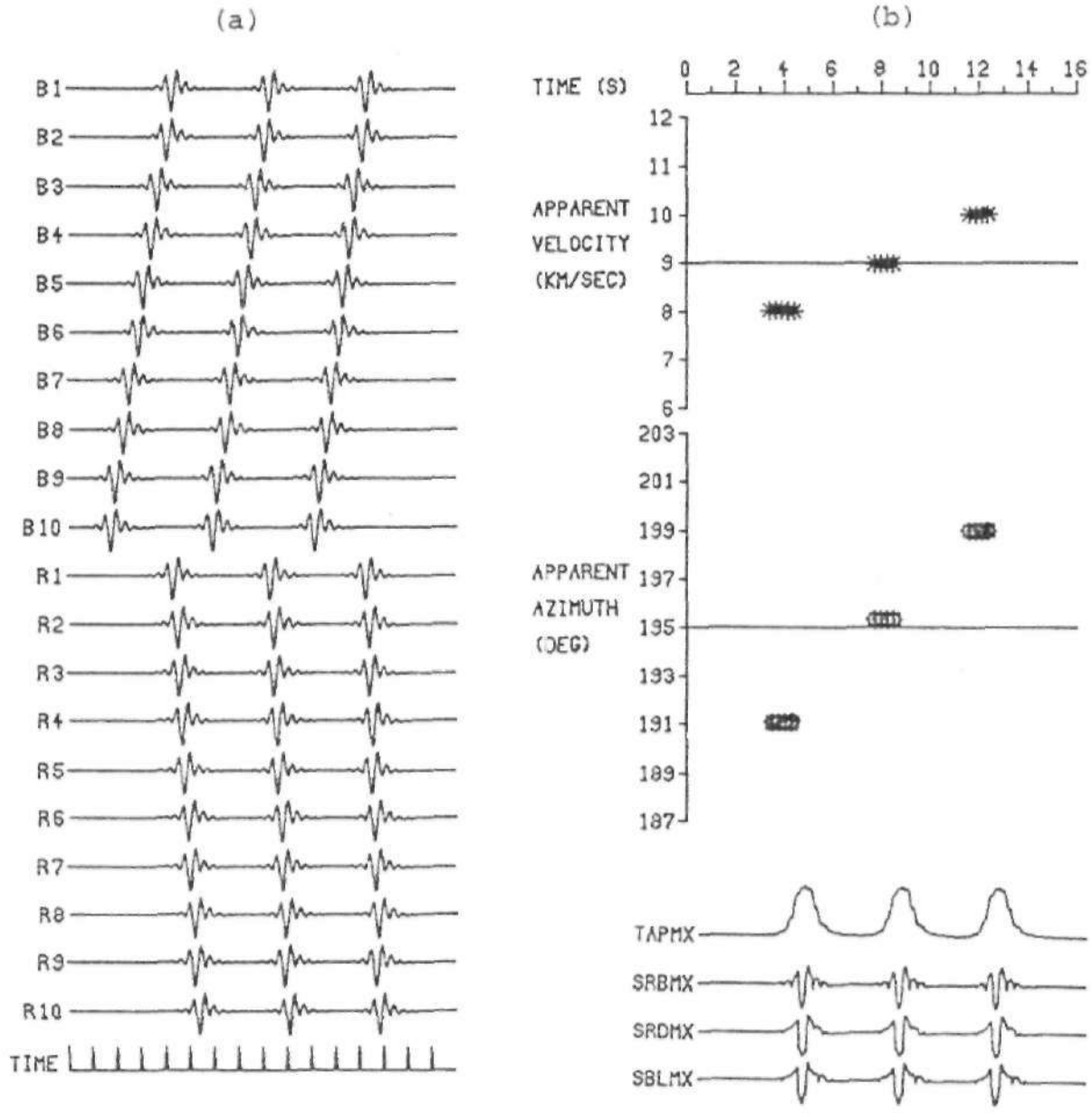


Figure 5.4: (a) Same as Figure 5.3(a)
(b) Adaptive processed solutions and beam (SRBMX) formed by velocity and azimuth sweep.

respectively should then always remain valid when all the energy incident at the array is coherent. In the presence of random noise, the noise term in equation (5-2) for the beam has a near-zero average value, and the beam energy (E_B) is approximately the energy of the coherent signals. Since E_{av} is the mean energy of the coherent signals plus noise, then E_B/E_{av} or $E_T/(N.E_{av})$ should give the fraction of the total energy that is coherent. In the presence of incoherent energy which is not random, destructive interference reduces the incoherent energy in the beam but does not reduce it to zero. In the TAP trace however, the incoherent energy has a near-zero value, and the ratio $E_T/(N.E_{av})$ should then always give the fraction of the total energy that is coherent, and the incoherent or scattered fraction can thus be determined.

The velocity- and azimuth-sweeping process just described resulted in some slight distortion to the beam (Figure 5.4b), and also generated some random noise which caused the beam energy to increase slightly. However, because the TAP is a measure of the correlation of the coherent energy along the trace, the iterative TAP energy for TAPMX was not adversely affected by the sweeping process, and the average error introduced was only about 2%. For this reason, the relationship given by equation (5-9) which uses the TAPMX energy instead of the SRB energy is considered the more reliable of the two.

5.3 DATA ANALYSIS PROCEDURE

Since the initial computing steps for the coherence parameters described in the last section is very similar to those used in adaptive processing techniques, a computer program was developed around a package for the analysis of array data using adaptive processing methods described by Mereu and Ram (1975). The program which was written in Fortran IV reads data from cards for synthetic data, and off a magnetic tape for earthquake data.

Table 5-1 lists the main computational steps required for processing both synthetic and real data. In steps 4 to 10 of the table, the range of velocities and azimuths which must be scanned is determined by the apriori information that is available about the events. For example, an inspection of the adaptive processed solutions of some of the earthquake data used (Ram and Mereu, 1977) showed that a velocity sweep of 5 km/s and an azimuth sweep of 8 degrees about the starting values selected in step 4 were sufficiently adequate to cover the spread which occurred for most of the events. If records which have not been previously processed are to be used, however, a larger sweeping range must be used.

In steps 11 to 14, the energy per point was used in all computations instead of the total energy per trace in order to compensate for the slightly variable data length from channel to channel, and from record to record. The

TABLE 5-1

MAIN STEPS IN COMPUTING SCATTERED ENERGY FROM ARRAY DATA

1. Read in control parameters e.g. array location, sampling rate, cutoff frequencies, expected azimuth and velocity, etc.
2. Select earthquake event, and read data from tape.
3. Filter and normalize data.
4. Select starting velocity and azimuth sufficiently smaller than expected values.
5. Calculate steering delays, form beam and Time Averaged Product (TAP), and store.
6. Add increment to starting velocity and repeat step 5.
7. Compare each point of the new beam and TAP with the old, and store the values of greater magnitude.
8. Repeat steps 6 and 7 until adequate velocity sweep has been obtained, and store the optimum beam and TAP.

TABLE 5-1 Continued

9. Repeat steps 6 to 8 for the azimuth, and store the optimum beam and TAP.

10. Compare the velocity and azimuth beams of steps 8 and 9, and obtain "super" beam (SRBMX) and TAP (TAPMX).

11. Determine onset times of event on all traces automatically and compute energy per point of the individual traces. Also compute the average energy per point of all the traces (E_{av}), and of the first few seconds prior to the P-wave onset for noise correction.

12. Compute energy per point of SRBMX and TAPMX.

13. Compute the complexity factor (F_c) of the beam (see for example Lambert et al. (1969)).

14. Compute the coherence parameter using equation (5-9) after correcting for noise if necessary.

15. Print results and punch on cards.

complexity factor (F_c) (Lambert et al., 1969) was also computed for comparison. It involved squaring the digitized signal amplitudes and smoothing the result with a 3-second integrating window moved by increments of 1/20 of a second to produce each point on the integrated trace. The square root of this trace was then taken as the final trace. Finally, the ratio of the area under the curve from 5 to 35 seconds to the area under the curve in the first 5 seconds was taken to obtain F_c. For simple signals F_c was close to 2 or less, for complex signals F_c is usually greater than 2 (Douglas et al.,1973).

In order to correct for moderate random noise levels in the signal, the P-wave onset for each channel was determined by an automatic procedure, and the energy per point of 1 second of noise sample at the beginning of the trace, prior to the onset of the signal was determined, and subtracted from the total energy per point to remove the effect of random noise.

Thirty-six seconds of 20 channel array data were available for investigation, and all computation was performed by the CDC Cyber 73 computer described in Chapter 2. For a typical run of one earthquake record consisting of 20 by 36-second traces, an average of 56K words of memory and 42 seconds execution time was required. All the synthetic data were restricted to 16 seconds.

5.4 TESTS WITH SYNTHETIC DATA

In order to investigate the performance and feasibility of the method, tests were carried out with the aid of some synthetic data. The tests were directed at determining the effectiveness of the velocity and azimuth sweep, the effectiveness of the noise correction procedure, and the ability of the method to determine accurately from array data the relative amount of incoherent energy incident at the array. They were also to serve as a check for the computer program used.

Coherence measurements were made on synthetic records similar to those shown in Figures 5.1 to 5.3 using different values of velocity and azimuth to initiate the sweeping process. It was found that the procedure worked very well and predicted the apparent velocities and azimuths used to generate the records accurately. The maximum deviation from unity of the ratio $E_T/(N.E_{av})$ for coherent wavelets was in all the tests less than 0.05.

The normal procedure for reducing the effect of noise on a signal is to substract a noise correction from the signal using a portion of trace prior to the P arrival to determine the correction factor. In order to establish the effectiveness of such a procedure for the coherence measurements, variable amounts of random noise were generated and added to a set of synthetic data made up of a single wavelet which was coherent between the traces.

Figure 5.5 shows such a set of synthetic data for a noise-free case, and for two other cases where the total trace energy was made up of 20% and 60% random noise respectively. The deviation from unity of the ratio $E_T/(N.E_{av})$ for the synthetic array data after the noise correction has been applied was plotted as a function of the per cent noise content of the signals, and is shown in Figure 5.6. It will be noted that for moderately low noise levels, the correction is relatively very good as shown by the low deviation; but for high noise levels, the deviation increased rapidly reaching 0.9 for 90% noise energy (not shown in the figure). This result was justification for later rejecting excessively noisy records in the analyses with real data.

Finally, to establish the ability of the method to accurately predict the amount of incoherent energy present in the signal, the incoherent part of the test signals was again represented by variable amounts of random noise of pre-determined energy. As the SRBMX traces and, especially, the TAPMX traces of Figure 5.5 show, such randomly generated signals are incoherent between the traces when generated independently for each trace. The ratio $E_T/(N.E_{av})$ was computed for several test signals with incoherent energies which varied from 0% (Figure 5.5a) through 60% (Figure 5.5c) to 90%. At least five measurements were made for each incoherent energy value using a differently generated random signal each time, and then determining the mean because the

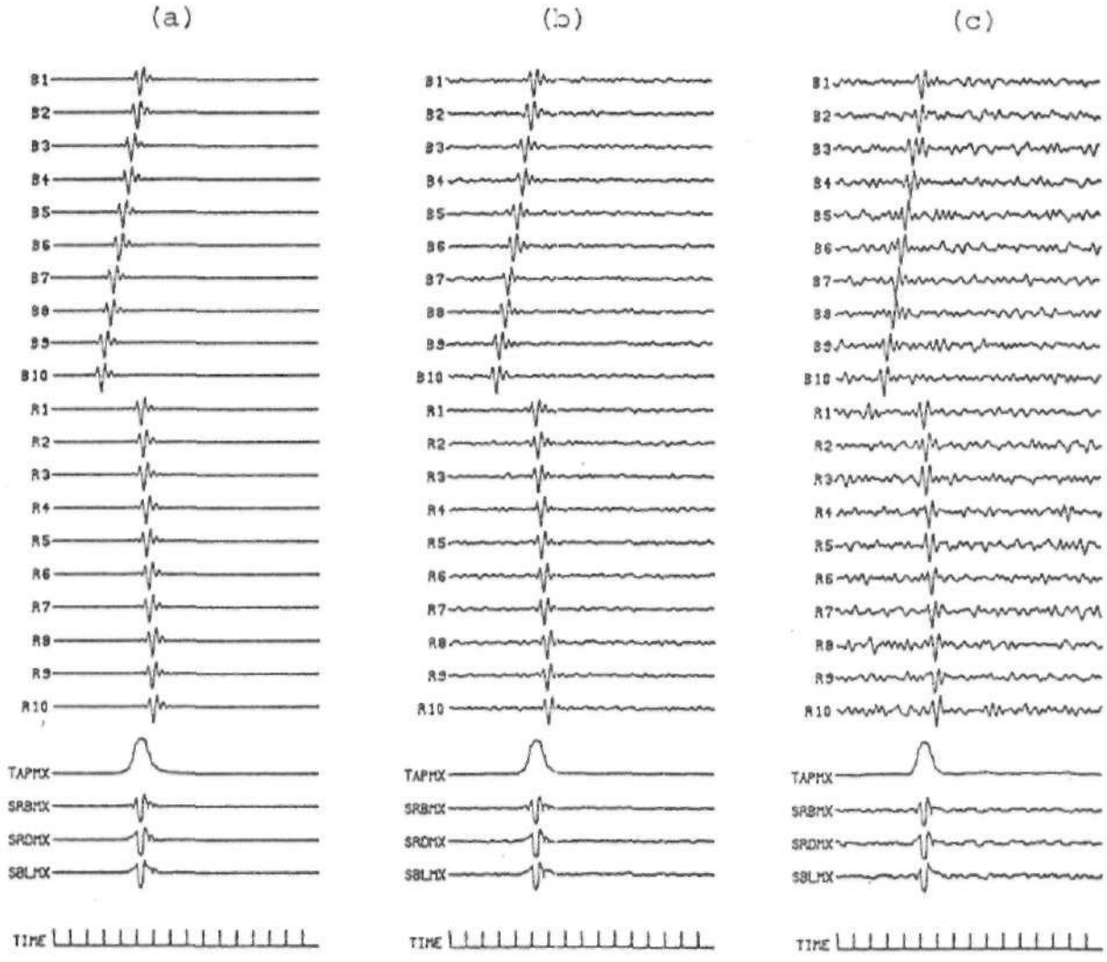


Figure 5.5: (a) Synthetic array data with no noise.
(b) Synthetic data with 20% of total trace energy comprised of random noise.
(c) Synthetic data with 60% of total trace energy comprised of random noise.

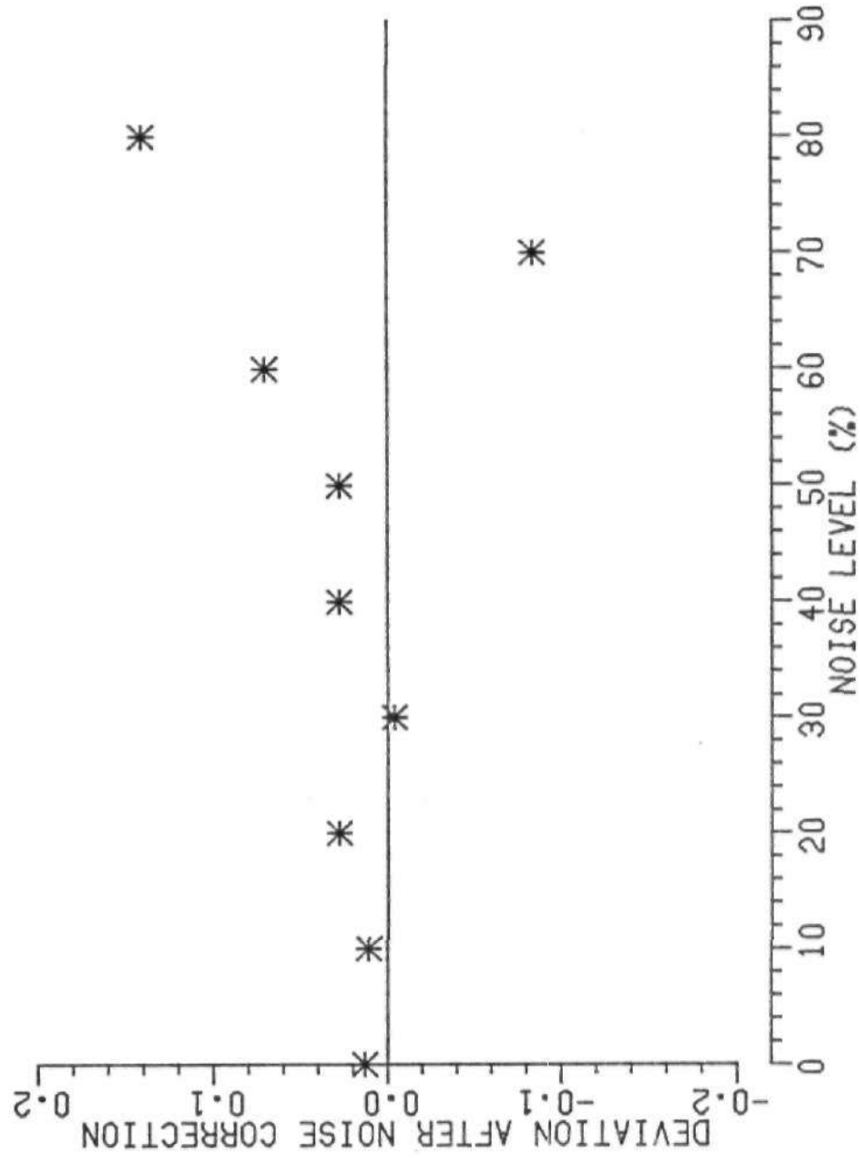


Figure 5.6: A measure of the effectiveness of noise correction for different noise levels. Noise residuals are deviation of $E_T/(N.E_{av})$ from unity.

results were very much dependent on the characteristics of the random signal used for the incoherent part. The predicted mean values of the incoherent energy given as a percentage of the total energy are compared with the real values in Figure 5.7, where the error bars on the predicted values represent the standard deviation of the mean. As Figure 5.7 shows, the predicted values are relatively accurate, but generally fell slightly below the expected or real values especially as the percentage of incoherent energy increases. It would therefore appear that the beam formed for signals with large incoherent energy levels failed to completely suppress all the incoherent energy.

5.4.1 ADDITIONAL TESTS WITH NTH ROOT BEAM FORMING

The Nth root beam forming method was first suggested by Muirhead (1968) because it was found particularly effective in enhancing coherent energy, and suppressing noise spikes in an automatic event detection system. It is a non-linear multichannel filtering technique, and has been described and applied by Kanasewich et al. (1973), Ram and Mereu (1975), and Muirhead and Ram Datt (1976). It is very similar in principle to the beam forming process described earlier, but involves taking the Nth root (usually 2, 4 or 8) of each signal before summing, and then raising the summed result to the Nth power with the original sign preserved during the Nth root and Nth power processes. The Nth root beam forming equations are then,

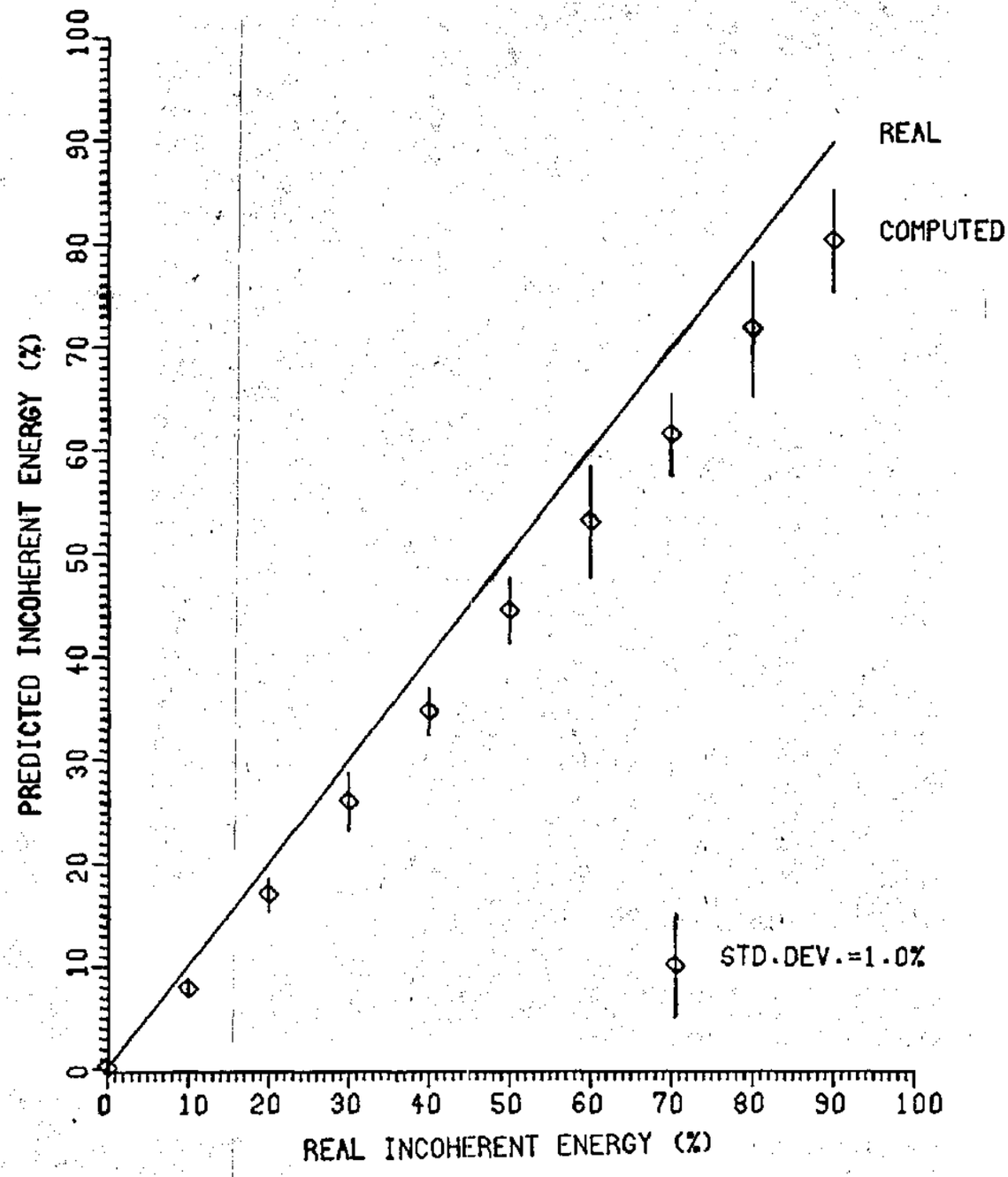


Figure 5.7: Predicted incoherent or scattered energy versus true incoherent energy in synthetic data.

$$S_j = W_j \cdot |W_j|^{N-1} \tag{5-10}$$

where

$$W_j = \frac{1}{M} \sum_{i=1}^{M} \frac{g_{i,j+L}}{|g_{i,j+L}|} \cdot \left[\frac{G}{G_i} |g_{i,j+L}|\right]^{\frac{1}{N}} \tag{5-11}$$

and

$$L = T_o - t_i \tag{5-12}$$

S_j is the filter output, g_j is the seismometer output of the i-th channel and j-th time for the case with M channels; G and G_i are the common gain to which all channels are normalized and the gain of the i-th channel respectively; T_o is the arrival time of the wavefront at the cross-over point; and t_i is defined by equation (5-3).

The signal enhancement capability of the Nth root method suggest that some improvements on the results of our coherence measurements might be achieved by this method. Consequently, known quantities of coherent and incoherent signals were again mixed as in the earlier tests, and predicted values were computed using Nth root beam method for Nth root of 2 and 4. A comparison of the results with that of the regular beam forming method is shown in Figure 5.8 without the error bars which were generally of the same order of magnitude as those shown in Figure 5.7. As Figure 5.8 indicates, considerable improvement in the predicted

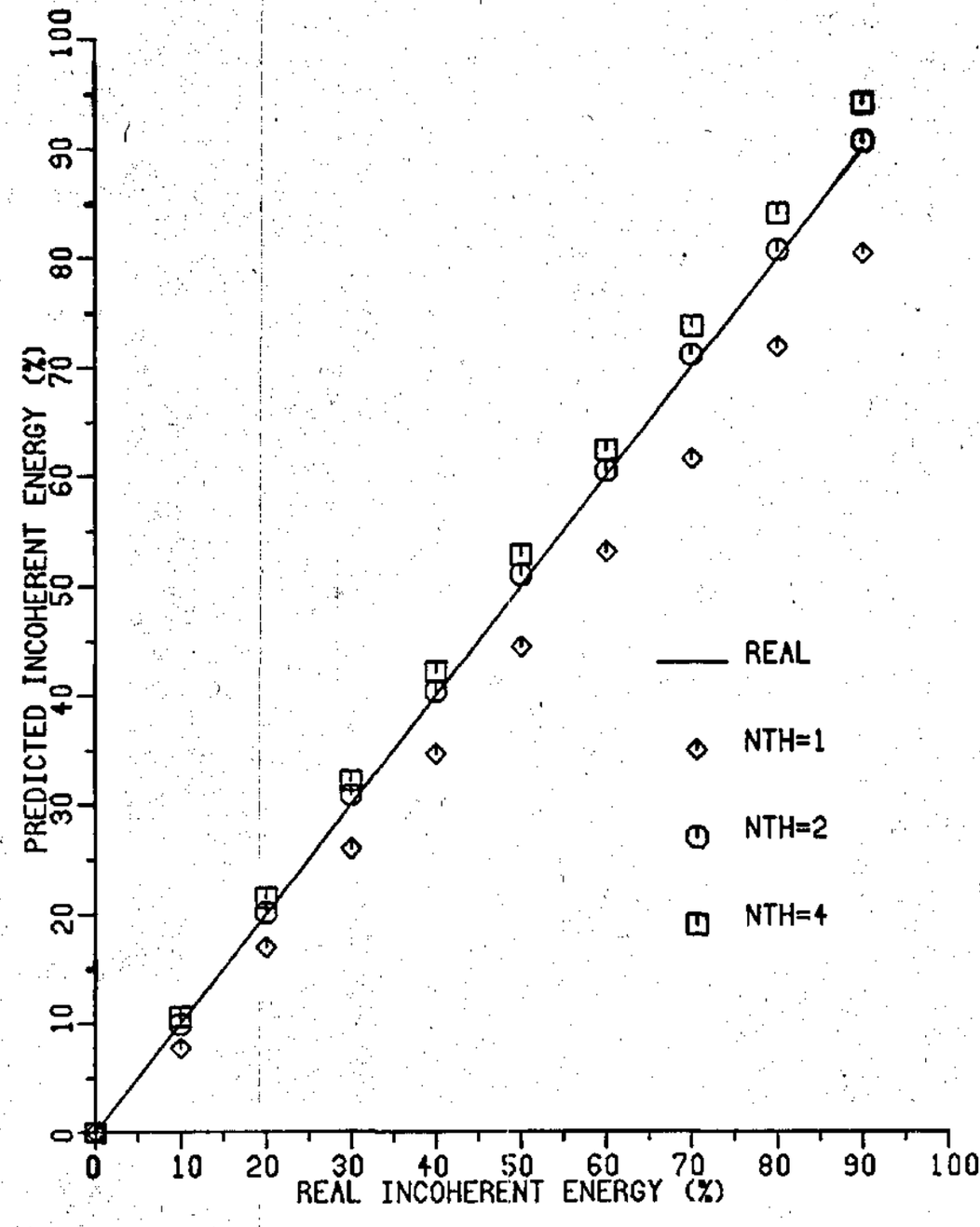


Figure 5.8: A comparison of the coherence results for Nth rooth processing.

values was achieved, and the values which are in closest agreement with the expected or real values were obtained with Nth root of 2. For Nth root of 4, predicted values generally tend to be greater than the real values indicating that part of the coherent signal was suppressed by the high root.

In summary, although the Nth root method appeared to give more accurate predictions of the percentage of total trace energy that was incoherent, it also resulted in an average increase of about 48% in the computing time and cost. On the other hand, reasonable accuracy was achieved by the direct beam forming approach for incoherent energy less than 60%. For 60% incoherent energy which as will be seen in Chapters 6 and 7 is about the upper limit determined for the earthquake data investigated, the error in prediction was less than 7% and down to 4% for 30% incoherent energy. These values, as will also be seen later, fall well within the range of the scatter of points for the events investigated. For this reason, it would be prudent to employ the regular method when a very large data set is to be used.

CHAPTER 6

PRELIMINARY ASSESSMENT OF COHERENCE MEASUREMENTS ON GBA AND YKA DATA

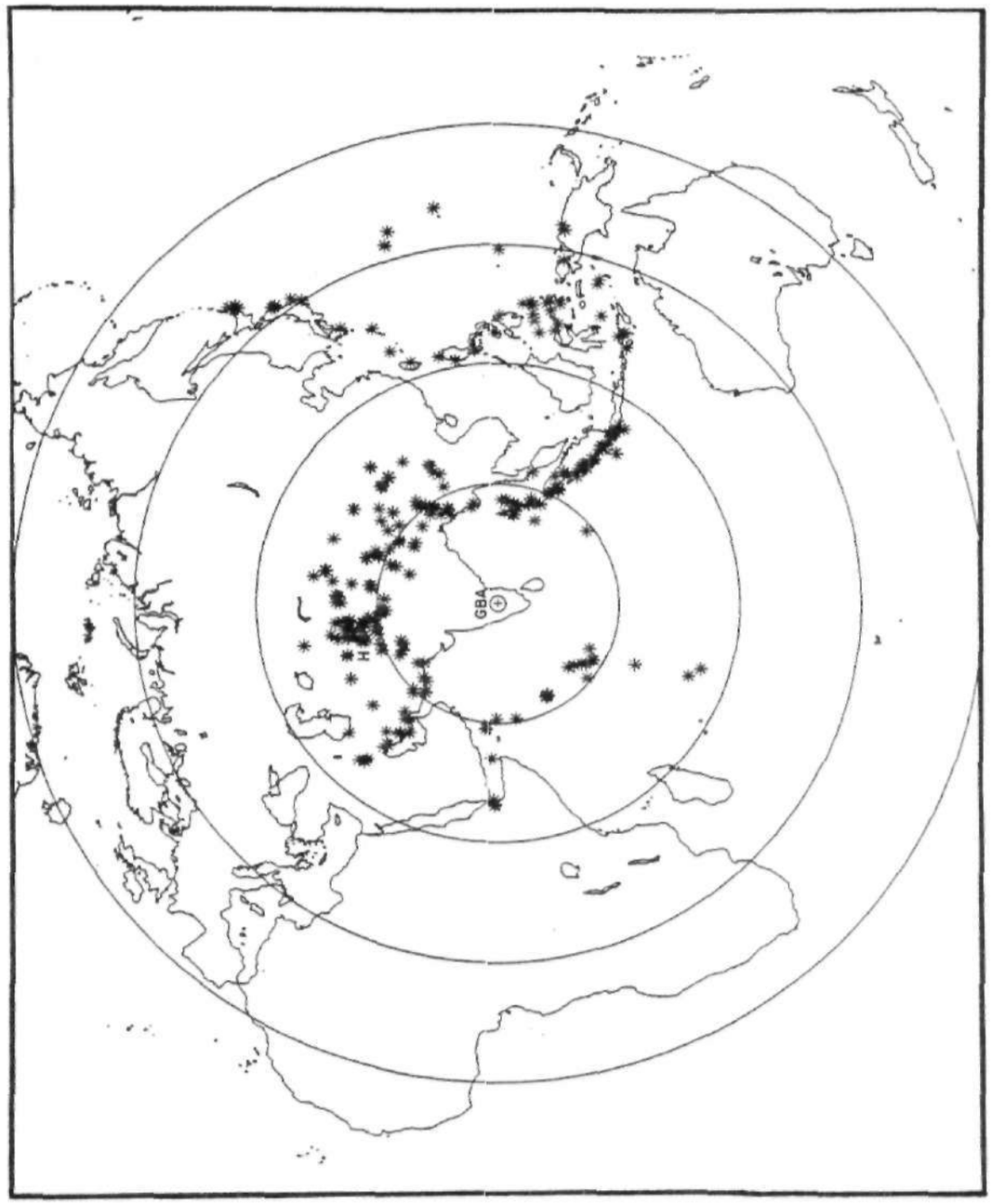
6.1 OBJECTIVE AND RATIONALE

Having determined from tests with synthetic data that the procedure developed in Chapter 5 was capable of producing a quantitative measure of the coherence of a seismic signal, it was decided to apply the method to a real data set from the GBA and YKA arrays. The aim was to determine to what extent the coherence parameter could be used as a measuring instrument for comparing the heterogeneity of different upper mantle regions.

The GBA and YKA arrays were chosen for the study for a number of reasons. Firstly, data from the arrays, which formed a reasonably uniform distribution of events for the distance range of interest were already available in digitized form on tape. In addition, there were the adaptive processed solutions for these data together with the results of some earlier studies on the slowness and travel-time anomalies (Ram and Mereu, 1977; Ram et al., 1978) which provided a good starting point for the present study. Secondly, GBA is ideally situated for upper mantle

studies because the earthquake belts associated with the Himalayan mountains to the north of the array, the spreading centre of the mid-oceanic ridges to the south-west, and the subducting plate margin to the south-east (Figure 6.1) suggest that the upper mantle structure in this region is considerably heterogeneous. Thirdly, because the Nevada Test Site (NTS) lies within our distance of interest from YKA, it provided a set of events with near-identical epicentral distances and azimuths which could be used to test the consistency of the method, and hence help to determine what the effects of other signal factors might be (see Figure 6.2).

The extent to which the coherence measurements may then be related to the heterogeneity of the upper mantle will depend on the extent to which these other factors can be successfully identified and removed, or corrected for. In some of the following sections therefore, we shall discuss the effects which the intrinsic signal complexity, the frequency composition of the signal, the focal depth of the source, and the local crustal structure near the array and in the source region are likely to have on the results. This discussion should hopefully illustrate why such a knowledge would lead to an objective selection and analysis of events which would minimize these effects, and allow for a meaningful interpretation of the results.


GBA
H

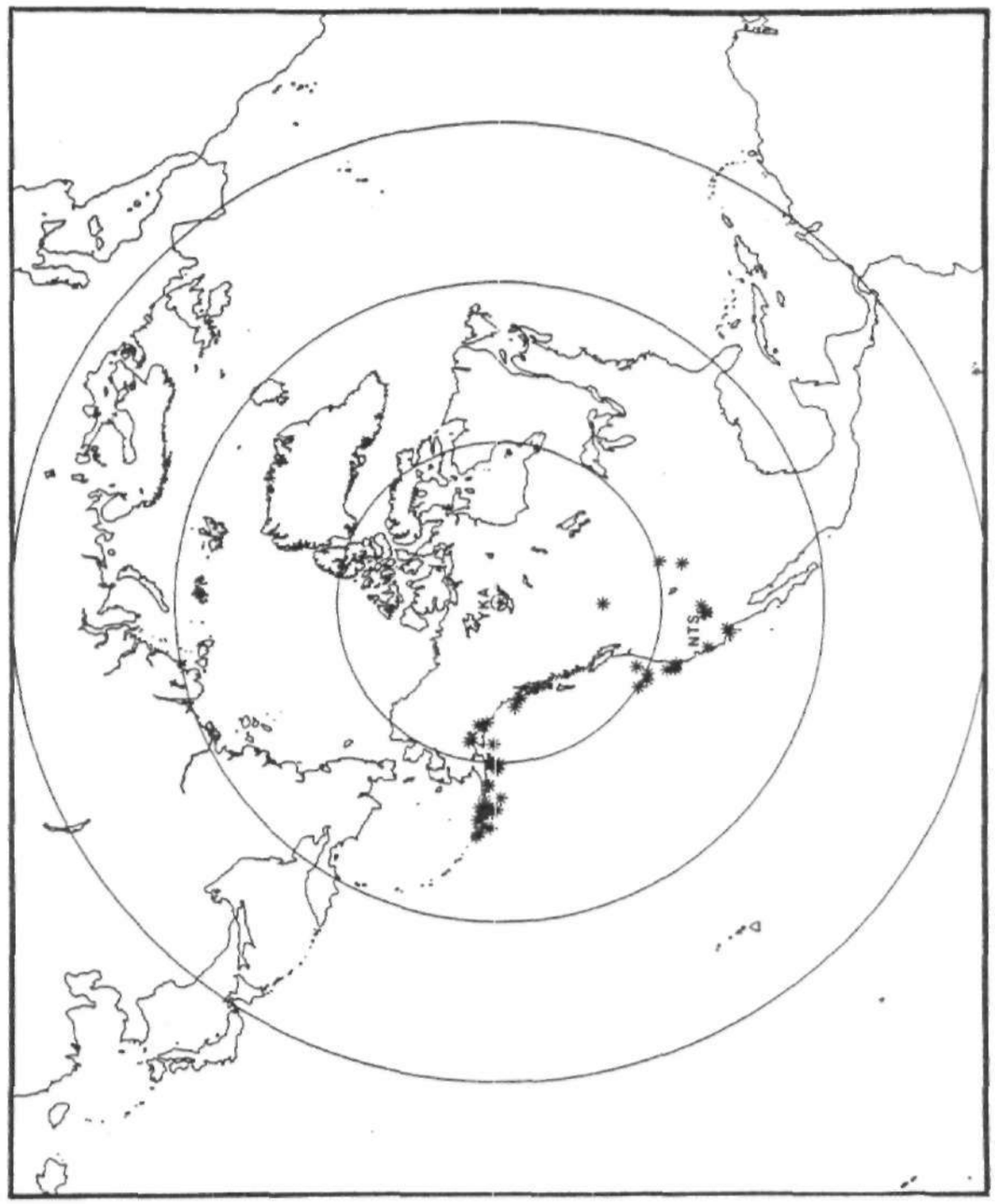

ADAK
NTS

Figure 6.1: Epicentral map for earthquakes (GBA) used in the upper mantle study around India. Concentric circles denote epicentral distances of 20°, 40°, 60° and 80° from inner to outer circle. The azimuth distributions of events are: 1. Himalayan region (0°-90°), 2. Java trench (90°-180°), 3. Mid-Indian oceanic ridge (180°-280°), and 4. Hindukush region (280°-360°). The select Hindukush events used for the Focal depth study in Section 6.7 are identified by "H".

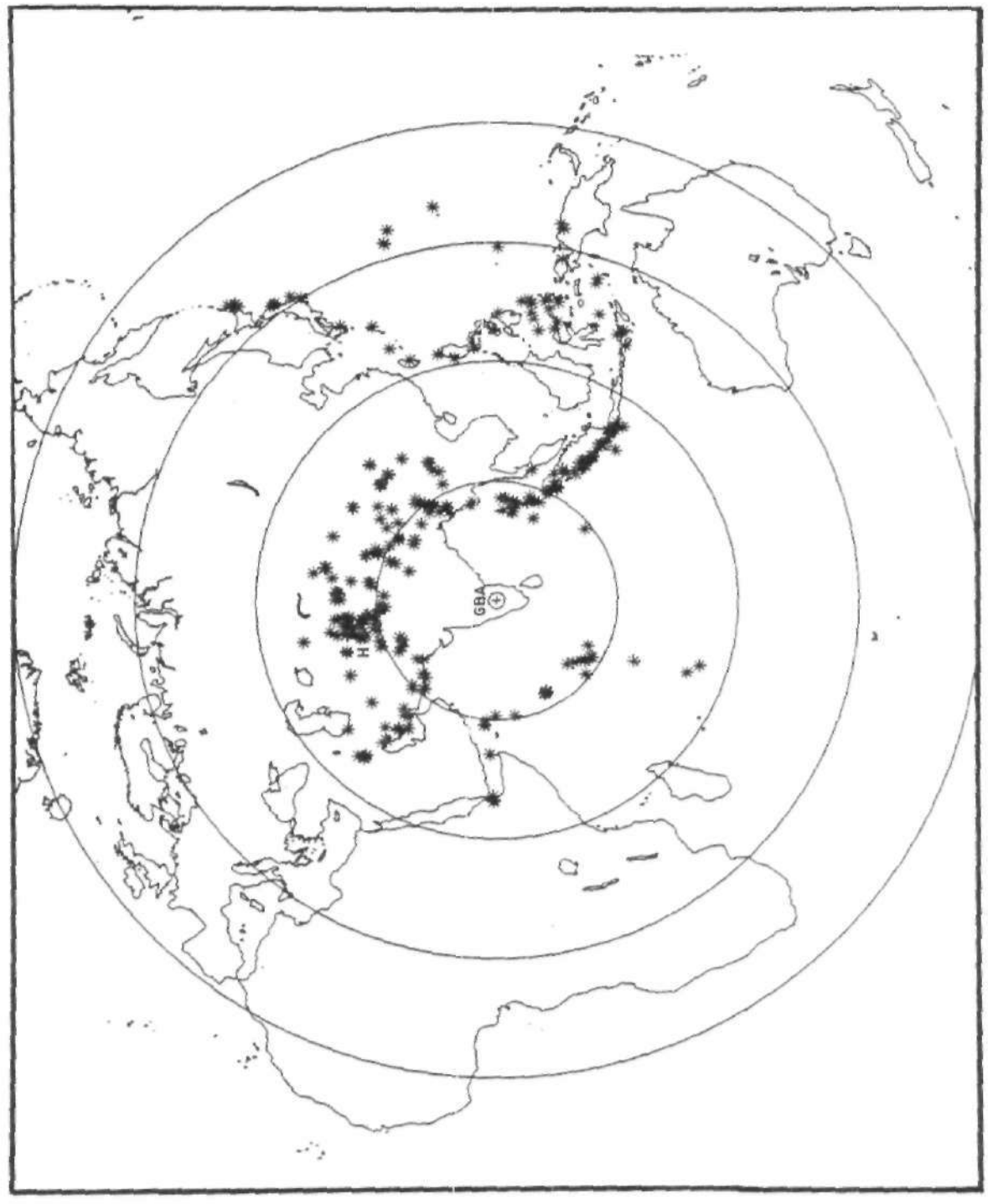

GBA
H

Figure 6.1: Epicentral map for earthquakes (GBA) used in the upper mantle study around India. Concentric circles denote epicentral distances of 20°, 40°, 60° and 80° from inner to outer circle. The azimuth distributions of events are: 1. Himalayan region (0°-90°), 2. Java trench (90°-180°), 3. Mid-Indian oceanic ridge (180°-280°), and 4. Hindukush region (280°-360°). The select Hindukush events used for the Focal depth study in Section 6.7 are identified by "H".

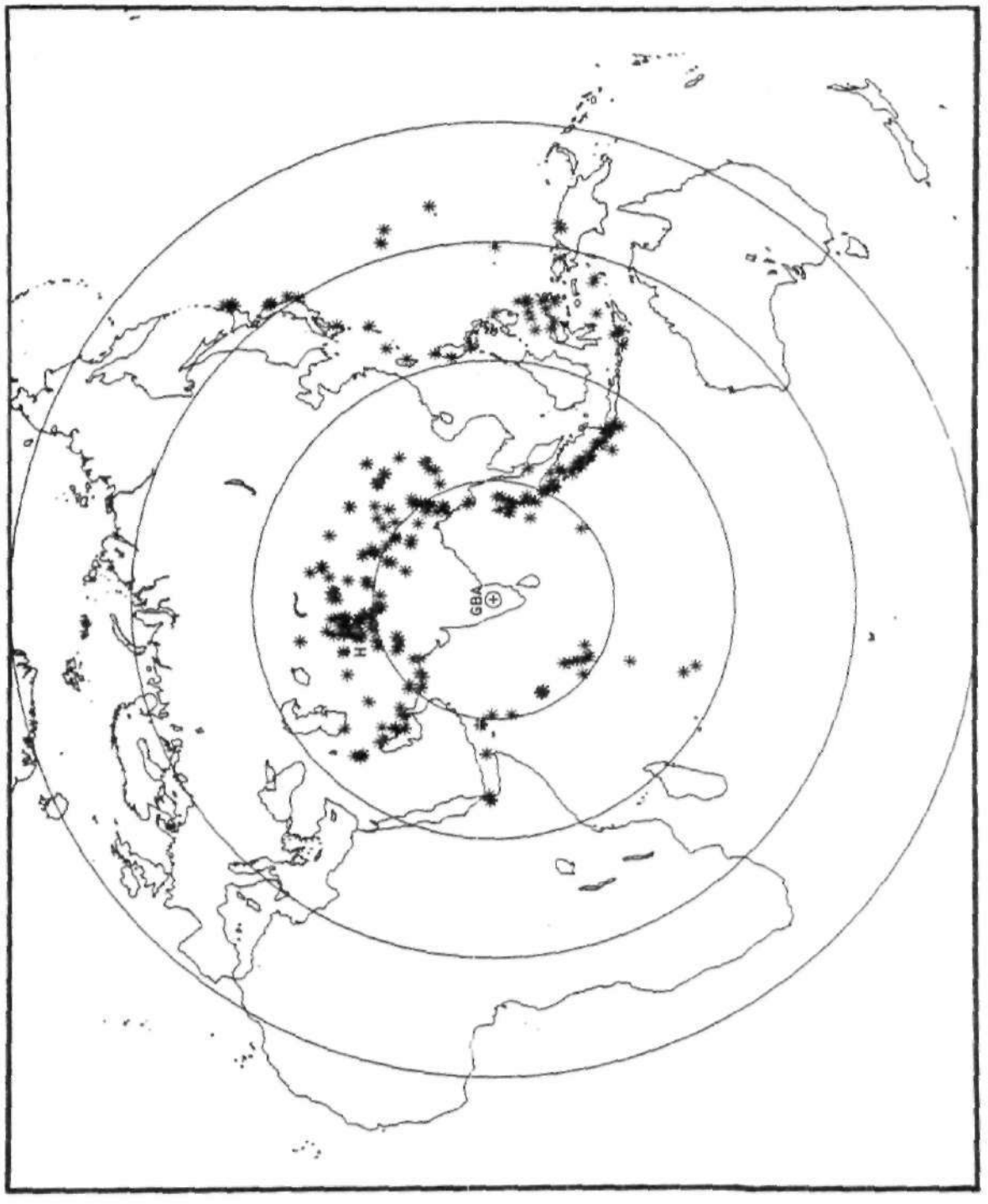
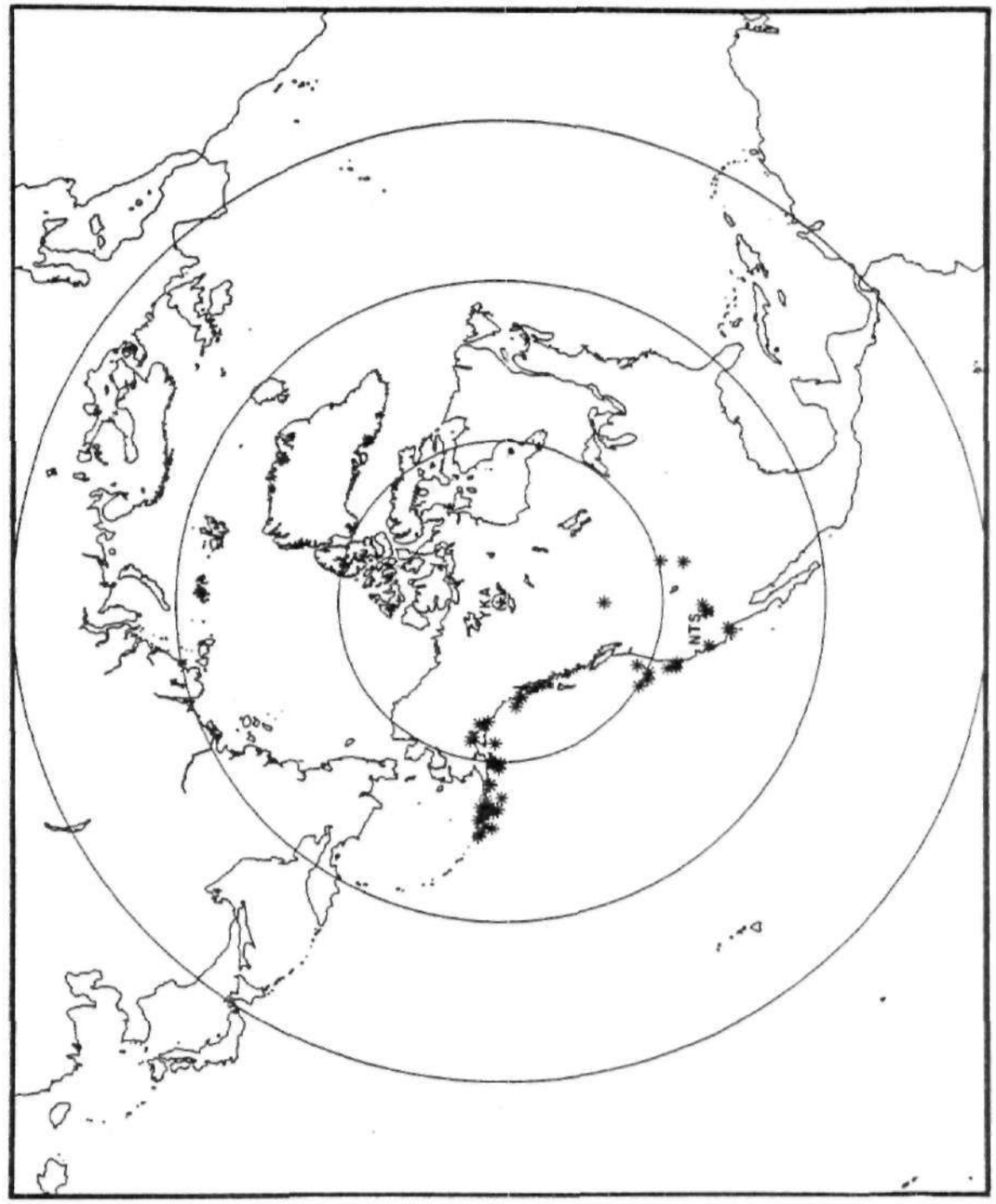

GBA
H

Figure 6.2: Epicentral map for earthquake recorded at the YKA. Concentric circles denote epicentral distances of 20°, 40° and 60° from inner to outer circle. The azimuth distributions of events are: 1. California region (165°-265°), 2. Alaska Peninsula (265°-285°).


NTS

6.2 THE GAURIBIDANUR SEISMIC ARRAY

The Gauribidanur seismic array (GBA) was sponsored by the United Kingdom Atomic Energy Authority (UKAEA) in the early sixties with cooperation of the Bhabha Atomic Research Centre (BARC), Government of India. A detailed description of the array was given by Mowat and Burch (1974), and some of the relevant information about the array are described here for completeness.

It is L-shaped, and each leg contains 10 short-period vertical Willmore MK II seismometers spaced at intervals of 2.5 km (Figure 6.3). The output of each instrument is carried by a telemetry system to a central laboratory where it is recorded in analog form on a 24-channel FM magnetic tape.

The area around GBA is almost flat and the array is underlain by Archean gneisses, schists and igneous metamorphosed rocks with foliation which trend NNW-SSE (Berteussen et al., 1977). A thin layer of soil varying in thickness from 1.5 to 4.6 meters covers the siting area. GBA records of several local earthquakes and chemical explosions gave evidence of a two-layered crust of thickness 16 and 19 km respectively, and corresponding P-phase velocities of 5.7, 6.5 and 8.0 km/s (Arora et al., 1970; Arora, 1971). Corbishley (1970) found that site corrections required for the array were very small and concluded that GBA is situated on a uniform layered structure. Berteussen

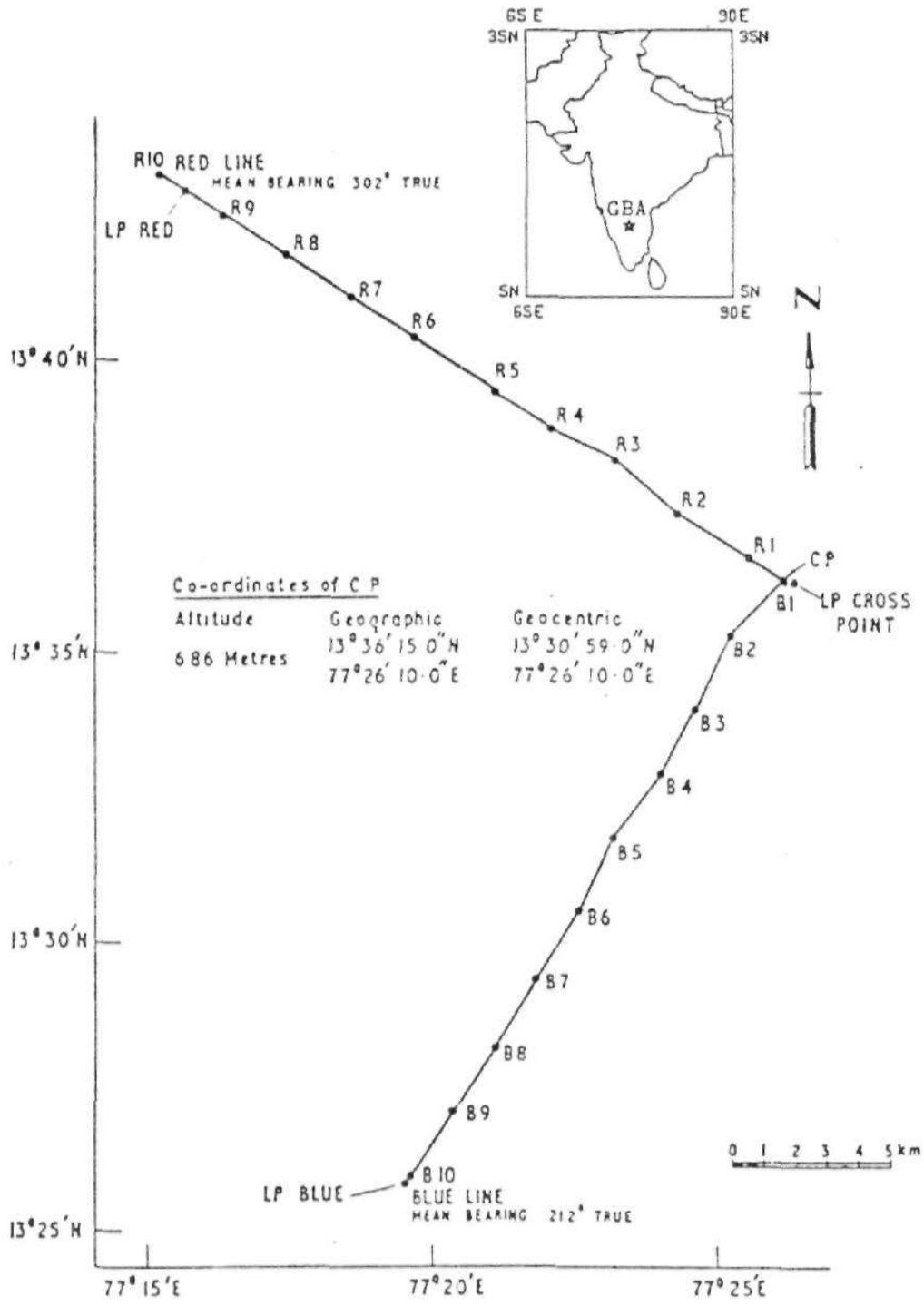


Figure 6.3: Configuration of the Gauribidanur medium apenture seismic array (GBA) (after Mowat and Burch, 1974).

et al. (1977) also concluded from an extensive analysis of travel time residuals at GBA that the structures in the array siting area are exceptionally homogeneous.

6.3 THE YELLOWKNIFE SEISMIC ARRAY

The Yellowknife array (YKA) was also established in cooperation with the UKAEA in 1962 by the Canadian Department of Energy, Mines and Resources. It is located near Yellowknife in the Northwest Territories, and consists of two orthogonal lines (called blue and red lines) each containing ten short-period vertical Willmore MK II seismometers spaced at intervals of 2.5 km to make an overall length of 22.5 km for each arm (Figure 6.4). The output of each instrument is transmitted by a radio-telemetry system to a Control Centre where it is recorded on a 24-channel FM tape, as well as digitized and entered into a small on-line computer (Weichert, 1975). The original construction and instrumentation of the YKA were described by Manchee and Somers (1966), and details of the subsequent improvements to the system may be found in Weichert's review.

Geologically, the array siting location is near the western margin of the Canadian Precambrian Shield. The granitic outcrops of the Slave (structural) Province, about 2400 million years old, extend far to the north and northwest of the array (Weichert and Whitham, 1969). Immediately to the east and south-east, however, the

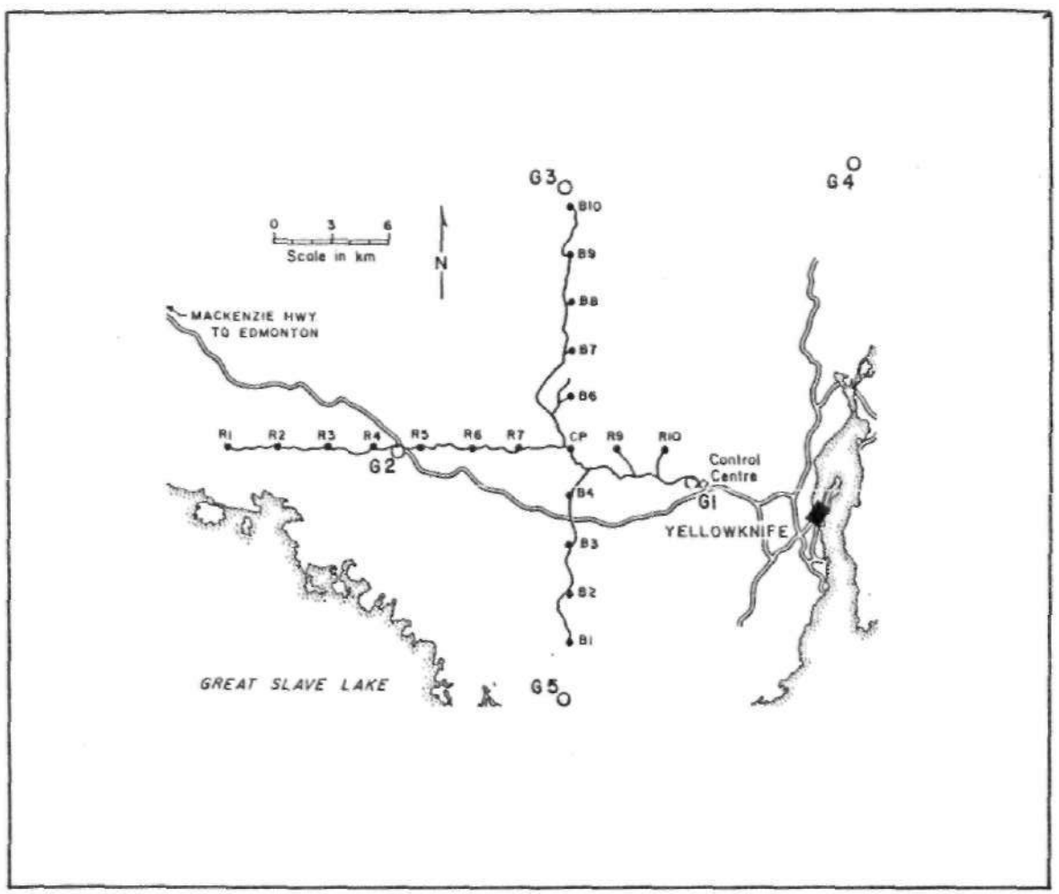


Figure 6.4: Configuration of the Yellowknife medium aperture seismic array (YKA) (after Weichert, 1975)

uniformity of the shield is interrupted by the south-westerly tip of an extended area of Archean sedimentary and volcanic rocks, including the Yellowknife Greenstone Belt. Apart from an upper layer of about 1 to 2 km thickness, Weichert and Whitham (1969) found from a refraction experiment that the crust surrounding the array has a well established P velocity of 6.04 ± 0.01 km/s and extends downwards to about 34 km without evidence for an intermediate layer; the P_n velocity was found to be 8.15 ± 0.05 km/s. They also found the azimuth-dependent component of the site corrections to be very small. Corbishley (1970) also found from an average slowness curve derived from earthquakes and underground explosions recorded at the array that site corrections for the seismometer locations showed very little dependence on azimuth, and were small. He therefore concluded that YKA is situated in a region of very uniform crustal material with horizontal layering.

6.4 ANALYSES AND CORRECTION OF THE DATA

As indicated earlier, all the data used in this study were already available in digitized form on tape. The sampling rate was approximately 20 samples per second, and the analogue pre-filter settings were 0.25 - 8 Hz. The digital tape was written in 7 tracks at 800 bpi (Ram, 1976). The exact sampling rate together with all other pertinent information on the earthquakes (e.g. origin time, epicentral distance and azimuth from array, etc.) which were punched

on cards were supplied by Dr. Mereu. The epicentral map for all the event used are shown in Figures 6.1 and 6.2.

Computation was performed by a CDC Cyber 73 computer during the block-time hours of the Computing Centre (midnight to 0400 Hrs) to reduce cost. All events were bandpass filtered digitally (0.4 - 3.0 Hz) and normalized before processing. All YKA events were processed by the Nth root method, and all GBA events were processed by the normal beam forming method (see Chapter 5). A summary of the results is listed in Appendix C.1 (for GBA), and C.2(for YKA). Because the method is very sensitive to noise, plots of all the earthquake data were scrutinized beforehand, and recordings which were considered excessively noisy were discarded. Other events with moderate noise levels were corrected for noise by using the method described in Chapter 5.

Ram (1976) discussed some of the problems which were encountered with the original GBA analogue tapes during the transcription of the data. Some of these problems were still evident in this study, and one particular problem which was encountered during the data processing, was the realization that some of the channels were recorded with reversed polarity. The important significance of this will be discussed later. The reversed polarity was indicated by a direction of first motion which was opposite to those of the other channels in the same arm of the array. This suspicion was further strengthened by the fact that the

polarity reversals all appeared to have occurred in the channels after the stations were reactivated, following some period when they were dead, suggesting some inadvertent human error. A case in point is illustrated in Figure 6.5, in which the record of GBA 164 shows that station B9 was reversed after GBA 155 was recorded. In fact, a closer scrutiny of all the data showed that stations B6, B7, B9 and R8 were reversed during certain intervals of an extended six-month period which started in April 19, 1973; all reversals and corrections occurred after the stations had been dead for some time and were reactivated.

The preceding is very important because while the effect of one or two reversed channels on the adaptive processing method is to reduce the TAP amplitude and the measuring threshold of the various events in the signal, the effect on the coherence measurement is more drastic. For example, when coherence measurements were made on the record of GBA 164 the computed scattered energy (incoherent energy of the incident signal expressed as a percentage of the total incident energy) was 52%. When B9 was corrected (multiplied by -1), the value dropped to 17.9%, and when B9 was blanked out the value was 29.2%. It is thus seen that correcting for the polarity reversal in B9 resulted in a more coherent beam. That this did not occur fortuitously was established by inverting B8 instead of B9 resulting in even poorer coherence indicated by an apparent scattered energy of 56.1%. These tests led to the conclusion that a

Figure 6.5: Two array record section from GBA illustrating the polarity reversal of station B9 for the record section on the right.

GBA 155

D M YEAR
11 4 1973

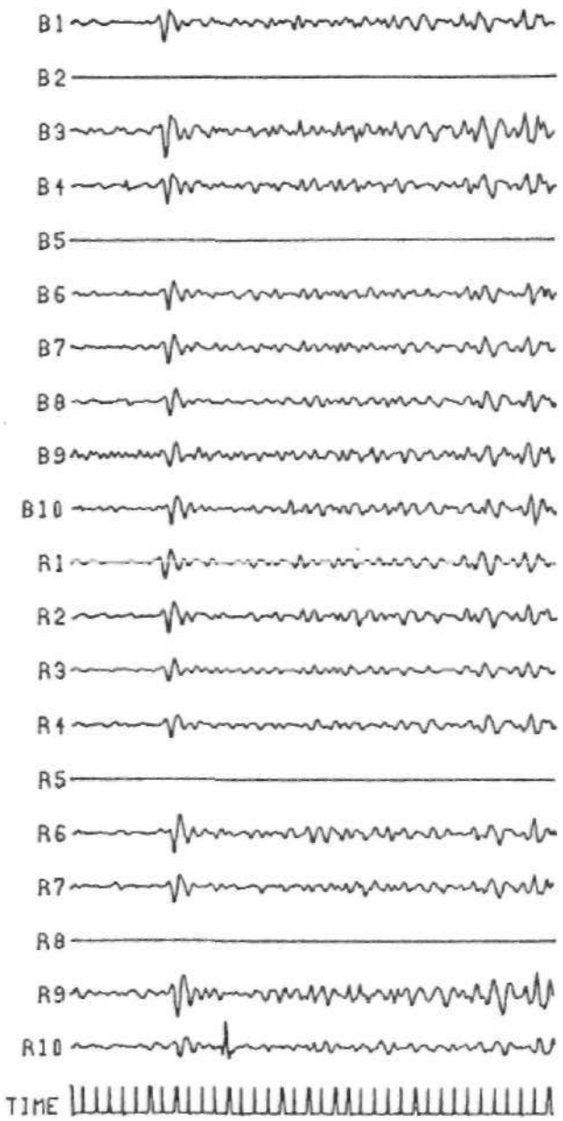
ORIG. TIME
H M SEC
2 9 33.1

ARRI. TIME
H M SEC
2 16 14.3

LOCATION
11.783 N
42.847 E

T=401.20 SEC
RT=25.58 SEC
DELTA=33.78
PHI=270.9
FD=33 KM
MB=4.6

BAND PASS
FL=3.0 HZ
FH=0.4 HZ



GBA 164

D M YEAR
26 4 1973

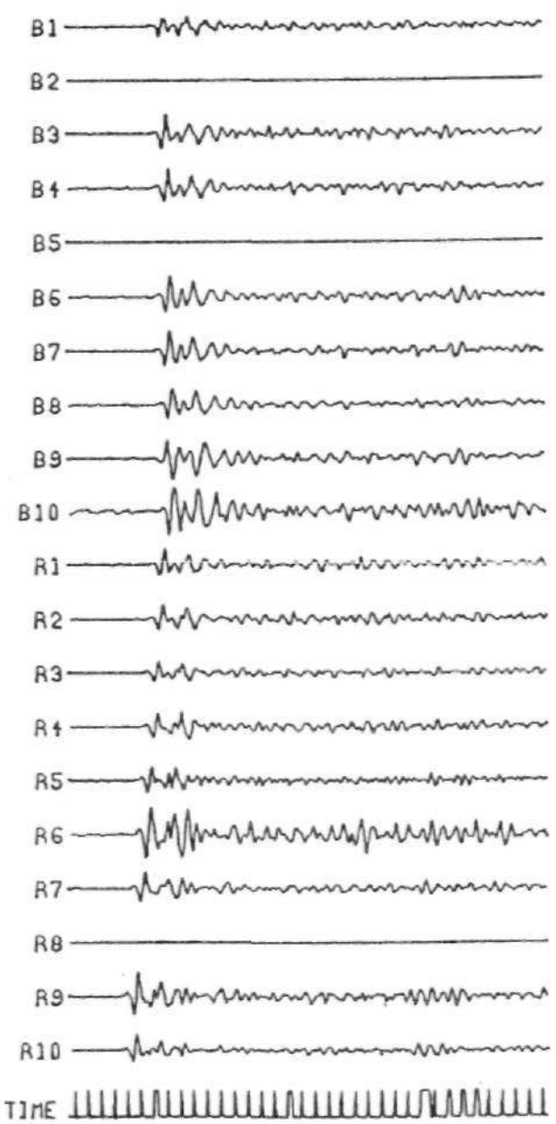
ORIG. TIME
H M SEC
14 30 5.4

ARRI. TIME
H M SEC
14 34 42.4

LOCATION
27.092 N
60.837 E

T=277.00 SEC
RT=48.83 SEC
DELTA=20.52
PHI=313.4
FD=46 KM
MB=5.2

BAND PASS
FL=3.0 HZ
FH=0.4 HZ



reversed polarity in any of the channels would affect the coherence measurements in a disastrous manner. For this reason, all the records were therefore carefully checked for reversal, and channels with doubts about the correctness of their polarity during recording were blanked out.

6.5 EFFECTS OF SIGNAL COMPLEXITY

The earthquake data used may be broadly divided into two groups consisting of events with relatively simple signals (F_C<2.0), and those with very complex signals (F_C>2.0). These could in turn be divided into two subgroups of events with high scattered energy (>30%) and events with low scattered energy (< 30%). Examples of these four types of signals are shown in Figures 6.6 and 6.7 together with their adaptive processed solutions. The size of the points used to display the answers in the solutions is a measure of how well the signals correlated (King et al., 1973; Ram and Mereu, 1977), and the error bars are those from the least square solutions (Kelly, 1964; Otsuka, 1966).

Figures 6.6a and 6.6b show two examples of signals with complexity factor less than 2.0 and scattered energy of 12% and 7% respectively. It will be noted that the slowness solutions show little variation while a large scatter occurs in the azimuth solutions. However, the solutions generally appear good as are indicated by the size of the points. The pertinent features of Figures 6.6c and 6.6d are low complexity factor, but high scattered energy (61% and 56%

Figure 6.6a, b, c, and d: Examples of record sections from GBA to illustrate the relationship between simple signals and scattered energy. The adaptive processed solutions of the sections (after Ram and Mereu, 1977) are also shown for comparison.

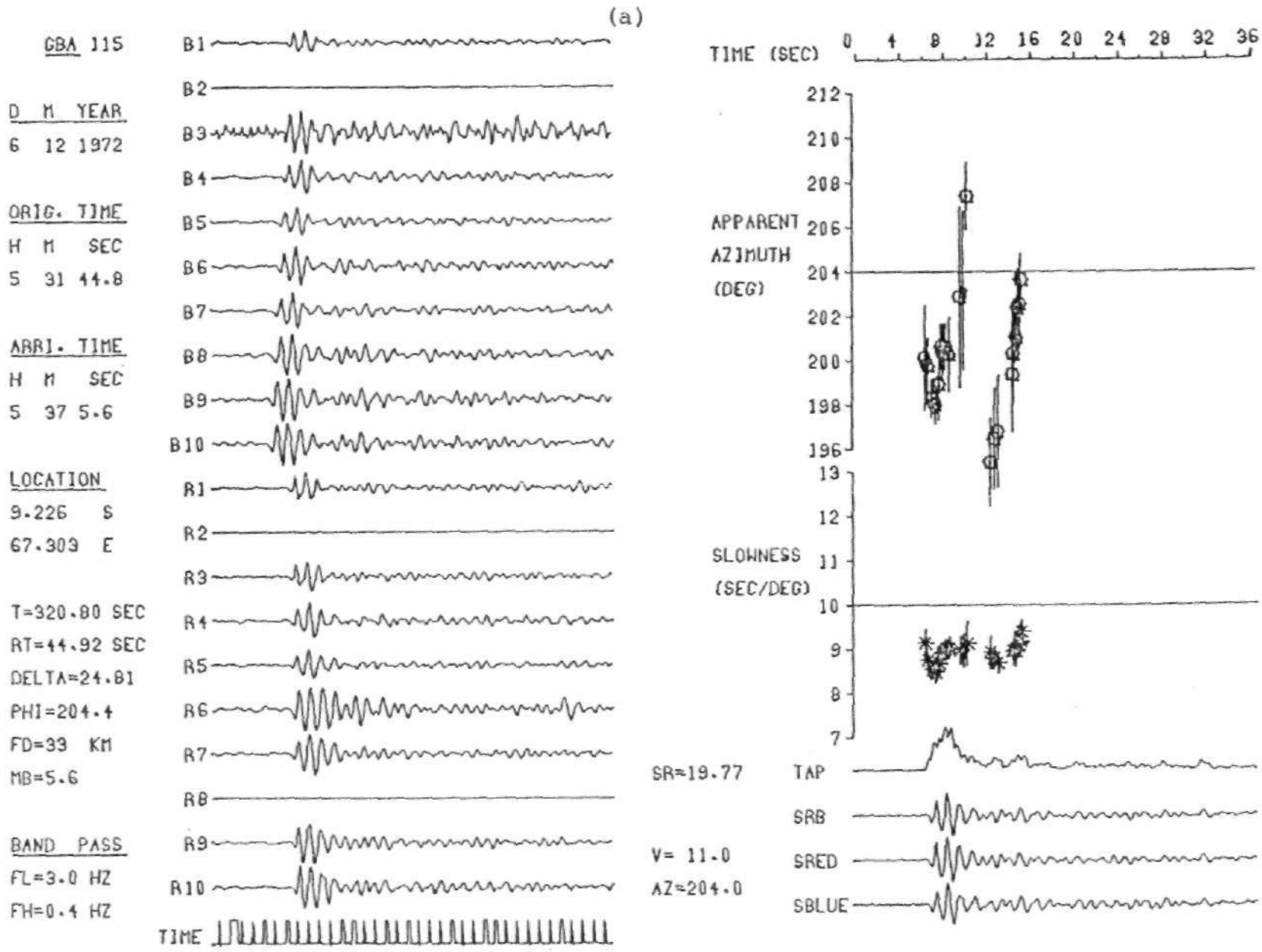
(a) Complexity factor (F_C) if 1.4; scattered energy (S.E.) is 12%.

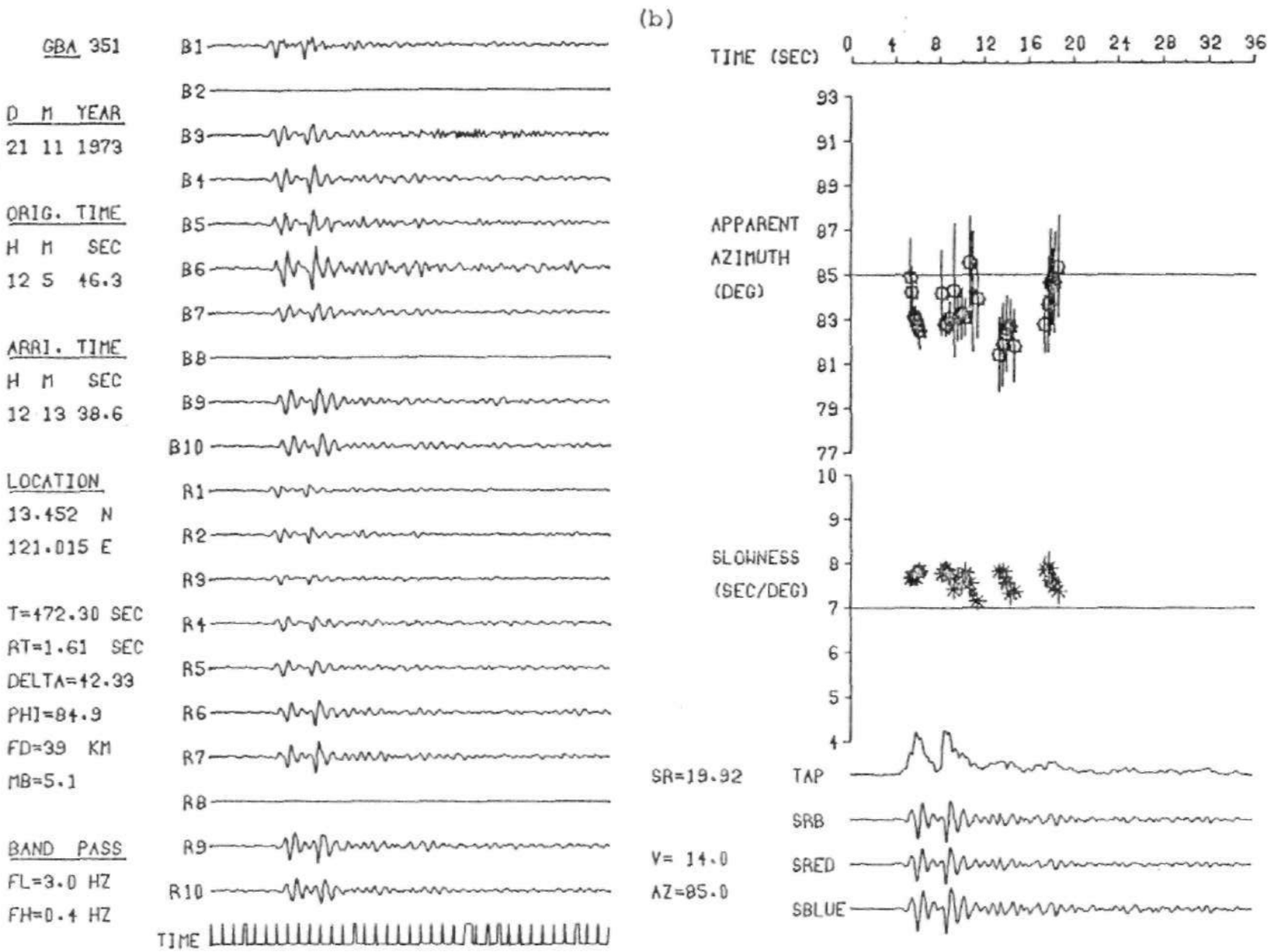
(b) F_C = 1.7; S.E. = 7%

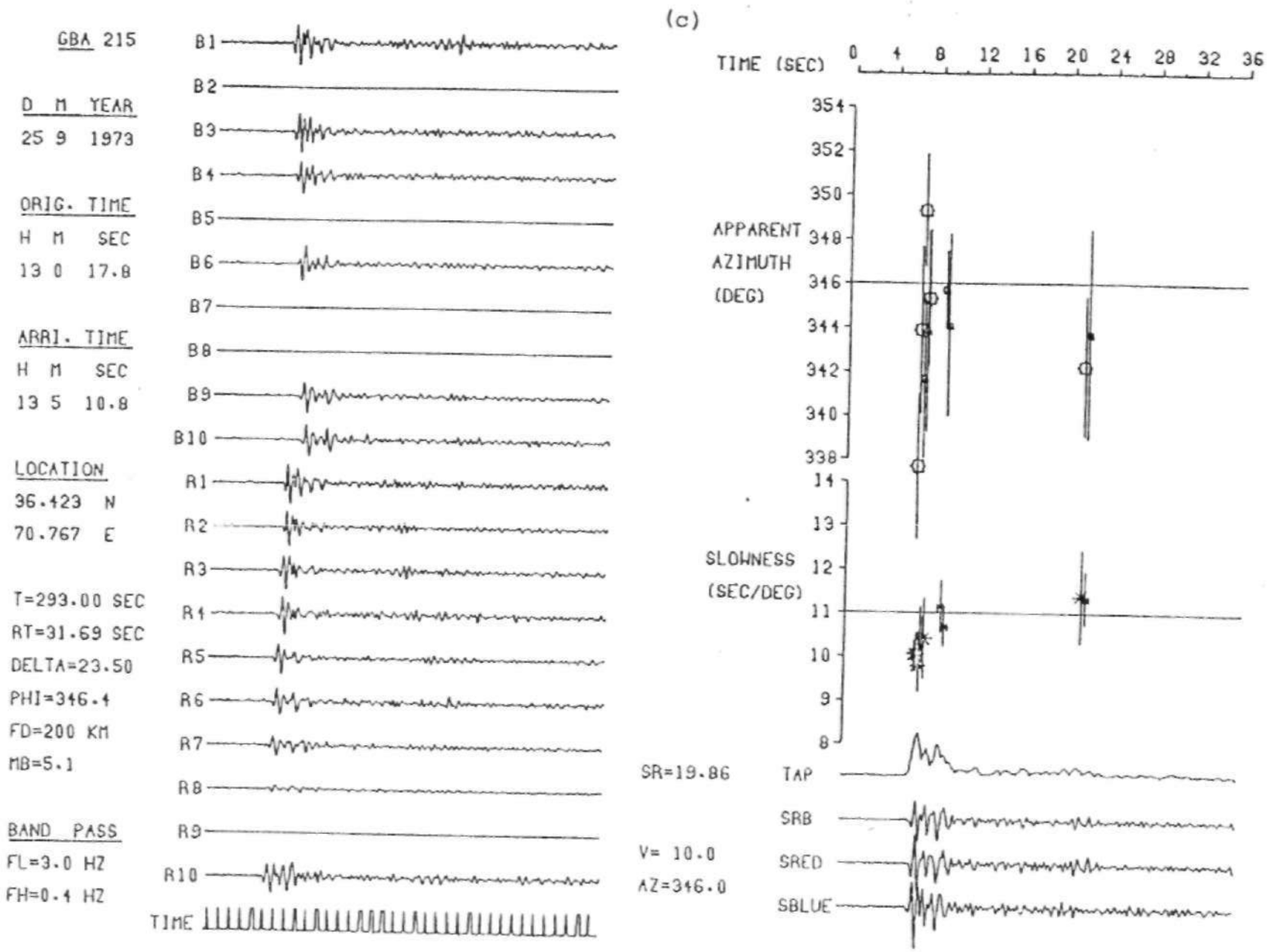
(c) F_C = 1.2; S.E. = 61%

(d) F_C = 1.1; S.E. = 56%

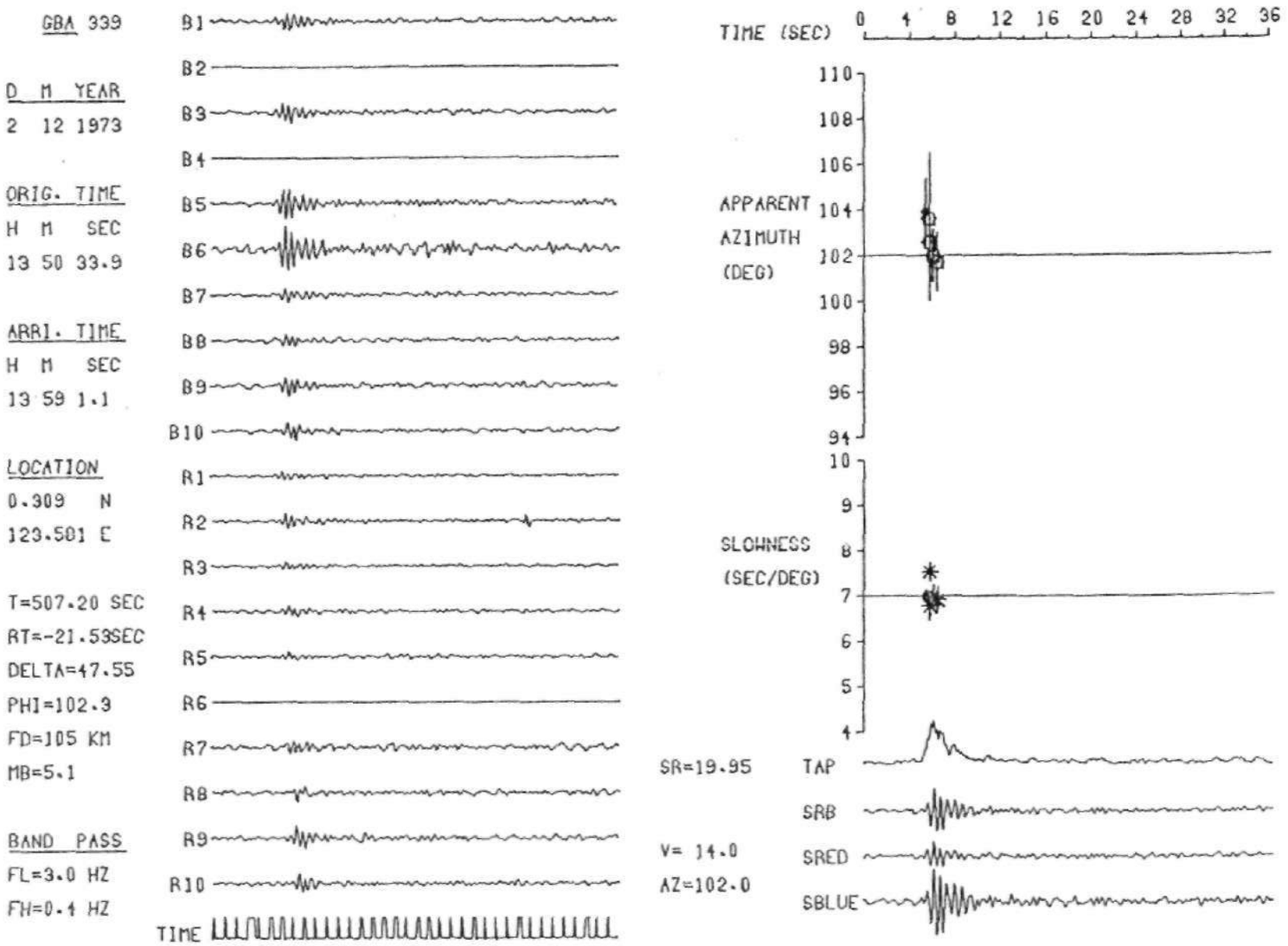
(a)


GBA 115
D M YEAR
6 12 1972
ORIG. TIME
H M SEC
5 31 44.8
ARRI. TIME
H M SEC
5 37 5.6
LOCATION
9.226 S
67.303 E
T=320.80 SEC
RT=44.92 SEC
DELTA=24.81
PHI=204.4
FD=33 KM
MB=5.6
BAND PASS
FL=3.0 HZ
FH=0.4 HZ
B1
B2
B3
B4
B5
B6
B7
B8
B9
B10
R1
R2
R3
R4
R5
R6
R7
R8
R9
R10
TIME
TIME (SEC)
0 4 8 12 16 20 24 28 32 36
APPARENT AZIMUTH (DEG)
212
210
208
206
204
202
200
198
196
SLOWNESS (SEC/DEG)
13
12
11
10
9
8
7
SR=19.77
V= 11.0
AZ=204.0
TAP
SRB
SRED
SBLUE


(b)
GBA 351
D M YEAR
21 11 1973
ORIG. TIME
H M SEC
12 5 46.3
ARRI. TIME
H M SEC
12 13 38.6
LOCATION
13.452 N
121.015 E
T=472.30 SEC
RT=1.61 SEC
DELTA=42.33
PHI=84.9
FD=39 KM
MB=5.1
BAND PASS
FL=3.0 HZ
FH=0.4 HZ
B1
B2
B3
B4
B5
B6
B7
B8
B9
B10
R1
R2
R3
R4
R5
R6
R7
R8
R9
R10
TIME
TIME (SEC) 0 4 8 12 16 20 24 28 32 36
APPARENT AZIMUTH (DEG)
93
91
89
87
85
83
81
79
77
SLOWNESS (SEC/DEG)
10
9
8
7
6
5
4
SR=19.92
V= 14.0
AZ=85.0
TAP
SRB
SRED
SBLUE


GBA 215
D M YEAR
25 9 1973
ORIG. TIME
H M SEC
13 0 17.8
ARRI. TIME
H M SEC
13 5 10.8
LOCATION
36.423 N
70.767 E
T=293.00 SEC
RT=31.69 SEC
DELTA=23.50
PHI=346.4
FD=200 KM
MB=5.1
BAND PASS
FL=3.0 HZ
FH=0.4 HZ
B1
B2
B3
B4
B5
B6
B7
B8
B9
B10
R1
R2
R3
R4
R5
R6
R7
R8
R9
R10
TIME
(c)
TIME (SEC)
0 4 8 12 16 20 24 28 32 36
APPARENT AZIMUTH (DEG)
354
352
350
348
346
344
342
340
338
SLOWNESS (SEC/DEG)
14
13
12
11
10
9
8
SR=19.86
V= 10.0
AZ=346.0
TAP
SRB
SRED
SBLUE

(d)

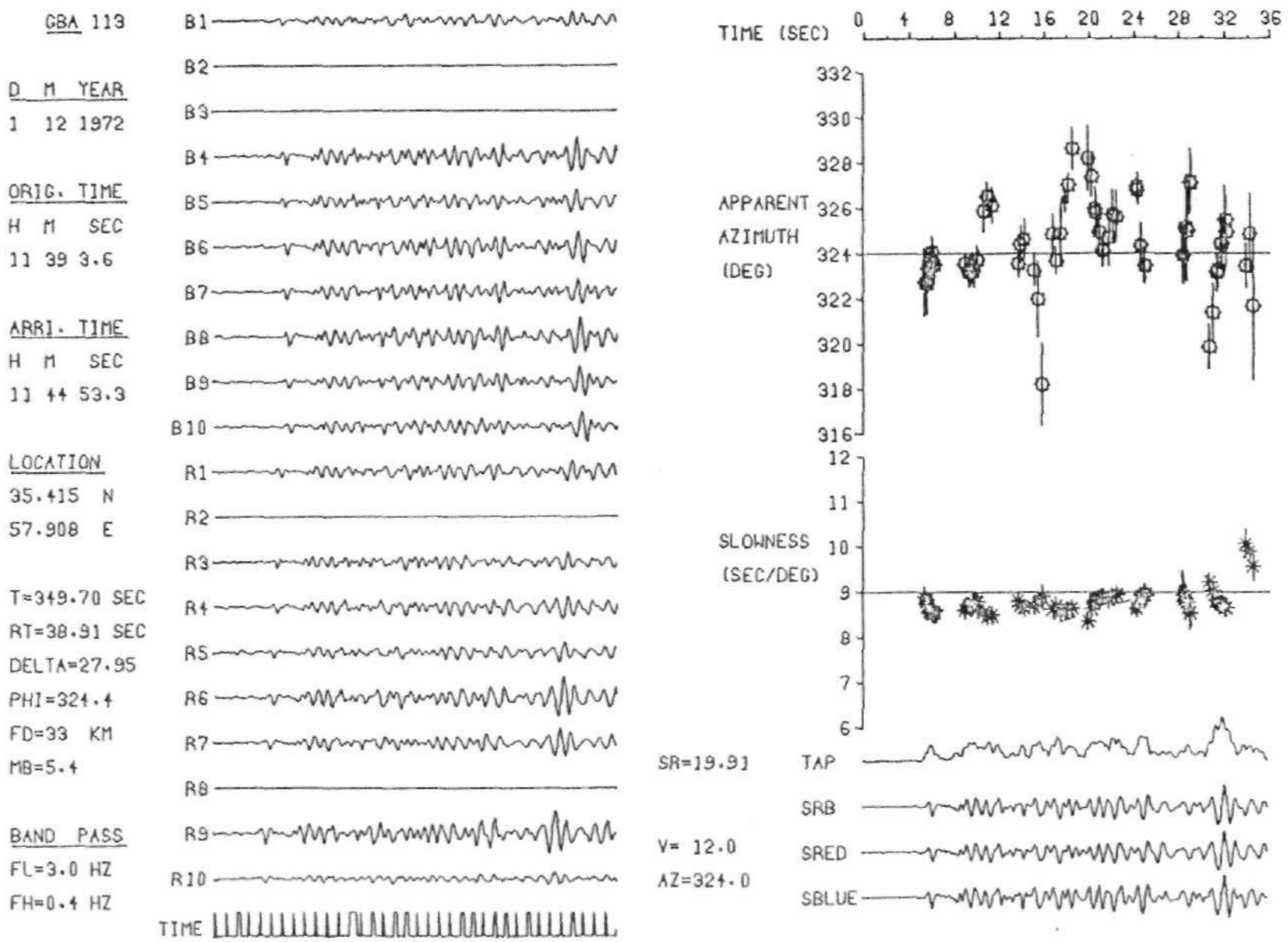

GBA 339
D M YEAR
2 12 1973
ORIG. TIME
H M SEC
13 50 33.9
ARRI. TIME
H M SEC
13 59 1.1
LOCATION
0.309 N
123.501 E
T=507.20 SEC
RT=-21.53SEC
DELTA=47.55
PHI=102.3
FD=105 KM
MB=5.1
BAND PASS
FL=3.0 HZ
FH=0.4 HZ
B1
B2
B3
B4
B5
B6
B7
B8
B9
B10
R1
R2
R3
R4
R5
R6
R7
R8
R9
R10
TIME
TIME (SEC)
0 4 8 12 16 20 24 28 32 36
APPARENT AZIMUTH (DEG)
110 108 106 104 102 100 98 96 94
SLOWNESS (SEC/DEG)
10 9 8 7 6 5 4
SR=19.95
V= 14.0
AZ=102.0
TAP
SRB
SRED
SBLUE

respectively), and poorer solutions which are particularly evident in Figure 6.6c. The signals also appear to contain more higher frequency component than those of Figures 6.6a,b which may explain the high scattered energy.

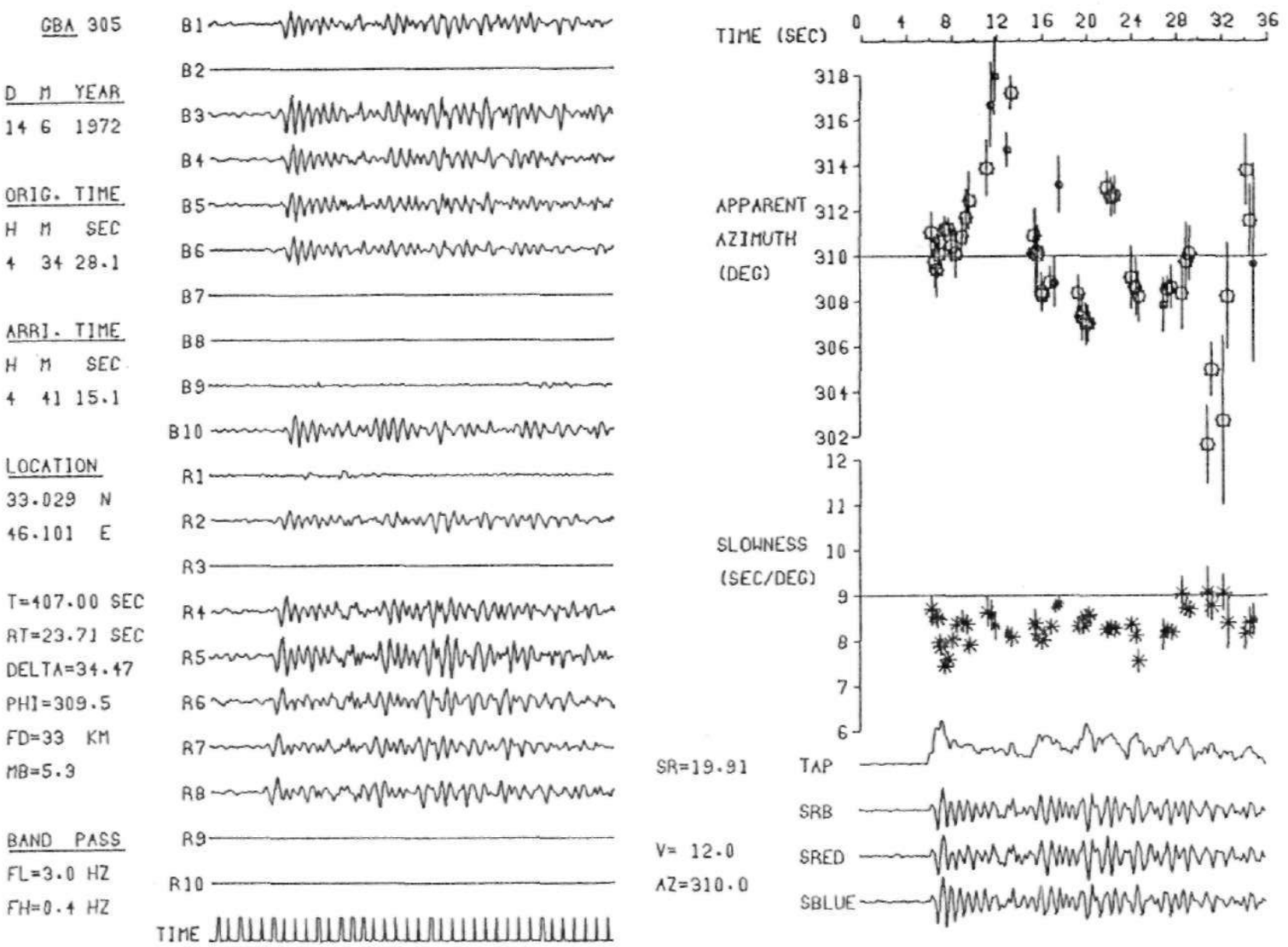
In Figures 6.7a and 6.7b, the pertinent features are high complexity factor and low scattered energy (9% and 7% respectively). Solutions are again good, and relatively more scatter is still evident in the azimuth solutions. In Figures 6.7c and 6.7d, the signals have high complexity factor and high scattered energy (49% and 54% respectively). Solutions, however, show more scatter in both slowness and azimuth, and several poorer solutions are also evident. Figure 6.7d also shows relatively higher frequency content.

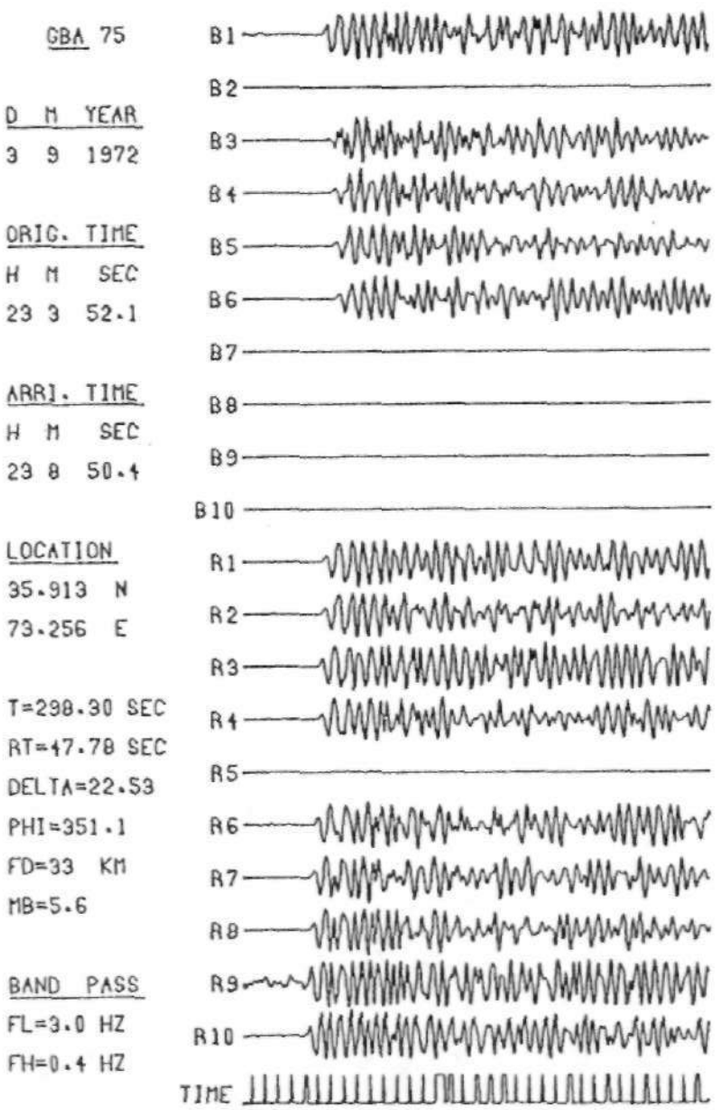
It would therefore appear from this visual inspection that scattering is not necessarily a function of the complexity factor of the signal since both simple and complex signals appear to show equal affinity for low and high scattered energy. It would also appear that while the scatter in the azimuth solutions is more profuse than the scatter in the slowness solutions, the latter however has the dominant effect on the coherence of the signals, which suggests that the vertical variations or perturbations in velocity of the upper mantle are more significant in causing scattering than the lateral variations.

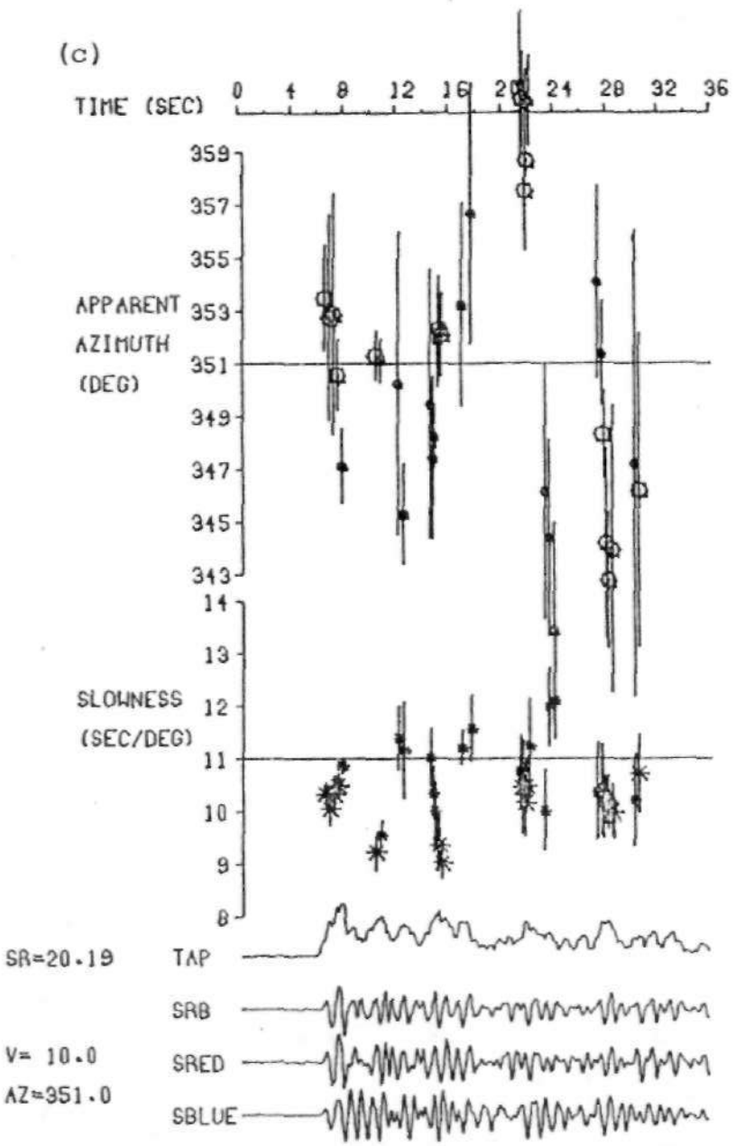
(a)


GBA 113
D M YEAR
1 12 1972
ORIG. TIME
H M SEC
11 39 3.6
ARRI. TIME
H M SEC
11 44 53.3
LOCATION
35.415 N
57.908 E
T=349.70 SEC
RT=38.91 SEC
DELTA=27.95
PHI=324.4
FD=33 KM
MB=5.4
BAND PASS
FL=3.0 HZ
FH=0.4 HZ
B1
B2
B3
B4
B5
B6
B7
B8
B9
B10
R1
R2
R3
R4
R5
R6
R7
R8
R9
R10
TIME
TIME (SEC) 0 4 8 12 16 20 24 28 32 36
APPARENT AZIMUTH (DEG)
332
330
328
326
324
322
320
318
316
SLOWNESS (SEC/DEG)
12
11
10
9
8
7
6
SR=19.91
V= 12.0
AZ=324.0
TAP
SRB
SRED
SBLUE

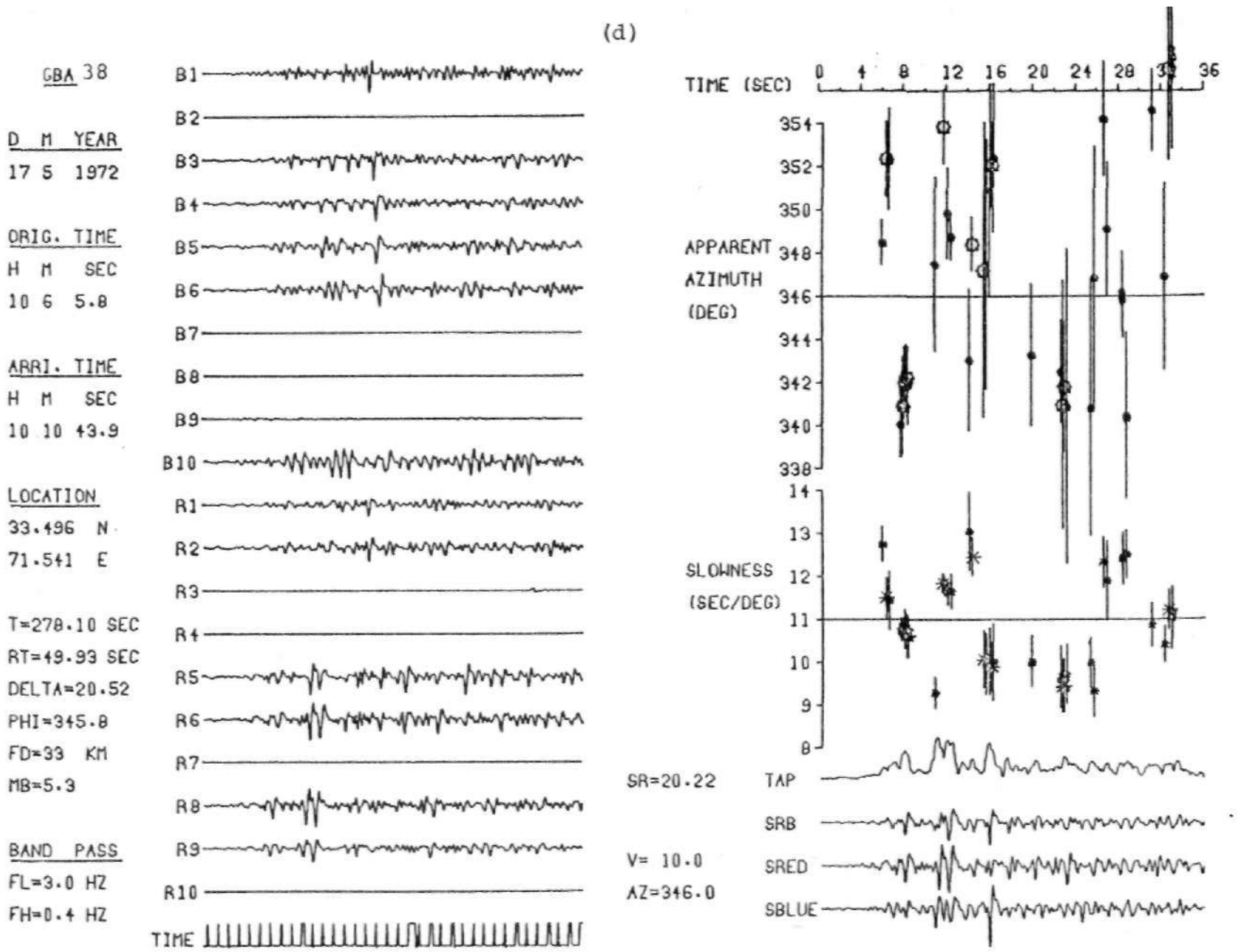
(b)


GBA 305
D M YEAR
14 6 1972
ORIG. TIME
H M SEC
4 34 28.1
ARRI. TIME
H M SEC
4 41 15.1
LOCATION
33.029 N
46.101 E
T=407.00 SEC
RT=23.71 SEC
DELTA=34.47
PHI=309.5
FD=33 KM
MB=5.3
BAND PASS
FL=3.0 HZ
FH=0.4 HZ
B1
B2
B3
B4
B5
B6
B7
B8
B9
B10
R1
R2
R3
R4
R5
R6
R7
R8
R9
R10
TIME
TIME (SEC)
0 4 8 12 16 20 24 28 32 36
APPARENT AZIMUTH (DEG)
318 316 314 312 310 308 306 304 302
SLOWNESS (SEC/DEG)
12 11 10 9 8 7 6
SR=19.91
V= 12.0
AZ=310.0
TAP
SRB
SRED
SBLUE


GBA 75
D M YEAR
3 9 1972
ORIG. TIME
H M SEC
23 3 52.1
ARRI. TIME
H M SEC
23 8 50.4
LOCATION
35.913 N
73.256 E
T=298.30 SEC
RT=47.78 SEC
DELTA=22.53
PHI=351.1
FD=33 KM
MB=5.6
BAND PASS
FL=3.0 HZ
FH=0.4 HZ
B1
B2
B3
B4
B5
B6
B7
B8
B9
B10
R1
R2
R3
R4
R5
R6
R7
R8
R9
R10
TIME


(c)
TIME (SEC)
0 4 8 12 16 20 24 28 32 36
APPARENT AZIMUTH (DEG)
359
357
355
353
351
349
347
345
343
SLOWNESS (SEC/DEG)
14
13
12
11
10
9
8
SR=20.19
V= 10.0
AZ=351.0
TAP
SRB
SRED
SBLUE

(d)


GBA 38
D M YEAR
17 5 1972
ORIG. TIME
H M SEC
10 6 5.8
ARRI. TIME
H M SEC
10 10 43.9
LOCATION
33.496 N
71.541 E
T=270.10 SEC
RT=49.93 SEC
DELTA=20.52
PHI=345.8
FD=33 KM
MB=5.3
BAND PASS
FL=3.0 HZ
FH=0.4 HZ
B1
B2
B3
B4
B5
B6
B7
B8
B9
B10
R1
R2
R3
R4
R5
R6
R7
R8
R9
R10
TIME
TIME (SEC)
0 4 8 12 16 20 24 28 32 36
APPARENT AZIMUTH (DEG)
354
352
350
348
346
344
342
340
338
SLOWNESS (SEC/DEG)
14
13
12
11
10
9
8
SR=20.22
V= 10.0
AZ=346.0
TAP
SRB
SRED
SBLUE

6.6 EFFECTS OF SIGNAL FREQUENCY

Figure 6.8 shows the computed scattered energy for 25 recordings from NTS explosions plotted as a function of their epicentral distances from YKA. The locations of these events (see Figure 6.2) are very accurately known and as the figure shows, their epicentral distances from YKA are approximately identical. The mean epicentral distance for these events is 25.41 degrees, and the maximum deviation from this value is 0.16 degrees. The corresponding mean azimuth with respect to YKA, and the maximum deviation from this mean are 182.72 and 0.58 degrees respectively. Since their focal depths are also approximately identical, the propagation paths of the signals from NTS to YKA should almost be identical and their scattered energies should be the same approximately. Figure 6.8 shows that although there is a fair degree of consistency in the results, some scatter does exist in the points. Except for three points which have the lowest scattered energy, and three points with the highest scattered energy, all other points lie within 7% of the mean scattered energy. Clearly, some explanations are necessary for this scatter which is more than could be accounted for by errors in the computational procedure.

In the last section, it was indicated that some of the high scattered energy obtained might be accounted for by the higher frequency component of those signals. Following that observation, the relative amplitude spectra of the signal

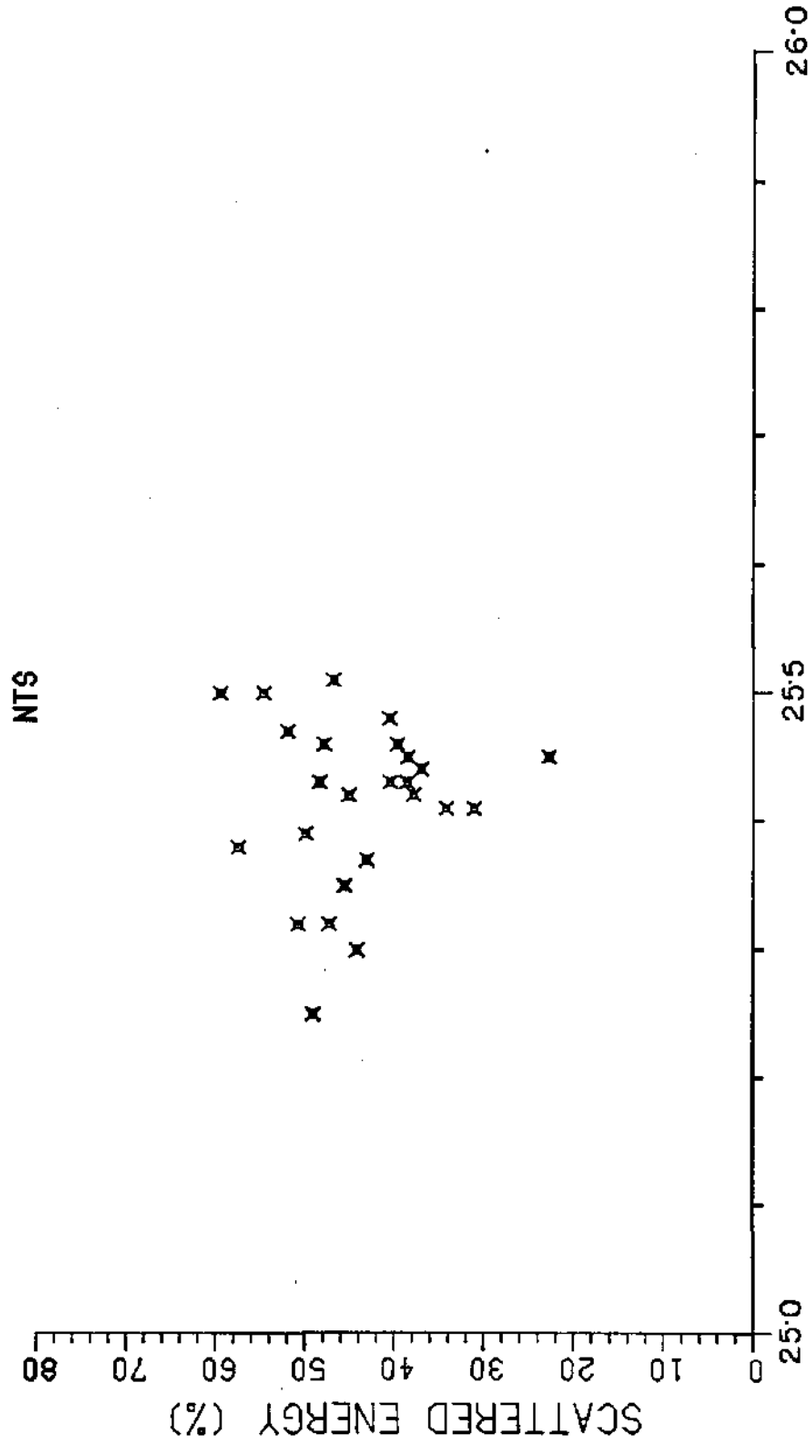


Figure 6.8: Scattered energy versus distance for NTS events.

beams formed without pre-filtering were computed using a Fast Fourier Transform (FFT) NLOGN subroutine (Robinson, 1967a). The beams were tapered with a 26-second Hamming window to prevent truncation errors. Four spectra for YKA recordings of NTS events are shown in Figure 6.9, and for completeness and comparisons, a set of four spectra of recordings from each of the regions investigated are shown in Figures 6.10(a-f). The regions are the California region and Alaska Peninsula for the YKA study; and the Himalayan region, the Java trench, the Mid-Indian Oceanic ridge, and the Hindukush region for the GBA study.

A visual inspection of the amplitude spectra showed that most of the signals contained very little energy in the frequency range above 3 Hz, and in general, have one or two prominent peak amplitudes in this frequency range. Others have multiple-peaked amplitude or spiky spectra. For a more quantitative assessment of the frequency effect on the scattered energy, spectral amplitude ratios were computed for all the beams using a method similar to that discussed by Kelly (1968), and described and applied by Lambert et al. (1969), Douglas et al. (1973). In this determination, the spectral amplitudes were computed using the equation

$$R = \sum_{f_3}^{f_4} A(f_i) \Big/ \sum_{f_1}^{f_2} A(f_i) \qquad (6\text{-}1)$$

where $A(f_i)$ = value of amplitude spectrum at each 0.1 Hz interval.

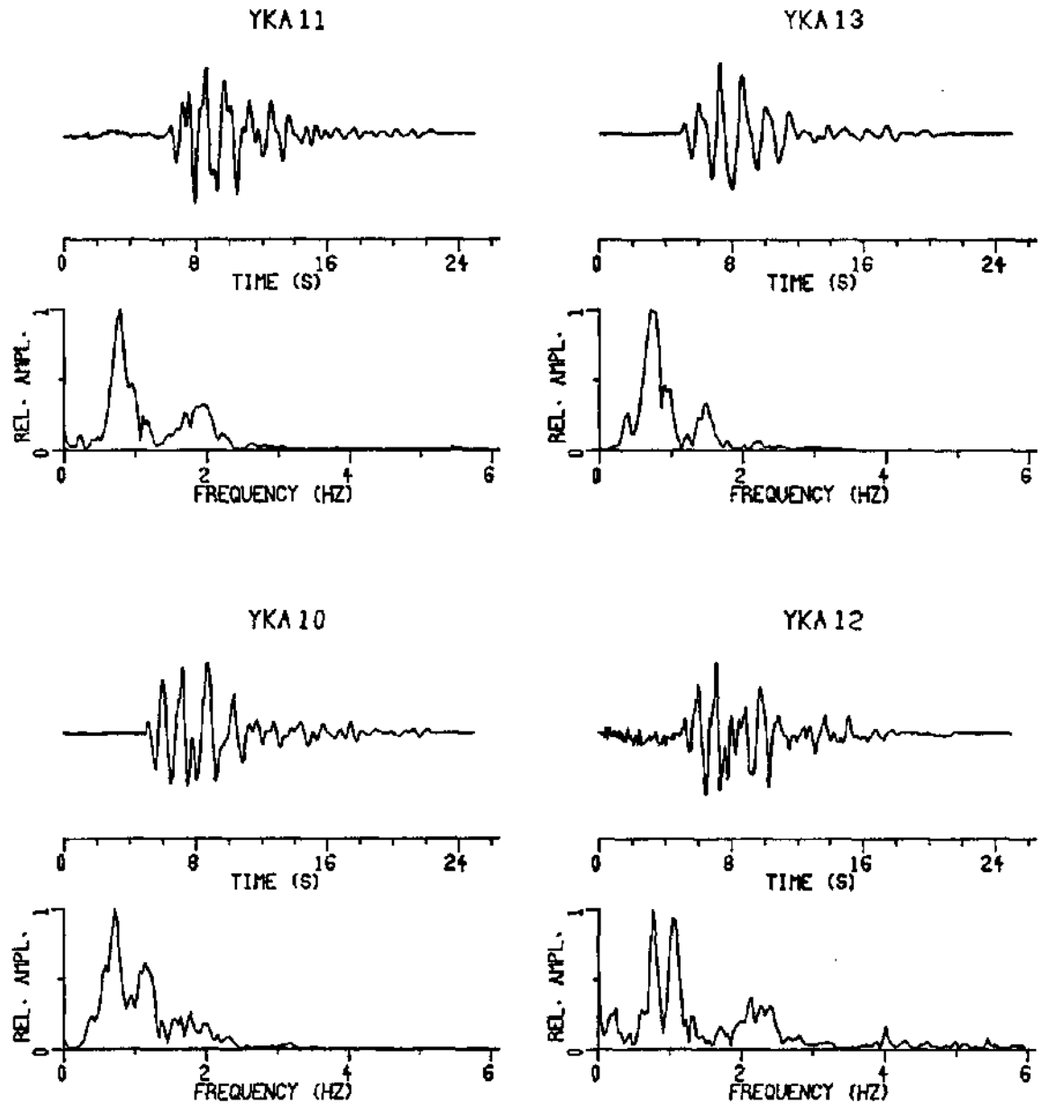


Figure 6.9: Some typical beams and their corresponding relative amplitude for NTS events recorded at YKA.

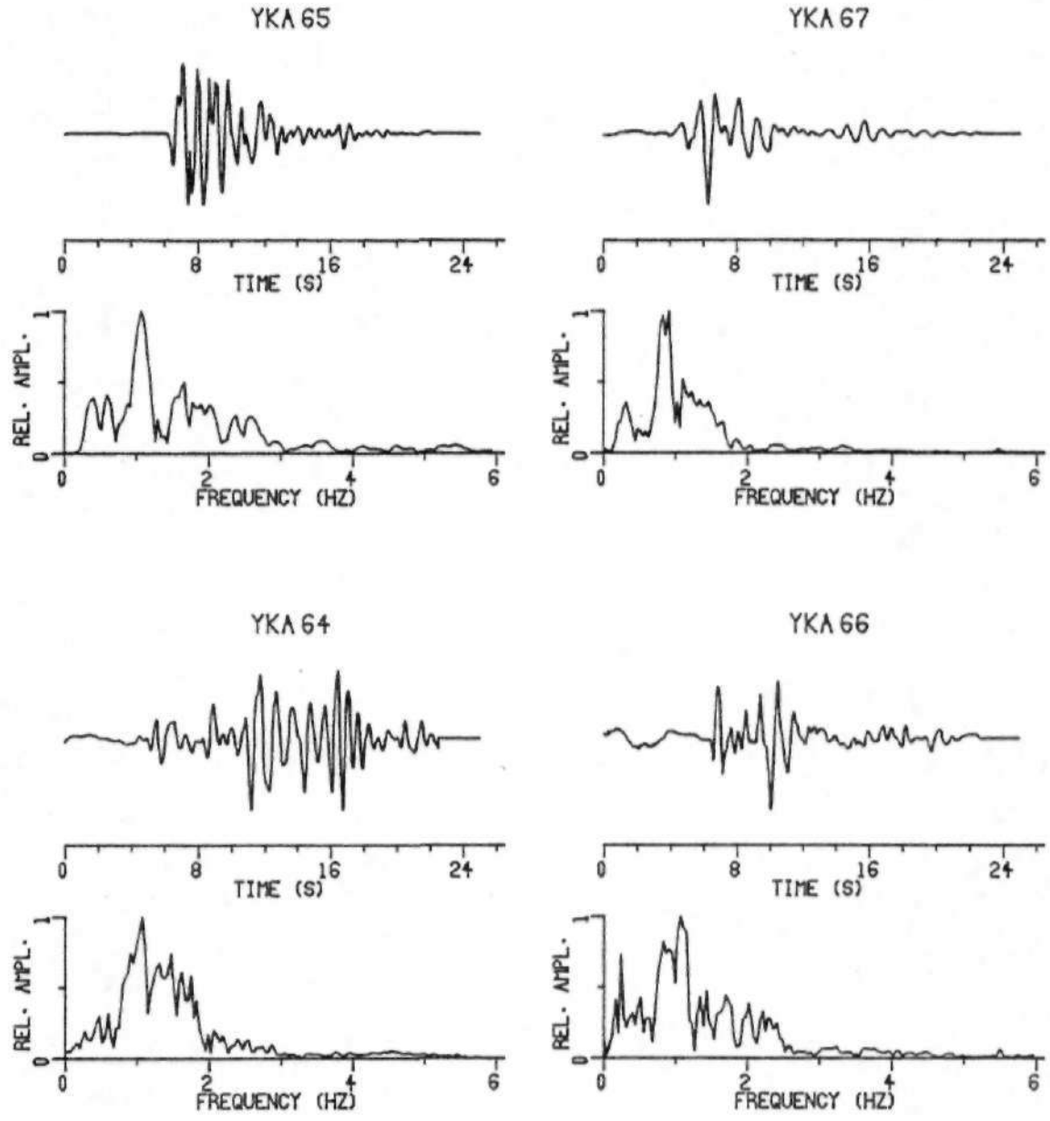


Figure 10a: Some typical beams and their corresponding relative amplitude spectra for events recorded at YKA from the Alaska region.

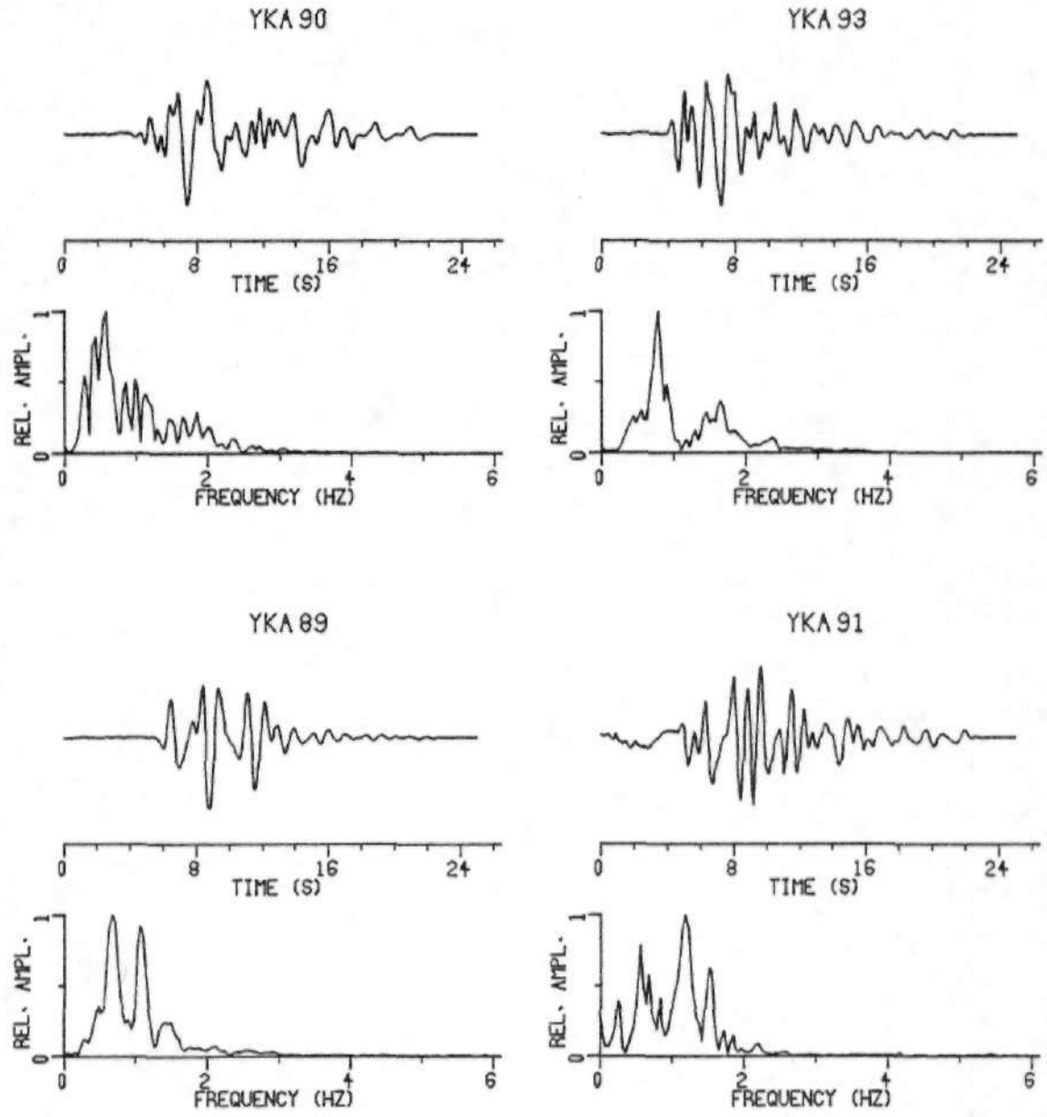


Figure 6.10b: Some typical beams and their corresponding relative amplitude spectra for spectra for events recorded at YKA from the California region.

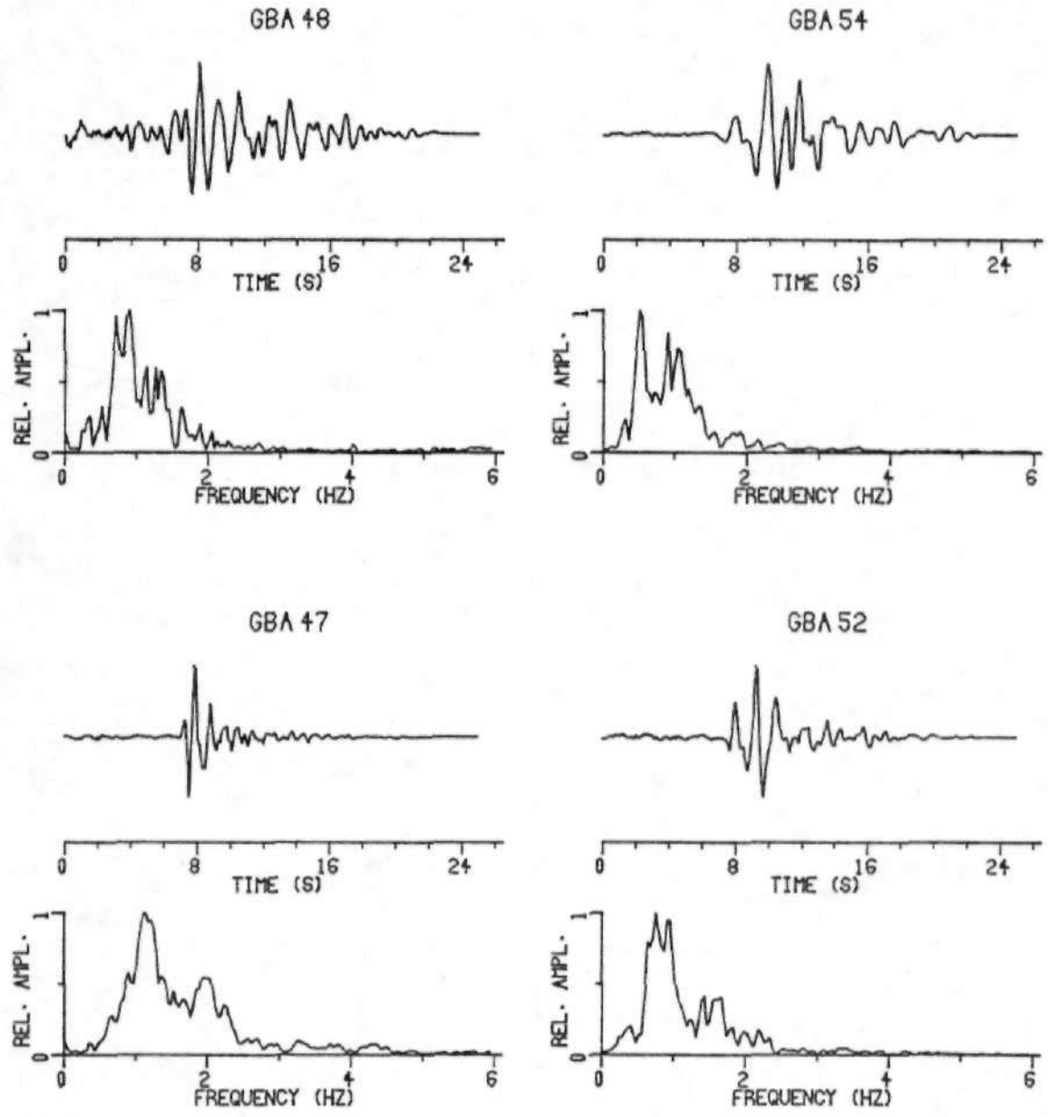


Figure 10c: Some typical beams and their corresponding relative amplitude spectra for events recorded at GBA from the Himalayan region.

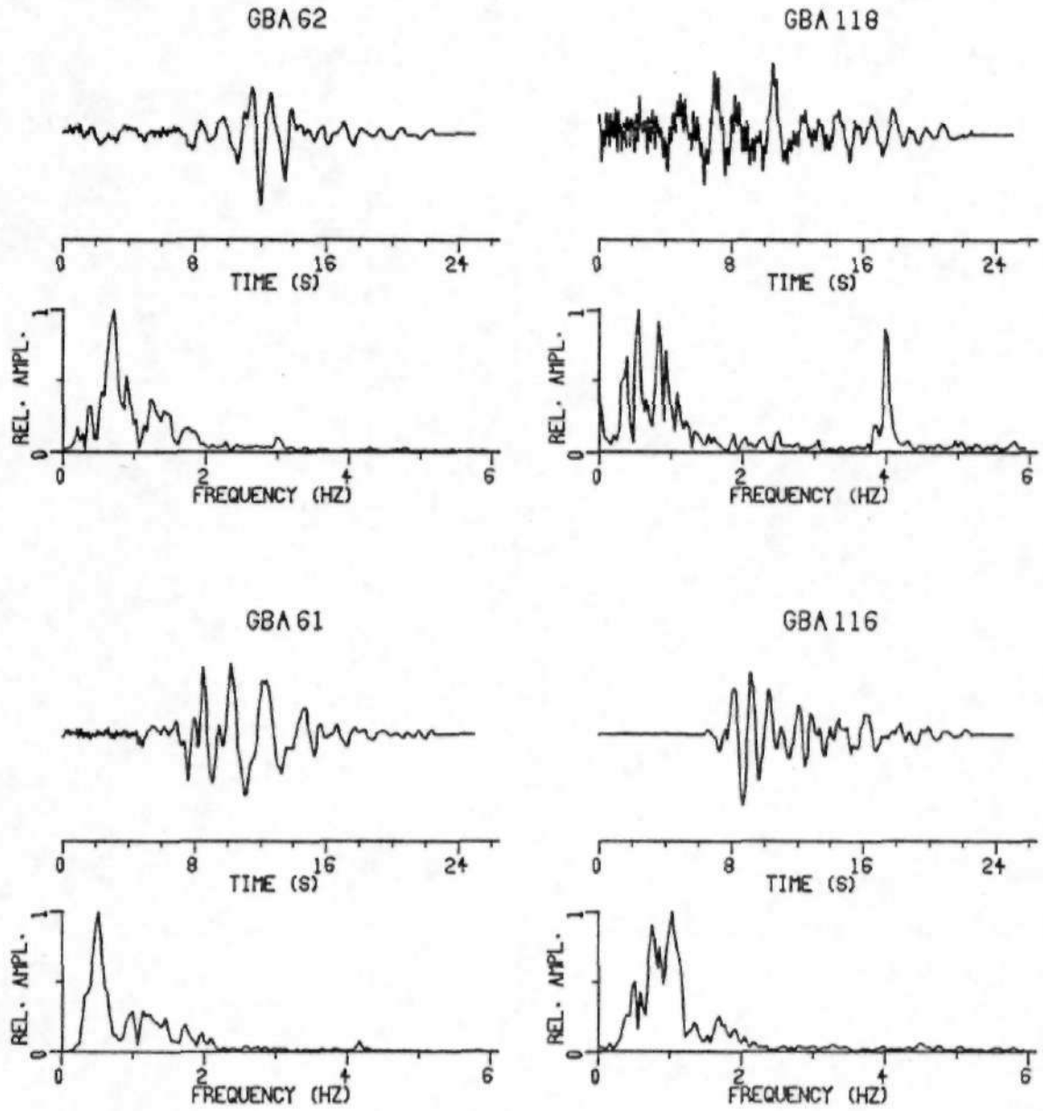


Figure 6.10d: Typical beam and relative amplitude spectra for events recorded at GBA from the Java trench.

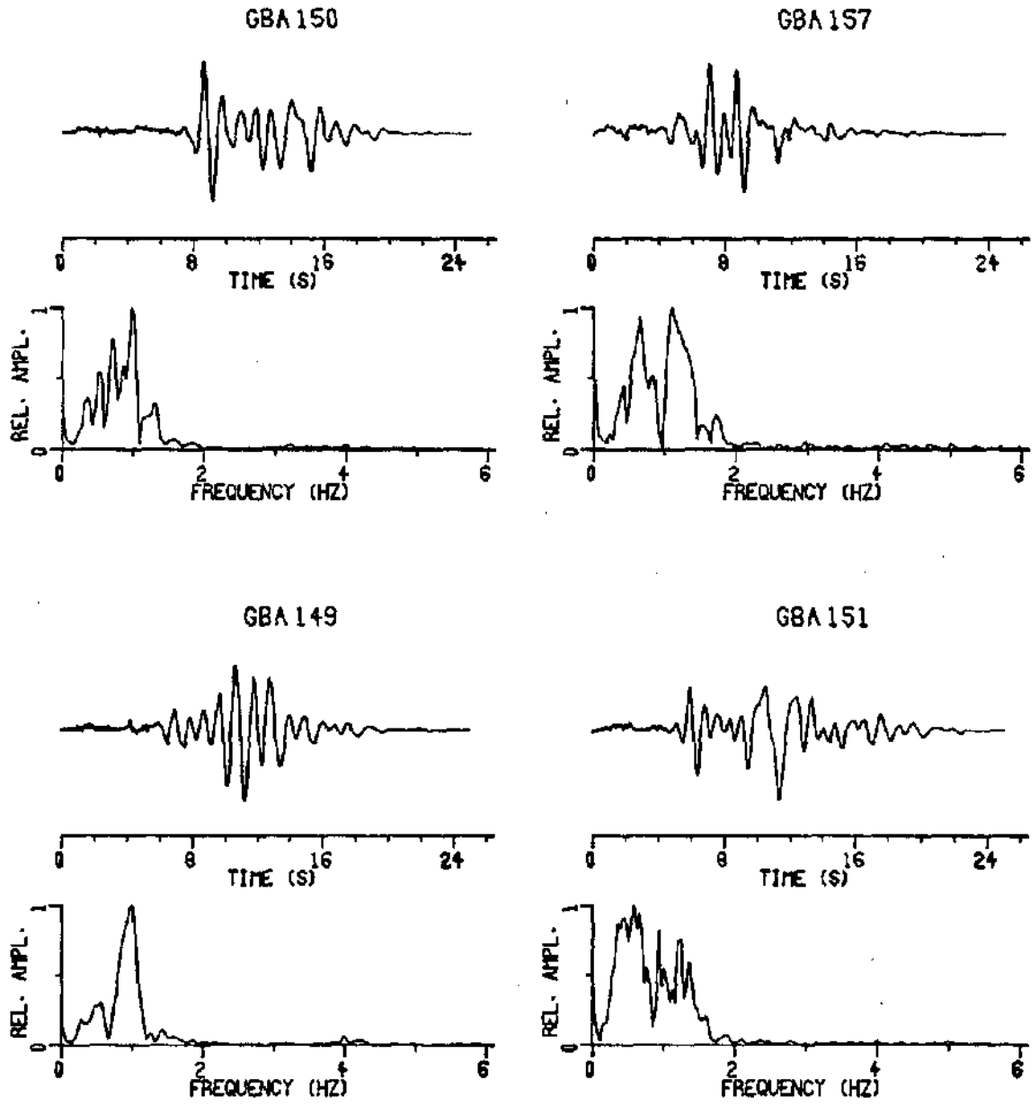


Figure 6.10e: Typical beams and relative amplitude spectra for events recorded at GBA from the Mid-Indian ocean ridge.

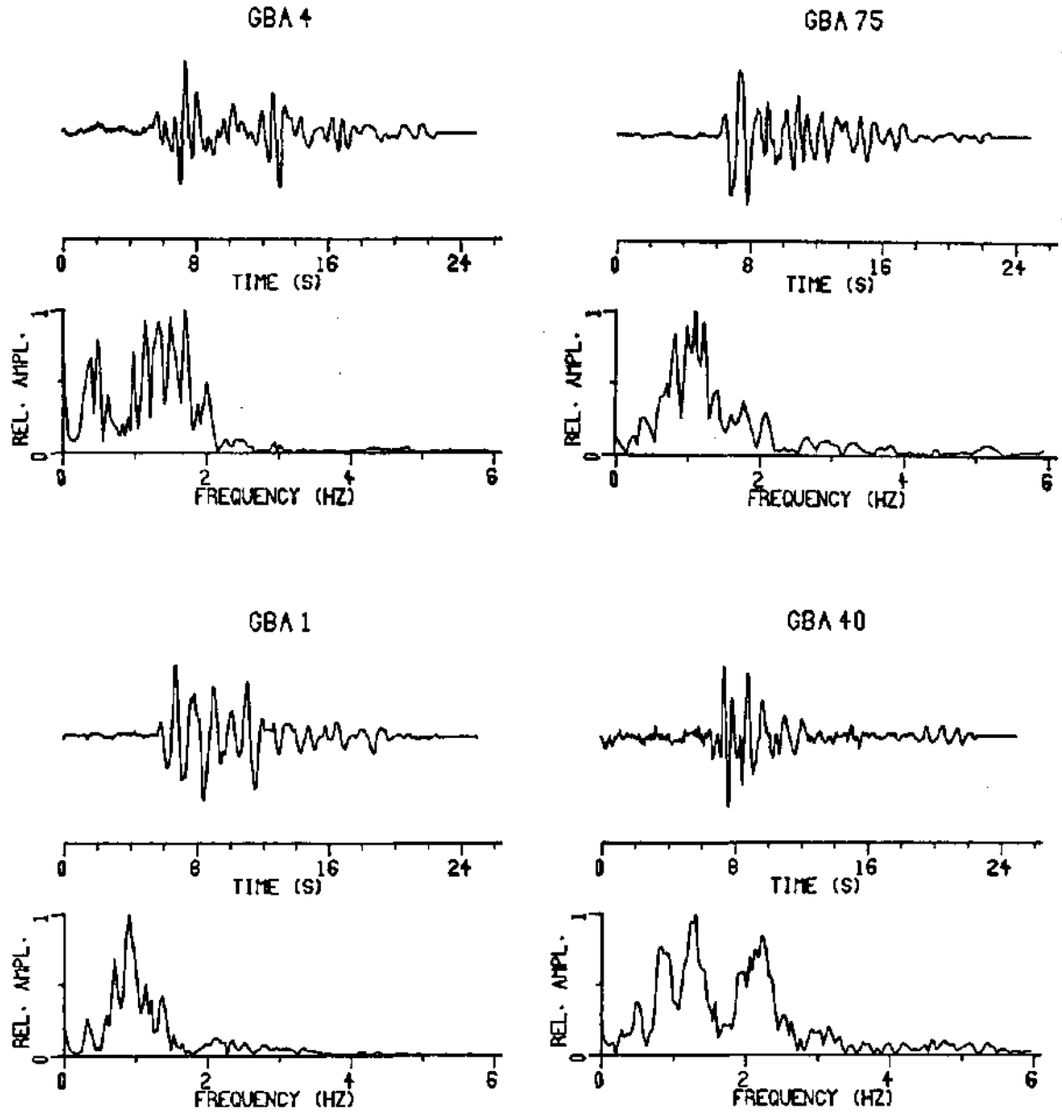


Figure 10f: Typical beams and relative amplitude spectra for events recorded at GBA from the Hindukush region.

f_1 = 0.4 Hz

f_2 = 1.65 Hz

f_3 = 1.75 Hz

f_4 = 3.0 Hz

The frequency bands used were arbitrarily chosen to be equal, and the cutoff of 3 Hz was determined by the fact that there was very little energy in the signal above this frequency as earlier indicated.

The variation of the scattered energy with spectral amplitude ratio for the 25 NTS recordings is shown in Figure 6.11 from which it will be seen that the scattered energy increases slightly as the spectral ratio increases. All the points with spectral ratios greater than 0.3 have scattered energy which are greater than the mean for all the events, while those points with spectral ratios less than 0.3 have scattered energy distributed almost evenly about the mean. The implication therefore is that some of the high scattered energy observed are, in fact, caused by the high frequency component of those signals. Correction for this bias in subsequent interpretation (Chapter 7) was achieved by inspecting the spectral ratio plots, and resctricting comparisons, if necessary, to signals with spectral ratios less than a given value determined from the plots. This procedure was found to marginally reduce the scatter in most of the observations.

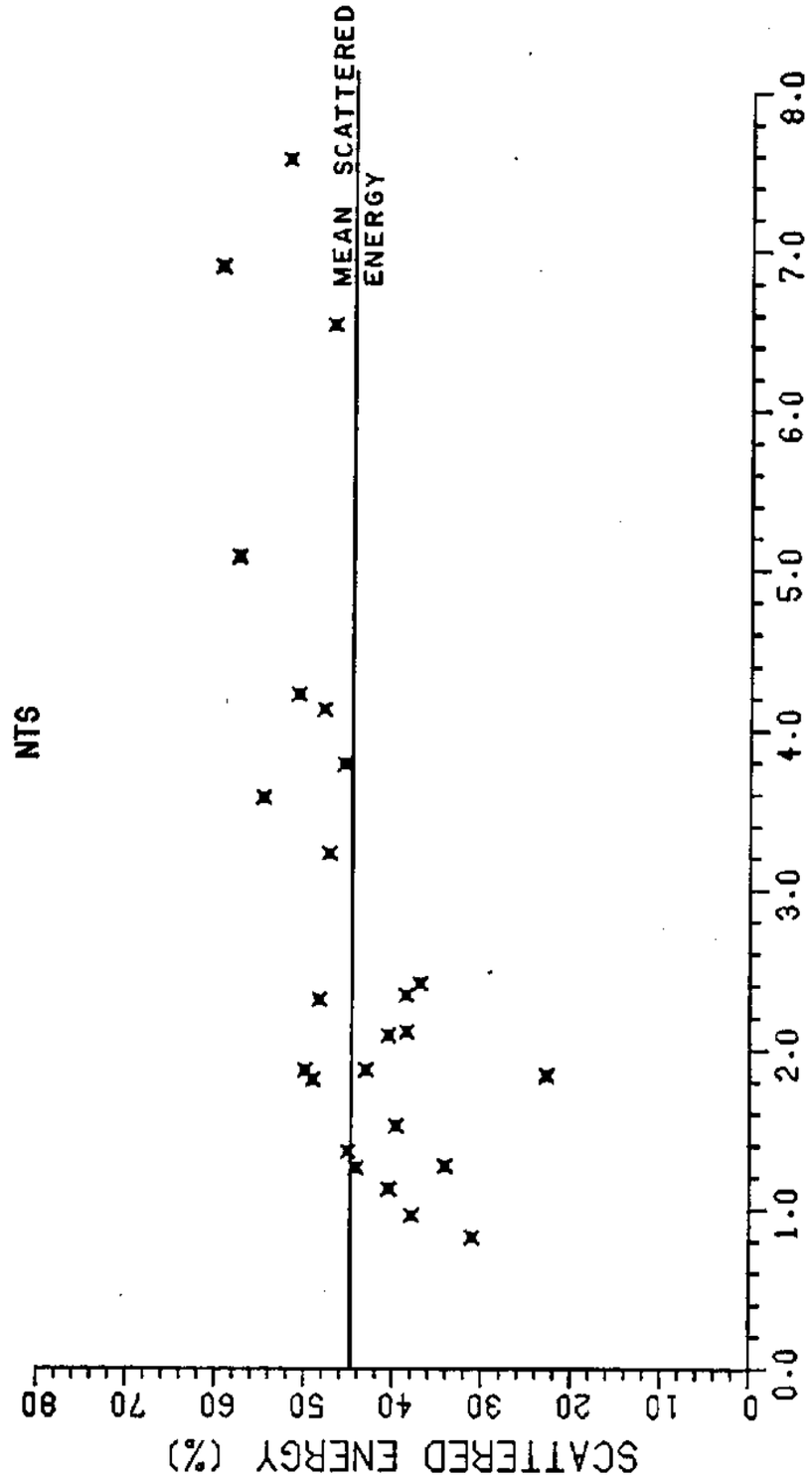


Figure 6.11: Scattered energy versus spectral ratio for the NTS events.

In Figure 6.11 the points with spectral ratios less than 0.3 still show a scatter which could not be accounted for by the frequency content of the signals. Some other explanations must therefore be sought for this. It was noted earlier on that the explosions were located very close together and far from the array. It follows then that the signal ray paths especially remote from NTS and, in particular, under the array must essentially be the same. Structure between NTS and the array, or for that matter under the array must therefore affect the signals in the same manner and cannot account for the differences in the measured scattered energy. The explanation for this difference must therefore lie in the effect of the crustal structure in the vicinity of the explosions. This possibility is probably the only logical one, and will be further explored in the following section.

6.7 EFFECTS OF FOCAL DEPTH

The NTS events which were used in the last section because of their approximately identical epicentral distances and azimuths from YKA could not be used in investigating the effects of focal depth variation because of their equally identical focal depths. Instead, 63 earthquakes from the Hindukush focal region (see Figure 6.1) with very similar epicentral distances and azimuths from GBA but focal depths varying from 11 km to 236 km were selected from a large number of events which were later investigated

from that region. Like the NTS events, the similar epicentral distances and azimuths should reduce to a minimum the azimuthal and epicentral bias in the data.

Figure 6.12 shows the variation of scattered energy as a function of the focal depth of the events. It will be noted that, as with frequency, the scattered energy increases gradually with increasing focal depth for the depth range investigated. In fact, the trend is so similar to that observed in Figure 6.11 that the inclination is to conclude that the deeper events must propagate signals with a higher spectral ratio than the shallower events. This impression is, however, not borne out by Figure 6.13 which shows the variation of spectral ratio with focal depth for the same events. As the figure shows, there is no definite relationship between the focal depth of the events and the spectral ratio of the signals.

Figure 6.14 shows that except for events with focal depths less than 65 km, the first arrival slownesses for all but a few of the other signals have values which lie close to 9.4 sec/degree. This fact suggests that the signal ray paths for most of the events with focal depths greater than 65 km have very similar bottoming depths, and should therefore approach the array along approximately identical paths. The increased scattered energy with focal depth cannot therefore be accounted for by structure under the array, and must be explained by a significant disturbance of the source region with depth.

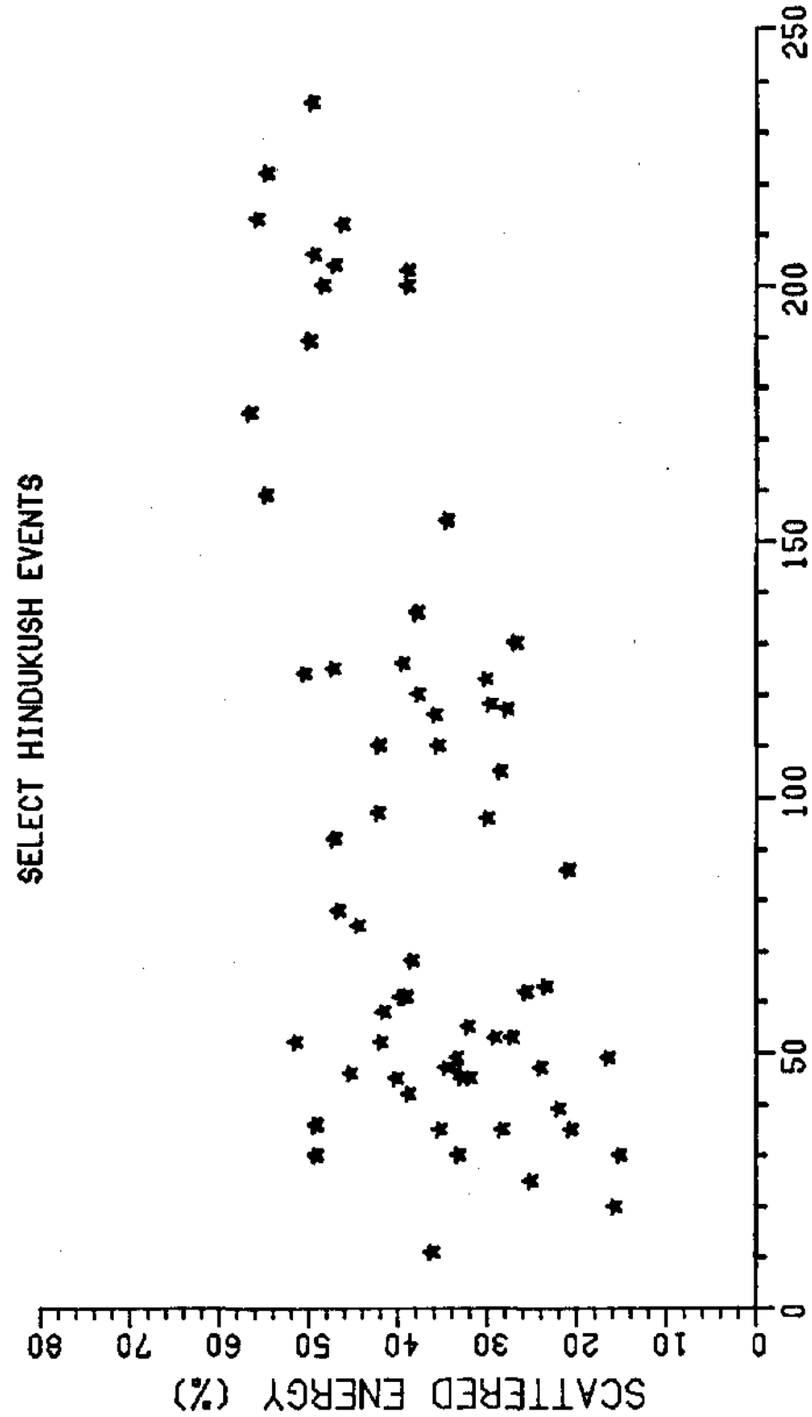


Figure 6.12: Scattered energy versus focal depth for select Hindukush events.

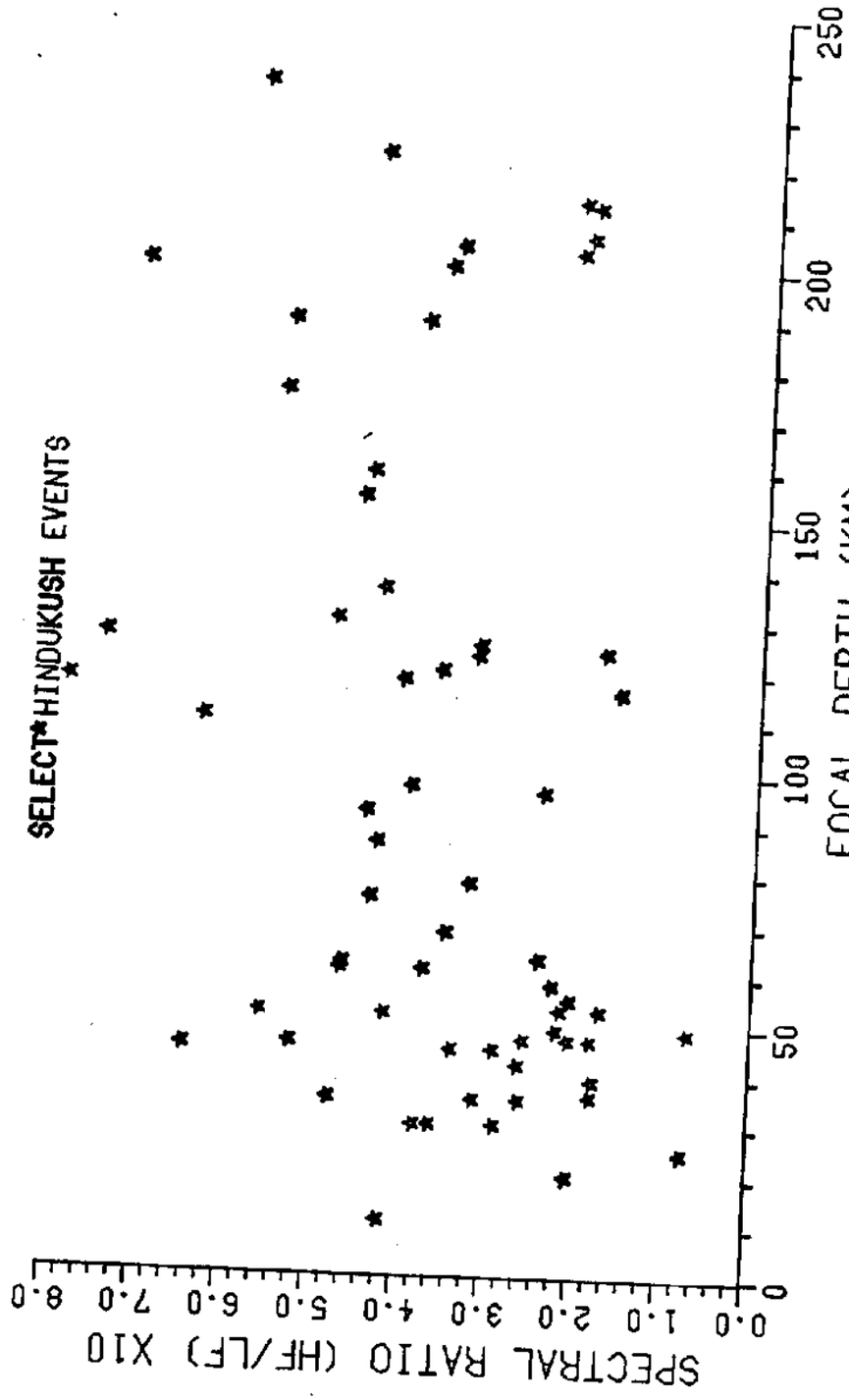


Figure 6.13: Spectral ratio versus focal depth for select Hindukush events.

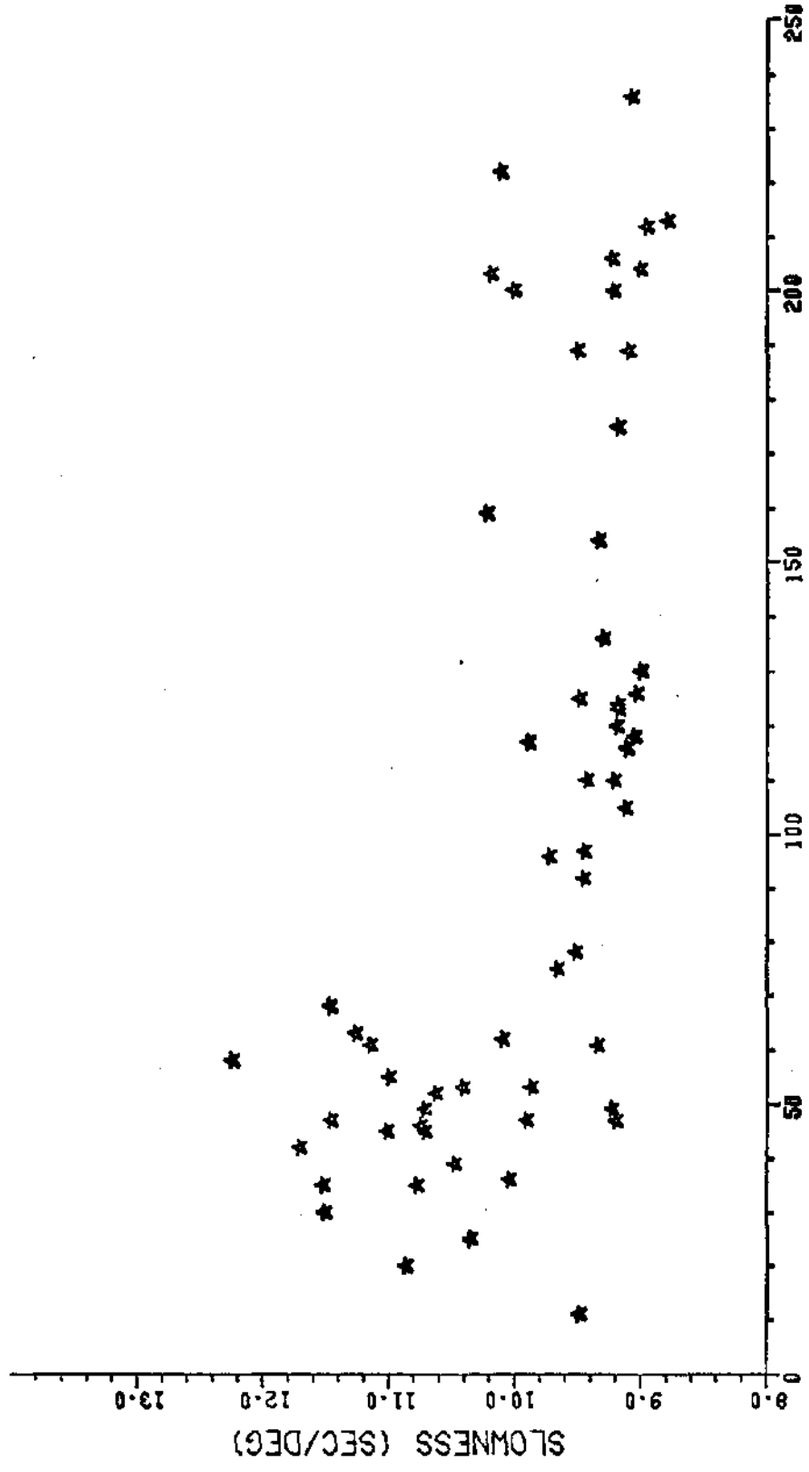


Figure 6.14: Observed slowness versus focal depth for select Hindukush events. The slowness values were taken from the study of Ram and Mereu (1977)

The large scatter in first arrival slownesses of signals with focal depth less than 65km suggests that considerable multiplicity in ray paths of signals occurs for shallow focus events. This also probably explains the large scatter which was evident in Figure 6.12 for shallow focus events, and also for the large scatter evident in Figure 6.11 for the surface focus NTS events. The effect of local crustal structure near the source would then always be to increase the scatter in the data. This may be reduced by selecting events with moderately deep focus, which was not possible in this study because shallow focus events were in the majority, and their exclusion would result in a paucity of data which was undesirable.

6.8 SUMMARY

In the preceding discussions, some clear patterns emerged which indicate that certain considerations must be given to the results before a meaningful interpretation could be achieved. Of these problems, the frequency bias in the measurements was found to be straightforward to deal with because its effect could easily be identified and corrected for. On the other hand, it was found that the effect of structure in the source region could not be easily removed, and could only be minimized by a careful selection of events with intermediate or deep focus. Since that was not possible in this study, a larger scatter in the data than is considered ideal will be observed in some of the

results that will be presented in Chapter 7. However, as will be seen later, this did not preclude the identification of trends which were either sufficiently consistent in pattern, or at variance for different regions to permit some definite conclusions about the relative scattering properties of these regions.

CHAPTER 7

INTERPRETATION OF DATA FROM GBA AND YKA

7.1 INTRODUCTION

After discarding the excessively noisy records and those for which adaptive processed solutions did not converge because of poor signal quality, over 300 earthquake recordings from GBA and over 40 recordings from YKA were available for analysis. The distance range covered by these events was approximately 15-36 degrees for GBA, and 12-30 degrees for YKA; the corresponding azimuth range were 0-360 and 165-285 degrees respectively (see Figures 6.1 and 6.2). Also included in the GBA events were 46 recordings for earthquakes in the distance range 40-67 degrees from the Celebes, Philippines, Mariana and Japan-Kurile Island regions. This latter set of events afforded us some comparisons of the responses of lower mantle structure with those of the upper mantle for the region under investigation.

The total distance range of 12-36 degrees that was covered by the former set of events suggests that the bottoming depths for ray paths from these regions have an approximate range of 100-850 km. The results and interpretation to be described here therefore apply, for the

most part, to the upper mantle structure between the source region and the array from the uppermost mantle down to depths of about 850 km. This depth range was further extended to about 1750 km in the lower mantle for the regions to the north-east and south-east of GBA by the several events beyond 40 degrees.

The events were divided into groups based on their regional distribution since to treat them as one single set of data would be to ignore the effect of lateral variations which, without doubt, exist over such a wide region. Besides, as indicated earlier (Chapter 6), it was desirable to confine observations to narrow azimuth ranges in order to minimize the effects of local structure near the array. For GBA, events in a moderately narrow azimuth range were available in the Java trench region (115 ± 15 degrees). However, in order to achieve a uniform distribution of events in the other azimuths, a wider range had to be chosen for the Himalayan region (0-90 degrees), the Mid-Indian ocean ridge (180-280 degrees), and the Hindukush region (280-360 degrees). For YKA (Figure 6.2), the events from the Alaska Peninsula also provided a narrow azimuth range (275 ± 10 degrees), and the events from California region consisted of those in the azimuth range 165-265 degrees.

7.2 RESULTS - GBA

The important diagnostic parameter of interest was the scattered energy of the array signals which has been defined

and discussed in Chapters 5 and 6. Figure 7.1 shows how the scattered energy for all the GBA events in the distance range 15-38 degrees vary with the azimuthal distribution of the events. A careful examination of the figure shows that the scattered energies for events in the Mid-Indian ocean ridge (azimuth = 180-280 degrees) are out of character with those for the other regions since, for the most part, they are consistently low and less than 20% while the others are in general greater than 20%. Since the range of distances covered by the events was a common factor for all the azimuth range, it was suggested in our preliminary interpretation (Ojo and Mereu, 1980) that the low scattered energy for ray paths from the Mid-Indian ocean might be evidence for differences in oceanic and continental upper mantle structure.

The fact that results for azimuths between 90 and 130 degrees, which also represent oceanic upper mantle paths, show relatively higher scattered energy can be explained by inhomogeneities caused by descending slabs of the subducting plate margin in the Java trench. As Figure 6.1 shows, part of the surface manifestation of the subduction zone (i.e. the epicentres of the earthquakes in the Java trench region) has a bearing which is almost in line with GBA. The region where the ray paths from events at the farther end of this distance range bottom would therefore be expected to be under structures close to the subduction zone, and parts of the ray paths would in fact pass through the subduction

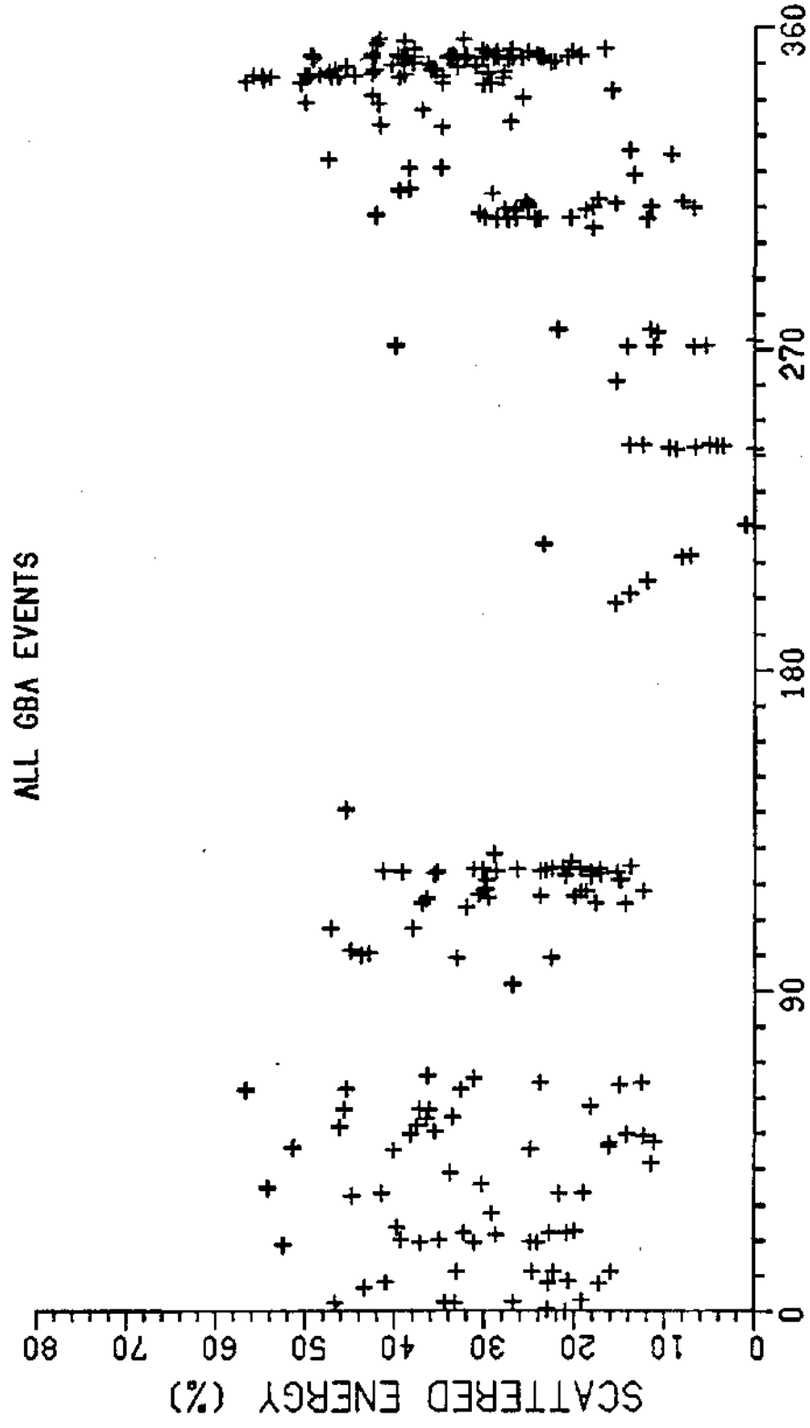


Figure 7.1: Observed scattered energy as a function of the azimuthal distribution of events

zone.

Figure 7.2 shows how the spectral ratio varies with the azimuthal distribution of the events. It will be clearly observed that a striking similarity exists between Figure 7.1 and Figure 7.2 which suggests that the apparently low scattered energies in the azimuth range 180-280 degrees might be due to the relatively large, low-frequency component in the signals from the Mid-Indian ocean ridge events. This fact again emphasizes the point that adequate consideration must be given to the frequency factor before any interpretation can be meaningful.

7.2.1 THE HIMALAYAN REGION

The set of events from the Himalayan region which describe the region to the north-east of GBA is shown in Figures 7.3 and 7.4. An examination of Figure 7.3 shows that for this set of data, the scattered energy does not increase with spectral ratio. However, it does appear that there is a low-frequency bias for those signals with spectral ratios less than 0.1, but since the problem affects only a few events, it was considered justifiable to neglect the frequency effect on this set of data.

Figure 7.4 shows how the scattered energy varies with the epicentral distance of the events. At the relatively shorter epicentral distances between 15 and 21 degrees, the scattered energies are predominantly high and greater than 30%, rising to over 50% near 15 degrees. Between 21 and 25

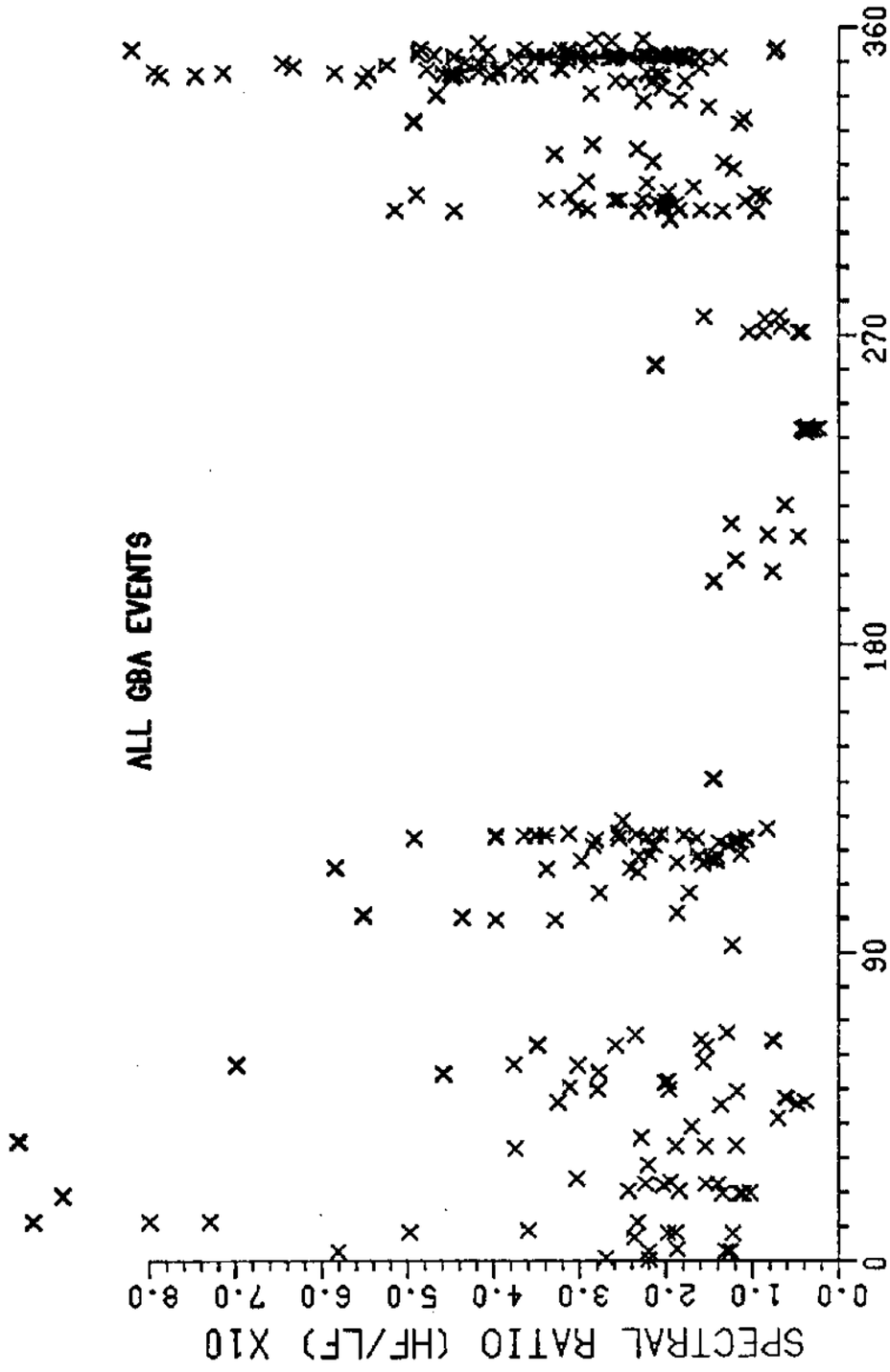


Figure 7.2: Signal spectral ratio versus azimuth of events.

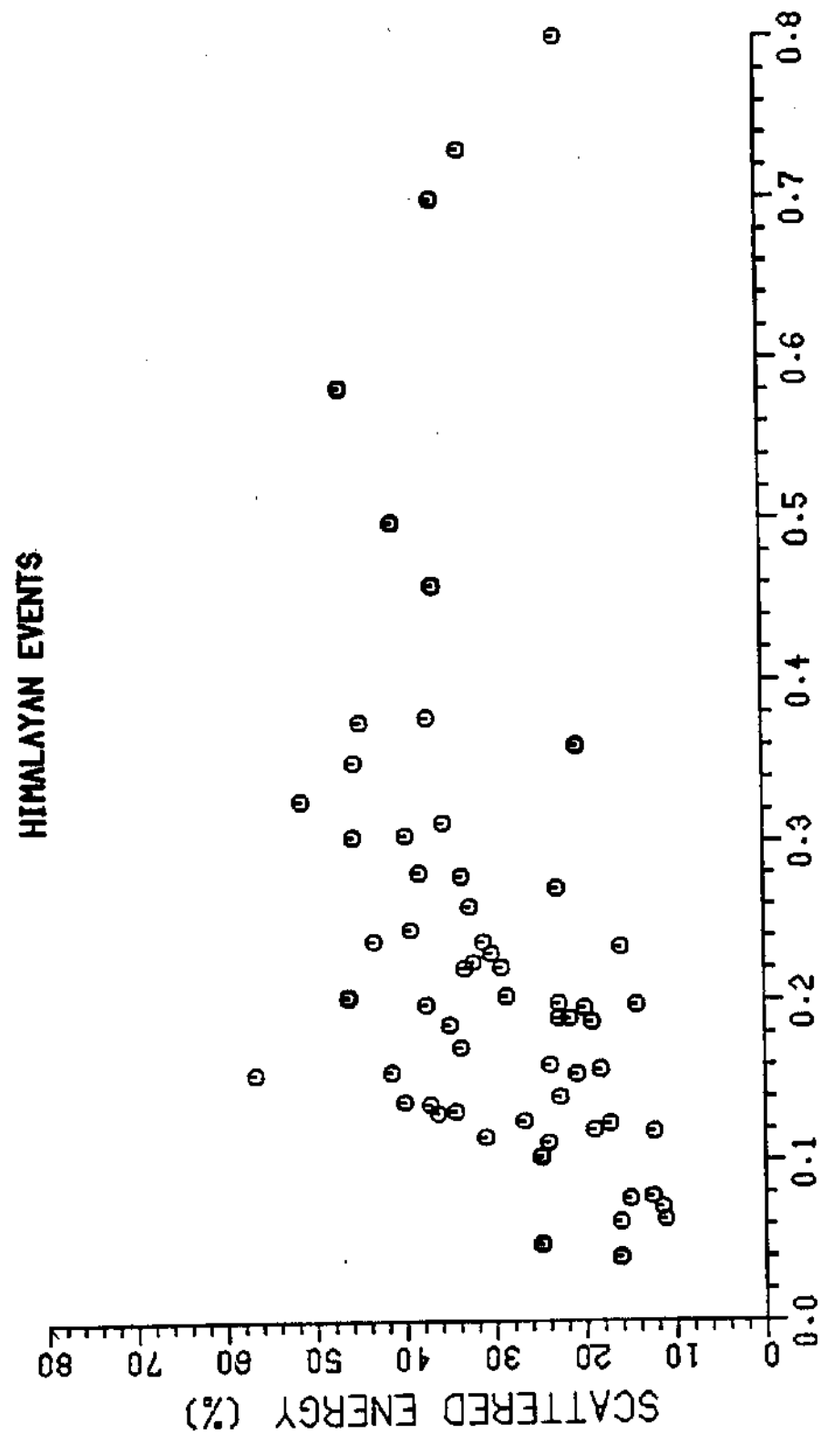


Figure 7.3: Observed scattered energy versus signal spectral ratio.

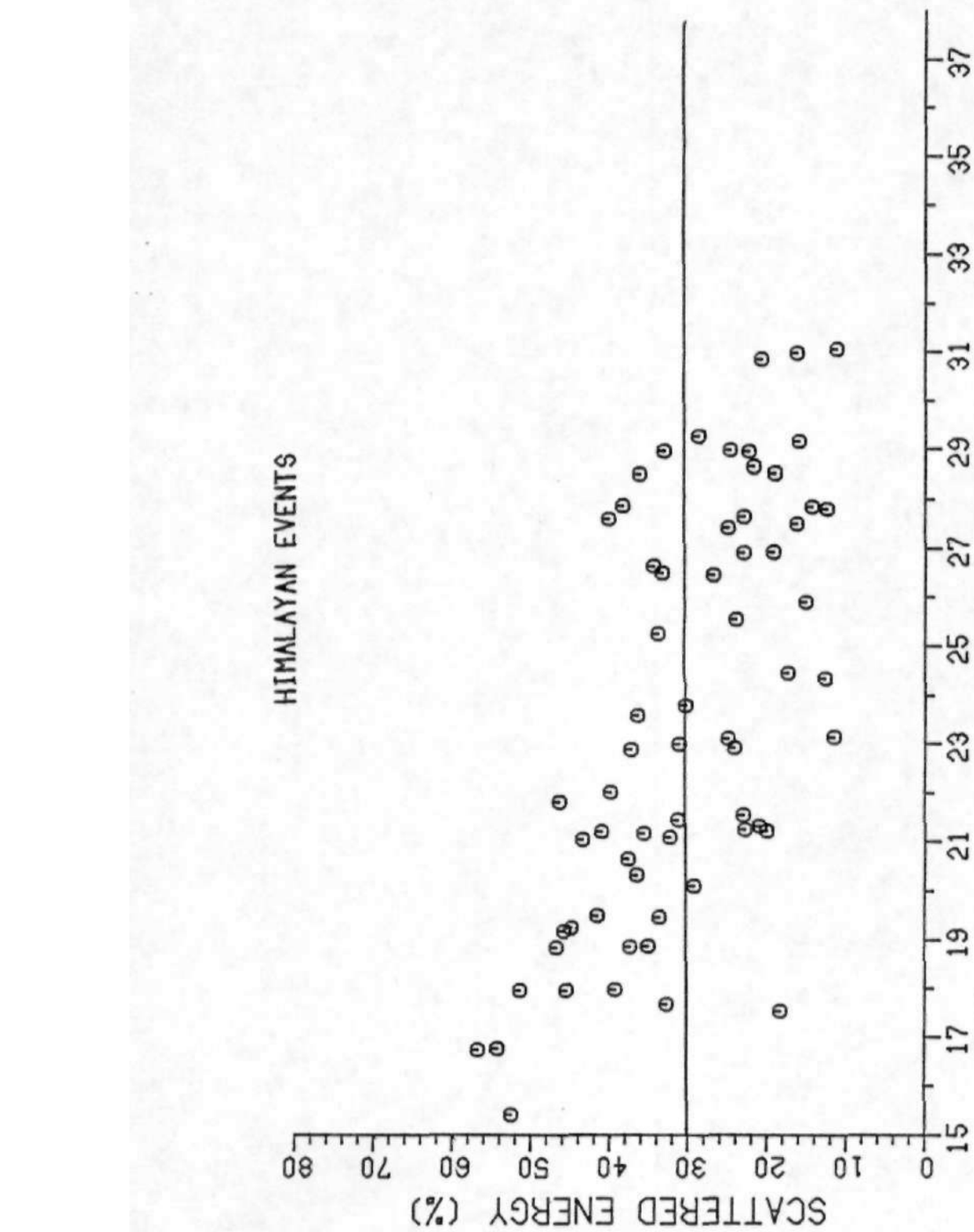


Figure 7.4: Observed scattered energy as a function of the epicentral distance of the events. The line parallel to the distance axis is used to emphasize the observed trend.

degrees the points are evenly dispersed about a scattered energy of about 30%, and beyond 25 degrees they are predominantly lower than 30%, averaging near 24%. This trend, which has been emphasized in Figure 7.4 by drawing a line parallel to the distance axis at the 30% mark, is clearly evident in spite of a scatter of the data points. This scatter which, as stated earlier, could not be accounted for by errors in the computational procedure is caused by many factors which include errors in epicentre determinations, complexity of structure along the ray paths, differences in focal depth of events, the local crustal structure in the source region and beneath the array, and the effect of lateral variation in source-receiver paths caused by the slightly large azimuth range used.

From the trend shown in Figure 7.4, it is inferred that vertical variation exists in the heterogeneity of upper mantle structure between GBA and the Himalayas to the north-east. It would also appear that considerably more heterogeneity exists for the uppermost mantle, and upper mantle structure above a depth of 400 km than for the structure below this depth.

7.2.2 THE JAVA TRENCH

The events from the Java trench describe the region to the south-east of GBA, and are presented in Figure 7.5 which shows that the frequency effect is again negligible. Figure 7.6 shows how the scattered energy varies with the

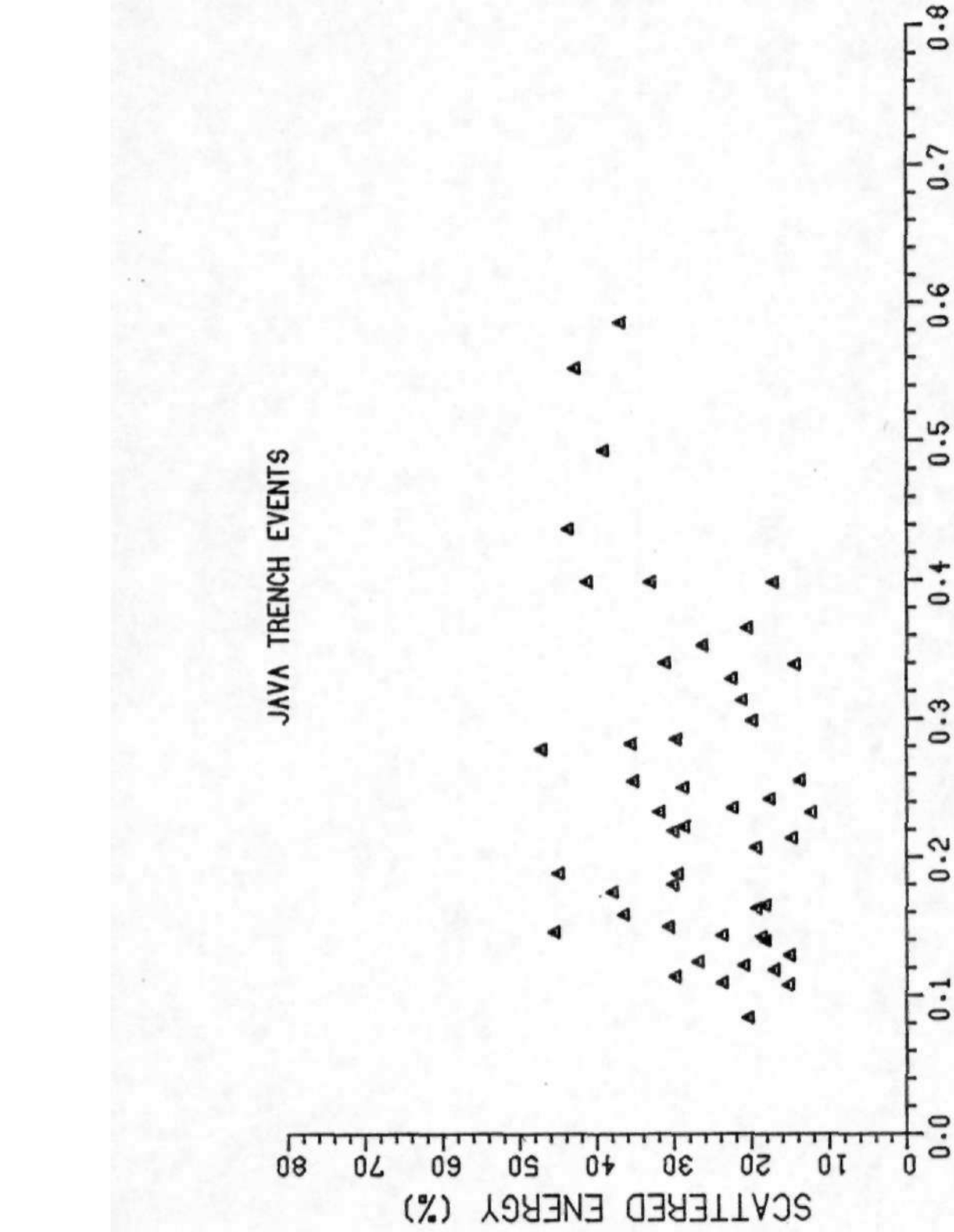


Figure 7.5: Observed scattered energy versus signal spectral ratio.

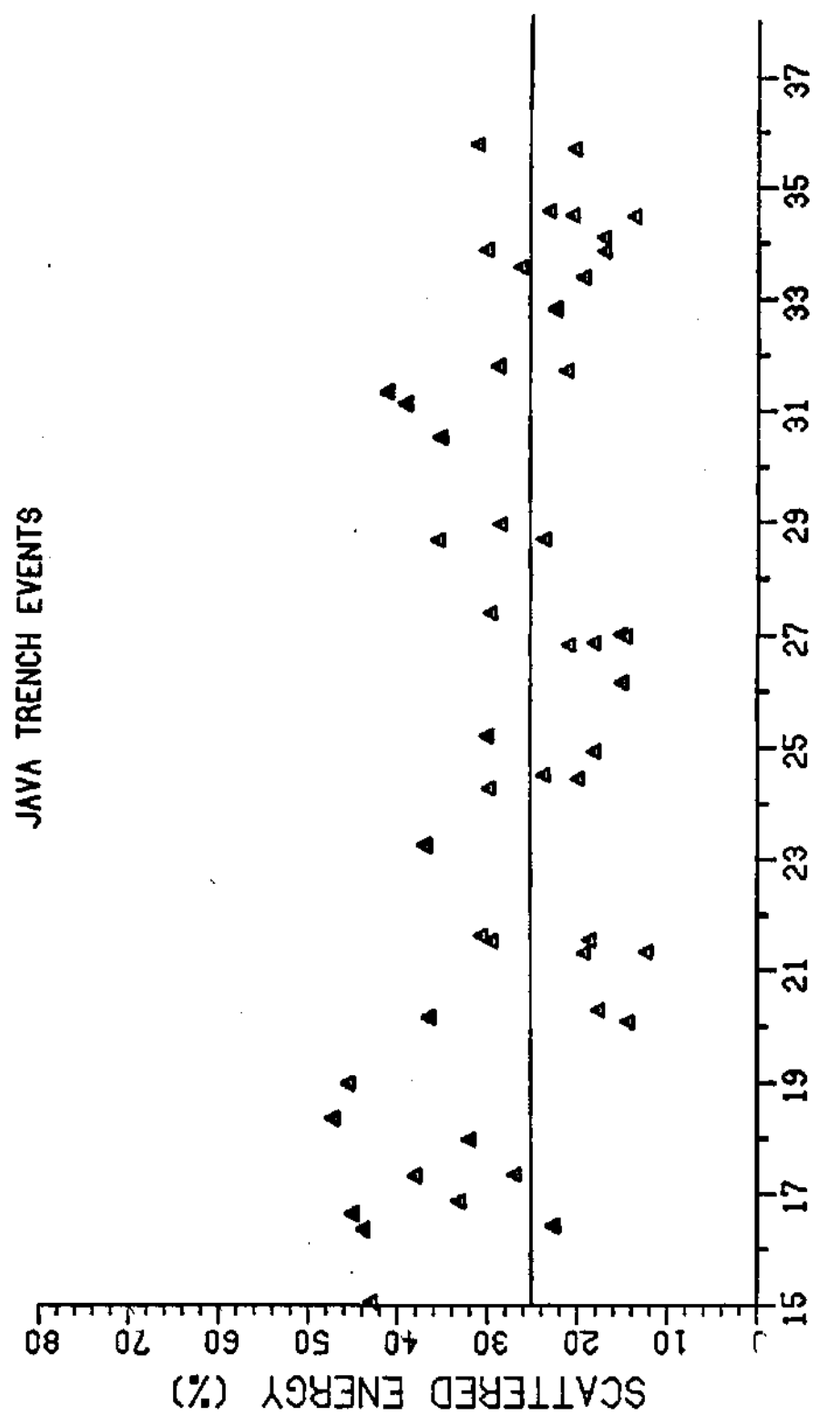


Figure 7.6: Observed scattered energy as a function of the epicentral distance of the events. The line parallel to the distance axis emphasizes the observed trend.

epicentral distance of the events. At the relatively shorter distances between 15 and 20 degrees, the points indicate scattered energies which are predominantly greater than 25%, but beyond 20 degrees, the scattered energies oscillate about the 25% level. The scatter of the data is only marginally less than that for the Himalayan region and, using the 25% scattered energy level as reference, we note that except for the slight increase of the general level of the scattered energy between the distance of 15 and 20 degrees, there appears to be a relatively uniform average response for all the distances shown. It would therefore appear that, in contrast to the Himalayan region, the complexity of upper mantle structure between GBA and the Java trench shows little variation with depth except in the uppermost mantle where the effect of the subducting plate margin may be significant.

7.2.3 THE MID-INDIAN OCEAN RIDGE

The results for events from the Mid-Indian ocean ridge are presented in Figures 7.7 and 7.8. It is immediately clear that the events described by Figure 7.7, in general, contain a lower high-frequency component than those described in Figures 7.3 and 7.5. We suspect that this could be a manifestation of the differences in focal mechanisms of the mid-ocean ridge events which are associated with transform faulting as opposed to the events in the other regions which are generally associated with zones of plate convergence and subduction. More probable is

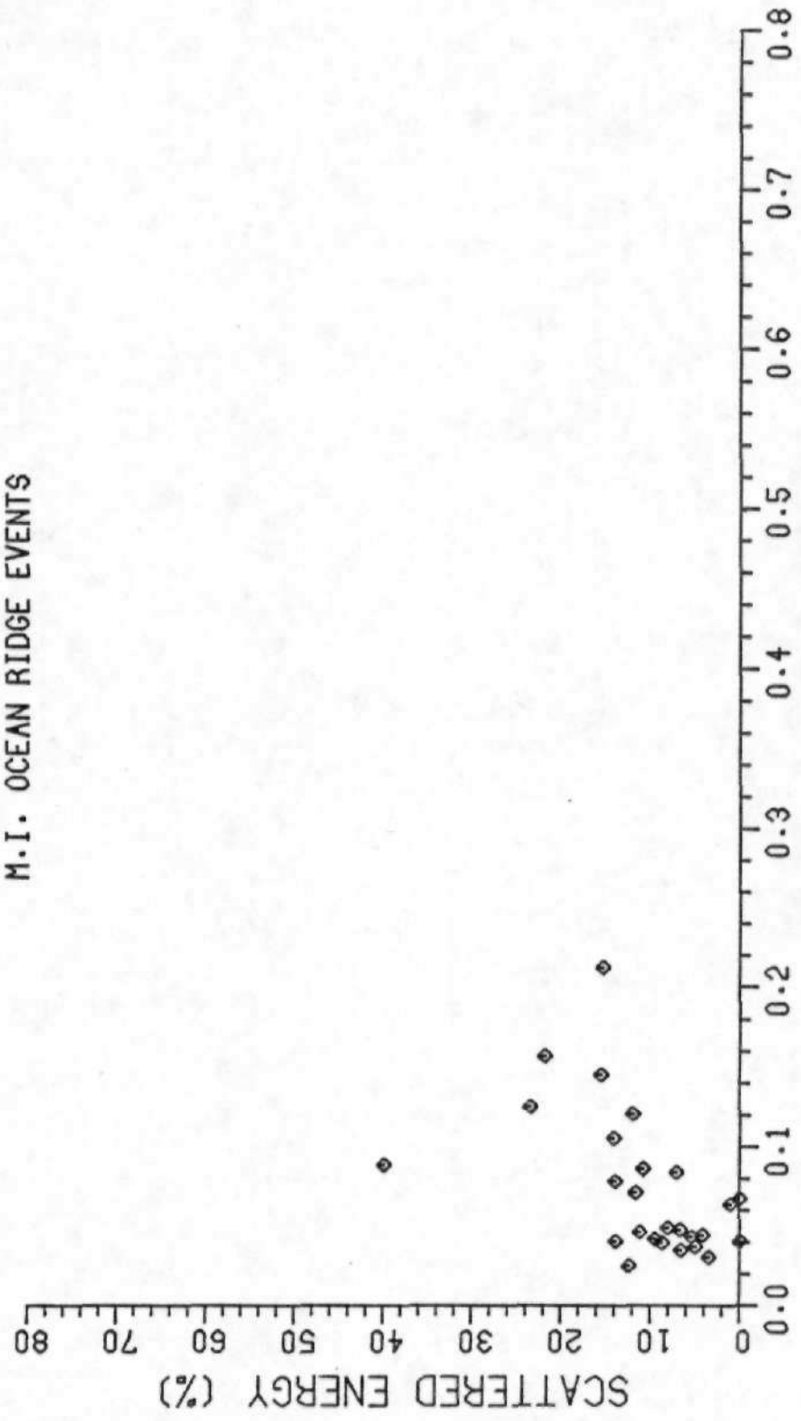


Figure 7.7: Observed scattered energy versus signal spectral ratio.

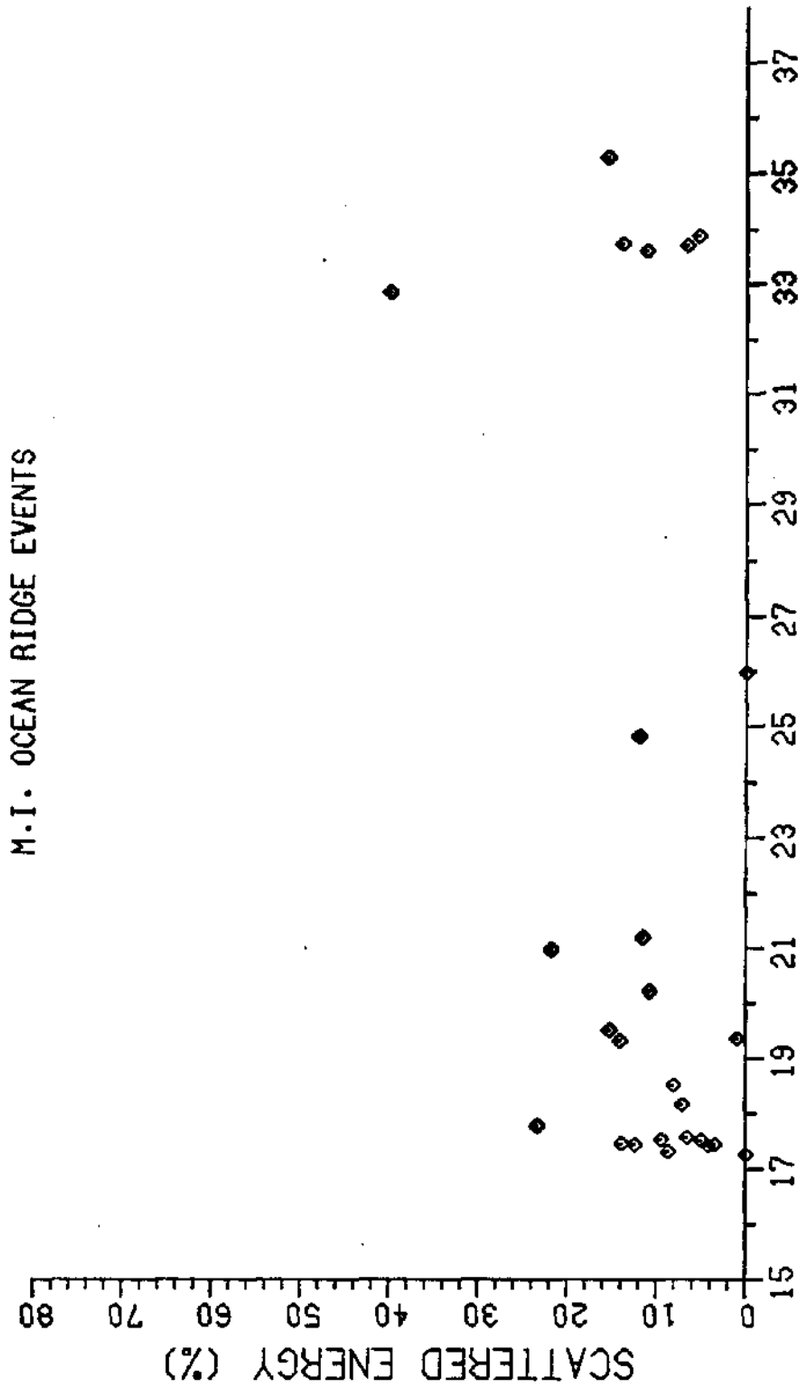


Figure 7.8: Observed scattered energy versus epicentral distance of events.

an explanation to be found in an oceanic upper mantle with a Q value which causes differential attenuation of the high-frequency component relative to the lower frequencies. This latter explanation is in agreement with the results of Ram and Mereu (1977) who found that inversion of slowness data revealed that there was evidence for a larger low-Q layer along the oceanic paths as compared to the continental paths.

In view of the low-frequency bias of this set of events, comparisons of the results for the Mid-Indian ocean region with those of the other regions are made with some caution. However, comparisons for different ray paths within this region are still very valid since there is an internal consistency in the set of data.

Figure 7.8 shows that the scattered energies, which are predominantly very low in value, are not dependent on epicentral distance up to the 35 degrees covered by these events. There is a gap between 27 and 33 degrees for which no data was available, and the general paucity of data for this region is a reflection of the relatively low seismicity of the ridge compared to the convergence zones. In spite of this however, there is sufficient consistency in the available data from which it would appear that there is little vertical variation in the heterogeneity of the upper mantle structure between GBA and the Mid-Indian ocean ridge. In addition, it would also appear from the low scattered energies that this region is more homogeneous than the

Himalayan, the Java trench, or the Hindukush region to be described in the next section.

7.2.4 THE HINDUKUSH REGION

This is a region in which it would appear that considerable complexity exists. In a study of some selected events from this region (Chapter 6), it was found that this source region indicated the presence of increased inhomogeneities with depth. Allusion was also made to the fact that more scatter was observed in the data. Figures 7.9 and 7.10 show the complete set of data for the region.

In Figure 7.9, one notes that for spectral ratios less than 0.4 the points are almost uniformly distributed between scattered energy values of 7% and 57%, while for spectral ratios greater than 0.4 the points represent, for the most part, scattered energies greater than 30%. A frequency bias therefore exists for this set of data. Figure 7.10 shows how the scattered energy varies as a function of epicentral distance for the same events, from which it will be noted that a trend which is unlike that shown in Figure 7.4 for the Himalayan region is indicated; i.e. there is a gradual migration of points from high scattered energy at the relatively shorter distances to low scattered energy for the more distant events. The large scatter which is prominent around 23 degrees distance is caused by the select Hindukush events which were shown in Chapter 6 to indicate very strong focal depth effects. In order to remove both the focal

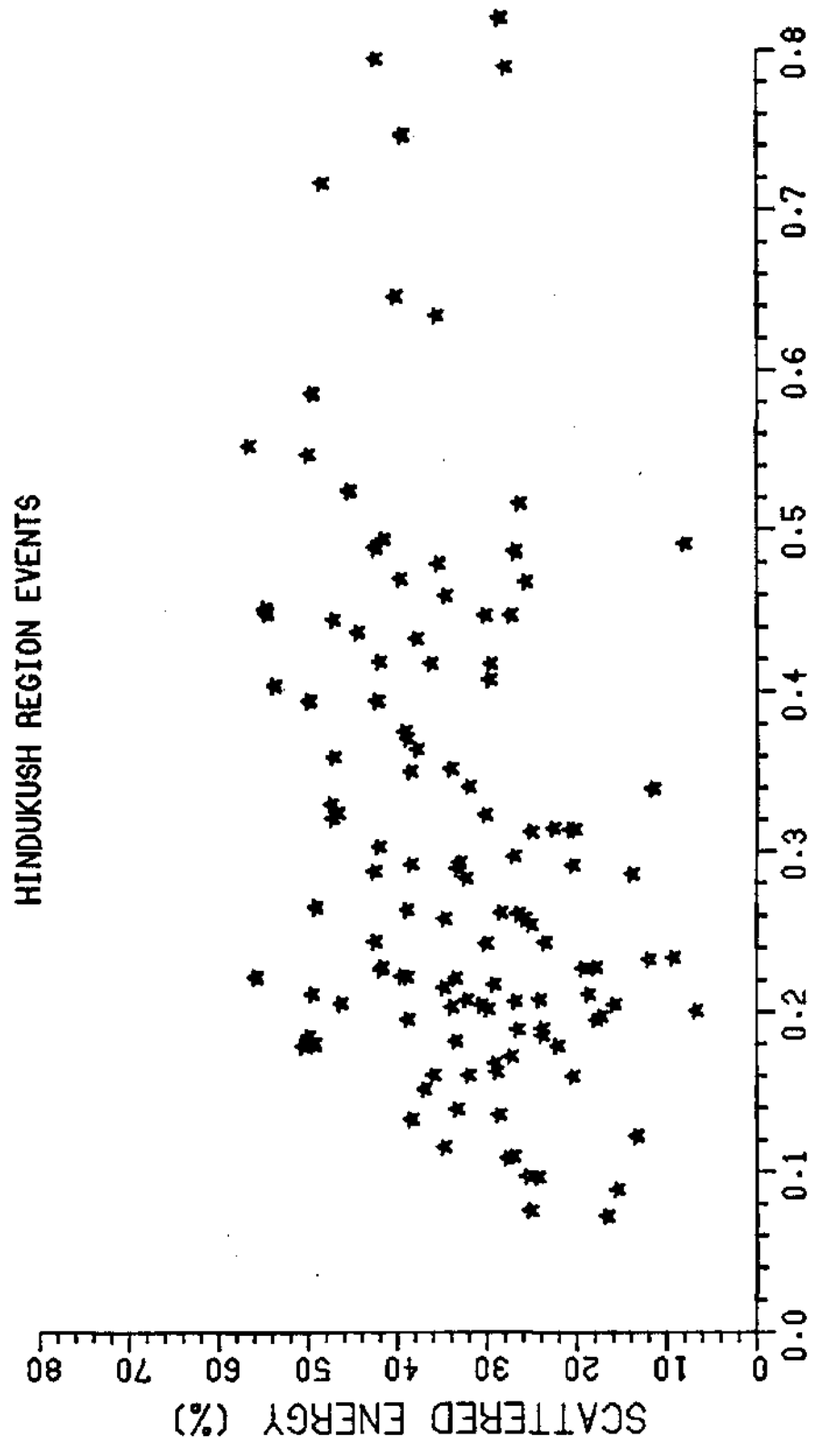


Figure 7.9: Observed scattered energy versus signal spectral ratio.

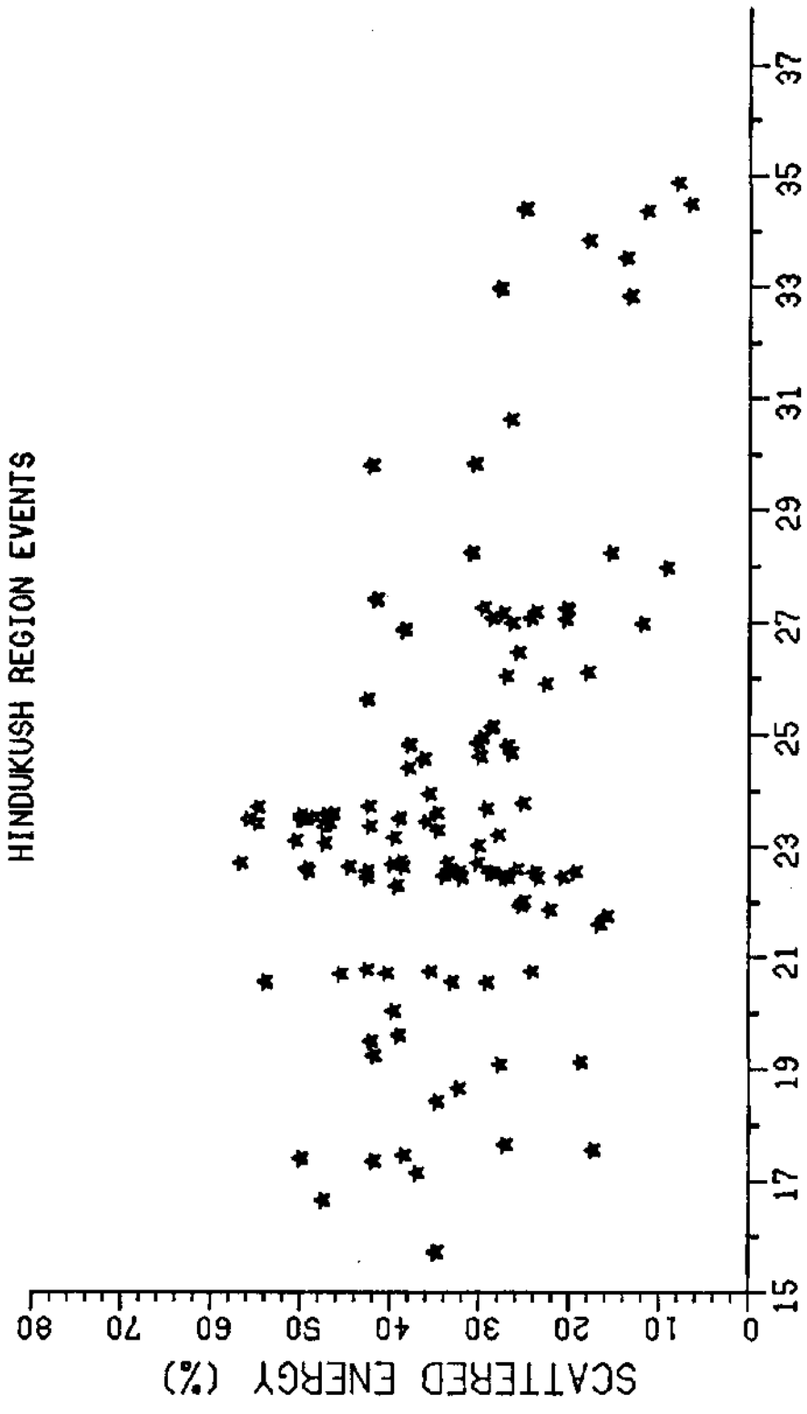


Figure 7.10: Observed scattered energy versus epicentral distance of events.

depth bias and the high frequency bias from Figure 7.10, the data have been re-plotted for only those events with spectral ratio less than 0.4, and without the select Hindukush events. The result is shown in Figure 7.11, and the similarity with Figure 7.4 is again emphasized by the 30% scattered energy reference line.

One may again conclude from these figures that, as with the Himalayan region, considerable lateral and vertical variations in complexity exist for different ray paths through the upper mantle between GBA and the Hindukush region, with the region below a depth of about 400 km tending to be much simpler than the region above this depth.

7.3 LOWER MANTLE DATA FROM GBA

Over 40 earthquake recordings from events in the distance range 40 to 67 degrees from the Celebes, Philippines, Mariana and Japan-Kurile Island regions were also available, and have been included here for comparison. The azimuth range of these events was 45 to 130 degrees. The vertex of the ray paths between these events and GBA have depths which range from about 950 km to 1750 km, and for this distance range, the greater part of the ray path would travel through very deep mantle. One would therefore expect the dominant characteristic of the signals to be derived from the lower mantle.

In order to reduce the effect of lateral variation in structure, the events were divided into the following

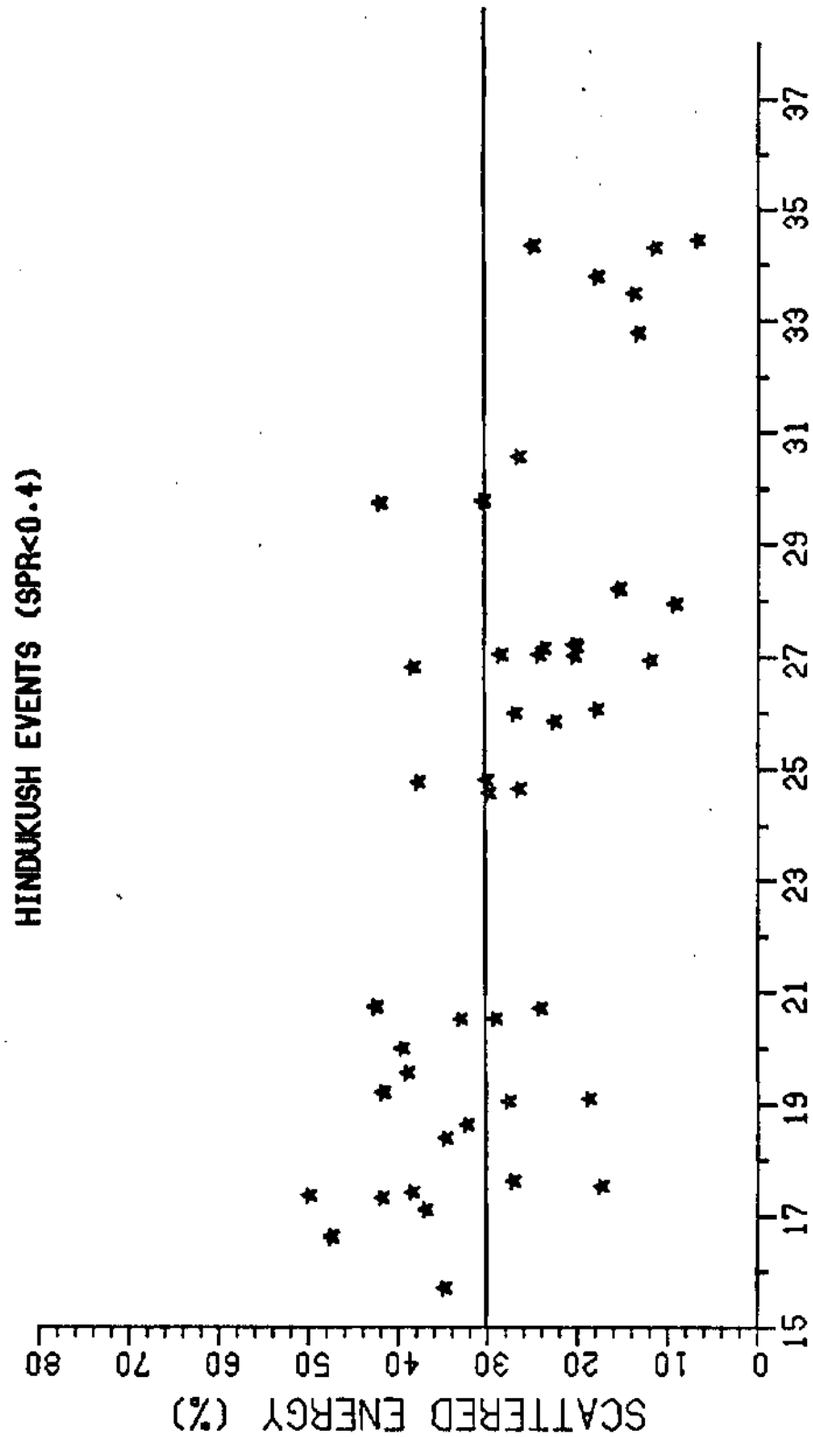


Figure 7.11: Observed scattered energy versus epicentral distance excluding the select Hindukush events and events with spectral ratio greater than 0.4.

azimuth ranges: (i) 45-90 degrees, and (ii) 90-130 degrees; and in order to show how they compare with the upper mantle results, they were combined with the upper mantle data of the corresponding azimuths. The resulting variation of scattered energy with epicentral distance are shown in Figures 7.12 and 7.13 for events with spectral ratio values less than 0.4 to minimize the effect of the variation in frequency content.

Figure 7.12 shows the combined result for the azimuth range 0-90 degrees (i.e. including the Himalayan events). It is clear from this figure that the scattered energy beyond 40 degrees remain consistently low with an average which dropped to about 14% from the average of about 24% for the distance range 25-40 degrees. Similarly, Figure 7.13 shows the combined result for the azimuth range 90-130 degrees (i.e. including the Java trench events), from which it will again be observed that the scattered energy remains low beyond 45 degrees, dropping down to values close to 0% near 60 degrees. It would thus appear that the lower mantle heterogeneity for this region is considerably less than was observed for the upper mantle.

7.4 RESULTS - YKA

The ray paths described by the YKA data lie predominantly in continental upper mantle for the California region events, and partly in oceanic upper mantle for the Alaska Peninsula events. The former rays bottom under parts

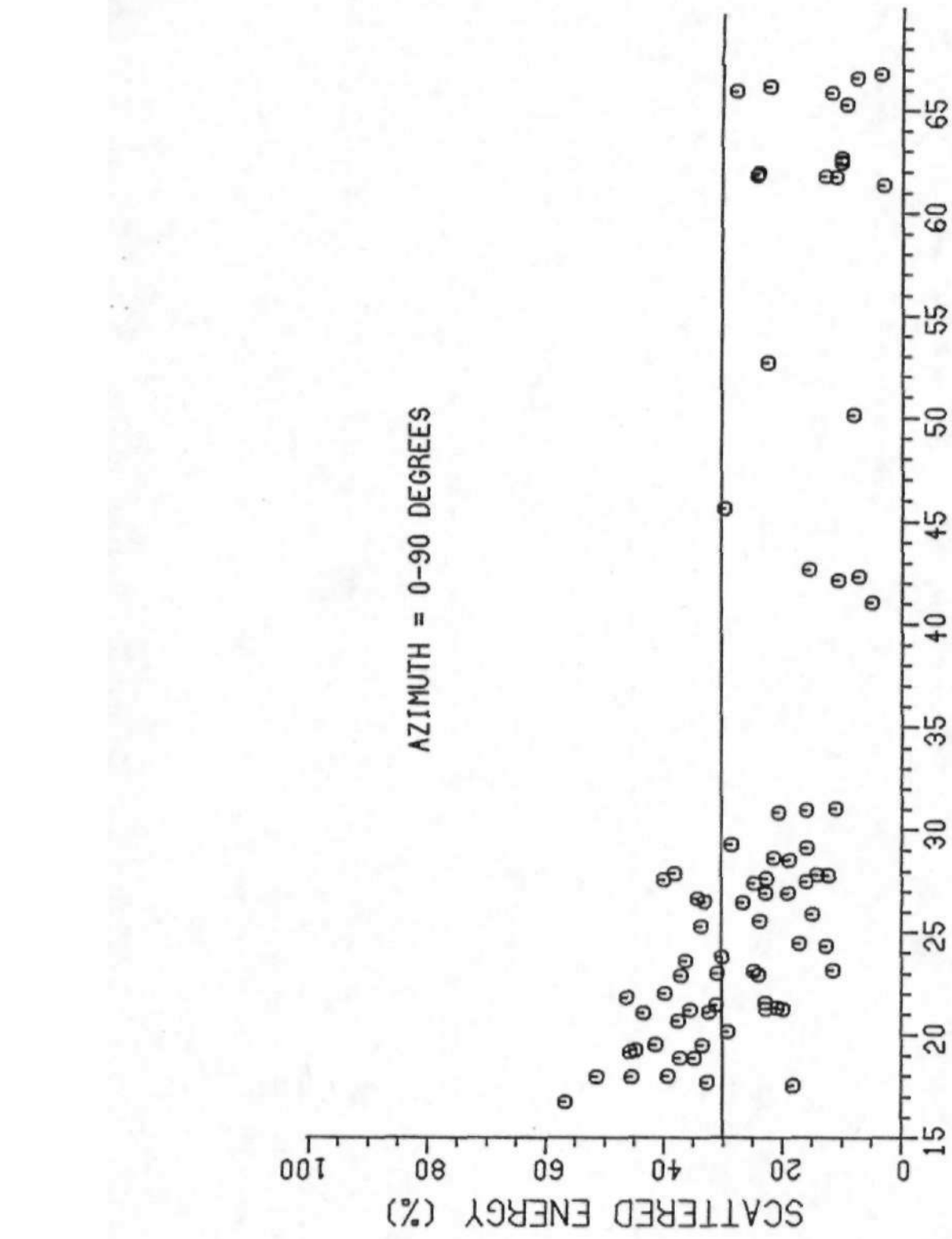


Figure 7.12: Observed scattered energy versus epicentral distance for upper and lower mantle data. The line parallel to the distance axis emphasizes the differences in scattered energy between upper mantle data (15°-35°) and lower mantle data (40°-67°).

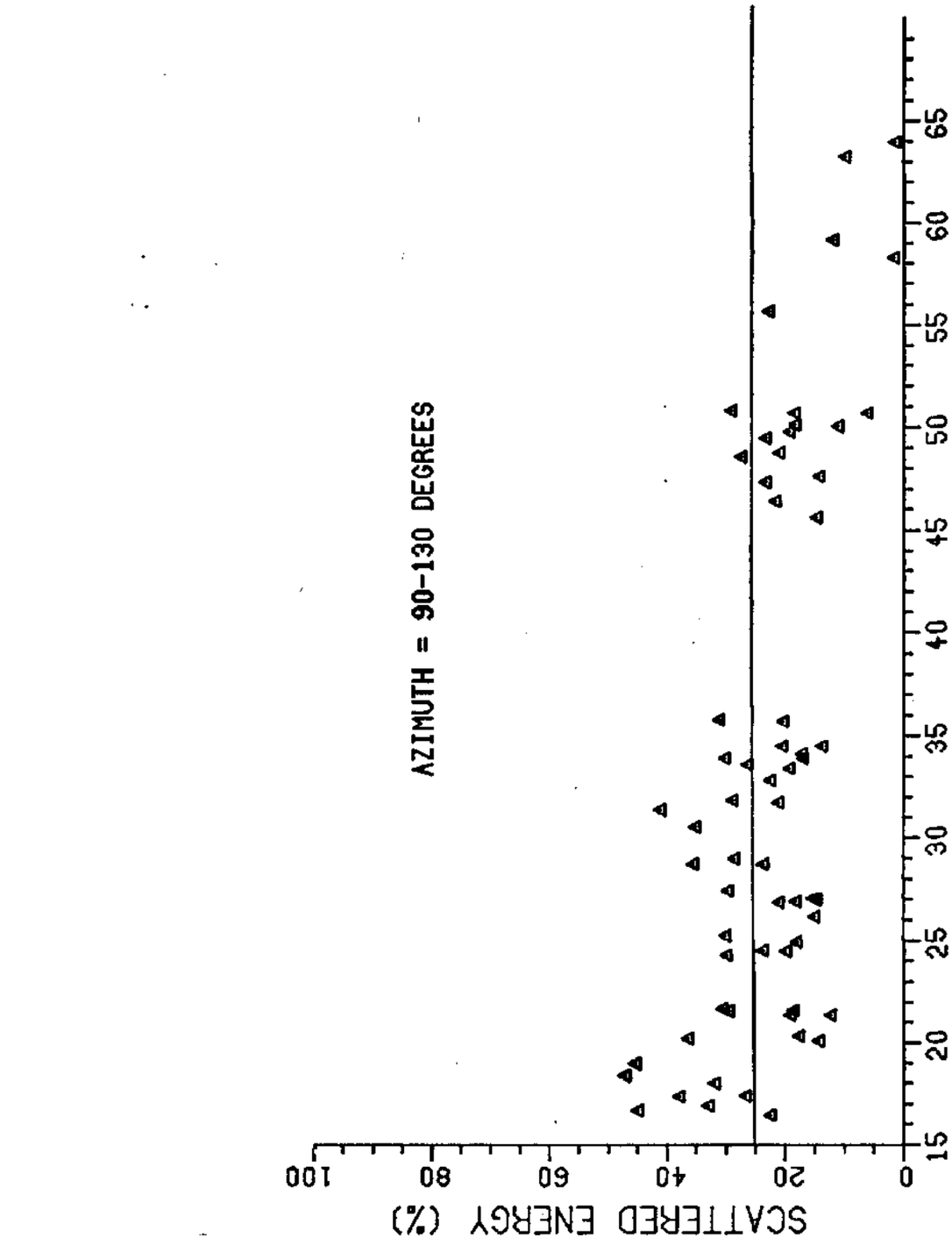


Figure 7.13: Observed scattered energy versus epicentral distance for upper and lower mantle data. The line parallel to the distance axis emphasizes the difference between upper mantle data (15^{o}-360^{o}) and lower mantle data (45^{o}-65^{o}).

of north-western United States and south-western Canada, while the latter bottom under parts of Gulf of Alaska and north-western Canada.

7.4.1 THE CALIFORNIA REGION

The plot of the scattered energy as a function of the signal spectral ratio for the California region events is shown in Figure 7.14. It is apparent from the figure that events with spectral ratio greater than 0.4 tend to have high scattered energies, and for this reason, the frequency bias was removed in the plot of scattered energy versus distance (Figure 7.15) by using only those events with spectral ratio less than 0.4.

An examination of Figure 7.15 shows that the scattered energy rises gradually from a value of about 25% between the distance of 18 and 21 degrees to 50% near 28 degrees. This is markedly in contrast with the results for the region around GBA which either showed relatively constant scattered energy, or scattered energy that decreases with distance. This trend between 20 and 30 degrees could be caused by upper mantle structure which is progressively more heterogeneous with depth between 400 and 750 km; or by near-array structure if the difference in ray paths from the extremities of the source region is significant near the array. However, this latter possibility is considered a remote one because the narrow azimuth range covered by these events, and the distances involved were such that if some

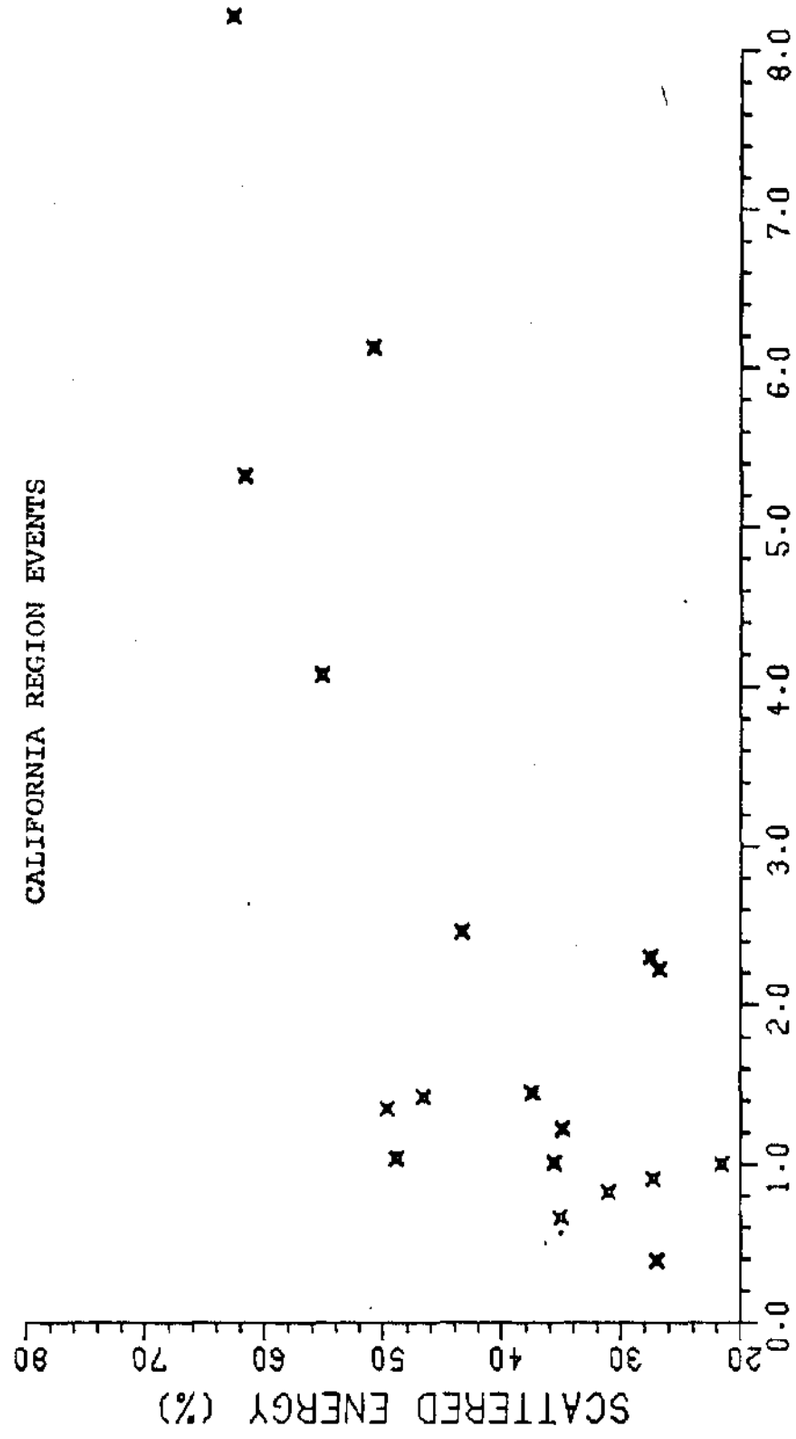


Figure 7.14: Observed scattered energy versus signal spectral ratio.

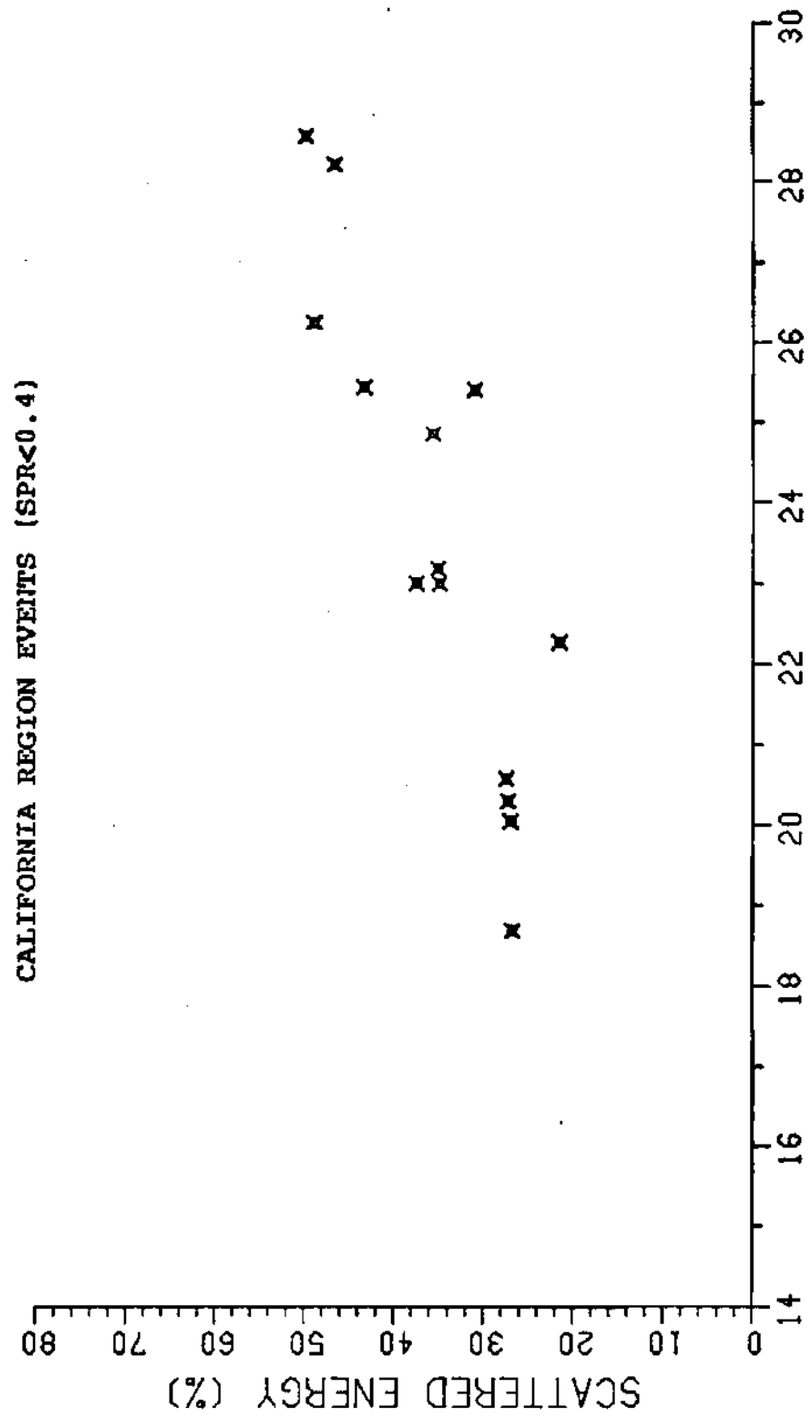


Figure 7.15: Observed scattered energy versus epicentral distance.

structure was present beneath the array, it would affect the ray paths similarly. Furthermore, results from a refraction experiment in the array area (Weichert and Whitham, 1969; Barr, 1971) showed that only shallow teleseismic ray paths from the east to south-east were likely to be affected by crustal structure. Manchee and Weichert (1968) also found some anomalies of both slowness and azimuth for P arrivals at YKA which could not be explained by near-array structure, but could be accounted for by lateral variations in the deep mantle (Weichert, 1972).

7.4.2 THE ALASKA PENINSULA

Figure 7.16 shows how the scattered energy varies as a function of the spectral ratio for the complete set of events from the Alaska Peninsula. It will again be noted that a frequency bias exists for these events with those with spectral ratio greater than 0.4 having high scattered energy. Figure 7.17 shows the variation of scattered energy with distance for only those events with spectral ratio less than 0.4. We note that near a distance of 12 degrees, the scattered energy is relatively high, and this is attributed to the presence of a large number of inhomogeneities in the uppermost mantle. However, the scattered energy becomes low near 15 degrees (about 20%), and then gradually increases with distance to about 40-45% near 30 degrees. This trend is apparent in spite of the scatter of the data, and is similar to that obtained for the California region, although the absence of a large number of data points around 12

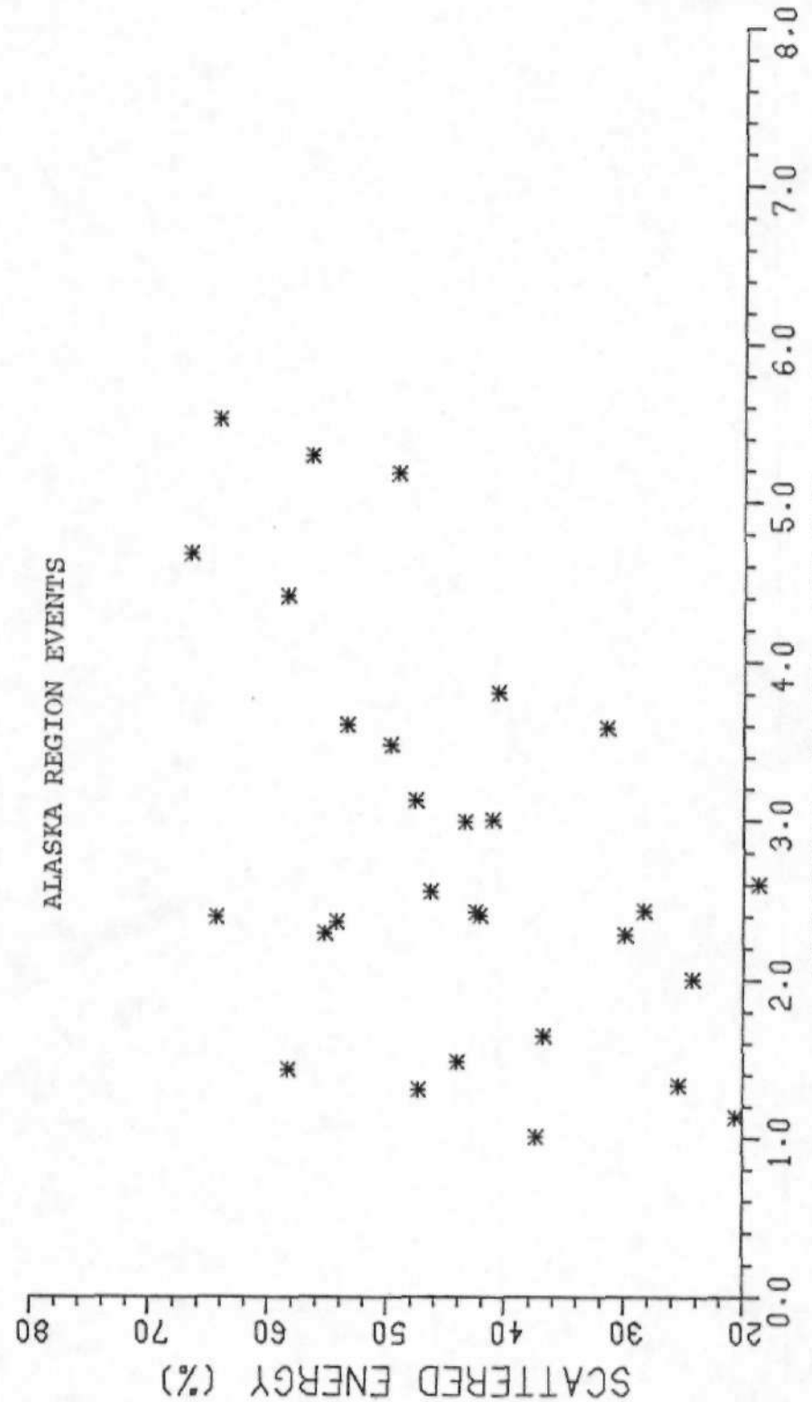


Figure 7.16: Obsersed scattered energy versus signal spectral ratio.

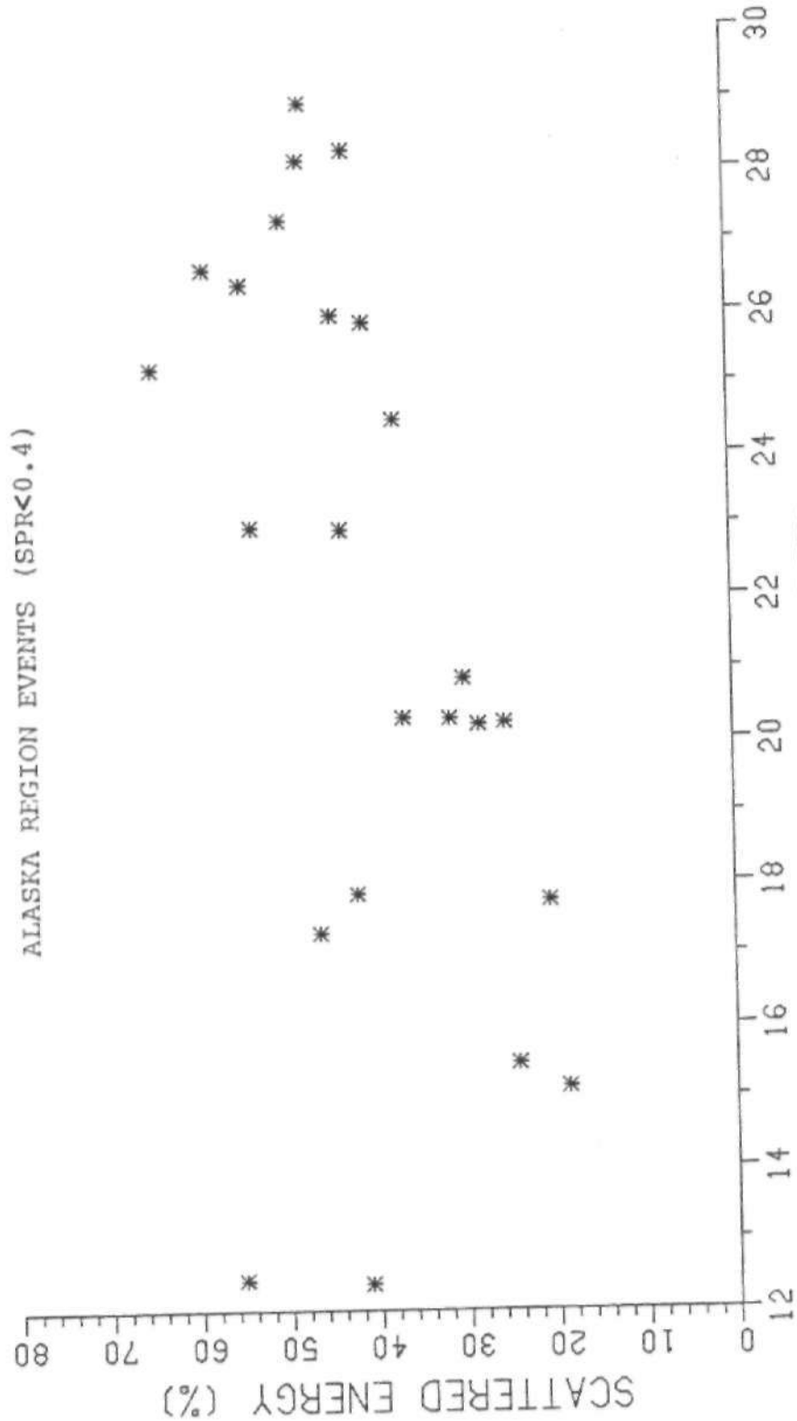


Figure 7.17: Observed scattered energy versus epicentral distance.

degrees precludes a satisfactory comparison of this portion of the figures. One cannot explain the scatter of the data in Figure 7.17 by lateral variation in structure because the Alaska Peninsula events occurred in a relatively narrow azimuth range with respect to YKA. A more probable explanation must again be sought in the source region for as was demonstrated in Chapter 6, the effect of anomalies in the source region appeared to be to increase the scatter of the points.

For the same reasons that were proposed for the California region, the high scattered energy which is evident for more distant Alaska events relative to the nearer events between 15 and 30 degrees cannot be accounted for by near-array structure. Explanation for this must therefore lie in upper mantle heterogeneity which increases with depth below 400 km, and up to at least 750 km which is the maximum depth which the more distant events here relate to.

7.5 DISCUSSION

These past three chapters (including this one) have been concerned with relating P-wave signal coherence to P-wave scattering along the signal travel path, and a method was developed that produced a quantitative measure of this scattering. We have then proceeded to infer and compare the lateral and vertical variations in the heterogeneity of upper and lower mantle structures from such measurements for

different ray paths. The validity of this procedure was demonstrated with results from tests with synthetic data, and from the subsequent application to both GBA and YKA data.

Most of the other previous upper mantle studies around the Indian subcontinent were on the velocity structure, seismicity, and earthquake focal mechanisms in the region (e.g. Tandon, 1967; Kaila et al., 1968, 1969, 1978; Fitch, 1970; Vinnik et al., 1977; Ram and Mereu, 1977; Singh et al., 1979; Chen, 1980; Simpson, 1980), and very little is known about the upper mantle heterogeneity of this region. Ram and Mereu (1977) found evidence for a large low-velocity or low-Q layer along oceanic paths as compared to the continental paths in their study. This is consistent with the result illustrated in Figure 7.2, especially for the Mid-Indian ocean region which showed considerable attenuation for the high frequency component. They also found that both the slowness and azimuth anomalies from Java trench, Mid-Indian ocean ridge and far east regions showed consistent patterns as compared to the Himalayan and Hindukush regions. This is also consistent with our results which indicated that the former regions showed less variations in scattered energy than the latter.

Berteussen et al. (1977) used the Chernov medium approach in an extensive analysis of travel time residuals from 20 events recorded at GBA, and concluded from their results that the crust/upper mantle beneath GBA appeared to

be relatively homogeneous. Similar conclusions were reached by Corbishley (1970) who found that the residual site corrections for GBA and YKA were small. These results, combined with the precautions taken in this study to minimize the effect of near-array structure, suggest that the dominant factor in the changes that occurred in the observed scattered energy described in this study was the variations in upper mantle heterogeneity in regions where the rays bottom, and not beneath the arrays.

It is fair to assume from the results presented in this chapter for the region around India that the continental upper mantle structure to the north of GBA is, in general, more complex than the equivalent oceanic upper mantle structure to the south. It is equally apparent that some differences exist between the Mid-Indian ocean ridge region and the Java trench region, the latter being more complex. This latter difference between the oceanic regions is consistent with the hypothesis that the oceanic lithosphere changes in character with increasing age. P and S waves which travel through oceanic upper mantle, for instance, show delays relative to standard earth models which can be correlated with the age of the sea floor above the travel path (Forsyth, 1977). Girardin (1980) found that P-wave travel-time delays decrease with the age of the plate for oceanic structures, and that the average oceanic lithosphere (100 my) has a residual similar to that of a typical continental platform. It would thus appear that the

increase in the average scattered energy for ray paths from the Java trench relative to the Mid-Indian ocean ridge can be attributed partly to the descending slabs at the subduction zone, and partly to the changes in structure caused by the ageing plate as one moved from the ridge to the subduction zone.

For YKA results, the same assumptions about the GBA array site and events were still essentially valid; in other words, structure beneath YKA is relatively uniform and horizontal as evidenced from refraction experiments in the area (Weichert and Whitham, 1969; Barr, 1971), and the very small site corrections required for the array (Corbishley, 1970). In addition, the azimuth range of the Alaska and California events were small, which also minimized the effect of structure beneath the arrays. The dominant factor in the changes which were observed in the scattered energy for various distances must therefore also lie in regions where the rays bottom, and not near the array. This is, however, as far as the similarities between the two regions appeared to go, for in contrast to the region around GBA where the upper mantle heterogeneity decreases with depth, the reverse was found to be true for the upper mantle in the Alaska and California region between 400 and 750 km depths. It is therefore appropriate to consider these latter results in the light of results from other existing studies for the region.

Western North America has been extensively studied to determine upper mantle P velocity structure (Niazi and Anderson, 1965; Johnson, 1967; Masse et al., 1972; Wiggins and Helmberger, 1973; Dey-Sarkar and Wiggins, 1976; Burdick and Helmberger, 1978; and others). An important result of these investigations is that there are significant lateral variations in the upper mantle structure, and a general feature is a low-velocity zone (LVZ) in the uppermost mantle and two zones of sharp P-velocity increases near depths of 400 km and 650 km. Many other studies of teleseismic P and S delays also showed consistent late arrivals in most parts of western United States as compared to central or eastern United States (Cleary and Hales, 1966; Lilwall and Douglas, 1970; Sengupta and Julian, 1976). In general, the arrivals are early in shield areas and late where there has been tectonic activity within the past 100 million years, or where the heat flow is high (Hales et al., 1968). The major part of the variations in these anomalies were attributed to a change in the thickness of the upper mantle LVZ.

Davies and Sheppard (1972) using $dT/d\Delta$ and azimuth anomalies detected at LASA, and Powell (1975) in a similar study with data from the Hanford array, Washington found strong evidence that lateral heterogeneity occurs at all depths throughout the Earth's mantle. There are also other indications that mantle heterogeneities are not confined to the upper mantle (e.g. Chinney, 1969; Jordan and Lynn,

1974; Engdahl, 1975; Dziewonski et al.,1977). Although most of these studies give no quantitative estimates on the relative scale of upper mantle heterogeneity, they however all describe a general trend in which the largest part of the anomalies were attributed to structure in the top 200-250 km of the upper mantle.

The results of the present study are not inconsistent with the above deductions for the uppermost mantle, although the scanty data in the distance range 12-15 degrees precludes a definite conclusion. However, the consistency of our results for distances between 20 and 30 degrees leads us to believe that our interpretation for the depth range 400-750 km of this region is, in general, correct. The interpretation of certain anomalies of $dT/d\Delta$ and azimuth of P-waves at YKA from the Aleutians (Weichert, 1972), which could not be accounted for by near-array and near-source structure, as being caused by lateral variation of velocities near depths of 800 km is in line with the present results. Furthermore, the results of Romanowicz (1979) who in a study by three-dimensional inversion of body wave arrival times in the United States located the primary heterogeneities responsible for the travel-time delays in the first 250 km of the upper mantle, but also found that significant heterogeneities subsist to depths of at least 700 km, indicate that it is also probable that large variations exist in some parts of the deep mantle.

CHAPTER 8

DISCUSSION AND CONCLUSIONS

8.1 MINERALOGICAL CONSIDERATIONS FOR VELOCITY FLUCTUATIONS

Over the years a wide variety of models for the crust have evolved. The commonest and, perhaps, the oldest one divides the crust into an upper granitic layer, and a lower gabbroic layer. This division was mainly based on the fact that velocities which are characteristic of the upper and lower crust readily correspond to the velocities of rocks with granitic composition, and to those of basalts and gabbros respectively. As Pakiser and Robinson (1966) pointed out, it is not entirely valid to relate compositions to seismic velocities especially if individual velocity measurements were related to individual chemical analyses of rock samples. However, generalizations are possible since the seismic refraction method averages the velocities of large volumes of rocks, and averaged composition of rocks are often used for comparison.

Although layering is now not considered continuous, the above model appears consistent, in general terms, with geological observations of the composition of the upper crust. However, Ringwood and Green (1966) observed that the suggestion that the lower crust is composed of gabbroic or

basaltic rocks cannot be correct. They pointed out that the mineral assemblage of gabbros indicate chemical equilibrium at temperatures and pressures which are inconsistent with conditions in the stable lower crust, and concluded from some experimental investigations that the lower crust consists on the average of intermediate rocks in the eclogite facies. Other variations on this theme with slightly different end results for the composition of the lower crust will be found in the literature, for example, Green and Lambert (1965), Berckhemer (1969), Green (1970), and others. Smithson and Dekker (1974) observed that general geologic considerations and geological observations suggest a lower crust composed of dry granulite facies metamorphic rocks that would have very low heat production as is necessary for plausible values of heat flow from the mantle. They summarized the overall impression on compositional considerations adequately when they stated that heterogeneity is the rule rather than homogeneity.

It is therefore appropriate to consider how mineralogical considerations relate to the magnitude of the velocity fluctuation that we found to be consistent with certain observations in Chapters 2, 3, and 4.

Although seismic velocity distributions in the crust and upper mantle vary considerably from place to place there is, however, strong evidence both from numerous refraction experiments and laboratory measurements that large vertical gradients exist (numerous laboratory measurements of P-wave

velocities are available in the literature, for example, Birch, 1960, 1961; Christensen, 1965; and Manghnani et al., 1974). The gradients may be associated with high pressure physical effects with depth. The characteristic curve of velocity versus pressure shows an initial rapid increase of velocity with pressure due to closure of pore space followed by a rapid decrease in slope at a pressure near 1 kb and approximate linearity at pressures between 4 and 10 kb (Christensen, 1965).

On the other hand, lateral variations may be explained in terms of the variation in mineral composition. Figure 8.1 shows compressional wave velocities for plagioclase feldspar series as a function of composition. As the figure shows, considerable velocity variation occurs for plagioclase rocks as they change from purely albite composition to purely anorthite composition. On a larger scale, Figure 8.2a is a diagram showing proportions of principal minerals in a series of igneous rocks ranging from granite to dunite; and Figure 8.2b is a diagram showing the variation of calculated velocity with composition for the same sequence of rocks in Figure 8.2a. Again, the same compositional dependence of velocity is observed.

Other factors responsible for velocity differences in rocks are porosity (Nur and Simmons, 1969), and the degree of orientation of the mineral components. While the effect of porosity becomes neglible above the relatively low pressure of 1 kb, the effect of mineral anisotropy is still

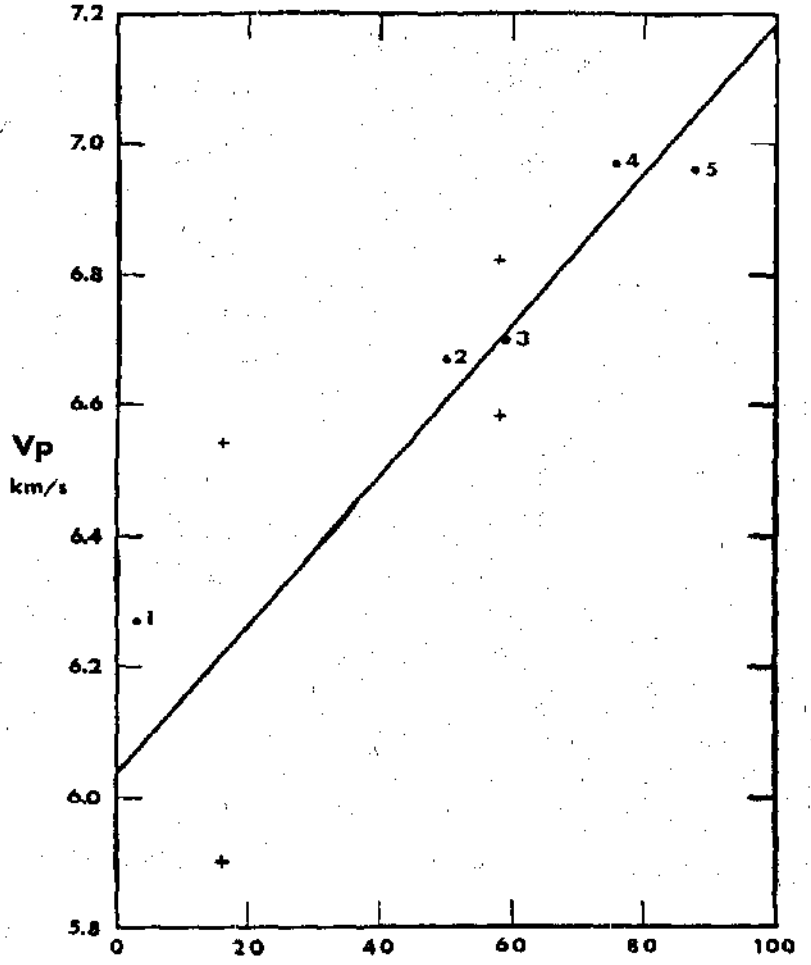


Figure 8.1: Velocity versus plagioclase composition calculated from aggregate theory. Crosses represent Voigt and Reuss averages. Dots refer to observed velocities in plagioclase rocks at 1.5kb (after Christensen, 1965).

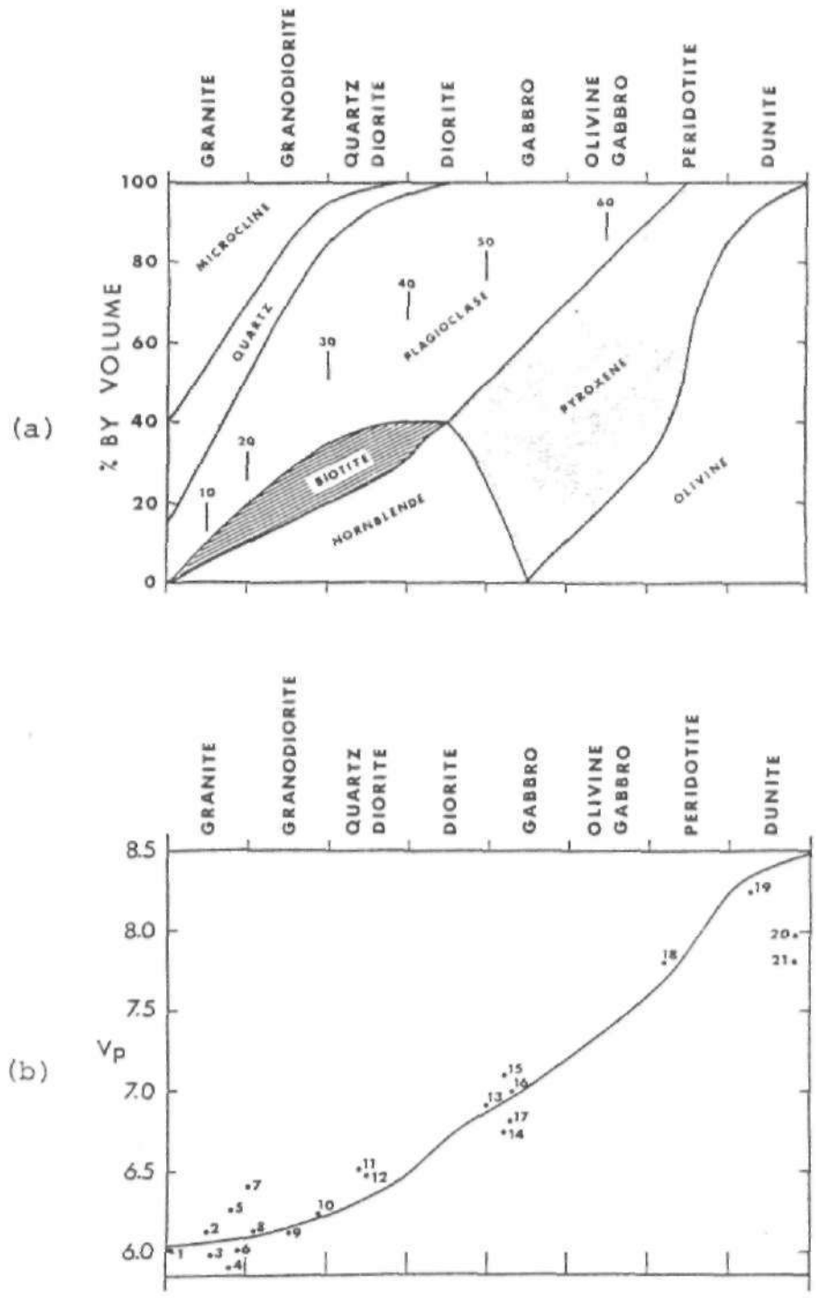


Figure 8.2: (a) Diagram showing proportions of principal minerals in a series of igneous rocks ranging from granite to dunite. (b) Variation of calculated velocity with composition for the same sequence of rocks as in (a). Dots refer to observed velocities at 1.5 kb for rocks approximating the mineral composition in (a) ranging from granite to dunite (after Christensen, 1965).

significant at high pressures. For example, the greatest difference in velocity among the three mutually perpendicular directions at 10 kb reaches 7 to 10% for dunites (Birch, 1961). By extension, these small-scale anisotropic effects have also been investigated on a larger scale in upper mantle material. In a seismic refraction experiment carried out in the ocean basin off the coast of British Columbia, Canada, to measure anisotropy of the mantle P-wave velocity, Keen and Barrett (1971) observed significant anisotropy of the mantle rocks with a change in velocity of as much as about 8% of the mean value. Morris et al. (1969) also obtained similar results in studies of mantle anisotropy near Hawaii, and discussed the possibility that it might result from a regional orientation of olivine in the upper mantle; or by stress-strain field associated with sea-floor spreading.

In general terms, the upper mantle consists essentially of pyrolite which might occur as the mineral assemblage olivine-pyroxene-plagioclase or olivine-pyroxene-garnet (Ringwood, 1962), and variations in mineralogical compositions are mainly caused by phase transformations due to high pressure and temperature effects. Such phase transitions have been used to explain or predict the presence of large velocity gradients or discontinuities in the upper mantle, for example, the pyroxene-garnet transformation near 350 km, and the olivine-spinel transformation near 400-500 km (Ringwood, 1967). Green and

Ringwood (1967) also demonstrated that mineralogical variation along geothermal gradients, particularly in oceanic regions, may be expected to strongly influence the seismic velocity distribution in the upper mantle.

All the velocity variations discussed above are, for the most part, considerably more than the maximum value of 0.15 km/s that was necessary to account for the observed fluctuation in travel times and amplitudes (Chapter 3), and 0.2 km/s for the rapid variation in $dT/d\Delta$ necessary to predict the existence of velocity discontinuities in the upper mantle where none existed (Chapter 4). In addition, the density variation that would result from a P-wave velocity variation of 0.15 km/s is less than 2%. It is therefore significant that the order of magnitude of the velocity perturbation required in our models to predict variations similar to observed ones is comparable or much less than those which have been found from other studies (e.g. Aki, 1973; Capon, 1974; Berteussen et al., 1975).

8.2 SUGGESTIONS FOR FURTHER WORK

The results of the study on P-wave scattering and upper mantle heterogeneity described in this thesis suggest a few avenues for further work which could be pursued along the same lines described in this work. In particular,

(1) the numerical experiments on the random crustal models indicate the need to study other arrivals beyond the first arrival times. There is therefore a need for some wave-form

analysis using synthetic seismograms. In this respect, a limited version of the finite difference approach (e.g. Kelly et al., 1976) or a similar method is essential.
(2) There is also a need to study the crust-mantle transition zone in more detail with respect to the magnitude of the velocity fluctuation at this boundary that is consistent with the behaviour of the retrograde branch.
(3) A better control on the effect of the source parameter was desired for the coherence studies described in this thesis. Further studies along this line should therefore attempt to use one or two earthquakes as the source, and numerous recordings of the earthquake(s) from a network of seismic array with similar azimuth with respect to the source. Some encouraging preliminary results were obtained in the application of the method, by this approach, to two seismic arrays which were located 200 km apart, on either side of the boundary between the West Africa Precambrian craton, and the relatively young Mauritanide orogenic belt in eastern Senegal (see Briden et al., 1980). The signals arriving at one of the arrays (on the orogenic belt) were consistently less coherent than those on the craton beneath which the structure is simpler (Briden, personal communication).

8.3 CONCLUSIONS

The principal aim of this work was (1) to investigate how small-scale fluctuations in travel-time, amplitude and slowness measurements may be accounted for by P-wave

scattering in the crust and upper mantle, and (2) to investigate the relationship between the scattering along the signal travel path, and upper mantle heterogeneity. The principal results of the work may then be summarized as follows:

1. Numerical experiments on models of the Earth's crust and uppermost mantle created from a single layered crust with a vertical gradient and horizontal random velocity model showed that (Chapter 2):

   (i) the resulting two-dimensional models exhibited short discontinuous reflectors at various depths in agreement with deep seismic reflection experimental observations.

   (ii) On the other hand, results using ray-tracing techniques showed that the effect of the velocity anomalies is to scatter the energy and break up the continuous travel-time curve into segments with different slopes similar to those observed in many long range refraction experiments.

   (iii) The arrival times also showed focussing and defocussing effects that could be related to erratic amplitude variation similar to the behaviour of observed refraction amplitudes.

   (iv) Interpretation of the apparent velocities and intercept times using conventional refraction techniques gave depths to an apparent discontinuity in the crust which could be correlated to the correlation distance used in deriving the random models.

(v) The effect of increasing the maximum velocity perturbation used in deriving the models was to also increase the travel-time fluctuations.

2. The application of the above results to the 1979 COCRUST refraction experiments in southern Manitoba and Saskatchewan showed the following (Chapter 3):

(i) travel-time and amplitude fluctuation of the refraction data could be explained by a random model.

(ii) The correlation distance and r.m.s. velocity fluctuation that best describe the crust in this area are 5 km and 1% respectively.

(iii) An extremal inversion of the refraction data using tau (τ) estimates from the travel times yielded well-constrained velocity-depth bounds for the crust above depths of 30 km. A comparison of the velocity-depth bounds with layer solutions showed that the latter were, for the most part, well constrained by the former; and a comparison of the random model with the extremal bounds indicated that the random model may be considered as a tightly constrained extremal solution.

3. Numerical ray-tracing through models of the upper mantle created by superimposing some random velocity variation on a basic Herrin model showed that (Chapter 4):

(i) As a result of multipathing caused by the small velocity fluctuations, several arrivals of distinctly different $dT/d\Delta$ should be observed over very short distances. This is similar to observations obtained from a number of array studies.

(ii) An inversion of the travel-time and slowness data obtained from such a model gave velocity-depth bounds which when compared with velocity models from array data in Australia and Western Canada were found to contain significant similarities.

(iii) The experiments indicated that it might not always be necessary to invoke major discontinuities in the upper mantle to explain rapid variations in slowness and travel-time observations.

4. The development of a coherence method (Chapter 5) for measuring the amount of scattered energy in a recorded signal showed that:

(i) Array signal processing techniques (including beam forming) provide an attractive method for achieving this.

(ii) The coherence parameter that was evolved is relatively independent of the intrinsic signal complexity (e.g. source generated complexity).

(iii) The coherence parameter effectively determines the ratio of the coherent energy to the incoherent energy in the signal.

(iv) The method confirms the signal enhancement capability of the nth root beam forming method.

5. Coherence measurements on array data from GBA in southern India, and YKA in western Canada were made to study the heterogeneity of the upper mantle in these regions (Chapters 5 and 6). Our major findings showed that:

(i) the observed scattered energy is not a function of

signal complexity. Complex signals showed both high and low scattered energy.

(ii) The observed scattered energy was found to be dependent on the frequency content of the signal.

(iii) It was also found to depend significantly on the local structure in the source region. It might therefore be a function of earthquake focal depth.

6. Specific results for GBA showed that the observed scattered energy was azimuthally dependent, with the signals having oceanic travel paths (especially from the Mid-Indian ocean ridge) showing relatively less scattered energy. The summary for GBA results are:

(i) Analyses of Himalayan region events indicated that vertical variation exists in the heterogeneity of the upper mantle structure in the this region, with structures above about 400 km tending to be more complex.

(ii) The heterogeneity of the upper mantle of the Java trench region showed little variation with depth except in the uppermost mantle where the effect of the subducting plate margin may be significant.

(iii) The Mid-Indian ocean region showed little vertical variation in heterogeneity of the upper mantle, and appeared to be more homogeneous than the Himalayan, the Java trench, and the Hindukush region.

(iv) Analyses of earthquake recordings from the Hindukush region, showed that considerable lateral and vertical variations in complexity exist for different

ray paths through the upper mantle of this region, with the region below 400 km tending to be simpler than the region above this depth.

(v) Analyses of some earthquake events in the distance range 40 to 70 degrees from the far east region, for which ray paths bottom in the lower mantle showed that the lower mantle heterogeneity for this region is considerably less than was observed for the upper mantle.

7. Earthquake recordings at YKA from two azimuthal regions were analysed. In contrast to the GBA results, the YKA results which are consistent for both the Alaska Peninsula events and the California region events showed that the upper mantle structure under the north-western part of the North American continent could be progressively more heterogeneous with depth between 400 and 750 km. This surprising result was discussed in light of the existing knowledge of the structure of the region at the end of Chapter 7.

APPENDIX A.1

Listings of the ray tracing computer program for flat earth model

```
      PROGRAM RAYTRAC2(INPUT,OUTPUT,PUNCH,TAPE5=INPUT,TAPE6=OUTPUT,TAPE7=   A    1
     1PUNCH,TAPE10)                                                         A    2
C                                                                           A    3
C     THIS PROGRAM TRACES RAYS THROUGH A FLAT EARTH MODEL CONSISTING OF     A    4
C     OF A TWO-DIMENSIONAL GRID OF POINTS WITH RANDOM VELOCITY VARIATION    A    5
C                                                                           A    6
C                                                                           A    7
C     INPUT PARAMETERS                                                      A    8
C     ****************                                                      A    9
C        LX         NO OF GRID POINTS IN THE HORIZONTAL DIRECTION          A   10
C        LZ         NO OF GRID POINTS IN THE VERTICAL DIRECTION            A   11
C        HX=HZ      DISTANCE BETWEEN GRID POINTS IN KM.                    A   12
C        XI,ZIN     COORDINATES OF THE STARTING POINT OF RAY, NORMALLY     A   13
C                   THE ORIGIN.                                            A   14
C        RINC       MAXIMUM INCIDENT ANGLE TO BE INVESTIGATED              A   15
C        RMIN       MINIMUM INCIDENT ANGLE TO BE INVESTIGATED              A   16
C        AINC       INCREMENTAL VALUE OF INCIDENT ANGLE                    A   17
C        IPLOT      AN OPTION FOR PLOTTING OUTPUT                          A   18
C                   IPLOT=2    TRAVEL TIME AND RAY PATH PLOTTED            A   19
C                   IPLOT=1    TRAVEL TIME PLOTTED                         A   20
C                   IPLOT=0    NO PLOT                                     A   21
C        IPUNCH     AN OPTION TO PUNCH TRAVEL TIME RESULTS ON CARDS        A   22
C                   IPUNCH=1   OUTPUT PUNCHED ON CARDS                     A   23
C                   IPUNCH=0   NO CARD OUTPUT                              A   24
C        IWRT       AN OPTION TO PRINT DETAIL RAY INFO   FOR ERROR SEARCH  A   25
C                   IWRT=1     DETAIL INFO PRINTED...ONLY FOR ERROR SEARCH A   26
C                   IWRT=0     NO PRINTING                                 A   27
C                                                                           A   28
      COMPLEX Z                                                             A   29
      DIMENSION ASP(30),BSP(300),BB(900)                                    A   30
      DIMENSION X2(4500),Z2(4500),TOTIM(200),TOTO(200),RTM(200)             A   31
      COMMON /SBD/ AX(300,3),AZ(300,3),V(300,3),VGX(300,3),VGZ(300,3)       A   32
C                                                                           A   33
      RADIUS=6371.028                                                       A   34
      PI=3.14159265                                                         A   35
      ONPI=180.0/PI                                                         A   36
      LQ=3                                                                  A   37
C                                                                           A   38
      REWIND 10                                                             A   39
      READ(10)LX,LZ,HX,HZ                                                   A   40
      ARC=HZ/5.0                                                            A   41
      ARK=ARC                                                               A   42
      XMX=FLOAT(LX-1)*HX                                                    A   43
      ZMX=FLOAT(LZ-1)*HZ                                                    A   44
      TMX=3.0                                                               A   45
      DMN=-1.0*XMX                                                          A   46
C                                                                           A   47
      READ(5,2)XI,ZIN,RINC,IPLOT,IWRT,IPUNCH                               A   48
      READ(5,3)RMIN,AINC                                                    A   49
      PHII=90.0-RINC                                                        A   50
      AIMX=90.0-RMIN                                                        A   51
      IF(IPLOT.GT.0)CALL RAYPLTA(XMX,ZMX,TMX,XMN,XOA,ZMN,ZOA,TMN,TOA,IPL    A   52
     1OT)                                                                   A   53
      X1=XI                                                                 A   54
      Z1=ZIN                                                                A   55
      CALL WRITER(LX,LZ,HX,HZ,X1,Z1,RINC,RMIN,AINC,BB,BSP)                  A   56
C                                                                           A   57
C     DATA MAY BE READ FROM DISC OR TAPE OR CARDS.                          A   58
C     V=VELOCITY OF GRID ELEMENTS.                                          A   59
C     A=COORDINATE OF GRID POINTS.                                          A   60
C                                                                           A   61
      CALL VELALOC(LZ,MDIST,HX,HZ,BB,1.0)                                   A   62
C                                                                           A   63
```

```
C     DETERMINE HOST CELL OF RAY HEAD.                                  A  64
C                                                                       A  65
      DO 40 I=1,3                                                       A  66
40    ASP(I)=AX(1,I)                                                    A  67
      DO 50 J=1,LZ                                                      A  68
50    BSP(J)=AZ(J,1)                                                    A  69
      IF(IWRT.EQ.1)WRITE(6,12)                                          A  70
      WRITE(6,17)                                                       A  71
      LL=IFIX(((AIMX-PHII)/AINC)+1.0)                                   A  72
      J=0                                                               A  73
      KM=0                                                              A  74
51    J=J+1                                                             A  75
      T=0.3                                                             A  76
      DIST=0.0                                                          A  77
      DEPTH=HZ*2.0                                                      A  78
      IF(J.GT.1)PHII=PHII+AINC                                          A  79
      PHI=PHII*PI/180.0                                                 A  80
      X1=XI                                                             A  81
      Z1=ZIN                                                            A  82
      RA=RADIUS-Z1                                                      A  83
      X2(1)=X1                                                          A  84
      Z2(1)=Z1                                                          A  85
      CALL  LOCATE(LQ,ASP,X1,EL,EH,K1,K2,K3,CON)                        A  86
      IF(CON.EQ.0.0)GO TO 110                                           A  87
      CALL  LOCATE(LZ,BSP,Z1,FL,FH,J1,J2,J3,CON)                        A  88
      IF(CON.EQ.0.0)KM=KM+1                                             A  89
      IF(CON.EQ.0.0)GO TO 110                                           A  90
C                                                                       A  91
C     DETERMINE VELOCITY GRADIENT AT EACH GRID POINT.                   A  92
C                                                                       A  93
      CALL GRADXZ(LX,LZ,MOIST,HX,HZ,J1,J2,0.0)                          A  94
      C1=(X1-AX(J1,K1))/HX                                              A  95
      C2=0.0                                                            A  96
      V1=V(J1,K1)+(V(J1,K2)-V(J1,K1))*C1                                A  97
      V2=V(J2,K1)+(V(J2,K2)-V(J2,K1))*C1                                A  98
      V3=V(J3,K1)+(V(J3,K2)-V(J3,K1))*C1                                A  99
      VA=V1+(V2-V1)*C2                                                  A 100
      GZ=(V3-V1)/(2.0*HZ)                                               A 101
      IF(J3.EQ.J2)GZ=(V3-V1)/HZ                                         A 102
      GX=VGX(J1,K1)+(VGX(J1,K2)-VGX(J1,K1))*C1                          A 103
      PP=(RADIUS-Z1)*SIN(PI/2.0-PHI)/V1                                 A 104
      I=6                                                               A 105
55    CONTINUE                                                          A 106
      I=I+1                                                             A 107
      IF(I.EQ.1)GO TO 80                                                A 108
      IF(I.GT.1)X2(I)=X1                                                A 109
      IF(I.GT.1)Z2(I)=Z1                                                A 110
C                                                                       A 111
C     DETERMINE GRAD V AT RAY HEAD LOCATION.                            A 112
C                                                                       A 113
      GXL=VGX(J1,K1)+(VGX(J2,K1)-VGX(J1,K1))*(Z1-AZ(J1,K1))/HZ          A 114
      GXH=VGX(J1,K2)+(VGX(J2,K2)-VGX(J1,K2))*(Z1-AZ(J1,K2))/HZ          A 115
      GX=GXL+(GXH-GXL)*(X1-AX(J1,K1))/HX                                A 116
      C1=(Z1-AZ(J1,K1))/HZ                                              A 117
      C2=(X1-AX(J1,K1))/HX                                              A 118
      V1=V(J1,K1)+(V(J2,K1)-V(J1,K1))*C1                                A 119
      V2=V(J1,K2)+(V(J2,K2)-V(J1,K2))*C1                                A 120
      IF(I.GT.1)VA=VB                                                   A 121
      RA=RADIUS-Z1                                                      A 122
      GZL=VGZ(J1,K1)+(VGZ(J1,K2)-VGZ(J1,K1))*(X1-AX(J1,K1))/HX          A 123
      GZH=VGZ(J2,K1)+(VGZ(J2,K2)-VGZ(J2,K1))*(X1-AX(J2,K1))/HX          A 124
      GZ=GZL+(GZH-GZL)*(Z1-AZ(J1,K1))/HZ                                A 125
80    CONTINUE                                                          A 126
      Z=CMPLX(GX,GZ)                                                    A 127
      GRADV=CABS(Z)                                                     A 128
      THETA=ARCTAN(GZ,GX)                                               A 129
```

```
      ANGI=THETA-PHI                                                    A 130
      IF(GRADV.EQ.0.0)GO TO 90                                          A 131
      IF(SIN(ANGI).EQ.0.0)GO TO 100                                     A 132
C                                                                       A 133
C     COMPUTE RADIUS OF CURVATURE OF RAY PATH AND DETERMINE NEW POSITION A 134
C                                                                       A 135
      RHO=VA/(GRADV*SIN(ANGI))                                          A 136
      IF(ABS(RHO).GE.100.0)ARK=HZ/5.0                                   A 137
      IF(ABS(RHO).LT.100.0)ARK=ABS((HZ*RHO)/(5.0*100.0))                A 138
      DELPHI=ARK/RHO                                                    A 139
      ZI=RHO*SIN(DELPHI)                                                A 140
      ETA=RHO*(1.0-COS(DELPHI))                                         A 141
      X1=X1+ZI*COS(PHI)+ETA*SIN(PHI)                                    A 142
      Z1=Z1+ZI*SIN(PHI)-ETA*COS(PHI)                                    A 143
      RB=RADIUS-Z1                                                      A 144
C                                                                       A 145
C     IF RB IS GREATER THAN EARTH RADIUS, THEN RAY HAS PENETRATED EARTH A 146
C      SURFACE...,THEREFORE DETERMINE PRECISE END OF RAY AT SURFACE     A 147
C                                                                       A 148
      IF(RB.GT.RADIUS)13,14                                             A 149
13    X1=X1-ZI*COS(PHI)-ETA*SIN(PHI)                                    A 150
      Z1=Z1-ZI*SIN(PHI)+ETA*COS(PHI)                                    A 151
      CALL INTFACE(X1,Z1,PHI,RHO,DELPHI,T,GRADV,ANGI)                   A 152
      BETA=DELPHI*180.0/PI                                              A 153
      ANGL=ANGI*ONPI                                                    A 154
      TETA=THETA*ONPI                                                   A 155
      GAMA=PHI*ONPI                                                     A 156
      IF(IWRT.EQ.1)WRITE(6,15)X1,Z1,GAMA,RHO,BETA,VA,TETA,ANGL          A 157
      DIST=X1                                                           A 158
      I=I+1                                                             A 159
      X2(I)=X1                                                          A 160
      Z2(I)=Z1                                                          A 161
      GO TO 110                                                         A 162
14    CONTINUE                                                          A 163
      DELT=(1.0/GRADV)*(ATANH(COS(ANGI))-ATANH(COS(ANGI+DELPHI)))       A 164
      T=T+DELT                                                          A 165
      PHI=PHI-DELPHI                                                    A 166
85    CONTINUE                                                          A 167
      BETA=DELPHI*180.0/PI                                              A 168
      ANGL=ANGI*ONPI                                                    A 169
      TETA=THETA*ONPI                                                   A 170
      GAMA=PHI*ONPI                                                     A 171
      IF(IWRT.EQ.1)WRITE(6,15)X1,Z1,GAMA,RHO,BETA,VA,TETA,ANGL          A 172
      IF(NDIST.EQ.LX)87,86                                              A 173
86    IF(X1.GT.ASP(2))CALL CLEAN(LX,LZ,NDIST,HX,HZ,BB,ASP)              A 174
87    CALL  LOCATE(LQ,ASP,X1,EL,EH,K1,K2,K3,CON)                        A 175
      IF(CON.EQ.3.0)GO TO 110                                           A 176
      CALL  LOCATE(LZ,BSP,Z1,FL,FH,J1,J2,J3,CON)                        A 177
      IF(CON.EQ.3.0)KM=KM+1                                             A 178
      IF(CON.EQ.0.0)GO TO 110                                           A 179
      DEP=FLOAT(J2-1)*HZ                                                A 180
      IF(X1.GT.ASP(2) .OR. DEP.GT.DEPTH)CALL GRADXZ(LX,LZ,NDIST,HX,HZ,J1 A 181
     1,J2,1.0)                                                          A 182
      IF(DEP.GT.DEPTH)DEPTH=DEP                                         A 183
      C1=(Z1-AZ(J1,K1))/HZ                                              A 184
      C2=(X1-AX(J1,K1))/HX                                              A 185
      V1=V(J1,K1)+(V(J2,K1)-V(J1,K1))*C1                                A 186
      V2=V(J1,K2)+(V(J2,K2)-V(J1,K2))*C1                                A 187
      VB=V1+(V2-V1)*C2                                                  A 188
      GO TO 55                                                          A 189
C                                                                       A 190
C     SPECIAL CASE OF GRAD(V)=0                                         A 191
C                                                                       A 192
90    ZI=ARC                                                            A 193
      ETA=0.0                                                           A 194
      DELT=ZI/VA                                                        A 195
```

```
      X1=X1+ZI*COS(PHI)+ETA*SIN(PHI)                                    A 196
      Z1=Z1+ZI*SIN(PHI)-ETA*COS(PHI)                                    A 197
      RB=RADIUS-Z1                                                      A 198
      IF(RB.LT.RADIUS)T=T+DELT                                          A 199
      IF(RB.GT.RADIUS)99,85                                             A 200
99    X1=X1-ZI*COS(PHI)                                                 A 201
      Z1=Z1-ZI*SIN(PHI)                                                 A 202
      CALL INTFAC1(X1,Z1,PHI,VA,T,ARC)                                  A 203
      BETA=DELPHI*180.0/PI                                              A 204
      ANGL=ANGI*ONPI                                                    A 205
      TETA=THETA*ONPI                                                   A 206
      GAMA=PHI*ONPI                                                     A 207
      IF(IWRT.EQ.1)WRITE(6,15)X1,Z1,GAMA,RHO,BETA,VA,TETA,ANGL          A 208
      DIST=X1                                                           A 209
      I=I+1                                                             A 210
      X2(I)=X1                                                          A 211
      Z2(I)=Z1                                                          A 212
      GO TO 110                                                         A 213
C                                                                       A 214
C     SPECIAL CASE OF SIN(ANGI)=0                                       A 215
C                                                                       A 216
100   Z1=ARC                                                            A 217
      ETA=0.0                                                           A 218
      X1=X1+ZI*COS(PHI)                                                 A 219
      Z1=Z1+ZI*SIN(PHI)                                                 A 220
      RB=RADIUS-Z1                                                      A 221
      PHI=PHI                                                           A 222
      IF(RB.GT.RADIUS)101,102                                           A 223
101   X1=X1-ZI*COS(PHI)                                                 A 224
      Z1=Z1-ZI*SIN(PHI)                                                 A 225
      CALL INTFAC1(X1,Z1,PHI,VA,DUMM,ARC)                               A 226
      DIST=X1                                                           A 227
      I=I+1                                                             A 228
      X2(I)=X1                                                          A 229
      Z2(I)=Z1                                                          A 230
102   CONTINUE                                                          A 231
      IF(MOIST.EQ.LX)104,103                                            A 232
103   IF(X1.GT.ASP(2))CALL CLEAN(LX,LZ,MOIST,HX,HZ,BB,ASP)              A 233
104   CALL  LOCATE(LQ,ASP,X1,EL,EH,K1,K2,K3,CON)                        A 234
      IF(CON.EQ.0.0)GO TO 110                                           A 235
      CALL  LOCATE(LZ,BSP,Z1,FL,FH,J1,J2,J3,CON)                        A 236
      IF(CON.EQ.0.0)KM=KM+1                                             A 237
      IF(CON.EQ.0.0)GO TO 110                                           A 238
      DEP=FLOAT(J2-1)*HZ                                                A 239
      IF(X1.GT.ASP(2) .OR. DEP.GT.DEPTH)CALL GRADXZ(LX,LZ,MOIST,HX,HZ,J1 A 240
     1,J2,1.0)                                                          A 241
      IF(DEP.GT.DEPTH)DEPTH=DEP                                         A 242
      C1=(Z1-AZ(J1,K1))/HZ                                              A 243
      C2=(X1-AX(J1,K1))/HX                                              A 244
      V1=V(J1,K1)+(V(J2,K1)-V(J1,K1))*C1                                A 245
      V2=V(J1,K2)+(V(J2,K2)-V(J1,K2))*C1                                A 246
      VB=V1+(V2-V1)*C2                                                  A 247
      DELT=(1.0/GRADV)*ALOG(VB/VA)                                      A 248
      T=T+DELT                                                          A 249
      BETA=DELPHI*180.0/PI                                              A 250
      ANGL=ANGI*ONPI                                                    A 251
      TETA=THETA*ONPI                                                   A 252
      GAMA=PHI*ONPI                                                     A 253
      IF(IWRT.EQ.1)WRITE(6,15)X1,Z1,GAMA,RHO,BETA,VA,TETA,ANGL          A 254
      IF(RB.GT.RADIUS)110,55                                            A 255
C                                                                       A 256
C     SUMMARIZE TRAVEL TIME RESULTS                                     A 257
```

```
C                                                                               A 258
110   TOTIM(J)=T                                                                A 259
      TOTD(J)=DIST                                                              A 260
      RTM(J)=T-(DIST-X2(1))/6.5                                                 A 261
      IF(IPUNCH.EQ.1 .AND. CON.EQ.1.0)WRITE(7,19)TOTD(J),TOTIM(J),RTM(J)        A 262
     1,PP                                                                       A 263
      WRITE(6,19)TOTD(J),TOTIM(J),RTM(J),PP                                     A 264
      LPLT=I                                                                    A 265
      IF(CON.EQ.0.0)RTM(J)=999.9999                                             A 266
      IF(KM.EQ.10)LL=J                                                          A 267
      IF(IPLOT.GT.0)CALL RAYPLTB(LPLT,XZ,TOTD,ZZ,RTM,CMN,XOA,ZMN,ZOA,TMN       A 268
     1,TOA,J,LL,IPLOT)                                                          A 269
      REWIND 10                                                                 A 270
      READ(10)IDUM,JDUM,CUM1,CUM2                                               A 271
      CALL VELALOC(LZ,MDIST,HX,HZ,88,0.0)                                       A 272
      DO 119 K=1,3                                                              A 273
119   ASP(K)=AX(1,K)                                                            A 274
      IF(J.EQ.LL)120,51                                                         A 275
120   CONTINUE                                                                  A 276
      WRITE(6,17)                                                               A 277
      DO 18 J=1,LL                                                              A 278
18    WRITE(6,19)TOTD(J),TOTIM(J),RTM(J)                                        A 279
      CALL PLTEPP(1)                                                            A 280
      IF(IPLOT.GT.0)CALL ENDPLT                                                 A 281
      STOP                                                                      A 282
2     FORMAT(2F5.1,F5.2,4I5)                                                    A 283
3     FORMAT(2F5.2)                                                             A 284
12    FORMAT(1H0,*       X1        Z1       PHI         RHO        DELPHI     A 285
     1 VA     THETA     ANGI*)                                                  A 286
15    FORMAT(1X,3F10.4,1X,E12.6,1X,2(F7.3,1X),2(F8.3,1X))                       A 287
16    FORMAT(1H1,*TOTAL TRAVEL TIME =*,F10.4,*SEC.*)                            A 288
17    FORMAT(1H0,*   DIST(KM)   TIME     REC.TT.       RAY P*)                A 289
19    FORMAT(1X,3F10.4,9X,F10.4)                                                A 290
      END                                                                       A 291
```

```
      FUNCTION ARCTAN(Y,X)                                              B   1
C                                                                       B   2
C     THIS FUNCTION COMPUTES THE ARCTANGENT OF PARAMETER                B   3
C                                                                       B   4
      PI=3.14159265                                                     B   5
      IF(X.EQ.0.0)2,1                                                   B   6
1     ARCTAN=ATAN2(Y,X)                                                 B   7
      GO TO 6                                                           B   8
2     IF(Y-0.0)3,4,5                                                    B   9
3     ARCTAN=-PI/2.0                                                    B  10
      GO TO 6                                                           B  11
4     ARCTAN=0.0                                                        B  12
      GO TO 6                                                           B  13
5     ARCTAN=PI/2.0                                                     B  14
6     RETURN                                                            B  15
      END                                                               B  16


      SUBROUTINE PAYPLTA(XMX,ZMX,YMX,XMN,XD,ZMN,ZD,YMN,YD,IPLOT)        C   1
C                                                                       C   2
C     PLOTS AXES                                                        C   3
C                                                                       C   4
      DIMENSION TITL1(10),TITL2(10)                                     C   5
      CALL PLOTS(60,25.0,10.75,2)                                       C   6
      CALL FACTOR(0.9)                                                  C   7
      XMN=0.0                                                           C   8
      YMN=0.0                                                           C   9
      XD=22.0                                                           C  10
      YD=5.0/8.0                                                        C  11
      ZD=XD                                                             C  12
      XL=XMX/XD                                                         C  13
      YL=(YMX-YMN)/YD                                                   C  14
      ZL=ZMX/ZD                                                         C  15
      XIN=(1.0/XD)*5.0                                                  C  16
      YIN=(1.0/YD)*0.2                                                  C  17
      ZIN=(1.0/ZD)*5.0                                                  C  18
      ZMN=-ZMX                                                          C  19
      TITL1(1)=10HT-X/6.5 (S                                            C  20
      TITL1(2)=3HEC)                                                    C  21
      TITL2(1)=10HDEPTH (KM)                                            C  22
      A1=1.0                                                            C  23
      A2=15.0                                                           C  24
      IF(IPLOT.EQ.1)CALL PLOT(2.0,10.5,-3)                              C  25
      IF(IPLOT.EQ.2)CALL PLOT(8.5,10.5,-3)                              C  26
      CALL AXIS4(0.0,0.0,14HDISTANCE X(KM),14,-.2,-.15,XL,-90.,XMN,XD,-1C  27
     1,XIN,4)                                                           C  28
      CALL XAXIS(0.,0.,TITL1,13,.2,.15,YL,0.,YMN,YD,YIN,1.0,5,A1,1)     C  29
      IF(IPLOT.EQ.1)CALL PLOT(0.0,-XL,-3)                               C  30
      IF(IPLOT.EQ.1)GO TO 5                                             C  31
      CALL PLOT(-1.5,0.0,-3)                                            C  32
      CALL PLOT(0.0,-XL,2)                                              C  33
      CALL PLOT(0.0,0.0,3)                                              C  34
      CALL XAXIS(0.,0.,TITL2,10,.2,.15,ZL,180.,XMN,XD,ZIN,-1.0,3,A2,-1) C  35
      CALL PLOT(-ZL,-XL,-3)                                             C  36
5     CONTINUE                                                          C  37
      RETURN                                                            C  38
      END                                                               C  39
```

```
      SUBROUTINE XAXIS(XO,YO,TITLE,NSYM,THT,HT,XL,THETA,XMN,XO,XIN,SIGN,   0   1
     1K,FACT,IDEC)                                                         0   2
C                                                                          0   3
C     THIS SUBROUTINE IS USED TO DRAW A Y-AXIS WITH UPRIGHT LABELS.        0   4
C     XO,YO....COORD OF START OF AXIS.                                     0   5
C     TITLE....TITLE OF AXIS. NSYM....NO OF CHARACTERS IN TITLE.           0   6
C     THT,HT....HEIGHTS OF TITLE AND ANOTATION. YL....LENGHT OF AXIS.      0   7
C     THETA....ANGLE IN DEGREES OF AXIS. YMN,YO....MINIMUM Y AND SCALE F   0   8
C     YIN....DISTANCE BETWEEN TICK MARKS. SIGN=1.0....Y-AXIS IS +VE.       0   9
C     SIGN=-1.0....Y-AXIS IS -VE. FACT.... Y INCREMENT.                    0  10
C                                                                          0  11
      DIMENSION TITLE(1)                                                   0  12
      AXL=XL*SIGN                                                          0  13
      CALL PLOT(0.0,0.0,3)                                                 0  14
      CALL PLOT(AXL,0.0,2)                                                 0  15
      CALL PLOT(0.0,0.0,3)                                                 0  16
      XLOC=XMN-HT/2.0                                                      0  17
      XLOCT=XMN                                                            0  18
      XTIC=XMN                                                             0  19
      A=XMN                                                                0  20
      HTF=HT*6.0/7.0                                                       0  21
      E=2.0                                                                0  22
      F=3.0                                                                0  23
      G=4.0                                                                0  24
      H=5.0                                                                0  25
      I=0                                                                  0  26
      IF(IDEC.EQ.-1)GO TO 1                                                0  27
      E=E+2.0                                                              0  28
      F=F+2.0                                                              0  29
      G=G+2.0                                                              0  30
      H=H+2.0                                                              0  31
1     CONTINUE                                                             0  32
      IF(XLOCT.GT.XL)GO TO 2                                               0  33
      IF(A.LT.10.0)YY=E*HTF                                                0  34
      IF(A.GE.10.0 .AND. A.LT.100.0)YY=F*HTF                               0  35
      IF(A.GE.100.0 .AND. A.LT.1000.0)YY=G*HTF                             0  36
      IF(A.GE.1000.0 .AND. A.LT.10000.0)YY=H*HTF                           0  37
      YLOC=YY                                                              0  38
15    I=I+1                                                                0  39
      II=(I-1)                                                             0  40
      KK=MOD(II,K)                                                         0  41
      IF(KK.EQ.0)TICL=0.12                                                 0  42
      IF(KK.NE.0)TICL=0.06                                                 0  43
      IF(XLOCT.GT.XL)GO TO 2                                               0  44
      CALL PLOT(XTIC,0.0,3)                                                0  45
      CALL PLOT(XTIC,TICL,2)                                               0  46
      CALL PLOT(XTIC,TICL,3)                                               0  47
      XTIC=XTIC+(XIN*SIGN)                                                 0  48
      IF(TICL.EQ.0.12)CALL NUMBER(XLOC,YLOC,HT,A,-90.0,IDEC)               0  49
      XLOC=XLOC+(XIN*SIGN)                                                 0  50
      XLOCT=XLOCT+XIN                                                      0  51
      IF(KK.EQ.0)A=A+FACT                                                  0  52
      IF(KK.NE.0)GO TO 15                                                  0  53
      GO TO 1                                                              0  54
2     CONTINUE                                                             0  55
      YLOC=YLOC+HT                                                         0  56
      XA=(XL-(NSYM*THT*6.0/7.0))/2.0                                       0  57
      IF(SIGN.GT.0.0)XX=XA                                                 0  58
      IF(SIGN.LT.0.0)XX=XA-XL                                              0  59
      CALL SYMBOL(XX,YLOC,THT,TITLE,0.0,NSYM)                              0  60
      RETURN                                                               0  61
      END                                                                  0  62
```

```
      SUBROUTINE WRITER(LX,LZ,HX,HZ,X1,Z1,PHI,PHMN,PAIN,BB,BSP)          E   1
C                                                                        E   2
C     THIS SUBROUTINE PRINTS OUT THE INPUT DATA                          E   3
C                                                                        E   4
C                                                                        E   5
      COMMON /SBO/ AX(300,3),AZ(300,3),V(300,3),VGX(300,3),VGZ(300,3)    E   6
      DIMENSION BB(900)                                                  E   7
      WRITE(6,10)                                                        E   8
      WRITE(6,11)                                                        E   9
      WRITE(6,12)                                                        E  10
      WRITE(6,13)                                                        E  11
      WRITE(6,14)LX,LZ,HX,HZ                                             E  12
      WRITE(6,15)X1,Z1,PHI                                               E  13
      WRITE(6,23)PHMN,PAIN                                               E  14
      WRITE(6,16)                                                        E  15
      LLZ=LZ/4+1                                                         E  16
      READ(10)MOIST                                                      E  17
      READ(10)(BB(I),I=1,LZ)                                             E  18
      DO 5 J=1,LLZ                                                       E  19
      K=J+LLZ                                                            E  20
      KK=K+LLZ                                                           E  21
      JJ=KK+LLZ                                                          E  22
      AZ(J)=(J-1)*HZ                                                     E  23
      AZ(K)=(K-1)*HZ                                                     E  24
      AZ(KK)=(KK-1)*HZ                                                   E  25
      AZ(JJ)=(JJ-1)*HZ                                                   E  26
      WRITE(6,21)J,AZ(J),BB(J),K,AZ(K),BB(K),KK,AZ(KK),BB(KK),JJ,AZ(JJ),  E  27
     1BB(JJ)                                                             E  28
5     CONTINUE                                                           E  29
      REWIND 10                                                          E  30
      READ(10)IDUM,JDUM,DUM1,DUM2                                        E  31
      WRITE(6,19)                                                        E  32
      WRITE(6,20)                                                        E  33
      WRITE(6,22)                                                        E  34
21    FORMAT(1H ,4(I5,2F10.4,5X))                                        E  35
22    FORMAT(1H1////1X)                                                  E  36
23    FORMAT(40X,*FINAL ANGLE OF INCIDENCE =*,F5.2,5X,*INCREMENTAL ANGLE  E  37
     1 =*,F5.2)                                                          E  38
10    FORMAT(1H1,30X,*RAY TRACING*)                                      E  39
11    FORMAT(31X,11H**********)                                          E  40
12    FORMAT(1H0,*INPUT DATA*)                                           E  41
13    FORMAT(1X,10H----------)                                           E  42
14    FORMAT(1H0,*NO OF X-ELEMENTS =*,I5,5X,*NO OF Z-ELEMENTS =*,I5,5X,*  E  43
     1X-SPACING =*,F5.1,* KM  *,*Z-SPACING =*,F5.1,* KM*)                E  44
15    FORMAT(1H0,*COORD OF RAY ENTRY IS*,F5.1,*,*,F5.1,5X,*INITIAL ANGLE  E  45
     1 OF INCIDENCE =*,F5.1,*DEGREES*)                                   E  46
16    FORMAT(1H0,*VELOCITY DATA*)                                        E  47
19    FORMAT(1H0,*OUTPUT DATA*)                                          E  48
20    FORMAT(1X,11H----------)                                           E  49
      RETURN                                                             E  50
      END                                                                E  51
```

```
      SUBROUTINE VELALOC(LZ,MOIST,MX,MZ,BB,SIGN)                        F   1
C                                                                       F   2
C     VELALOC (VELOCITY AND LOCATION) IS DESIGNED TO READ 3 COLUMNS OF  F   3
C     VELOCITY AND LOCATION GRID FROM DISC.  OR SINGLE COLUMNS FOR      F   4
C     UPDATING VELOCITY AND LOCATION DATA.                              F   5
C                                                                       F   6
      COMMON /SBO/ AX(300,3),AZ(300,3),V(300,3),VGX(300,3),VGZ(300,3)   F   7
      DIMENSION BB(900)                                                 F   8
C                                                                       F   9
      IF(SIGN.EQ.0.0)10,11                                              F  10
10    CONTINUE                                                          F  11
      DO 2 J=1,3                                                        F  12
      READ(10)MOIST                                                     F  13
      READ(10)(BB(I),I=1,LZ)                                            F  14
      DO 1 I=1,LZ                                                       F  15
      AX(I,J)=FLOAT(MOIST-1)*MX                                         F  16
      AZ(I,J)=FLOAT(I-1)*MZ                                             F  17
      V(I,J)=BB(I)                                                      F  18
1     CONTINUE                                                          F  19
2     CONTINUE                                                          F  20
      GO TO 12                                                          F  21
11    CONTINUE                                                          F  22
      READ(10)MOIST                                                     F  23
      READ(10)(BB(I),I=1,LZ)                                            F  24
      DO 3 I=1,LZ                                                       F  25
      V(I,3)=BB(I)                                                      F  26
      AX(I,3)=FLOAT(MOIST-1)*MX                                         F  27
      AZ(I,3)=FLOAT(I-1)*MZ                                             F  28
3     CONTINUE                                                          F  29
12    RETURN                                                            F  30
      END                                                               F  31
```

```
      SUBROUTINE  LOCATE(LM,X,A,X1,X2,II,JJ,KK,CONST)                   G   1
C                                                                       G   2
C     THIS SUBROUTINE LOCATES THE POINT (A) WRT (X)-ARRAY LOCATION FOR  G   3
C     USE IN INTERPOLATING GRADIENT FUNCTIONS OF THE POINTS.            G   4
C     X1, X2 ARE THE TWO DISCRETE BOUNDS OF (A). II IS THE ARRAY LOCATIO G   5
C     OF THE LOWER BOUND. LM IS THE MAXIMUM NUMBER OF ARRAY POINTS.     G   6
C                                                                       G   7
      DIMENSION X(300)                                                  G   8
      CONST=1.0                                                         G   9
      I=0                                                               G  10
1     I=I+1                                                             G  11
      IF(I.GE.LM)GO TO 4                                                G  12
      IF(A.EQ.X(1))GO TO 3                                              G  13
      IF(A.GT.X(I) .AND. A.LE.X(I+1))GO TO 2                            G  14
      GO TO 1                                                           G  15
2     X1=X(I)                                                           G  16
      X2=X(I+1)                                                         G  17
      II=I                                                              G  18
      JJ=II+1                                                           G  19
      KK=II+2                                                           G  20
      IF((KK-LM).EQ.1)KK=JJ                                             G  21
      GO TO 5                                                           G  22
3     X1=X(1)                                                           G  23
      X2=0.0                                                            G  24
      II=1                                                              G  25
      JJ=II+1                                                           G  26
      KK=II+2                                                           G  27
      GO TO 5                                                           G  28
4     WRITE(6,6)                                                        G  29
      CONST=0.0                                                         G  30
5     RETURN                                                            G  31
6     FORMAT(1H0,*POINT IS OUTSIDE GRID*)                               G  32
      END                                                               G  33
```

```
      SUBROUTINE GRADXZ(LX,LZ,MOIST,HX,HZ,J1,J2,SIGN)                    H   1
C                                                                        H   2
C     GRADXZ COMPUTES THE X- AND Z- COMPONENTS OF VELOCITY GRADIENT      H   3
C     FOR 2 COLUMNS OF A 3-COLUMN GRID DATA       OR THE CENTRE          H   4
C     COLUMN FOR UPDATING THE GRID IN RAYTRAC2 PROGRAM                   H   5
C                                                                        H   6
      COMMON /S90/ AX(300,3),AZ(300,3),V(300,3),VGX(300,3),VGZ(300,3)    H   7
      IF(SIGN.EQ.0.0)10,11                                               H   8
10    CONTINUE                                                           H   9
      DO 2 I=1,LZ                                                        H  10
      DO 1 J=1,2                                                         H  11
      IF(J.EQ.1)K=J+1                                                    H  12
      IF(J.EQ.1)VGX(I,J)=(V(I,(K+1))-V(I,(K-1)))/(2.0*HX)                H  13
      IF(J.EQ.2)VGX(I,J)=(V(I,(J+1))-V(I,(J-1)))/(2.0*HX)                H  14
      IF(I.EQ.1)L=I+1                                                    H  15
      IF(I.EQ.1)VGZ(I,J)=(V((L+1),J)-V((L-1),J))/(2.0*HZ)                H  16
      IF(I.GT.1 .AND. I.LT.LZ)VGZ(I,J)=(V((I+1),J)-V((I-1),J))/(2.0*HZ)  H  17
      IF(I.EQ.LZ)L=I-1                                                   H  18
      IF(I.EQ.LZ)VGZ(I,J)=(V((L+1),J)-V((L-1),J))/(2.0*HZ)               H  19
1     CONTINUE                                                           H  20
2     CONTINUE                                                           H  21
      GO TO 12                                                           H  22
11    CONTINUE                                                           H  23
      DO 4 I=J1,J2                                                       H  24
      VGX(I,2)=(V(I,3)-V(I,1))/(2.0*HX)                                  H  25
      IF(MOIST.EQ.LX)VGX(I,3)=VGX(I,2)                                   H  26
      IF(I.EQ.1)K=I+1                                                    H  27
      IF(I.EQ.1)VGZ(I,2)=(V((K+1),2)-V((K-1),2))/(2.0*HZ)                H  28
      IF(I.EQ.1 .AND. MOIST.EQ.LX)VGZ(I,3)=(V((K+1),3)-V((K-1),3))/(2.0* H  29
     1HZ)                                                                H  30
      IF(I.GT.1 .AND. I.LT.LZ) VGZ(I,2)=(V((I+1),2)-V((I-1),2))/(2.0*HZ) H  31
      IF(I.GT.1 .AND. I.LT.LZ .AND. MOIST.EQ.LX)VGZ(I,3)=(V((I+1),3)-V(( H  32
     1I-1),3))/(2.0*HZ)                                                  H  33
      IF(I.EQ.LZ)K=I-1                                                   H  34
      IF(I.EQ.LZ)VGZ(I,2)=(V((K+1),2)-V((K-1),2))/(2.0*HZ)               H  35
      IF(I.EQ.LZ .AND. MOIST.EQ.LX)VGZ(I,3)=(V((K+1),3)-V((K-1),3))/(2.0 H  36
     1*HZ)                                                               H  37
4     CONTINUE                                                           H  38
12    RETURN                                                             H  39
      END                                                                H  40
```

```
      SUBROUTINE CLEAN(LX,LZ,MOIST,HX,HZ,BB,ASP)                         I   1
C                                                                        I   2
C     THIS SUBROUTINE SHIFTS DATA GRID ONE COLUMN TO THE RIGHT           I   3
C                                                                        I   4
C                                                                        I   5
      COMMON /S90/ AX(300,3),AZ(300,3),V(300,3),VGX(300,3),VGZ(300,3)    I   6
      DIMENSION BB(900),ASP(30),BSP(300)                                 I   7
      DO 1 I=1,LZ                                                        I   8
      AX(I,1)=AX(I,2)                                                    I   9
      AX(I,2)=AX(I,3)                                                    I  10
      V(I,1)=V(I,2)                                                      I  11
      V(I,2)=V(I,3)                                                      I  12
      VGX(I,1)=VGX(I,2)                                                  I  13
      VGZ(I,1)=VGZ(I,2)                                                  I  14
1     CONTINUE                                                           I  15
      CALL VELALOC(LZ,MOIST,HX,HZ,BB,1.0)                               I  16
      DO 2 J=1,3                                                         I  17
2     ASP(J)=AX(1,J)                                                     I  18
      RETURN                                                             I  19
      END                                                                I  20
```

```
      SUBROUTINE INTFAC1(X1,Z1,PHI,V,DD,ARC)                            K   1
C                                                                       K   2
C     THIS SUBROUTINE BRINGS RAY END PRECISELY TO EARTHeS SURFACE FOR   K   3
C     SPECIAL CASE OF GRAD(V)=0 OR SIN(ANGI)=0                          K   4
C                                                                       K   5
      ALMT=0.01                                                         K   6
      DEN=10.0                                                          K   7
      RE=6371.029                                                       K   8
1     DEN=DEN*2.0                                                       K   9
      GO TO 3                                                           K  10
2     DEN=DEN*0.8                                                       K  11
3     Z=ARC/DEN                                                         K  12
      Z2=Z1+Z*SIN(PHI)                                                  K  13
      RB=RE-Z2                                                          K  14
      IF(RB.GT.RE)1,4                                                   K  15
4     RT=RE-RB                                                          K  16
      IF(RT.GT.ALMT)2,5                                                 K  17
5     X1=X1+Z*COS(PHI)                                                  K  18
      Z1=Z2                                                             K  19
      T=Z/V                                                             K  20
      DD=DD+T                                                           K  21
      RETURN                                                            K  22
      END                                                               K  23
```

```
      SUBROUTINE INTFACE(X1,Z1,PHI,RHO,DPHI,DD,GV,AI)                   J   1
C                                                                       J   2
C     THIS SUBROUTINE BRINGS RAY END PRECISELY TO EARTHeS SURFACE       J   3
C                                                                       J   4
      ALMT=0.01                                                         J   5
      RE=6371.029                                                       J   6
      DEN=10.0                                                          J   7
      ALFA=0.0                                                          J   8
      GO TO 2                                                           J   9
1     ALFA=0.0                                                          J  10
      DEN=DEN*2.0                                                       J  11
2     ALFA=ALFA+(DPHI/DEN)                                              J  12
      Z=RHO*SIN(ALFA)                                                   J  13
      ET=RHO*(1.0-COS(ALFA))                                            J  14
      Z2=Z1+Z*SIN(PHI)-ET*COS(PHI)                                      J  15
      RB=RE-Z2                                                          J  16
      IF(RB.GT.RE)1,3                                                   J  17
3     RT=RE-RB                                                          J  18
      IF(RT.GT.ALMT)2,4                                                 J  19
4     X1=X1+Z*COS(PHI)+ET*SIN(PHI)                                      J  20
      Z1=Z2                                                             J  21
      T=(1.0/GV)*(ATANH(COS(AI))-ATANH(COS(AI+ALFA)))                   J  22
      DD=DD+T                                                           J  23
      RETURN                                                            J  24
      END                                                               J  25
```

```
      SUBROUTINE RAYPLTB(LP,FX,GX,FZ,FT,XMN,XO,ZMN,ZO,TMN,TO,IS1,IS2,IPL  L   1
     1OT)                                                                 L   2
C                                                                         L   3
C     THIS SUBROUTINE PLOTS THE RAY PATH                                  L   4
C     AND THE REDUCED TRAVEL TIME-DISTANCE PLOT                           L   5
C                                                                         L   6
      DIMENSION FX(1),GX(1),FZ(1),FT(1)                                   L   7
      DIMENSION BX(4500),BZ(4500)                                         L   8
      IF(LP.LT.2)GO TO 2                                                  L   9
      IF(IPLOT.EQ.1)GO TO 4                                               L  10
      LQ=0                                                                L  11
      DO 10 K=1,LP                                                        L  12
      IF(FX(K).LT.20.0 .AND. FZ(K).LT.15.0)GO TO 10                       L  13
      LQ=LQ+1                                                             L  14
      BX(LQ)=FX(K)                                                        L  15
      BZ(LQ)=FZ(K)                                                        L  16
10    CONTINUE                                                            L  17
      DO 1 K=1,LQ                                                         L  18
      BX(K)=-1.0*BX(K)                                                    L  19
1     BZ(K)=-1.0*BZ(K)                                                    L  20
      IF(LQ.LT.2)GO TO 4                                                  L  21
      CALL LINE4(BZ,BX,LQ,1,ZMN,ZO,XMN,XO,0,0,7)                          L  22
      GO TO 4                                                             L  23
2     WRITE(6,3)                                                          L  24
3     FORMAT(1HO,17H*****LP=0****LP=0)                                    L  25
4     CONTINUE                                                            L  26
      IF(IS1.EQ.IS2)5,7                                                   L  27
5     ZL=ABS(ZMN/ZO)                                                      L  28
      AMV=1.5+ZL                                                          L  29
      IF(IPLOT.EQ.2)CALL PLOT(AMV,0.0,-3)                                 L  30
      DO 6 I=1,IS2                                                        L  31
      IF(FT(I).GT.5.0)GO TO 6                                             L  32
      IF(GX(I).LT.20.0)GO TO 6                                            L  33
      GX(I)=-1.0*GX(I)                                                    L  34
      X=(GX(I)-XMN)/XO                                                    L  35
      T=(FT(I)-TMN)/TO                                                    L  36
      CALL SYMBOL(T,X,0.08,14,90.0,-1)                                    L  37
      GX(I)=-1.0*GX(I)                                                    L  38
6     CONTINUE                                                            L  39
7     RETURN                                                              L  40
      END                                                                 L  41
```

APPENDIX A.2

Listings of the ray tracing computer program for spherical earth model

```
      PROGRAM RAYTRAC4(INPUT,OUTPUT,PUNCH,TAPE5=INPUT,TAPE6=OUTPUT,TAPE7=  AA   1
     1PUNCH,TAPE10,TAPE1)                                                  AA   2
C                                                                          AA   3
C                                                                          AA   4
C     THIS PROGRAM TRACES RAYS THROUGH A SPHERICAL EARTH MODEL CONSISTIN   AA   5
C     OF A TWO-DIMENSIONAL GRID OF POINTS WITH RANDOM VELOCITY VARIATION   AA   6
C     BY  S.B. OJO.                                                        AA   7
C                                                                          AA   8
C     INPUT PARAMETERS                                                     AA   9
C     ****************                                                     AA  10
C        LX         NO OF GRID POINTS IN THE HORIZONTAL DIRECTION         AA  11
C        LZ         NO OF GRID POINTS IN THE VERTICAL DIRECTION           AA  12
C        HX=HZ      DISTANCE BETWEEN GRID POINTS IN KM.                   AA  13
C        XI,ZIN     COORDINATES OF THE STARTING POINT OF RAY, NORMALLY    AA  14
C                   THE ORIGIN.                                           AA  15
C        RINC       MAXIMUM INCIDENT ANGLE TO BE INVESTIGATED             AA  16
C        RMIN       MINIMUM INCIDENT ANGLE TO BE INVESTIGATED             AA  17
C        AINC       INCREMENTAL VALUE OF INCIDENT ANGLE                   AA  18
C        ITYPE      AN OPTION REDUCING VELOCITY FOR PLOT OUTPUT           AA  19
C                   ITYPE=1    REDUCING VELOCITY = 6.5                    AA  20
C                   ITYPE=2    REDUCING VELOCITY = 8.0                    AA  21
C                   ITYPE=3    REDUCING VELOCITY = 10.6                   AA  22
C        IPLOT      AN OPTION FOR PLOTTING OUTPUT                         AA  23
C                   IPLOT=1    TRAVEL TIME PLOTTED WITH SLOWNESS          AA  24
C                   IPLOT=0    NO PLOT                                    AA  25
C        IPUNCH     AN OPTION TO PUNCH TRAVEL TIME RESULTS ON CA          AA  26
C                   IPUNCH=1   OUTPUT PUNCHED ON CARDS                    AA  27
C                   IPUNCH=0   NO CARD OUTPUT                             AA  28
C        IWRT       AN OPTION TO PRINT DETAIL RAY INFO,  FOR ERROR SEARCH AA  29
C                   IWRT=1     DETAIL INFO PRINTED...ONLY FOR ERROR SEARCH AA  30
C                   IWRT=0     NO PRINTING                                AA  31
C        IDSK       AN OPTION TO STORE RAY WITH COORD. ON DISC...FOR RAY  AA  32
C                   DIAGRAM ONLY.                                         AA  33
C                   IDSK=1     STORED ON DISC                             AA  34
C                   IDSK=0     NO DISC STORAGE                            AA  35
C                                                                          AA  36
C                                                                          AA  37
      COMPLEX Z                                                            AA  38
      DIMENSION ASP(30),BSP(600),BB(900),SL(20),OPMAX(200)                 AA  39
      DIMENSION TOTIM(200),TOTD(200),DX(200),RTM(200)                      AA  40
      COMMON /S30/ V(600,3),VGX(600,3),VGZ(600,3)                          AA  41
C                                                                          AA  42
      RADIUS=6371.028                                                      AA  43
      PI=3.14159265                                                        AA  44
      ONPI=180.0/PI                                                        AA  45
C                                                                          AA  46
      REWIND 10                                                            AA  47
      READ(10)LX,LZ,HX,HZ                                                  AA  48
      ARC=HZ/10.0                                                          AA  49
      ARK=ARC                                                              AA  50
C                                                                          AA  51
      READ(5,2)XI,ZIN,RINC,ITYPE,IPLOT,IPUNCH,IWRT,IDSK                    AA  52
      READ(5,3)RMIN,AINC                                                   AA  53
      RI=RADIUS-ZIN                                                        AA  54
      THI=0.0                                                              AA  55
      X1=XI                                                                AA  56
      Z1=ZIN                                                               AA  57
      IF(ITYPE.EQ.1) REDV=6.5                                              AA  58
      IF(ITYPE.EQ.2) REDV=8.0                                              AA  59
      IF(ITYPE.EQ.3) REDV=10.0                                             AA  60
      CALL WRITER(LX,LZ,HX,HZ,X1,Z1,RINC,RMIN,AINC,BB,BSP)                 AA  61
C                                                                          AA  62
C     DATA MAY BE READ FROM DISC OR TAPE OR CARDS.                         AA  63
```

```
C     V=VELOCITY OF GRID ELEMENTS.                                          AA  64
C     A=COORDINATE OF GRID ELEMENTS                                         AA  65
C                                                                           AA  66
      CALL LOCAVEL(LZ,ASP,BSP,MDIST,HX,HZ,BB,0.0)                           AA  67
      LL=IFIX(((RINC-RMIN)/AINC)+1.0)                                       AA  68
      J=0                                                                   AA  69
      KM=0                                                                  AA  70
51    J=J+1                                                                 AA  71
      T=0.0                                                                 AA  72
      DIST=0.0                                                              AA  73
      DPMX=0.0                                                              AA  74
      DEPTH=HZ*2.0                                                          AA  75
      IF(J.GT.1)RINC=RINC-AINC                                              AA  76
      RIN=RINC/ONPI                                                         AA  77
      PHI=(PI/2.0)-RIN                                                      AA  78
      RA=RI                                                                 AA  79
      RB=RI                                                                 AA  80
      THETA=THI                                                             AA  81
C                                                                           AA  82
C     DETERMINE HOST CELL OF RAY HEAD.                                      AA  83
C                                                                           AA  84
      CALL LOCATX(LX,ASP,THETA,EL,EH,K1,K2,K3,CON)                          AA  85
      IF(CON.EQ.0.0)KM=KM+1                                                 AA  86
      IF(CON.EQ.0.0)GO TO 110                                               AA  87
      CALL LOCATZ(LZ,BSP,RA,FL,FH,J1,J2,J3,CON)                             AA  88
      IF(CON.EQ.0.0)KM=KM+1                                                 AA  89
      IF(CON.EQ.0.0)GO TO 110                                               AA  90
C                                                                           AA  91
C     DETERMINE VELOCITY GRADIENT AT EACH GRID POINT.                       AA  92
C                                                                           AA  93
      CALL GRADXZ(LX,LZ,MDIST,HX,HZ,J1,J2,0.0)                              AA  94
      CALL HELPA(RADIUS,RA,HX,HZ,DTETA,K1,K2,J1,J2,J3,VA,V1,GX,GZ,THETA)    AA  95
      PP=RADIUS*SIN(RIN)/V1                                                 AA  96
      I=0                                                                   AA  97
55    CONTINUE                                                              AA  98
      I=I+1                                                                 AA  99
      IF(I.EQ.1)GO TO 80                                                    AA 100
      RA=RB                                                                 AA 101
C                                                                           AA 102
C     DETERMINE GRAD V AT RAY HEAD LOCATION.                                AA 103
C                                                                           AA 104
      VA=VB                                                                 AA 105
80    CONTINUE                                                              AA 106
      Z=CMPLX(GX,GZ)                                                        AA 107
      GRADV=CABS(Z)                                                         AA 108
      T1=ARCTAN(GZ,GX)                                                      AA 109
      ANGI=T1-(PI/2.0)+RIN                                                  AA 110
      IF(GRADV.EQ.0.0)GO TO 90                                              AA 111
      IF(SIN(ANGI).EQ.0.0)GO TO 100                                         AA 112
      IF(IOSK.EQ.1)CALL CISQUE(RADIUS,RB,THETA,X1,Z1)                       AA 113
      PHI=(PI/2.0)-RIN                                                      AA 114
C                                                                           AA 115
C     COMPUTE RADIUS OF CURVATURE OF RAY PATH AND DETERMINE NEW POSITION    AA 116
C                                                                           AA 117
      RHO=VA/(GRADV*SIN(ANGI))                                              AA 118
      IF(ABS(RHO).GE.100.0)ARK=HZ/10.0                                      AA 119
      IF(ABS(RHO).LT.100.0)ARK=ABS((HZ*RHO)/(10.0*100.0))                   AA 120
      DELPHI=ARK/RHO                                                        AA 121
      IF(IWRT.EQ.1)CALL WRTER(RA,DP,ONPI,DELPHI,ANGI,T1,PHI,RHO,VA,GX,GZ    AA 122
     1,GRADV,THETA,T,RIN)                                                   AA 123
      CALL RPMOVE(RA,DELPHI,RIN,RHO,THETA,ATETA,RB)                         AA 124
      RMR=RADIUS-RB                                                         AA 125
      IF(RMR.GT.DPMX)DPMX=RMR                                               AA 126
C                                                                           AA 127
C     IF RB IS GREATER THAN EARTH RADIUS, THEN RAY HAS PENETRATED EARTH     AA 128
C      SURFACE...THEREFORE DETERMINE PRECISE END OF RAY AT SURFACE          AA 129
```

```
C                                                                       AA 130
      IF(RB.GT.RADIUS)13,14                                             AA 131
13    CONTINUE                                                          AA 132
      CALL INTFACE(RA,RB,RIN,RHO,DELPHI,T,GRADV,ANGI,THETA,ATETA)       AA 133
      I=I+1                                                             AA 134
      GO TO 110                                                         AA 135
14    CONTINUE                                                          AA 136
      DELT=(1.0/GRADV)*(ATANH(COS(ANGI))-ATANH(COS(ANGI+DELPHI)))       AA 137
      T=T+DELT                                                          AA 138
85    CONTINUE                                                          AA 139
      IF(MOIST.EQ.LX)87,86                                              AA 140
86    IF(THETA.GT.ASP(2))CALL CLEAN(LX,LZ,MOIST,HX,HZ,B3,ASP,BSP)       AA 141
87    CALL LOCATX(LX,ASP,THETA,EL,EH,K1,K2,K3,CON)                      AA 142
      IF(CON.EQ.0.0)KM=KM+1                                             AA 143
      IF(CON.EQ.0.0)GO TO 110                                           AA 144
      CALL LOCATZ(LZ,BSP,RB,FL,FH,J1,J2,J3,CON)                         AA 145
      IF(CON.EQ.0.0)KM=KM+1                                             AA 146
      IF(CON.EQ.0.0)GO TO 110                                           AA 147
      DEP=FLOAT(J2-1)*HZ                                                AA 148
      IF(THETA.GT.ASP(2) .OR. DEP.GT.DEPTH)CALL GRADXZ(LX,LZ,MOIST,HX,HZ AA 149
     1,J1,J2,1.0)                                                       AA 150
      IF(DEP.GT.DEPTH)DEPTH=DEP                                         AA 151
C                                                                       AA 152
      CALL HELP3(RADIUS,RB,HX,HZ,DTETA,K1,K2,J1,J2,V0,GX,GZ,THETA)      AA 153
      GO TO 55                                                          AA 154
C                                                                       AA 155
C     SPECIAL CASE OF GRAD(V)=0                                         AA 156
C                                                                       AA 157
90    ZI=ARC                                                            AA 158
      ETA=0.0                                                           AA 159
      DELPHI=0.0                                                        AA 160
      IF(IWRT.EQ.1)CALL WRTER(RA,DP,DNPI,DELPHI,ANGI,T1,PHI,RHO,VA,GX,GZ AA 161
     1,GRADV,THETA,T,RIN)                                               AA 162
      IF(IDSK.EQ.1)CALL DISQUE(RADIUS,RB,THETA,X1,Z1)                   AA 163
      DELT=ZI/VA                                                        AA 164
      CALL RPMOV1(RA,ZI,RIN,THETA,ATETA,RB)                             AA 165
      RMR=RADIUS-RB                                                     AA 166
      IF(RMR.GT.DPMX)DPMX=RMR                                           AA 167
      IF(RB.LT.RADIUS)T=T+DELT                                          AA 168
      IF(RB.GT.RADIUS)99,85                                             AA 169
99    CALL INTFAC1(RA,RB,RIN,VA,T,THETA,ATETA,ZI)                       AA 170
      I=I+1                                                             AA 171
      GO TO 110                                                         AA 172
C                                                                       AA 173
C     SPECIAL CASE OF SIN(ANGI)=0                                       AA 174
C                                                                       AA 175
100   ZI=ARC                                                            AA 176
      ETA=0.0                                                           AA 177
      IF(IWRT.EQ.1)CALL WRTER(RA,DP,DNPI,DELPHI,ANGI,T1,PHI,RHO,VA,GX,GZ AA 178
     1,GRADV,THETA,T,RIN)                                               AA 179
      IF(IDSK.EQ.1)CALL DISQUE(RADIUS,RB,THETA,X1,Z1)                   AA 180
      CALL RPMOV1(RA,ZI,RIN,THETA,ATETA,RB)                             AA 181
      RMR=RADIUS-RB                                                     AA 182
      IF(RMR.GT.DPMX)DPMX=RMR                                           AA 183
      PHI=PHI                                                           AA 184
      IF(RB.GT.RADIUS)101,102                                           AA 185
101   CALL INTFAC1(RA,RB,RIN,VA,DUMM,THETA,ATETA,ZI)                    AA 186
      I=I+1                                                             AA 187
102   CONTINUE                                                          AA 188
      IF(MOIST.EQ.LX)104,103                                            AA 189
103   IF(THETA.GT.ASP(2))CALL CLEAN(LX,LZ,MOIST,HX,HZ,B3,ASP,BSP)       AA 190
104   CALL LOCATX(LX,ASP,THETA,EL,EH,K1,K2,K3,CON)                      AA 191
      IF(CON.EQ.0.0)KM=KM+1                                             AA 192
      IF(CON.EQ.0.0)GO TO 110                                           AA 193
      CALL LOCATZ(LZ,BSP,RB,FL,FH,J1,J2,J3,CON)                         AA 194
      IF(CON.EQ.0.0)KM=KM+1                                             AA 195
```

```
      IF(CON.EQ.0.0)GO TO 110                                              AA 196
      DEP=FLOAT(J2-1)*HZ                                                   AA 197
      IF(THETA.GT.ASP(2) .OR. DEP.GT.DEPTH)CALL GRADXZ(LX,LZ,MDIST,HX,HZ AA 198
     1,J1,J2,1.0)                                                          AA 199
      IF(DEP.GT.DEPTH)DEPTH=DEP                                            AA 200
C                                                                          AA 201
      CALL HELPR(RADIUS,RB,HX,HZ,DTETA,K1,K2,J1,J2,VB,GX,GZ,THETA)         AA 202
      DELT=(1.0/GRADV)*ALOG(VB/VA)                                         AA 203
      T=T+DELT                                                             AA 204
      IF(RB.GT.RADIUS)110,55                                               AA 205
C                                                                          AA 206
C     SUMMARIZE TRAVEL TIME RESULTS                                        AA 207
C                                                                          AA 208
110   TOTIM(J)=T                                                           AA 209
      IF(CON.EQ.0.0)I=I+1                                                  AA 210
      IF(IWRT.EQ.1)CALL WRTER(RA,DP,ONPI,DELPHI,ANGI,TI,PHI,RHO,VA,GX,GZ AA 211
     1,GRADV,THETA,T,RIN)                                                  AA 212
      IF(IDSK.EQ.1)CALL DISQUE(RADIUS,R),THETA,X1,Z1)                      AA 213
      ANO=THETA                                                            AA 214
      DX(J)=RADIUS*ANO                                                     AA 215
      TOTO(J)=ANO*180.0/PI                                                 AA 216
      RTM(J)=T-(RADIUS*ANO)/REDV                                           AA 217
      SL(J)=PP*PI/180.0                                                    AA 218
      DPMAX(J)=DPMX                                                        AA 219
      IF(IPUNCH.EQ.1 .AND. CON.EQ.1.0)WRITE(7,19)DX(J),TOTO(J),TOTIM(J), AA 220
     1RTM(J),SL(J)                                                         AA 221
      WRITE(6,19)DX(J),TOTO(J),TOTIM(J),RTM(J),SL(J),DPMAX(J)              AA 222
      LPLT=I                                                               AA 223
      WRITE(6,111)LPLT                                                     AA 224
      IF(CON.EQ.0.0)RTM(J)=999.9999                                        AA 225
      IF(KM.EQ.5)LL=J                                                      AA 226
      REWIND 10                                                            AA 227
      READ(10)DUM,JDUM,DUM1,DUM2                                           AA 228
      CALL LOCAVEL(LZ,ASP,BSP,MDIST,HX,HZ,B8,0.0)                          AA 229
      IF(J.EQ.LL)120,51                                                    AA 230
120   CONTINUE                                                             AA 231
      WRITE(6,17)                                                          AA 232
      DO 21 J=1,LL                                                         AA 233
21    WRITE(6,19)DX(J),TOTO(J),TOTIM(J),RTM(J),SL(J),DPMAX(J)              AA 234
      IF(IPLOT.EQ.1)CALL TTPLOT(LL,TOTO,TOTIM,RTM,SL,REDV)                 AA 235
      CALL PLTERR(1)                                                       AA 236
      IF(IPLOT.EQ.1)CALL ENDPLT                                            AA 237
      STOP                                                                 AA 238
2     FORMAT(3F5.1,5I5)                                                    AA 239
3     FORMAT(F5.1,F5.2)                                                    AA 240
17    FORMAT(1H0,* DIST(KM)      DIST      TIME     RED.TT.    SLOWNESS    D AA 241
     1PMX*)                                                                AA 242
18    FORMAT(1X,I5)                                                        AA 243
19    FORMAT(1X,6F10.4)                                                    AA 244
20    FORMAT(3X,2E11.5)                                                    AA 245
111   FORMAT(1H ,*TOTAL NUMBER OF RAY SEGMENTS IS*,I5)                     AA 246
      END                                                                  AA 247
```

```
      FUNCTION ARCTAN(Y,X)                                              A8   1
C                                                                       A8   2
C                                                                       A8   3
      PI=3.14159265                                                     A8   4
      IF(X.EQ.0.0)2,1                                                   A8   5
1     ARCTAN=ATAN2(Y,X)                                                 A8   6
      GO TO 6                                                           A8   7
2     IF(Y-0.0)3,4,5                                                    A8   8
3     ARCTAN=-PI/2.0                                                    A8   9
      GO TO 6                                                           A8  10
4     ARCTAN=0.0                                                        A8  11
      GO TO 6                                                           A8  12
5     ARCTAN=PI/2.0                                                     A8  13
6     RETURN                                                            A8  14
      END                                                               A8  15
```

```
      SUBROUTINE DISQUE(RE,RB,THETA,X1,Z1)                              AC   1
C                                                                       AC   2
C     THIS SUBROUTINE WRITES THE COORDINATES OF RAY PATH ON DISC        AC   3
C                                                                       AC   4
      X1=RB*SIN(THETA)                                                  AC   5
      Z1=RE-(RB*COS(THETA))                                             AC   6
      WRITE(1)X1,Z1                                                     AC   7
      RETURN                                                            AC   8
      END                                                               AC   9
```

```
      SUBROUTINE RPMOVE(RA,DPHI,RIN,RHO,THETA,DTETA,RB)                 AD   1
C                                                                       AD   2
C     THIS SUBROUTINE MOVES RAY HEAD TO NEW POSITION AND COMPUTES THE   AD   3
C     NEW POLAR COORDINATES.                                            AD   4
C                                                                       AD   5
      RE=6371.023                                                       AD   6
      PI=3.14159265                                                     AD   7
      DPHI2=DPHI/2.0                                                    AD   8
      ALF=RIN+DPHI2                                                     AD   9
      A=SIN(DPHI2)                                                      AD  10
      B=A*A                                                             AD  11
      C=COS(ALF)                                                        AD  12
      D=SIN(ALF)                                                        AD  13
      P=RA*RA                                                           AD  14
      Q=4.0*RHO*RHO*B                                                   AD  15
      R=4.0*RA*RHO*A*C                                                  AD  16
      RB=SQRT(P+Q-R)                                                    AD  17
      DTETA=ASIN(2.0*RHO*A*D/RB)                                        AD  18
      THETA=THETA+DTETA                                                 AD  19
      RIN=RIN+DPHI+DTETA                                                AD  20
      RETURN                                                            AD  21
      END                                                               AD  22
```

```
      SUBROUTINE RPMOV1(RA,Z,RIN,THETA,DTETA,RB)                        AE   1
C     THIS SUBROUTINE MOVES RAY HEAD TO NEW POINT FOR SPECIAL CASE GRADV AE   2
C                                                                       AE   3
      RE=6371.028                                                       AE   4
      A=RA*RA                                                           AE   5
      B=Z*Z                                                             AE   6
      C=2.0*RA*Z*COS(RIN)                                               AE   7
      RB=SQRT(A+B-C)                                                    AE   8
      DTETA=ASIN((Z*SIN(RIN))/RB)                                       AE   9
      THETA=THETA+DTETA                                                 AE  10
      RIN=RIN+DTETA                                                     AE  11
      RETURN                                                            AE  12
      END                                                               AE  13


      SUBROUTINE WRTER(RA,DP,DNPI,DPH,AI,TE,PH,RHO,VA,GX,GZ,GRADV,ALF,TM AF   1
     1,RN)                                                              AF   2
C                                                                       AF   3
C     THIS SUBROUTINE PRINTS DETAIL PARAMETERS OF RAY PATH FOR DEBUGGING AF   4
C     PURPOSES ONLY                                                     AF   5
C                                                                       AF   6
      RE=6371.028                                                       AF   7
      DP=RE-RA                                                          AF   8
      BETA=DPH*DNPI                                                     AF   9
      ANGL=AI*DNPI                                                      AF  10
      TETA=TE*DNPI                                                      AF  11
      GAMA=PH*DNPI                                                      AF  12
      ALFA=ALF*DNPI                                                     AF  13
      WRITE(6,12)                                                       AF  14
12    FORMAT(1H0,*       RA       DEPTH     PHI         RHO        DELPHI     AF  15
     1 VA      T1        ANGI      GX        GZ       GRDV     THETA     RINC AF  16
     1    TIME*)                                                       AF  17
      WRITE(6,1)PA,DP,GAMA,RHO,BETA,VA,TETA,ANGL,GX,GZ,GRADV,ALFA,RN,TM AF  18
1     FORMAT(1X,3F16.4,1X,E12.6,1X,2(F7.3,1X),8(F8.3,1X))               AF  19
      RETURN                                                            AF  20
      END                                                               AF  21


      SUBROUTINE INTFACE(RA,RB,RIN,RHO,DPHI,DD,GV,AI,TETA,DTETA)        AG   1
C                                                                       AG   2
C     THIS SUBROUTINE BRINGS RAY END PRECISELY TO EARTH#S SURFACE       AG   3
C                                                                       AG   4
      RE=6371.028                                                       AG   5
      ALMT=0.01                                                         AG   6
      ALFA=0.0                                                          AG   7
      BETA=DPHI*0.01                                                    AG   8
      I=0                                                               AG   9
      IF(ABS(RE-RB).GT.ALMT)2,6                                         AG  10
2     TETA=TETA-DTETA                                                   AG  11
      RIN=RIN-DTETA-DPHI                                                AG  12
3     ALFA=ALFA+BETA                                                    AG  13
      I=I+1                                                             AG  14
      IF(I.GT.500)GO TO 7                                               AG  15
      CALL RPMOVE(RA,ALFA,RIN,RHO,TETA,DTETA,RB)                        AG  16
      IF(ABS(RE-RB).GT.ALMT)4,5                                         AG  17
4     TETA=TETA-DTETA                                                   AG  18
      RIN=RIN-DTETA-ALFA                                                AG  19
      GO TO 3                                                           AG  20
5     DPHI=ALFA                                                         AG  21
6     T=(1.0/GV)*(ATANH(COS(AI))-ATANH(COS(AI+DPHI)))                   AG  22
      DD=DD+T                                                           AG  23
      GO TO 8                                                           AG  24
7     WRITE(6,10)                                                       AG  25
10    FORMAT(1H1,51H*******INFINITE LOOP ENCOUNTERED IN INTERFACE******) AG  26
      STOP                                                              AG  27
8     RETURN                                                            AG  28
      END                                                               AG  29
```

```
      SUBROUTINE INTFAC1(RA,RB,RIN,V,OD,TETA,DTETA,ARC)                 AH   1
C                                                                       AH   2
C     THIS SUBROUTINE BRINGS RAY END PRECISELY TO EARTH'S SURFACE FOR   AH   3
C     SPECIAL CASE OF GRAD(V)=0 OR SIN(ANGI)=0                          AH   4
C                                                                       AH   5
      RE=6371.023                                                       AH   6
      ALMT=0.01                                                         AH   7
      ALFA=0.0                                                          AH   8
      BETA=ARC*0.01                                                     AH   9
      I=0                                                               AH  10
      IF(ABS(RE-RB).GT.ALMT)2,6                                         AH  11
2     TETA=TETA-DTETA                                                   AH  12
      RIN=RIN-DTETA                                                     AH  13
3     ALFA=ALFA+BETA                                                    AH  14
      I=I+1                                                             AH  15
      IF(I.GT.500)GO TO 7                                               AH  16
      CALL RMOV1(RA,ALFA,RIN,TETA,DTETA,RB)                             AH  17
      IF(ABS(RE-RB).GT.ALMT)4,5                                         AH  18
4     TETA=TETA-DTETA                                                   AH  19
      RIN=RIN-DTETA                                                     AH  20
      GO TO 3                                                           AH  21
5     ARC=ALFA                                                          AH  22
6     T=ARC/V                                                           AH  23
      OD=OD+T                                                           AH  24
      GO TO 8                                                           AH  25
7     WRITE(6,10)                                                       AH  26
10    FORMAT(1H1,51H*******INFINITE LOOP ENCOUNTERED IN INTERFAC1******)AH  27
      STOP                                                              AH  28
8     RETURN                                                            AH  29
      END                                                               AH  30


      SUBROUTINE TTPLOT(LT,DIST,TT,RTT,SL,REDV)                         AI   1
C                                                                       AI   2
C     THIS SUBROUTINE PLOTS TRAVEL TIME CURVE OUTPUT PLUS SLOWNESS      AI   3
C                                                                       AI   4
      DIMENSION DIST(1),TT(1),RTT(1),SL(1)                              AI   5
      PI=3.14159265                                                     AI   6
      REDF=6371.023*PI/180.0                                            AI   7
      REDVI=1.0/REDV                                                    AI   8
C                                                                       AI   9
      DMN=10.0                                                          AI  10
      DMX=38.0                                                          AI  11
      RTMN=25.0                                                         AI  12
      RTMX=70.0                                                         AI  13
      SLMN=7.0                                                          AI  14
      SLMX=15.0                                                         AI  15
      DDA=2.0                                                           AI  16
      RTDA=2.5                                                          AI  17
      SLDA=1.0                                                          AI  18
      XL=(DMX-DMN)/DDA                                                  AI  19
      AMV=XL+5.0                                                        AI  20
      CALL TTAXIS(DMN,DMX,DDA,RTMN,RTMX,RTDA,SLMN,SLMX,SLDA)            AI  21
      DO 1 I=1,LT                                                       AI  22
      IF(DIST(I).GT.DMX .OR. DIST(I).LT.DMN)GO TO 1                     AI  23
      IF(RTT(I).GT.RTMX .OR. RTT(I).LT.RTMN)GO TO 1                     AI  24
      X=(DIST(I)-DMN)/DDA                                               AI  25
      Y=(RTT(I)-RTMN)/RTDA                                              AI  26
      SLO=((SL(I)/REDF)-REDVI)*REDF*DDA/RTDA                            AI  27
      DECL=ATAN(SLO)                                                    AI  28
      DECL=(PI/2.0)-DECL                                                AI  29
      TETA=-1.0*DECL*180.0/PI                                           AI  30
      CALL SYMBOL(X,Y,0.5,13,TETA,-1)                                   AI  31
1     CONTINUE                                                          AI  32
      CALL PLOT(AMV,0.0,-3)                                             AI  33
      DO 2 K=1,LT                                                       AI  34
      IF(RTT(K).EQ.999.9999)GO TO 2                                     AI  35
      IF(DIST(K).GT.DMX .OR. DIST(K).LT.DMN)GO TO 2                     AI  36
      XX=(DIST(K)-DMN)/DDA                                              AI  37
      YY=(SL(K)-SLMN)/SLDA                                              AI  38
      CALL SYMBOL(XX,YY,.25,11,0.0,-1)                                  AI  39
2     CONTINUE                                                          AI  40
      RETURN                                                            AI  41
      END                                                               AI  42
```

```
      SUBROUTINE TTAXIS(XMN,XMX,XDA,TMN,TMX,TDA,SMN,SMX,SDA)                AJ   1
C                                                                           AJ   2
C     THIS SUBROUTINE PREPARES PARAMETER FOR PLOT                           AJ   3
C                                                                           AJ   4
      CALL PLOTS(30,20.0,10.75,2)                                           AJ   5
      CALL FACTOR(1.0/2.54)                                                 AJ   6
      XL=(XMX-XMN)/XDA                                                      AJ   7
      YL=(TMX-TMN)/TDA                                                      AJ   8
      ZL=(SMX-SMN)/SDA                                                      AJ   9
      AMV=XL+5.0                                                            AJ  10
      XIN=(1.0/XDA)                                                         AJ  11
      TIN=(1.0/TDA)                                                         AJ  12
      SIN=(1.0/SDA)*0.2                                                     AJ  13
      CALL PLOT(5.0,5.0,-3)                                                 AJ  14
      CALL AXIS4(0.0,0.0,14HDISTANCE (DEG),14,-.5,-.5,XL,0.,XMN,XDA,-1,X    AJ  15
     1IN,5)                                                                 AJ  16
      CALL AXIS4(0.0,0.0,25HREDUCED TRAVEL TIME (SEC),25,.5,.5,YL,90.,TM    AJ  17
     1N,TDA,-1,TIN,5)                                                       AJ  18
      CALL PLOT(AMV,0.0,-3)                                                 AJ  19
      CALL AXIS4(0.0,0.0,14HDISTANCE (DEG),14,-.5,-.5,XL,0.,XMN,XDA,-1,X    AJ  20
     1IN,5)                                                                 AJ  21
      CALL AXIS4(0.0,0.0,18HSLOWNESS (SEC/DEG),18,.5,.5,ZL,90.,SMN,SDA,-    AJ  22
     11,SIN,10)                                                             AJ  23
      CALL PLOT(-AMV,0.0,-3)                                                AJ  24
      RETURN                                                                AJ  25
      END                                                                   AJ  26
```

```
      SUBROUTINE CLEAN(LX,LZ,MDIST,MX,MZ,BB,ASP,BSP)                        AK   1
C                                                                           AK   2
C     THIS SUBROUTINE SHIFTS DATA GRID BY ONE COLUMN TO THE RIGHT           AK   3
C                                                                           AK   4
      COMMON /SBO/ V(600,3),VGX(600,3),VGZ(600,3)                           AK   5
      DIMENSION BB(1),ASP(1),BSP(1)                                         AK   6
      DO 1 I=1,LZ                                                           AK   7
      V(I,1)=V(I,2)                                                         AK   8
      V(I,2)=V(I,3)                                                         AK   9
      VGX(I,1)=VGX(I,2)                                                     AK  10
      VGZ(I,1)=VGZ(I,2)                                                     AK  11
1     CONTINUE                                                              AK  12
      CALL LOCAVEL(LZ,ASP,BSP,MDIST,MX,MZ,BB,1.0)                           AK  13
      RETURN                                                                AK  14
      END                                                                   AK  15
```

```
      SUBROUTINE GRADXZ(LX,LZ,MOIST,HX,HZ,J1,J2,SIGN)                    AL   1
C                                                                        AL   2
C     GRADXZ COMPUTES THE X- AND Z- COMPONENTS OF VELOCITY GRADIENT      AL   3
C     FOR 2 COLUMNS OF A 3-COLUMN GRID ,  OR THE CENTRE                  AL   4
C     COLUMN FOR UPDATING THE GRID IN RAYTRAC2 PROGRAM                   AL   5
C                                                                        AL   6
      COMMON /S90/ V(600,3),VGX(600,3),VGZ(600,3)                        AL   7
      RE=6371.028                                                        AL   8
      DTETA=HX/RE                                                        AL   9
      IF(SIGN.EQ.1.0)10,11                                               AL  10
10    CONTINUE                                                           AL  11
      DO 2 I=1,LZ                                                        AL  12
      DS=(RE-((I-1)*HZ))*SIN(DTETA)                                      AL  13
      DO 1 J=1,2                                                         AL  14
      IF(J.EQ.1)K=J+1                                                    AL  15
      IF(J.EQ.1)VGX(I,J)=(V(I,(K+1))-V(I,(K-1)))/(2.0*DS)                AL  16
      IF(J.EQ.2)VGX(I,J)=(V(I,(J+1))-V(I,(J-1)))/(2.0*DS)                AL  17
      IF(I.EQ.1)L=I+1                                                    AL  18
      IF(I.EQ.1)VGZ(I,J)=(V((L+1),J)-V((L-1),J))/(2.0*HZ)                AL  19
      IF(I.GT.1 .AND. I.LT.LZ)5,8                                        AL  20
5     IF(I.GT.2 .AND. I.LT.(LZ-2))6,7                                    AL  21
6     VGZ(I,J)=(V((I-2),J)-8.0*(V((I-1),J))+8.0*(V((I+1),J))-V((I+2),J)) AL  22
     1/(12.0*HZ)                                                         AL  23
      GO TO 1                                                            AL  24
7     VGZ(I,J)=(V((I+1),J)-V((I-1),J))/(2.0*HZ)                          AL  25
      GO TO 1                                                            AL  26
8     CONTINUE                                                           AL  27
      IF(I.EQ.LZ)L=I-1                                                   AL  28
      IF(I.EQ.LZ)VGZ(I,J)=(V((L+1),J)-V((L-1),J))/(2.0*HZ)               AL  29
1     CONTINUE                                                           AL  30
2     CONTINUE                                                           AL  31
      GO TO 20                                                           AL  32
11    CONTINUE                                                           AL  33
      DO 4 I=J1,J2                                                       AL  34
      DS=(RE-((I-1)*HZ))*SIN(DTETA)                                      AL  35
      VGX(I,2)=(V(I,3)-V(I,1))/(2.0*DS)                                  AL  36
      IF(MOIST.EQ.LX)VGX(I,3)=VGX(I,2)                                   AL  37
      IF(I.EQ.1)K=I+1                                                    AL  38
      IF(I.EQ.1)VGZ(I,2)=(V((K+1),2)-V((K-1),2))/(2.0*HZ)                AL  39
      IF(I.EQ.1 .AND. MOIST.EQ.LX)VGZ(I,3)=(V((K+1),3)-V((K-1),3))/(2.0* AL  40
     1HZ)                                                                AL  41
      IF(I.GT.1 .AND. I.LT.LZ)12,19                                      AL  42
12    IF(I.GT.2 .AND. I.LT.(LZ-2))13,16                                  AL  43
13    IF(MOIST.EQ.LX)14,15                                               AL  44
14    VGZ(I,3)=(V((I-2),3)-8.0*(V((I-1),3))+8.0*(V((I+1),3))-V((I+2),3)) AL  45
     1/(12.0*HZ)                                                         AL  46
      GO TO 4                                                            AL  47
15    VGZ(I,2)=(V((I-2),2)-8.0*(V((I-1),2))+8.0*(V((I+1),2))-V((I+2),2)) AL  48
     1/(12.0*HZ)                                                         AL  49
      GO TO 4                                                            AL  50
16    IF(MOIST.EQ.LX)17,18                                               AL  51
17    VGZ(I,3)=(V((I+1),3)-V((I-1),3))/(2.0*HZ)                          AL  52
      GO TO 4                                                            AL  53
18    VGZ(I,2)=(V((I+1),2)-V((I-1),2))/(2.0*HZ)                          AL  54
      GO TO 4                                                            AL  55
19    CONTINUE                                                           AL  56
      IF(I.EQ.LZ)K=I-1                                                   AL  57
      IF(I.EQ.LZ)VGZ(I,2)=(V((K+1),2)-V((K-1),2))/(2.0*HZ)               AL  58
      IF(I.EQ.LZ .AND. MOIST.EQ.LX)VGZ(I,3)=(V((K+1),3)-V((K-1),3))/(2.0 AL  59
     1*HZ)                                                               AL  60
4     CONTINUE                                                           AL  61
20    RETURN                                                             AL  62
      END                                                                AL  63
```

```
      SUBROUTINE LOCAVEL(LZ,ASP,BSP,MOIST,HX,HZ,BB,SIGN)                AM   1
C                                                                       AM   2
C     LOCAVEL (VELOCITY AND LOCATION) IS DESIGNED TO READ 3 COLUMNS OF  AM   3
C     VELOCITY AND LOCATION GRID FROM DISC,  OR SINGLE COLUMNS FOR      AM   4
C     UPDATING VELOCITY AND LOCATION DATA.                              AM   5
C                                                                       AM   6
      COMMON /SBO/ V(600,3),VGX(600,3),VGZ(600,3)                       AM   7
      DIMENSION BB(1),ASP(1),BSP(1)                                     AM   8
C                                                                       AM   9
      RE=6371.028                                                       AM  10
      DTHETA=HX/RE                                                      AM  11
      IF(SIGN.EQ.0.0)10,11                                              AM  12
10    CONTINUE                                                          AM  13
      DO 2 J=1,3                                                        AM  14
      READ(10)MOIST                                                     AM  15
      ASP(J)=FLOAT(MOIST-1)*DTHETA                                      AM  16
      READ(10)(BB(I),I=1,LZ)                                            AM  17
      DO 1 I=1,LZ                                                       AM  18
      BSP(I)=RE-(FLOAT(I-1)*HZ)                                         AM  19
      V(I,J)=BB(I)                                                      AM  20
1     CONTINUE                                                          AM  21
2     CONTINUE                                                          AM  22
      GO TO 12                                                          AM  23
11    CONTINUE                                                          AM  24
      READ(10)MOIST                                                     AM  25
      THETA=FLOAT(MOIST-1)*DTHETA                                       AM  26
      ASP(1)=ASP(2)                                                     AM  27
      ASP(2)=ASP(3)                                                     AM  28
      ASP(3)=THETA                                                      AM  29
      READ(10)(BB(I),I=1,LZ)                                            AM  30
      DO 3 I=1,LZ                                                       AM  31
      V(I,3)=BB(I)                                                      AM  32
3     CONTINUE                                                          AM  33
12    RETURN                                                            AM  34
      END                                                               AM  35
```

```
      SUBROUTINE HELPA(RE,RA,HX,HZ,DTETA,K1,K2,J1,J2,J3,VA,V1,GX,GZ,ALF) AN   1
C                                                                       AN   2
C     THIS SUBROUTINE INTERPOLATES VELOCITIES AND VELOCITY GRADIENTS    AN   3
C     BETWEEN GRID POINTS.                                              AN   4
C                                                                       AN   5
C                                                                       AN   6
      COMMON /SBO/ V(600,3),VGX(600,3),VGZ(600,3)                       AN   7
      DTETA=HX/RE                                                       AN   8
      BA=AMOD(ALF,DTETA)                                                AN   9
      BB=(RA*BA)/(RA*DTETA)                                             AN  10
      BC=(RE-(FLOAT(J1-1)*HZ)-RA)                                       AN  11
      V1=V(J1,K1)+(V(J1,K2)-V(J1,K1))*BB                                AN  12
      V2=V(J2,K1)+(V(J2,K2)-V(J2,K1))*BB                                AN  13
      V3=V(J3,K1)+(V(J3,K2)-V(J3,K1))*BB                                AN  14
      VA=V1+(V2-V1)*BC/HZ                                               AN  15
      GX=VGX(J1,K1)+(VGX(J1,K2)-VGX(J1,K1))*BC/HZ                       AN  16
      GZ=(V3-V1)/(2.0*HZ)                                               AN  17
      RETURN                                                            AN  18
      END                                                               AN  19
```

```
      SUBROUTINE HELPB(RE,RA,HX,HZ,DTETA,K1,K2,J1,J2,VA,GX,GZ,ALFA)      AO   1
C                                                                        AO   2
C     THIS SUBROUTINE INTERPOLATES VELOCITIES AND VELOCITY GRADIENTS     AO   3
C     BETWEEN GRID POINTS.                                               AO   4
C                                                                        AO   5
C                                                                        AO   6
      COMMON /SBO/ V(600,3),VGX(600,3),VGZ(600,3)                        AO   7
      BA=AMOD(ALFA,DTETA)                                                AO   8
      BB=(RA*BA)/(RA*DTETA)                                              AO   9
      BC=(RE-(FLOAT(J1-1)*HZ)-RA)                                        AO  10
      V1=V(J1,K1)+(V(J2,K1)-V(J1,K1))*BC/HZ                              AO  11
      V2=V(J1,K2)+(V(J2,K2)-V(J1,K2))*BC/HZ                              AO  12
      VA=V1+(V2-V1)*BB                                                   AO  13
      GXL=VGX(J1,K1)+(VGX(J2,K1)-VGX(J1,K1))*BC/HZ                       AO  14
      GXH=VGX(J1,K2)+(VGX(J2,K2)-VGX(J1,K2))*BC/HZ                       AO  15
      GX=GXL+(GXH-GXL)*BB                                                AO  16
      GZL=VGZ(J1,K1)+(VGZ(J1,K2)-VGZ(J1,K1))*BB                          AO  17
      GZH=VGZ(J2,K1)+(VGZ(J2,K2)-VGZ(J2,K1))*BB                          AO  18
      GZ=GZL+(GZH-GZL)*BC/HZ                                             AO  19
      RETURN                                                             AO  20
      END                                                                AO  21
```

```
      SUBROUTINE LOCATX(LM,X,A,X1,X2,II,JJ,KK,CONST)                     AP   1
C                                                                        AP   2
C     THIS SUBROUTINE LOCATES THE POINT (A) WRT (X)-ARRAY LOCATION FOR   AP   3
C     USE IN INTERPOLATING GRADIENT FUNCTIONS OF THE POINTS.             AP   4
C     X1, X2 ARE THE TWO DISCRETE BOUNDS OF (A). II IS THE ARRAY LOCATIO AP   5
C     OF THE LOWER BOUND. LM IS THE MAXIMUM NUMBER OF ARRAY POINTS.      AP   6
C                                                                        AP   7
      DIMENSION X(1)                                                     AP   8
      CONST=1.0                                                          AP   9
      I=0                                                                AP  10
1     I=I+1                                                              AP  11
      IF(I.EQ.3)GO TO 4                                                  AP  12
      IF(A.EQ.X(1))GO TO 3                                               AP  13
      IF(A.GT.X(I) .AND. A.LE.X(I+1))GO TO 2                             AP  14
      GO TO 1                                                            AP  15
2     X1=X(I)                                                            AP  16
      X2=X(I+1)                                                          AP  17
      II=I                                                               AP  18
      JJ=II+1                                                            AP  19
      KK=II+2                                                            AP  20
      GO TO 5                                                            AP  21
3     X1=X(1)                                                            AP  22
      X2=0.0                                                             AP  23
      II=1                                                               AP  24
      JJ=II+1                                                            AP  25
      KK=II+2                                                            AP  26
      GO TO 5                                                            AP  27
4     WRITE(6,6)                                                         AP  28
      CONST=0.0                                                          AP  29
5     RETURN                                                             AP  30
6     FORMAT(1H0,*POINT IS OUTSIDE GRID*)                                AP  31
      END                                                                AP  32
```

APPENDIX B

A simplified Tau Inversion method

for the inversion of slowness data (by R.F. Mereu)

Given a set of discrete velocity values in km/s

$$v_i, \quad i = 0,1,....N \qquad \text{B-1}$$

or a set of discrete slowness values in s/km

$$u_i = \frac{1}{v_i} ; \qquad \text{B-2}$$

also given a set of minimum values of tau corresponding to each value of u_i,

$$\underline{\tau}_i, \quad i = 0,1,....N \qquad \text{B-3}$$

and maximum values of tau corresponding to each value of u_i

$$\overline{\tau}_i, \quad i = 0,1,....N \qquad \text{B-4}$$

The problem is to find a set of minimum depths to layer with velocity v_i

$$\underline{d}_i, \quad i = 0,1,....N \qquad \text{B-5}$$

and a set of maximum depths to layer with velocity v_i

$$\overline{d}_i, \quad i = 0,1,....N \qquad \text{B-6}$$

i.e. $\underline{d}_i$ and $\overline{d}_i$ are depth limits for velocity v_i.

The travel-time equation for a one layer problem is

$$t - \frac{x}{v_1} = \tau_1 = 2z_1 \left(\frac{1}{v_0^2} - \frac{1}{v_1^2} \right)^{\frac{1}{2}} = 2z_1 \left(u_0^2 - u_1^2 \right)^{\frac{1}{2}} \qquad \text{B-7}$$

$$= a_{11} z_1$$

where z is the layer thickness. For a two layer problem, the equation is

$$t - \frac{x}{v_2} = \tau_2 = 2z_1 \left(u_0^2 - u_2^2 \right)^{\frac{1}{2}} + 2z_2 \left(u_1^2 - u_2^2 \right)^{\frac{1}{2}} \qquad \text{B-8}$$

$$= a_{21} z_1 + a_{22} z_2$$

For a three layer problem, the equation becomes

$$t - \frac{x}{v_3} = \tau_3 = 2z_1 \left(u_0^2 - u_3^2 \right)^{\frac{1}{2}} + 2z_2 \left(u_1^2 - u_3^2 \right)^{\frac{1}{2}} + \qquad \text{B-9}$$

$$2z_3 \cdot \left(u_2^2 - u_3^2 \right)^{\frac{1}{2}} = a_{31} z_1 + a_{32} z_2 + a_{33} z_3$$

In matrix form these equations become

$$\begin{pmatrix} a_{11} & 0 & 0 \\ a_{21} & a_{22} & 0 \\ a_{31} & a_{32} & a_{33} \end{pmatrix} \begin{pmatrix} z_1 \\ z_2 \\ z_3 \end{pmatrix} = \begin{pmatrix} \tau_1 \\ \tau_2 \\ \tau_3 \end{pmatrix} \qquad \text{B-10}$$

therefore

$$\begin{pmatrix} z_1 \\ z_2 \\ z_3 \end{pmatrix} = \begin{pmatrix} a_{11} & 0 & 0 \\ a_{21} & a_{22} & 0 \\ a_{31} & a_{32} & a_{33} \end{pmatrix}^{-1} \begin{pmatrix} \tau_1 \\ \tau_2 \\ \tau_3 \end{pmatrix} \qquad \text{B-11}$$

and

$$\begin{pmatrix} z_1 \\ z_2 \\ z_3 \end{pmatrix} = \begin{pmatrix} b_{11} & 0 & 0 \\ b_{21} & b_{22} & 0 \\ b_{31} & b_{32} & b_{33} \end{pmatrix} \begin{pmatrix} \tau_1 \\ \tau_2 \\ \tau_3 \end{pmatrix} \qquad \text{B-12}$$

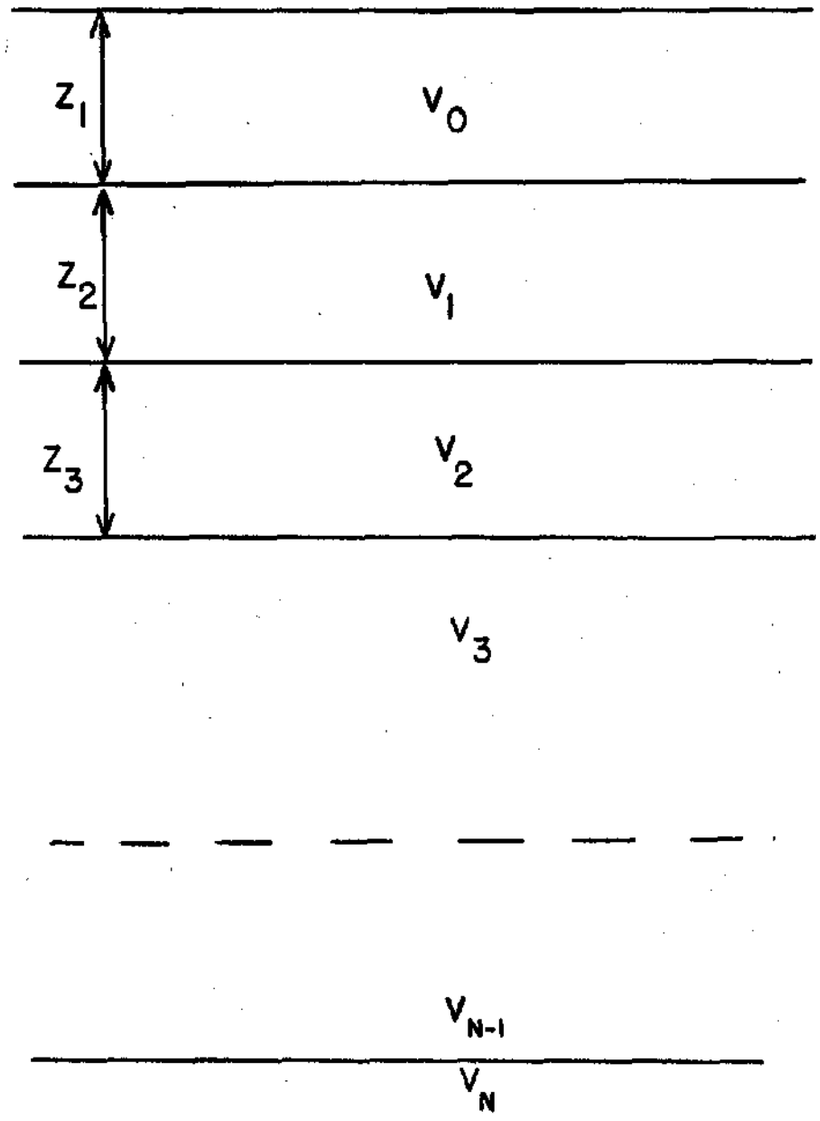


Figure B.1: Simple three layer model showing parameters discussed in equations B-7 to B-9.

where the matrix $B=A^{-1}$

therefore

$$z_1 = b_{11}\,\tau_1$$
$$z_2 = b_{21}\,\tau_1 + b_{22}\,\tau_2 \qquad \text{B-13}$$
$$z_3 = b_{31}\,\tau_1 + b_{32}\,\tau_2 + b_{33}\,\tau_3$$

Depth to $v_1 = d_1 = z_1 = b_{11}\,\tau_1$

Depth to $v_2 = d_2 = z_1 + z_2 = (b_{11} + b_{21})\tau_1 + b_{22}\,\tau_2$

Depth to $v_3 = d_3 = z_1 + z_2 + z_3 = (b_{11} + b_{21} + b_{31})\tau_1 + (b_{22} + b_{33})\tau_2 + b_{33}\,\tau_3$

$$d_1 = g_{11}\,\tau_1$$
$$d_2 = g_{21}\,\tau_1 + g_{22}\,\tau_2 \qquad \text{B-14}$$
$$d_3 = g_{31}\,\tau_1 + g_{32}\,\tau_2 + g_{33}\,\tau_3$$

where $g_{31} = b_{11} + b_{21} + b_{31}$ e.t.c.

Equation B-14 is the equation to use if exact values of tau are given. If bounds of tau are given for each slowness value i.e. $\underline{\tau}_i$ to $\bar{\tau}_i$, then minimum and maximum velocity depth limits can be computed from the following equation for a general N layer case bearing in mind which values of g_{ij} are positive or negative

$$\underline{d}_i = g_{ii}\,\underline{\tau}_i + g_{i,i-1}\,\bar{\tau}_{i-1} + \ldots + g_{il}\,\bar{\tau}_1$$
$$\bar{d}_i = g_{ii}\,\bar{\tau}_i + g_{i,i-1}\,\underline{\tau}_{i-1} + \ldots + g_{il}\,\underline{\tau}_1 \qquad \text{B-15}$$

where $\underline{d}_i$ and $\bar{d}_i$ are the minimum and maximum values of the depth for v_i.

APPENDIX C.1

GBA data for complexity factor, spectral ratio, and scattered energy data

TABLE C.1 GBA EARTHQUAKE DATA USED FOR THE HETEROGENEITY STUDY

AZ=GREAT CIRCLE AZIMUTH, SL=FIRST ARRIVAL SLOWNESS (SEC/DEG), AFTER RAM(1976)

FC=COMPLEXITY FACTOR, SPR=SPECTRAL RATIO (HF/LF), SE=SCATTERED ENERGY (%)

NO	I.D.	DATE	DELTA	AZ	FD	MB	ORIG. TIME	LOCATION	SL	FC	SPR	SE
1	GBA	2 4 72	22.69	352.0	47	5.0	3 34 27.8	36.13N 73.62E	9.91	3.2	.2	33.6
2	GBA	2 4 72	22.65	351.7	61	4.8	7 50 54.0	36.07N 73.51E	9.35	6.7	.5	39.8
4	GBA	3 4 72	23.75	310.6	52	5.0	9 7 16.0	28.12N 57.19E	10.32	8.9	.3	25.3
38	GBA	17 5 72	23.52	345.8	33	5.3	10 6 5.8	33.50N 71.54E	11.50	6.7	.4	53.9
40	GBA	23 5 72	25.61	346.7	33	4.9	18 17 14.1	38.49N 76.17E	9.41	3.4	.3	42.6
41	GBA	24 5 72	19.32	273.7	33	4.7	10 12 49.2	13.06N 57.59E	10.57	2.6	.1	14.1
42	GBA	28 5 72	23.03	346.1	92	4.6	16 52 27.9	35.94N 70.81E	9.46	2.3	.4	47.3
43	GBA	29 5 72	23.45	346.4	236	5.2	19 7 56.0	36.39N 70.76E	9.08	2.2	.6	49.7
45	GBA	5 6 72	21.59	116.9	33	5.3	23 17 33.7	3.22N 96.63E	10.22	2.6	.1	33.7
46	GBA	6 6 72	26.09	334.1	54	4.9	17 54 43.3	26.86N 53.37E	9.20	2.9	.2	18.8
49	GBA	24 6 72	23.58	344.2	47	6.4	15 29 22.2	36.23N 69.67E	9.20	5.9	.3	34.8
52	GBA	16 7 72	25.26	39.8	33	5.2	2 20 23.6	32.59N 35.89E	9.30	1.7	.2	33.8
53	GBA	16 7 72	23.68	123.5	28	5.6	17 9 5.6	3.04S 131.05E	8.61	3.7	.1	23.8
55	GBA	3 8 72	22.67	344.4	175	4.9	22 28 8.3	35.40N 70.16E	9.18	1.8	.6	56.7
56	GBA	6 8 72	19.06	309.2	33	5.5	1 12 50.4	25.07N 61.23E	12.13	4.9	.1	27.8
57	GBA	6 8 72	20.97	275.4	33	4.7	15 36 55.4	14.64N 55.84E	10.84	3.8	.2	21.8
58	GBA	6 8 72	21.19	275.6	33	5.2	15 53 55.6	14.71N 55.62E	10.74	3.7	.1	11.6
60	GBA	8 8 72	19.11	308.9	41	5.5	19 9 33.5	25.03N 61.13E	11.86	6.5	.2	18.8
61	GBA	9 8 72	17.36	107.3	33	5.1	4 17 37.3	7.93N 94.09E	11.30	5.7	.2	38.0
63	GBA	10 8 72	23.79	35.4	33	5.2	21 6 40.1	32.42N 93.47E	9.41	4.7	.2	38.3
116	GBA	14 12 72	18.94	140.6	33	5.4	20 49 34.8	1.31S 89.33E	11.43	4.1	.1	45.5
117	GBA	18 12 72	17.67	62.3	72	5.3	11 23 31.4	21.23N 94.17E	10.65	6.2	.3	32.7
118	GBA	28 12 72	26.83	123.2	33	5.6	13 57 3.8	1.83S 99.65E	8.69	10.8	.2	18.2
119	GBA	30 12 72	21.99	23.5	33	4.9	23 54 5.9	33.63N 37.72E	9.95	3.7	.3	39.9
120	GBA	2 1 73	20.10	27.4	33	5.2	22 25 57.0	31.24N 36.09E	10.69	1.7	.2	29.2
121	GBA	3 1 73	25.88	350.1	33	5.5	14 31 4.5	39.11N 71.89E	9.27	8.1	.3	22.7
122	GBA	9 1 73	26.02	353.4	33	4.9	16 17 55.2	39.51N 73.67E	9.21	3.0	.3	27.1
123	GBA	12 1 73	23.13	345.7	126	5.2	23 39 25.9	35.93N 70.58E	9.04	2.2	.7	39.6
124	GBA	13 1 73	28.66	122.7	105	5.2	11 10 20.4	2.71S 101.27E	8.37	3.6	.3	35.6
125	GBA	13 1 73	17.44	315.1	50	5.0	14 14 41.1	25.59N 63.90E	11.71	4.7	.3	38.5
126	GBA	15 1 73	29.27	21.6	13	5.1	12 55 44.8	46.43N 31.07E	8.78	1.6	.2	28.7
127	GBA	16 1 73	19.58	355.7	42	5.1	21 31 26.0	33.21N 75.72E	11.71	11.3	.3	39.0
129	GBA	20 1 73	17.64	333.6	17	5.3	12 34 13.6	29.28N 68.57E	12.79	4.7	.1	27.2
130	GBA	26 1 73	17.76	214.9	33	5.1	13 7 7.1	1.13S 67.37E	10.87	1.9	.1	23.4
131	GBA	29 1 73	22.42	351.1	53	5.0	4 32 8.6	35.82N 73.29E	9.87	2.3	.2	27.4
133	GBA	7 2 73	27.49	46.0	33	5.8	16 6 25.0	31.46N 130.29E	8.71	4.3	.0	16.2
134	GBA	9 2 73	22.60	346.3	75	4.5	14 57 51.3	35.54N 71.01E	9.66	2.6	.4	44.6
136	GBA	14 2 73	23.55	346.6	189	4.8	12 28 32.5	36.49N 70.82E	9.10	1.5	.4	50.0
139	GBA	7 3 73	23.38	347.9	78	5.0	7 7 39.8	36.49N 71.52E	9.52	1.7	.3	46.9
140	GBA	10 3 73	28.15	115.7	36	4.9	4 32 10.2	4.28N 95.57E	10.52	1.7	.2	36.5
141	GBA	17 3 73	31.70	124.4	68	5.7	15 40 48.0	5.19S 103.24E	8.27	3.0	.3	21.3
142	GBA	17 3 73	31.79	128.2	60	5.2	16 38 49.3	6.83S 102.07E	8.29	1.6	.3	28.9
144	GBA	22 3 73	23.58	66.0	33	4.7	6 10 29.3	22.02N 100.62E	9.59	6.4	.1	36.4
145	GBA	23 3 73	27.58	45.0	33	5.3	19 14 53.1	31.84N 100.36E	8.86	5.2	.1	40.1
146	GBA	24 3 73	21.43	65.2	33	4.9	0 27 32.7	21.62N 98.32E	9.91	7.8	.2	31.2
147	GBA	26 3 73	24.83	353.4	123	5.3	7 56 42.7	38.33N 73.93E	9.18	3.0	.3	30.3
148	GBA	26 3 73	24.79	353.4	120	5.2	8 33 30.6	38.23N 73.90E	9.19	1.8	.4	37.9
149	GBA	28 3 73	33.88	270.9	33	5.3	13 42 6.7	11.74N 42.75E	8.56	4.2	.0	5.5
150	GBA	28 3 73	33.71	270.8	33	5.4	14 13 52.3	11.73N 42.93E	8.52	2.7	.0	6.7
151	GBA	1 4 73	33.61	270.7	31	5.5	7 12 37.0	11.66N 43.04E	8.26	6.7	.0	11.2
152	GBA	2 4 73	23.61	314.5	33	5.0	1 27 9.0	27.03N 61.56E	11.77	5.0	.2	39.6
153	GBA	3 4 73	31.33	123.6	140	5.2	17 22 46.3	4.62S 103.19E	8.92	3.8	.4	41.3
154	GBA	10 4 73	23.32	347.5	125	4.5	16 7 47.4	36.37N 71.35E	9.49	1.2	.3	47.4
156	GBA	12 4 73	23.47	346.6	189	4.9	8 31 7.8	36.41N 70.84E	9.50	1.3	.5	50.1
157	GBA	13 4 73	32.84	271.0	33	4.8	14 13 56.9	11.94N 43.79E	8.52	2.4	.1	39.9
159	GBA	12 4 73	18.32	107.3	229	4.7	12 3 55.9	7.57N 95.05E	10.85	4.3	.3	47.2
161	GBA	25 4 73	24.37	349.7	136	5.2	3 16 52.3	37.61N 72.11E	9.30	2.9	.4	38.0
162	GBA	22 4 73	25.50	56.4	33	5.0	5 46 20.9	27.67N 134.07E	8.67	3.3	.7	36.2
163	GBA	22 4 73	35.63	308.4	57	5.0	21 29 57.2	30.74N 49.83E	9.33	3.4	.2	26.8
164	GBA	26 4 73	20.52	313.4	46	5.2	14 30 5.4	27.03N 60.84E	11.21	1.8	.2	29.2
165	GBA	28 4 73	33.51	123.3	82	5.4	10 49 23.2	4.04S 102.60E	8.28	4.8	.3	35.3
167	GBA	4 5 73	26.80	122.3	51	5.9	23 56 6.1	1.47S 99.85E	8.48	4.2	.1	21.0

TABLE C.1 CONTD.

NO	I.D.	DATE	DELTA	AZ	FD	MB	ORIG. TIME	LOCATION	SL	FC	SPR	SE
168	GBA	6 5 73	24.59	307.0	28	4.9	3 59 19.6	27.30N 55.52E	9.95	4.3	.2	30.0
170	GBA	11 5 73	26.83	320.5	50	5.1	13 52 31.7	33.36N 57.38E	9.63	2.2	.1	38.5
171	GBA	12 5 73	28.95	123.6	51	5.5	5 46 44.7	3.24S 141.24E	8.52	4.1	.2	28.7
172	GBA	12 5 73	22.99	343.7	96	5.1	22 25 3.8	35.61N 69.70E	9.73	2.0	.2	30.2
174	GBA	17 5 73	27.83	7.8	33	5.5	9 38 9.9	41.03N 92.20E	8.99	1.7	.2	22.9
175	GBA	25 5 73	19.71	320.7	57	4.9	8 39 53.9	25.64N 66.54E	13.77	10.9	.2	34.9
176	GBA	28 5 73	33.73	201.1	33	5.0	20 27 11.2	18.13S 65.29E	7.77	8.5	.1	13.9
178	GBA	2 6 73	30.84	4.6	26	5.8	23 57 4.2	44.11N 83.55E	8.82	3.8	.4	20.7
182	GBA	11 6 73	23.69	347.7	97	4.9	20 6 7.1	36.75N 71.34E	9.45	2.6	.4	42.4
183	GBA	14 6 73	23.47	346.6	203	5.0	18 20 29.3	36.41N 70.83E	10.19	1.1	.2	39.0
184	GBA	25 6 73	29.74	307.6	48	5.0	10 29 2.6	30.03N 50.46E	9.18	2.8	.3	42.2
187	GBA	13 7 73	19.48	355.1	52	4.8	22 3 38.7	33.10N 75.56E	10.63	3.6	.4	42.1
188	GBA	14 7 73	22.98	19.3	33	6.0	4 51 21.0	35.19N 86.48E	11.40	7.2	.1	31.1
189	GBA	14 7 73	23.09	19.4	33	5.9	13 39 33.0	35.26N 86.60E	10.54	3.8	.1	24.9
190	GBA	16 7 73	22.87	19.3	15	5.4	19 46 38.2	35.07N 86.45E	11.26	3.8	.1	37.2
191	GBA	21 7 73	22.98	19.2	33	5.3	19 50 6.3	35.11N 86.42E	11.11	3.2	.1	24.2
192	GBA	22 7 73	34.49	124.1	75	5.4	8 35 1.9	6.67S 135.61E	8.27	1.9	.4	20.6
193	GBA	26 7 73	16.83	93.2	33	4.5	19 25 25.1	10.37N 94.32E	12.70	11.7	.4	33.1
194	GBA	26 7 73	18.39	99.2	33	5.1	20 6 33.2	10.47N 93.89E	12.62	7.1	.3	22.6
195	GBA	27 7 73	18.85	56.7	79	5.3	20 23 50.7	23.33N 94.51E	11.09	3.4	.4	37.3
196	GBA	29 7 73	25.11	352.9	105	4.7	11 27 13.0	38.59N 73.59E	9.13	3.3	.8	28.7
197	GBA	1 8 73	19.23	32.3	71	4.9	14 5 16.2	29.61N 89.09E	11.03	2.8	.4	44.8
198	GBA	6 8 73	23.67	345.2	222	5.4	1 17 55.1	36.44N 70.13E	10.12	2.0	.4	54.9
199	GBA	11 8 73	30.97	46.9	33	5.4	7 15 39.7	33.00N 104.62E	8.96	4.9	.1	16.2
201	GBA	15 8 73	21.17	50.2	41	4.7	9 3 54.0	26.42N 95.47E	11.13	4.1	.3	35.6
202	GBA	15 8 73	25.18	115.2	33	4.9	11 18 52.3	6.93N 99.47E	8.61	1.8	.2	30.1
203	GBA	15 8 73	23.49	346.6	203	4.8	15 9 8.8	36.44N 70.85E	9.22	.9	.4	39.6
204	GBA	16 8 73	24.33	63.9	33	5.4	3 58 10.7	23.05N 111.11E	10.04	6.0	.1	12.7
205	GBA	16 8 73	21.21	22.4	33	5.3	8 2 53.8	33.09N 96.38E	10.77	3.7	.2	20.0
207	GBA	2 9 73	17.54	311.9	25	5.3	7 23 17.1	24.90N 63.14E	11.12	5.5	.2	17.4
212	GBA	17 9 73	32.81	318.8	47	4.8	4 6 3.7	36.52N 51.11E	8.87	1.8	.1	13.4
213	GBA	19 9 73	32.94	347.6	0	5.2	2 59 57.2	45.64N 67.85E	9.12	.9	2.9	27.9
214	GBA	22 9 73	23.17	345.5	117	5.0	11 36 2.7	36.01N 70.47E	9.89	1.3	.8	28.0
215	GBA	25 9 73	23.50	346.4	200	5.1	13 3 17.8	36.42N 70.77E	10.01	1.2	.7	48.5
216	GBA	25 9 73	23.92	348.2	110	5.1	18 39 .2	37.03N 71.48E	9.43	8.3	.6	35.7
217	GBA	27 9 73	2..72	347.5	35	4.9	2 4 23.0	33.85N 72.15E	11.52	7.2	.5	35.5
218	GBA	28 9 73	24.42	126.6	132	5.2	0 55 59.5	1.91N 99.19E	8.72	1.5	.3	23.8
219	GBA	28 9 73	25.98	272.4	33	5.5	11 32 23.3	13.24N 50.72E	9.29	4.6	.1	0.0
220	GBA	12 10 73	24.54	343.5	11	5.3	2 54 7.7	37.75N 71.95E	9.49	6.1	.4	36.3
221	GBA	15 10 73	15.42	18.6	33	5.2	9 50 43.3	26.22N 82.95E	12.65	6.7	.9	52.9
224	GBA	2 11 73	17.96	45.7	20	4.6	12 9 55.2	25.72N 81.62E	12.25	7.5	.3	51.4
225	GBA	3 11 73	19.50	261.1	33	5.1	8 29 35.3	9.87N 57.89E	9.72	2.9	.2	15.3
226	GBA	30 10 73	16.73	62.6	32	4.9	2 45 .6	20.93N 93.22E	12.43	3.7	.2	56.7
227	GBA	9 11 73	17.95	113.2	33	5.1	23 26 39.6	6.02N 93.98E	10.49	3.5	.2	32.0
228	GBA	11 11 73	28.23	310.7	11	6.5	7 14 51.5	30.57N 52.69E	9.03	2.4	.1	15.5
231	GBA	15 11 73	17.12	336.7	33	5.1	17 10 22.2	29.26N 69.77E	13.26	4.0	.2	37.1
232	GBA	17 11 73	35.29	198.2	33	5.0	14 26 43.1	20.19S 66.38E	8.06	2.7	.1	15.5
233	GBA	20 11 73	27.37	121.1	33	5.0	19 10 45.6	1.35S 110.63E	8.50	6.0	.3	29.8
234	GBA	21 11 73	21.20	8.1	26	5.0	19 47 56.3	34.66N 86.97E	10.62	3.4	.5	41.0
235	GBA	27 11 73	21.49	22.1	33	5.0	9 31 19.8	33.01N 96.72E	10.46	3.3	.2	32.3
236	GBA	28 11 73	21.52	119.0	33	5.2	7 5 39.0	2.87N 96.36E	10.21	2.3	.1	18.7
237	GBA	29 11 73	24.44	7.7	33	4.8	15 55 23.8	37.88N 51.46E	10.05	3.4	.1	17.3
239	GBA	3 12 73	24.91	121.9	33	5.7	6 10 3.5	.25S 98.40E	8.78	3.1	.1	18.2
241	GBA	16 12 73	18.64	356.3	33	4.9	9 16 14.1	30.29N 76.03E	11.99	6.1	.3	32.4
242	GBA	16 12 73	23.72	352.0	47	5.2	19 9 47.7	34.19N 74.65E	11.46	5.7	.2	24.2
244	GBA	21 12 73	23.13	41.3	33	4.8	2 8 47.5	30.29N 96.87E	10.10	1.4	.1	11.5
245	GBA	26 12 73	17.92	57.5	50	5.1	1 42 21.6	22.44N 93.36E	10.85	3.1	.2	19.3
246	GBA	1 1 74	20.27	114.4	59	5.4	14 7 43.1	4.63N 95.98E	10.22	2.5	.2	17.7
247	GBA	1 1 74	20.06	114.2	33	5.1	14 13 31.5	4.77N 95.73E	10.12	2.4	.3	14.4
248	GBA	4 1 74	26.90	.4	26	5.5	9 27 55.7	44.61N 77.65E	9.52	7.9	.3	23.0
249	GBA	7 1 74	19.17	56.6	105	4.9	5 14 24.3	23.52N 94.80E	10.98	3.4	.3	45.7
250	GBA	11 1 74	29.22	349.0	42	4.9	22 44 53.2	41.29N 70.59E	9.38	2.6	1.4	31.0

TABLE C.1 CONTD.

NO	I.D.	DATE	DELTA	AZ	FO	MB	ORIG.	TIME	LOCATION	SL	FC	SPR	SE
251	GBA	15 1 74	31.06	67.2	33	5.3	22	58 29.9	32.91N 104.20E	8.33	4.1	.1	11.2
253	GBA	20 2 74	27.21	353.6	25	5.1	11	43 3.9	46.65N 73.22E	9.06	2.5	.3	28.4
254	GBA	22 2 74	23.41	347.9	116	5.4	3	33 24.5	36.5JN 71.50E	9.11	3.1	.2	36.0
255	GBA	22 2 74	18.41	331.9	33	5.0	7	6 32.6	29.67N 67.60E	11.82	4.4	.1	34.8
256	GBA	24 2 74	33.66	124.1	93	4.9	19	7 54.5	6.35S 135.08E	8.38	1.9	.2	30.2
257	GBA	4 3 74	20.75	340.7	33	5.0	1	44 41.7	33.12N 69.40E	11.52	4.2	.1	42.6
258	GBA	17 3 74	24.25	118.5	61	5.7	3	57 7.1	1.30N 98.60E	8.96	8.7	.1	29.9
260	GBA	9 12 71	18.49	211.2	33	5.4	12	27 16.4	2.44S 67.98E	11.64	2.8	.0	8.1
261	GBA	15 12 71	25.81	318.1	42	4.9	19	24 57.4	30.25N 90.57E	9.06	3.2	.2	30.7
263	GBA	21 12 71	21.98	352.8	25	5.2	9	54 42.3	35.44N 74.16E	10.35	3.3	.1	25.2
264	GBA	21 12 71	24.49	116.6	142	5.6	19	23 34.1	1.85N 99.22E	8.84	2.7	.1	23.8
265	GBA	30 12 71	26.65	0.0	33	4.9	23	35 27.6	39.75N 77.46E	9.22	2.6	.2	21.0
266	GBA	14 1 72	33.81	309.7	33	5.1	22	10 3.7	32.82N 46.66E	8.96	2.0	.2	18.0
267	GBA	16 1 72	26.65	2.6	33	5.4	20	21 50.1	40.33N 78.99E	9.08	6.5	.1	34.4
268	GBA	19 1 72	26.50	2.2	33	5.0	23	45 59.3	40.15N 78.73E	8.93	2.6	.2	33.3
269	GBA	20 1 72	23.47	346.3	213	6.0	11	36 29.6	36.33N 70.71E	8.79	4.1	.2	55.9
270	GBA	23 1 72	25.90	63.6	33	5.2	2	6 1.2	23.65N 102.70E	9.02	1.7	.1	15.1
271	GBA	28 1 72	16.63	322.9	33	5.9	10	26 53.6	26.64N 66.32E	12.63	6.1	.3	47.5
272	GBA	29 1 72	19.21	356.2	58	4.7	6	49 11.1	32.86N 75.96E	12.25	11.4	.2	41.8
275	GBA	2 2 72	16.33	100.1	46	4.7	19	13 19.8	10.24N 93.77E	13.55	5.1	.4	43.8
276	GBA	3 2 72	25.54	64.1	33	4.5	7	22 44.5	23.35N 102.39E	8.76	2.4	.2	23.9
277	GBA	22 2 72	15.43	100.5	33	5.4	18	43 42.0	10.42N 92.46E	14.02	4.5	.6	42.9
278	GBA	27 2 72	19.36	220.3	33	5.0	11	8 19.9	1.47S 65.05E	11.38	3.3	.1	1.0
279	GBA	4 3 72	24.77	353.5	130	5.1	18	24 11.1	35.28N 73.98E	9.30	1.3	.9	27.0
280	GBA	11 3 72	20.52	348.7	45	4.9	14	36 15.5	33.76N 72.71E	11.02	4.7	.3	33.1
281	GBA	15 3 72	17.97	20.1	33	5.3	6	3 32.4	30.43N 84.50E	12.31	4.7	.2	39.3
282	GBA	17 3 72	27.23	347.0	26	5.2	9	17 13.5	44.08N 69.74E	9.02	4.7	.4	29.7
283	GBA	20 3 72	26.94	121.0	55	4.8	13	11 24.3	1.03S 130.28E	8.61	5.1	.2	14.8
284	GBA	20 3 72	34.47	124.7	65	5.3	22	56 8.5	6.98S 105.38E	8.52	3.6	.3	13.9
285	GBA	4 4 72	17.56	242.2	33	4.6	22	22 33.4	4.09N 61.90E	11.74	4.7	.3	6.7
286	GBA	5 4 72	17.43	242.8	33	5.2	4	27 31.4	5.13N 61.92E	11.99	7.2	.0	12.4
287	GBA	5 4 72	17.41	242.4	33	4.8	7	46 13.9	5.09N 62.00E	12.87	5.0	.0	4.2
288	GBA	5 4 72	17.30	241.6	33	4.8	10	1 34.1	4.93N 62.22E	13.08	5.9	.0	8.7
289	GBA	5 4 72	28.94	11.0	33	4.8	13	19 47.3	41.99N 84.58E	8.52	3.0	.3	22.3
290	GBA	5 4 72	17.52	242.1	33	4.7	13	31 53.3	4.97N 61.94E	12.15	3.6	.0	9.5
291	GBA	5 4 72	17.53	243.1	33	4.9	19	48 39.4	5.23N 61.82E	12.36	12.7	.0	5.0
292	GBA	5 4 72	24.92	352.6	118	5.0	22	38 56.9	38.38N 73.50E	9.05	3.8	.4	29.8
293	GBA	6 4 72	17.26	241.8	33	4.5	2	32 52.6	5.03N 62.21E	12.00	5.7	.0	0.0
294	GBA	7 4 72	17.44	242.8	33	5.1	0	30 55.8	5.13N 61.91E	11.91	3.1	.0	13.9
295	GBA	10 5 72	17.95	62.2	89	4.8	12	48 44.4	21.36N 94.44E	10.89	1.4	.3	45.5
296	GBA	2 6 72	21.50	115.9	33	5.5	22	50 47.4	3.58N 96.73E	10.21	9.7	.2	29.6
297	GBA	20 6 72	23.34	348.0	114	5.1	5	26 7.1	36.44N 71.56E	9.21	1.7	1.1	42.3
298	GBA	27 6 72	17.33	338.6	12	5.5	6	39 44.4	29.69N 70.27E	12.76	6.8	.2	41.9
299	GBA	27 6 72	17.38	339.7	8	5.4	10	48 55.6	29.75N 70.27E	12.23	5.7	.2	50.1
300	GBA	27 6 72	23.66	343.9	93	5.1	15	59 35.0	36.27N 69.52E	10.41	3.9	.2	29.3
301	GBA	1 9 72	31.11	123.3	90	5.4	19	45 57.5	4.36S 133.11E	8.56	2.1	.5	39.2
302	GBA	8 9 72	34.86	311.2	15	4.9	9	39 21.4	34.09N 46.23E	8.40	5.2	.5	9.1
303	GBA	12 9 72	34.34	309.7	33	5.4	13	34 .7	33.11N 46.32E	8.40	4.7	.3	11.7
304	GBA	13 9 72	34.38	309.7	27	5.1	0	55 37.3	33.13N 46.26E	8.55	2.2	.3	25.2
305	GBA	14 9 72	34.47	309.5	33	5.3	4	34 29.1	33.03N 46.10E	8.55	4.3	.2	6.8
306	GBA	15 9 72	34.63	124.6	68	5.6	11	52 3.5	6.42S 135.36E	8.57	.8	.4	17.2
308	GBA	4 7 72	35.77	123.9	94	5.2	4	3 21.9	7.39S 106.70E	8.36	2.0	.3	31.2
311	GBA	11 7 72	23.47	346.3	206	5.4	5	54 44.1	36.34N 70.73E	9.23	1.5	.2	49.6
312	GBA	11 7 72	19.46	94.4	48	4.6	21	46 11.6	24.29N 94.70E	11.19	1.8	.3	33.6
321	GBA	11 1 74	23.38	346.6	159	4.8	2	3 53.4	36.3JN 70.77E	10.22	8.7	.5	54.9
5	GBA	8 4 72	17.42	242.4	33	4.9	5	23 49.1	5.03N 61.99E	12.59	5.1	.1	3.5
6	GBA	8 4 72	19.49	32.9	33	4.8	6	42 13.3	29.67N 59.47E	11.12	1.6	.2	41.5
7	GBA	9 4 72	29.15	11.0	33	5.9	4	15 51.7	42.19N 94.65E	8.50	7.8	.2	16.0
8	GBA	9 4 72	26.45	2.4	14	4.7	8	43 44.5	40.13N 78.83E	9.01	1.9	.1	26.8
9	GBA	9 4 72	28.96	11.1	33	4.8	10	43 58.3	41.99N 84.64E	8.42	5.2	.7	33.1
10	GBA	9 4 72	21.58	353.7	49	4.9	22	47 36.8	35.13N 74.61E	10.72	1.0	.1	16.7
11	GBA	10 4 72	27.22	306.7	33	6.1	2	6 55.2	28.43N 52.83E	9.16	8.1	.2	20.5

TABLE C.1 CONTD.

NO	I.D.	DATE	DELTA	AZ	FD	MB	ORIG. TIME	LOCATION		SL	FC	SPR	SE
12	GBA	10 4 72	27.15	306.7	33	4.9	2 34 31.5	28.42N	52.91E	8.66	5.8	.2	23.9
13	GBA	10 4 72	27.04	306.6	33	4.6	4 36 15.5	28.30N	52.96E	8.94	2.7	.1	24.4
14	GBA	10 4 72	26.94	306.6	33	4.6	5 33 51.4	28.25N	53.08E	9.31	5.7	.2	12.0
16	GBA	10 4 72	27.14	306.6	33	4.7	20 27 7.5	28.37N	52.90E	8.57	6.2	.4	27.6
17	GBA	11 4 72	27.38	332.5	33	4.9	6 3 4.6	37.37N	62.00E	8.72	1.2	.5	41.7
19	GBA	12 4 72	26.97	306.7	33	5.1	18 37 40.8	28.32N	53.09E	8.97	4.9	.5	26.5
20	GBA	12 4 72	26.44	340.3	62	4.7	21 38 24.0	38.23N	66.46E	10.10	1.6	.5	25.8
21	GBA	12 4 72	27.03	306.8	33	5.0	23 7 49.9	28.38N	53.04E	8.68	5.1	.3	20.5
22	GBA	14 4 72	34.57	123.6	80	5.3	18 15 16.4	6.64S	135.76E	8.44	1.0	1.3	23.3
23	GBA	16 4 72	26.99	123.0	33	5.3	1 27 55.7	1.84S	99.83E	8.68	7.9	.1	15.3
24	GBA	17 4 72	20.69	349.2	45	4.8	2 24 49.3	33.96N	72.88E	11.02	4.5	.6	40.4
25	GBA	17 4 72	22.64	52.0	148	5.0	10 35 45.7	25.54N	95.36E	10.77	3.6	.2	37.6
28	GBA	20 4 72	28.97	11.0	33	5.1	0 35 56.7	42.01N	84.58E	8.41	4.5	.9	24.7
29	GBA	21 4 72	21.54	8.1	33	4.8	21 19 29.5	34.99N	91.83E	10.52	1.6	.2	22.9
31	GBA	23 4 72	32.81	124.2	163	5.5	20 40 11.0	5.74S	104.22E	8.60	8.8	.2	22.5
33	GBA	27 4 72	26.13	120.9	54	5.3	5 51 6.3	.53S	99.64E	8.67	2.9	.1	15.1
34	GBA	28 4 72	18.87	20.1	33	5.1	0 52 56.8	31.26N	84.90E	11.27	3.1	.2	35.8
36	GBA	29 4 72	27.05	306.6	33	4.9	16 4 21.1	28.29N	52.97E	9.12	2.2	.1	28.7
65	GBA	21 8 72	16.76	34.4	33	4.8	14 4 33.9	27.23N	87.98E	12.40	5.5	1.0	54.2
67	GBA	21 8 72	35.69	125.9	62	5.3	21 57 17.2	8.28S	105.95E	8.18	7.9	.1	20.4
68	GBA	31 8 72	28.64	33.1	33	5.5	15 14 3.9	36.72N	96.47E	8.22	13.3	.2	21.7
69	GBA	30 8 72	28.52	33.2	33	5.5	18 47 42.6	36.60N	96.42E	8.40	9.7	.1	19.8
70	GBA	2 9 72	33.50	325.8	33	4.9	10 37 39.4	39.98N	53.65E	8.43	2.4	.3	13.9
71	GBA	3 9 72	22.57	351.5	36	6.3	16 48 24.8	35.98N	73.42E	10.04	4.5	.2	49.4
72	GBA	3 9 72	22.56	351.3	33	5.4	17 3 14.9	35.96N	73.35E	9.84	1.7	.3	25.9
73	GBA	3 9 72	22.66	351.2	33	5.1	17 46 17.2	36.05N	73.26E	10.25	1.6	.4	33.3
74	GBA	3 9 72	22.50	351.6	33	5.2	20 32 13.4	35.92N	73.50E	11.27	1.4	.2	23.9
75	GBA	3 9 72	22.53	351.1	33	5.6	23 3 52.1	35.91N	73.26E	10.35	3.8	.3	49.2
76	GBA	4 9 72	22.52	351.3	55	5.5	0 14 10.4	35.92N	73.37E	11.00	2.5	.2	32.3
77	GBA	4 9 72	22.66	351.2	68	5.3	0 50 26.7	35.99N	73.27E	11.47	2.1	.3	38.6
78	GBA	4 9 72	22.41	351.2	33	5.4	1 23 49.5	35.80N	73.31E	10.80	2.9	.2	32.1
79	GBA	4 9 72	22.54	351.3	30	5.2	2 36 17.1	35.94N	73.35E	11.51	2.0	.3	33.4
80	GBA	4 9 72	22.51	351.5	35	5.3	3 51 23.9	35.93N	73.46E	10.78	2.0	.3	28.5
81	GBA	4 9 72	22.27	351.3	61	4.9	10 35 45.6	35.67N	73.42E	11.15	1.5	.4	39.3
82	GBA	4 9 72	22.41	351.2	33	5.2	13 37 51.4	35.80N	73.30E	10.27	2.3	.2	42.6
83	GBA	4 9 72	22.51	351.4	33	5.8	13 42 18.1	35.92N	73.41E	10.48	4.5	.2	29.0
84	GBA	5 9 72	22.43	351.6	45	5.2	3 8 .7	35.85N	73.52E	10.71	2.0	.3	32.1
85	GBA	5 9 72	22.46	351.4	33	5.2	4 7 27.0	35.87N	73.41E	11.15	2.9	.2	34.0
86	GBA	5 9 72	22.41	351.4	33	5.1	9 13 57.3	35.82N	73.41E	10.85	1.8	.2	27.0
87	GBA	5 9 72	23.26	346.3	154	4.7	20 8 35.0	36.18N	70.78E	9.33	7.2	.5	34.7
88	GBA	6 9 72	19.83	2.3	44	5.3	2 51 32.8	32.50N	78.31E	12.59	5.7	.6	46.7
89	GBA	7 9 72	18.15	211.7	33	5.8	2 54 53.3	2.05S	68.01E	10.78	3.5	.1	7.1
90	GBA	7 9 72	22.53	351.8	33	4.8	4 24 15.0	35.96N	73.56E	9.60	1.1	.2	19.4
91	GBA	20 9 72	20.20	274.8	33	5.3	20 44 53.2	14.42N	56.64E	11.32	6.5	.1	10.8
92	GBA	21 9 72	21.29	113.1	33	5.2	0 10 13.3	2.98N	96.15E	10.71	6.4	.2	19.3
93	GBA	21 9 72	21.31	113.1	33	5.0	0 46 40.4	2.96N	96.16E	10.39	9.4	.2	12.4
94	GBA	25 9 72	10.59	101.3	33	5.3	11 30 17.8	9.83N	93.94E	11.69	2.2	.2	45.0
95	GBA	26 9 72	22.53	351.9	33	4.9	19 10 31.4	35.96N	73.60E	11.17	1.5	.5	42.6
96	GBA	27 9 72	27.86	49.4	33	5.0	0 8 29.9	31.31N	101.67E	8.46	8.5	.3	38.3
97	GBA	27 9 72	26.67	348.8	48	4.9	2 3 39.1	33.92N	72.72E	10.75	5.6	.5	45.5
98	GBA	27 9 72	22.70	351.5	33	5.1	9 15 3.4	36.12N	73.42E	9.77	1.3	.2	38.9
99	GBA	27 9 72	21.94	350.3	39	5.0	20 24 55.6	35.17N	73.04E	10.48	4.6	.2	22.2
100	GBA	28 9 72	33.65	122.8	33	5.4	9 0 33.0	5.71S	105.52E	8.40	1.4	.1	17.1
101	GBA	29 9 72	27.79	49.1	33	5.1	16 21 38.0	30.40N	101.52E	8.92	5.3	.1	12.4
102	GBA	29 9 72	27.84	49.6	33	5.1	20 24 42.0	30.23N	101.67E	8.97	6.1	.2	14.3
103	GBA	30 9 72	23.55	346.6	204	4.9	6 59 59.8	36.43N	70.56E	9.01	1.5	.4	47.2
104	GBA	6 10 72	23.22	114.4	124	5.3	20 22 3.2	3.27N	98.52E	9.36	4.1	.6	37.0
105	GBA	9 10 72	24.64	339.4	33	5.2	7 15 23.6	28.17N	56.63E	8.48	8.8	.3	26.7
106	GBA	12 10 72	22.52	351.3	49	5.2	0 21 14.2	35.92N	73.33E	9.23	4.0	.2	33.6
107	GBA	13 10 72	22.45	351.2	33	5.2	5 4 36.6	35.84N	73.31E	11.90	4.5	.4	34.1
108	GBA	3 11 72	21.72	342.4	26	5.4	23 57 59.4	34.23N	69.66E	10.87	4.8	.2	15.9
109	GBA	11 11 72	20.32	54.0	143	5.0	1 47 13.4	24.84N	95.44E	10.66	2.4	.5	36.5

TABLE C.1 CONTD.

NO	I.D.	DATE	DELTA	AZ	FD	MB	ORIG.	TIME	LOCATION		SL	FG	SPR	SE
110	GBA	13 11 72	17.32	91.7	33	5.4	23	34 12.8	12.46N	95.17E	12.93	7.4	.1	26.9
111	G9A	16 11 72	23.07	344.2	124	5.6	12	43 5.5	35.75N	69.90E	9.18	4.2	.2	50.6
112	G9A	17 11 72	21.92	311.4	65	5.4	9	9 .1	27.35N	59.09E	10.40	3.8	.1	25.5
113	GBA	1 12 72	27.95	324.4	33	5.4	11	39 3.6	35.42N	57.91E	8.68	9.0	.2	9.3
115	G9A	6 12 72	24.81	204.4	33	5.6	5	31 44.8	9.23S	67.30E	8.76	1.4	.1	12.0
185	G9A	27 6 73	26.91	3.0	33	5.0	13	11 11.0	40.57N	79.21E	10.48	1.6	.2	19.2
208	GBA	8 9 73	21.31	21.9	33	5.5	7	25 43.9	33.24N	86.75E	10.03	2.4	.2	20.9
209	GBA	8 9 73	21.24	21.9	33	5.1	7	59 31.2	33.19N	86.72E	9.96	2.6	.1	22.8
210	GBA	9 9 73	27.41	45.3	33	5.5	2	13 39.4	31.65N	100.61E	8.45	2.3	.0	24.9
273	GBA	20 2 72	21.04	6.6	33	4.8	3	2 14.0	34.57N	80.32E	10.47	4.5	.2	43.4
274	GBA	22 2 72	23.56	346.0	212	5.3	1	14 47.5	36.44N	70.57E	8.96	2.4	.2	46.4
313	G9A	17 9 72	22.56	351.1	33	5.4	17	37 48.5	35.94N	73.26E	10.45	3.7	.1	33.4
314	GBA	18 9 72	22.43	351.6	35	4.8	21	42 .3	35.85N	73.50E	10.78	3.4	.3	20.8
315	GBA	15 10 72	22.41	351.4	63	5.1	14	47 53.2	35.82N	73.42E	11.27	4.1	.2	23.6
317	GBA	31 10 72	33.56	124.0	73	5.4	23	24 12.5	6.11S	104.88E	8.77	2.0	.4	26.4
318	G9A	1 11 72	21.81	51.4	97	5.3	21	53 48.0	26.42N	96.32E	10.51	2.9	.2	46.3
323	GBA	7 11 72	33.39	124.2	91	5.3	18	21 12.2	6.11S	104.67E	8.54	1.9	.2	19.4
324	GBA	3 11 73	47.32	97.5	272	5.0	18	49 15.2	3.79N	124.37E	7.27	.6	.2	23.3
325	GBA	4 11 73	50.80	109.5	605	5.5	12	2 9.1	6.03S	124.69E	6.42	1.0	.3	29.2
326	GBA	8 11 73	48.56	96.7	149	5.1	17	22 58.7	3.99N	125.69E	7.13	2.4	.3	27.5
327	G9A	10 11 73	56.45	107.3	69	5.3	1	20 54.2	6.43S	130.65E	6.41	2.1	.4	37.2
328	G9A	13 11 73	61.93	53.4	78	5.5	1	12 11.5	38.62N	142.15E	5.51	2.1	.2	24.3
329	G9A	15 11 73	44.01	90.1	63	5.0	23	19 13.8	8.95N	126.23E	6.84	4.5	.5	14.0
330	G9A	17 11 73	55.62	107.1	143	5.3	3	58 33.3	6.03S	129.91E	6.62	1.8	.2	22.8
331	G9A	19 11 73	61.76	53.0	56	6.1	13	1 56.1	38.91N	141.91E	5.91	5.0	.1	11.2
332	G9A	19 11 73	61.77	53.1	60	5.1	21	11 17.1	38.84N	141.92E	6.13	3.1	.1	13.1
333	G9A	28 11 73	50.67	96.0	83	5.0	10	59 15.0	4.02N	127.89E	6.77	2.3	.1	18.6
334	G9A	30 11 73	48.51	103.1	33	5.5	16	58 51.4	1.26N	125.93E	7.03	.9	.5	13.2
335	G9A	1 12 73	65.25	48.8	36	5.4	10	38 51.0	43.01N	146.08E	6.09	3.4	.2	9.4
336	G9A	1 12 73	59.29	100.8	20	5.1	21	15 23.9	1.88S	134.16E	6.31	5.4	.1	1.8
337	G9A	1 12 73	65.89	48.7	31	5.3	23	16 54.8	43.10N	146.94E	6.01	4.5	.4	13.4
338	G9A	1 12 73	65.54	48.7	40	5.6	23	18 1.9	43.16N	146.87E	6.11	3.8	.1	12.0
339	G9A	2 12 73	47.55	102.3	119	5.1	13	50 33.9	.31N	123.58E	6.97	1.1	.8	47.1
340	G9A	3 12 73	63.24	100.2	35	5.3	2	1 32.2	2.81S	139.05E	6.21	4.2	.2	9.9
341	G9A	4 12 73	65.49	48.6	33	5.1	1	26 3.2	43.19N	146.95E	6.00	5.2	.2	28.0
343	G9A	7 12 73	51.83	52.6	82	4.8	21	7 21.9	39.33N	141.95E	6.11	1.7	.4	24.6
344	G9A	9 12 73	50.11	94.7	121	5.0	4	47 59.5	5.14N	127.59E	6.82	1.5	.2	18.4
345	G9A	8 12 73	50.61	96.7	38	5.3	12	49 43.6	3.63N	127.12E	6.90	1.7	.2	11.1
346	G9A	10 12 73	54.69	101.6	33	5.0	14	44 6.0	.27S	126.90E	6.94	2.1	.4	25.0
347	G9A	11 12 73	45.58	98.6	560	5.4	8	13 12.6	3.44N	122.46E	6.96	.4	.2	14.9
348	G9A	12 12 73	59.14	90.2	28	5.0	22	2 23.4	6.79N	137.25E	6.09	4.4	.2	11.9
349	G9A	19 12 73	47.57	116.5	58	6.0	4	43 1.5	9.44S	119.45E	8.00	3.1	.2	14.4
350	G9A	20 12 73	63.95	99.6	33	5.0	2	41 37.4	2.50S	139.89E	5.76	1.8	.4	1.5
351	G9A	21 11 73	42.33	84.9	39	5.1	12	5 46.3	13.49N	121.62E	7.71	1.7	.2	7.4
352	G9A	3 12 73	54.15	85.5	65	4.8	11	57 1.7	27.47N	129.29E	7.76	4.9	.2	8.3
353	G9A	11 12 73	66.77	80.8	46	5.5	2	36 39.9	13.64N	146.38E	5.80	4.0	.2	3.7
354	G9A	23 12 73	50.68	99.2	126	5.3	23	46 45.1	1.61N	127.26E	6.87	.9	.1	6.3
355	G9A	22 12 73	60.43	57.2	70	4.9	1	19 59.5	35.11N	140.19E	6.37	4.2	1.2	13.8
356	G9A	31 12 73	48.37	101.8	33	5.4	8	38 17.0	1.01N	122.56E	7.16	2.2	.3	21.8
357	G9A	1 1 74	62.48	72.6	333	5.0	7	57 4.5	21.63N	142.85E	6.25	.8	.3	10.4
358	G9A	1 1 74	62.66	72.6	318	5.1	18	4 28.8	21.61N	143.05E	5.99	.8	.1	10.3
359	G9A	2 1 74	45.63	66.9	205	5.7	14	41 47.9	26.32N	124.38E	7.61	.9	.2	30.0
360	G9A	2 1 74	49.75	115.0	33	5.3	22	15 15.3	9.43S	121.96E	6.98	7.8	.3	19.3
361	G9A	3 1 74	64.62	73.6	139	5.1	3	52 52.4	20.34N	145.05E	6.14	.5	.5	21.0
362	G9A	3 1 74	49.45	114.8	50	5.0	17	35 19.3	9.16S	121.74E	7.27	5.8	.2	23.3
363	G9A	3 1 74	49.74	114.1	116	5.3	22	0 9.3	8.39S	121.33E	6.62	1.5	.3	21.1
364	G9A	7 1 74	42.15	76.5	39	5.0	3	55 33.4	19.13N	121.06E	7.92	3.3	.3	10.3
365	G9A	10 1 74	61.37	55.9	47	5.1	12	44 44.8	38.34N	141.67E	6.18	2.3	.3	3.2
366	G9A	10 1 74	52.69	80.4	37	5.2	16	13 25.8	31.79N	131.70E	7.42	3.1	.3	22.7
367	G9A	16 1 74	42.70	78.1	58	5.1	4	52 33.7	23.46N	121.43E	8.16	2.4	.1	15.7
368	G9A	17 1 74	41.65	80.1	74	5.2	2	44 9.9	16.73N	119.90E	7.79	4.4	.2	5.4
369	G9A	17 1 74	66.13	48.6	77	5.2	8	39 6.7	43.79N	147.21E	6.12	4.7	.1	22.4
370	G8A	25 2 74	66.57	47.8	12	5.9	5	46 25.1	44.04N	147.80E	6.07	2.8	.1	7.7

APPENDIX C.2

YKA data for complexity factor, spectral ratio and scattered energy data

TABLE C.2 YKA EARTHQUAKE DATA USED FOR THE HETEROGENEITY STUDY

AZ=GREAT CIRCLE AZIMUTH, SL=FIRST ARRIVAL SLOWNESS (SEC/DEG), AFTER RAM(1976)

FC=COMPLEXITY FACTOR, SPR=SPECTRAL RATIO (HF/LF),SE=SCATTERED ENERGY (%)

NO	I.D.	DATE	DELTA	AZ	FD	MB	ORIG.	TIME	LOCATION	SL	FC	SPR	SE
2	YKA	4 2 70	25.44	182.6	0	5.6	17	0 3.0	37.10N 116.03W	8.77	3.2	.2	36.9
3	YKA	25 2 70	25.53	182.6	0	5.2	14	28 38.0	37.04N 116.00W	9.03	1.7	.7	59.4
4	YKA	26 2 70	25.42	182.7	0	5.3	15	33 3.0	37.12N 116.07W	8.60	2.9	.1	45.0
6	YKA	23 3 70	25.46	182.6	0	5.5	23	5 3.0	37.05N 116.02W	8.90	2.6	.2	38.4
7	YKA	26 3 70	25.25	182.6	0	6.5	19	0 .2	37.30N 116.53W	8.59	4.3	.2	49.0
9	YKA	5 5 70	25.32	182.9	0	5.2	15	30 .2	37.22N 116.18W	8.79	3.0	.4	53.7
10	YKA	15 5 70	25.37	182.7	0	5.3	13	33 3.0	37.16N 116.04W	8.83	2.8	.2	43.0
11	YKA	21 5 70	25.46	182.6	0	5.1	14	15 3.0	37.07N 116.01W	8.85	2.3	.4	47.8
12	YKA	26 5 70	25.38	183.0	0	5.0	14	16 .2	37.07N 116.21W	8.96	2.6	.5	57.4
13	YKA	26 5 70	25.42	182.8	0	5.6	15	0 3.0	37.11N 116.11W	8.67	2.9	.1	37.8
17	YKA	13 9 70	23.19	200.8	33	5.4	21	10 23.0	40.22N 125.14W	10.79	8.6	.1	35.1
18	YKA	14 10 70	25.46	182.6	0	5.5	14	30 3.0	37.07N 116.01W	8.80	2.4	.2	39.6
20	YKA	16 12 70	25.43	182.6	0	5.1	16	0 .1	37.13N 116.01W	8.78	3.2	.2	48.3
21	YKA	17 12 70	25.41	182.4	0	5.7	16	5 .2	37.13N 116.08W	8.67	3.6	.1	34.1
23	YKA	9 2 71	28.22	186.6	13	6.2	14	0 41.6	34.40N 118.40W	9.02	5.6	.1	46.6
25	YKA	27 2 71	23.00	200.3	33	5.3	3	31 39.9	40.36N 124.80W	10.50	11.8	.1	34.9
29	YKA	23 6 71	25.51	182.6	0	4.8	15	33 3.0	37.02N 116.02W	9.10	1.7	.7	46.8
31	YKA	29 6 71	25.20	273.6	24	5.2	14	3 19.0	54.65N 161.59W	9.10	3.3	.2	64.3
32	YKA	5 7 71	25.43	182.7	0	5.5	14	0 .1	37.11N 116.05W	8.59	3.1	.1	48.4
34	YKA	13 7 71	25.48	182.7	0	5.4	14	0 3.0	37.06N 116.04W	8.86	2.2	.2	40.5
35	YKA	21 8 71	25.84	273.7	33	5.2	22	43 38.4	54.29N 162.49W	8.86	4.1	.4	40.6
36	YKA	4 9 71	25.82	275.6	107	5.8	15	53 25.4	54.99N 163.36W	9.04	2.4	.6	64.1
38	YKA	23 9 71	27.27	274.6	45	5.3	13	31 13.4	53.73N 164.84W	9.69	3.5	.3	49.7
39	YKA	19 10 71	26.94	274.6	22	5.6	11	2 37.7	52.66N 166.97W	9.32	1.9	.1	47.3
40	YKA	8 12 71	24.85	180.8	5	4.8	17	18 51.5	37.66N 115.01W	9.49	3.8	.1	35.6
41	YKA	21 2 72	22.92	273.4	60	5.7	19	34 51.9	55.90N 158.27W	9.33	6.5	.3	43.4
42	YKA	24 2 72	22.96	273.2	66	5.3	1	43 4.5	55.83N 158.25W	9.87	8.5	.4	53.4
43	YKA	24 2 72	26.26	192.1	5	4.9	15	56 51.1	36.58N 121.22W	9.55	6.3	.1	48.9
45	YKA	17 3 72	28.13	274.0	26	5.1	12	28 41.5	52.96N 165.63W	9.01	1.9	.3	47.6
47	YKA	2 5 72	25.39	183.0	20	5.0	13	15 1.8	37.15N 116.20W	8.81	3.0	.4	55.1
48	YKA	19 5 72	25.47	182.6	0	4.9	17	0 3.0	37.06N 116.00W	8.80	2.2	.3	51.9
49	YKA	20 7 72	25.32	182.9	0	5.0	17	16 .2	37.22N 116.18W	9.10	3.3	.3	47.2
51	YKA	21 9 72	25.45	182.7	0	5.7	15	33 .2	37.08N 116.04W	8.84	2.9	.2	22.7
54	YKA	25 10 72	20.58	228.1	33	5.3	1	1 41.0	43.44N 127.73W	11.34	8.3	.2	27.5
58	YKA	20 12 72	12.74	180.6	0	5.1	19	53 41.9	49.79N 114.82W	13.33	2.1	.5	61.6
59	YKA	21 12 72	25.50	182.8	0	5.0	20	15 .2	37.14N 116.08W	8.66	4.5	.4	54.6
62	YKA	3 1 73	20.05	211.7	18	5.3	21	14 16.4	44.34N 129.15W	10.94	5.1	.3	27.0
63	YKA	6 1 73	26.37	271.9	33	4.9	15	4 11.9	53.34N 162.36W	9.04	3.7	.2	54.2
65	YKA	16 1 73	27.35	275.8	31	5.3	9	57 33.6	54.12N 165.54W	8.94	1.9	.5	56.4
66	YKA	19 1 73	20.29	272.4	32	4.9	8	50 57.3	57.05N 153.94W	9.70	4.9	.4	31.5
67	YKA	14 2 73	24.49	269.6	32	4.9	7	11 32.0	53.77N 158.90W	8.40	2.2	.1	37.3
69	YKA	21 2 73	28.59	187.7	8	5.7	14	45 57.3	34.07N 119.04W	9.10	5.0	.1	49.7
70	YKA	5 3 73	25.43	182.6	0	5.4	16	10 .2	37.10N 116.03W	8.74	3.4	.2	38.5
71	YKA	12 3 73	29.48	275.4	15	4.8	3	20 16.8	52.61N 168.06W	8.92	4.1	.5	49.1
75	YKA	22 4 73	20.29	165.5	33	4.8	6	7 12.4	42.64N 137.85W	10.75	5.5	.8	62.7
76	YKA	26 4 73	25.41	182.7	0	5.6	17	15 .2	37.12N 116.06W	8.58	3.4	.1	31.8
78	YKA	17 5 73	23.04	167.6	0	5.4	16	3 3.0	39.73N 136.37W	9.79	3.1	.6	50.8
79	YKA	20 5 73	17.82	282.1	115	4.9	18	18 13.0	60.97N 152.44W	11.39	1.3	.2	42.1
82	YKA	26 5 73	25.95	270.7	39	4.9	13	17 26.1	53.20N 161.28W	9.97	3.7	.1	44.1
84	YKA	29 5 73	26.60	274.2	30	6.0	6	14 22.3	54.01N 163.78W	9.20	4.7	.1	58.3
85	YKA	5 6 73	26.71	274.5	17	4.8	2	58 15.3	54.04N 164.04W	9.15	4.0	.4	58.4
86	YKA	5 6 73	25.35	183.0	0	5.1	17	0 .2	37.19N 116.22W	8.95	2.4	.4	45.5
87	YKA	6 6 73	25.30	183.3	0	6.1	13	0 .1	37.25N 116.35W	8.67	4.4	.1	44.1
89	YKA	15 6 73	22.28	202.2	33	6.2	18	18 51.7	41.22N 125.94W	10.79	1.9	.1	21.6
90	YKA	16 6 73	18.70	205.4	33	5.6	14	43 47.1	44.98N 125.77W	11.73	5.5	.2	26.8
91	YKA	18 6 73	20.31	205.8	33	4.8	8	20 37.8	43.48N 126.60W	10.50	5.8	.1	27.3
92	YKA	18 6 73	28.28	272.1	15	5.4	10	17 26.3	52.18N 164.87W	7.56	4.9	.2	42.5
93	YKA	21 6 73	25.45	182.6	5	5.3	14	44 59.6	37.03N 115.99W	8.88	3.2	.2	43.3
94	YKA	28 6 73	25.39	182.8	0	4.9	19	15 12.4	37.15N 116.09W	8.67	3.9	.2	49.9
95	YKA	1 7 73	12.21	257.6	0	6.1	13	33 34.6	57.80N 137.30W	12.37	4.6	.5	66.6
96	YKA	3 7 73	12.42	259.3	0	6.0	16	59 35.1	56.03N 138.00W	12.83	5.3	.2	55.2
97	YKA	3 7 73	12.38	259.2	0	5.1	17	44 16.5	58.00N 139.90W	12.91	2.2	.3	41.1
105	YKA	9 8 73	23.01	199.1	2	5.1	2	16 25.8	40.26N 124.23W	10.91	7.5	.1	37.5
108	YKA	22 8 73	20.33	272.7	38	5.9	18	14 37.2	57.10N 154.10W	9.73	7.4	.2	36.7
115	YKA	19 9 73	20.87	270.6	0	5.0	10	32 3.0	56.20N 154.20W	11.39	10.1	.2	29.9
116	YKA	21 9 73	20.23	272.8	45	5.0	10	35 55.9	57.20N 154.00W	9.76	6.9	.2	28.3

REFERENCES

Aki, K., 1969. Analysis of the seismic coda of local earthquakes as scattered waves J. Geophys. Res., 74: 615-631.

Aki, K., 1973. Scattering of P-waves under the Montana LASA, J. Geophys. Res., 78: 1334-1346.

Aki, K., and Chouet, B., 1975. Origin of coda waves: source, attenuation, and scattering effects, J. Geophys. Res., 80: 3322-3342.

Aki, K., Christoffersson, A., and Husebye, E.S., 1976. Three dimensional seismic structure of the lithosphere under Montana-Lasa, Bull. Seism. Soc. Am., 66: 501-524.

Aki, K., Christoffersson, A., and Husebye, E.S., 1977. Determination of the three dimensional structure of the lithosphere, J. Geophysics. Res., 82: 277-296.

Alterman, Z.S., and Karal, F.C., Jr., 1968. Propagation of elastic waves in layered media by finite-difference methods, Bull. Seism. Soc. Am., 58: 367-398.

Anderson, D.L., and Toksoz, M.N., 1963. Surface waves on spherical earth, 1, upper mantle structure from love waves, J. Geophys. Res., 68: 3483-3500.

Archambeau, C.B., Flinn, E.A., and Lambert, D.G., 1969. Fine structure of the upper mantle, J. Geophys. Res., 74: 5825-5865.

Arora, S,K., 1971. A study of the earth's crust near Gauribidanur in southern India, Bull. Seism. Soc. Am., 61: 671-683.

Arora, S.K., Varghese, T.G., and Krishnan, C.A., 1970. Some aspects of the structure of southern India based on recent Bhadrachalam earthquakes, Nature, 225: 261-262.

Backus, G., and Gilbert, F., 1968. The resolving power of gross earth data. Geophys. J.R. astr. Soc., 16: 169-205.

Barley, B.J., 1977. The origin of complexity in some P seismograms from deep earthquakes, Geophys. J.R. astr. Soc., 49: 773-777.

Barr, K.G., 1971. Crustal refraction experiment: Yellowknife 1966. J. Geophys. Res., 76: 1929-1947.

Berckhemer, H., 1969. Direct evidence for the composition of the lower crust and the Moho, Tectonophysics, 8: 97-105.

Berry, M.J., and Fuchs, K., 1973. Crustal structure of the Superior and Grenville provinces of north-eastern Canadian Shield, Bull. Seism. Soc. Ame., 63: 1393-1432.

Berry, M.J., and Mair, J.A., 1980. Structure of the continental crust: A reconciliation of seismic reflection and refraction studies, in The Continental Crust and Its Mineral Deposits, edited by D.W. Strangway: 195-213. Geological Association of Canada Special Paper 20.

Berry, M.J., and West, G.F., 1966. Reflected and head wave amplitudes in a medium of several layers, in: The Earth beneath the continents, edited by J.S. Steinhart and T.J. Smith, AGU Monograph, 10:464-481.

Berteussen, K.A., Christoffersson, A., Dahle, A., and Husebye, E.S., 1975. Modelling the geological structures beneath the NORSAR array as a Chernov Medium, in Exploitation of Seismograph Networkds, edited by K.G. Beauchamp: 591-603. NATO Advanced Study Institute Series, Series E, No.11.

Berteussen, K.A., Husebye, E.S., Mereu, R.F., and Ram, A., 1977. Quantitative assessment of the crust-upper mantle heterogeneities beneath the Gauribidanur seismic array in southern India, Earth Planet. Sci. Letters, 37: 326-332.

Bessonova, E.N., Fishman, V.M., Ryaboyi, V.Z., and Sitnikova, G.A., 1974. The tau method for inversion of travel times-I. Deep seismic sounding data, Geophys. J.R. astr. Soc., 36: 377-398.

Bessonova, E.N., Fishman, V.M., Shnirman, M.G., Sitnikova, G.A., and Johnson, L.R., 1976. The tau method for inversion of travel time-II. Earthquake data, Geophys. J.R. astr. Soc., 46:87-108.

Birch, F., 1960. The velocity of compressional waves in

rocks to 10 kilobars, Part 1, J. Geophys. Res., 65: 1083-1102.

Birch, F., 1961. The velocity of compressional waves in rocks to 10 kilobars, Part 2, J. Geophys. Res., 66: 2199-2224.

Birtill, J.W., and Whiteway, F.E., 1965. The application of phased arrays to the analysis of seismic body waves, Phil. Trans. Roy. Soc. A, 258: 421-493.

Bolt, B.A., Doyle, H.A., and Sutton, D.J., 1958. Seismic observations from the 1956 atomic explosions in Australia, Geophys. J., 1: 135-145.

Bolt, B.A., O'Neill, M., and Qamar, A., 1968. Seismic wave near 110 : is structure in core or upper mantle responsible? Geophys. J.R. astr. Soc., 16: 475-487.

Briden, J.C., Fairhead, J.D., Stuart, G.W., Whitcombe, D.N., Dorbath, C., and Dorbath, L., 1980. Lateral variation in deep seismic structure across the margin of the West African craton, EOS, Trans. AGU, 61: 366(abstract).

Bullen, K.E., 1963. An introduction to the theory of seismology, 3rd Ed., Cambridge University Press, Cambridge.

Burdick, L.J., and Helmberger, D.V., 1978. The upper mantle P velocity structure of the western United States, J. Geophys. Res., 83: 1699-1712.

Capon, J., 1974. Characterization of crust and upper mantle structure under LASA as a random medium, Bull. Seism. Soc. Am., 64: 235-266.

Chen, Wang-Ping, 1980. Regional variation of the focal mechanism of intermediate depth earthquakes and seismicity in the Karakorum-east Hindukush area. EOS, Trans. AGU (abstract), 61: 1031.

Chernov, L., 1960. Wave propagation in a random medium, translated by R.A. Silverman, McGraw-Hill Book Company, New York.

Chinnery, M.A., 1969. Velocity anomalies in the lower mantle, Phys. Earth Planet. Int., 2: 1-10.

Christensen, N.I., 1965. Compressional wave velocities in metamorphic rocks at pressure to 10 kilobars., J. Geophys. Res., 70: 6147-6164.

Christoffersson, A., 1975. Estimation of parameters characterizing random medium, in Exploitation of Seismograph Networks, edited by K.G, Beauchamp: 577-589. NATO Advanced Study Institute Series, Series E, No.11.

Cleary, J., and Hales, A., 1966. An analysis of the travel times of P waves to North American Stations in the distance range 32° to 100°, Bull. Seism. Soc. Am., 56: 467-489.

Cleary, J.R., King, D.W., and Haddon, R.A.W., 1975. P-wave scattering in the Earth's crust and upper mantle, Geophys. J.R. astr. Soc., 43: 861-872.

Clee, T.E., Barr, K.G., and Berry, M.J., 1974. Fine structure of the crust near Yellowknife, Can. J. Earth Sci., 11: 1534-1549.

Corbishley, D.J., 1970. Multiple array measurements of P wave travel time derivative, Geophys. J.R. astr. Soc., 19: 1-14.

Cumming, G.L., and Chandra, N.N., 1975. Further studies of reflections from the deep crust in southern Alberta, Can. J. Earth Sci., 12: 539-557.

Dahle, A., Husebye, E.S., Berteussen, K.A., and Christoffersson, A., 1975. Wave scattering effects and sesimic velocity measurements, in Exploitation of Seismograph Networks, edited by K.G. Beauchamp: 559-575. NATO Advanced Study Institute Series, Series E, Appl. Sci. No. 11.

Davies, L.M., and Chapman, C.H., 1975. Some numerical experiments on the inversion of discrete travel-time data. Bull. Seism. Soc. Am., 65: 531-539.

Davies, D., Kelly, E.J., and Filson, J.R., 1971. Vespa process for analysis of seismic signals. Nature, Phys. Sci., 232, July 5th: 8-13.

Davies, D., and Sheppard, R.M., 1972. Lateral Heterogeneity in the Earth's Mantle. Nature 239: 318-323.

Dey-Sarkar, S.K., and Wiggins, R.A., 1976. Upper mantle structure in western Canada, J. Geophys. Res., 81: 3619-3632.

Doornbos, D.J., 1975. Characteristics of lower mantle inhomogeneities from scattered waves. EOS, Trans. AGU, 56: 395 (abstract).

Doornbos, D.J., and Vlaar, N.J., 1973. Region of seismic

wave scattering in the Earth's mantle and precursors to PKP. Nature, Phys. Sci., 243: 58-61.

Dorman, J., Ewing, M., and Oliver, J., 1960. Study of shear velocity distribution by mantle Rayleigh waves. Bull. Seism. Soc. Am., 50: 87-115.

Dorman, L.M., and Jacobson, R.S., 1980. Linear inversion of body wave data-Part I: velocity structure from travel times and ranges. Geophysics, 46: 138-151.

Douglas, A., Marshall, P.D., and Corbishley, D.J., 1971. Absorption and the complexity of P signals. Nature, Phys. Sci., 20: 50-51.

Douglas, A., Marshall, P.D., Gibbs, P.G., Young, J.B., and Blamey, C., 1973. P signal complexity re-examined. Geophys. J.R. astr. Soc., 33: 195-221.

Doyle, H.A., Everingham, I.B., and Hogan, T.K., 1959. Recording of large explosions in South-Eastern Australia, Australian J. Phys., 12: 222-230.

Doyle, H.A., and Hales, A.L., 1967. An analysis of the travel times of S wave to North American Stations in the distance range 28° to 82°. Bull. Seism. Soc. Am., 57: 761-771.

Dziewonsky, A.M., Hager, B.H., and O'Connell, R.J., 1977. Large-scale heterogeneities in the lower mantle. J. Geophys. Res., 82: 239-255.

Engdahl, E.R., 1975. Effects of plate structure and dilatancy on relative teleseismic P-wave residuals. Geophys. Res. Letters, 2: 420-422.

England, P.C., Worthington, M.H., and King, D.W., 1977. Lateral variations in structure of the upper mantle beneath Eurasia, Geophys. J.R. astr. Soc., 48: 71-79.

Fitch, T.J., 1970. Earthquake mechanisms in the Himalayan, Burmese and Andaman regions and continental tectonics in Central Asia. J. Geophys. Res., 75: 2699-2709.

Forsyth, D.W., 1977. The evolution of the upper mantle beneath mid-ocean ridges. Tectonophysics, 38: 89-118.

Gangi, A.F., and Fairborn, J.W., 1968. Accurate determination of seismic array steering delays by

an adaptive computer program, Suppl. Nuovo Cim. Serie 1, 6: 105-115.

Garmany, J. Orcutt, J.A., and Parker, R.L., 1979. Travel time inversion: a geometrical approach. J. Geophys. Res., 84: 3615-3622.

Gebrande, H., 1976. A seismic-ray tracing method for two-dimensional inhomogeneous media, in: Explosion Seismology in Central Europe edited by P. Giese, C. Prodehl, and A. Stein, Springer-Verlag, Berlin: 162-167.

Girardin, N., 1980. Travel-time residuals of PP waves reflected under oceanic and continental platform regions. Phys. Earth Planet. Int., 23: 199-206.

Green, A.G., Cumming, G.L., and Cedarwell, D., 1979. Extension of the Superior-Churchill boundary zone into southern Canada, Can. J. Earth Sci., 16: 1691-1701.

Green, A.G., and Stephenson, O.G., 1978. Report on a seismic survey across the Superior-Churchill boundary zone in southern Canada. Earth Physics Branch, Canadian Department of Energy, Mines and Resources, Open File Report, 78-9. 165p.

Green, A.G. Stephenson, O.G., Mann, G.D., Kanasewich, E.R., Cumming, G.L., Hajnal, Z., Mair, J.A., and West, G.F., 1980. Cooperative seismic surveys across the Superior-Churchill boundary zone in southern Canada. Can. J. Earth Sci., 17: 617-632.

Green, D.H., 1970. High pressure experimental studies on the mineralogical constitution of the lower crust, Phys. Earth Planet. Int., 3: 441-450.

Green, D.H., and Lambert, I.B., 1965. Experimental cystallization of anhydrous granite at high pressures and temperatures, J. Geophys. Res., 70: 5259-5268.

Green, D.H., and Ringwood, A.E., 1967. The stability fields of aluminous pyroxene peridotite and garnet peridotite and their relevance in upper mantle structure, Earth Planet. Sci. Letters, 3: 151-160.

Green, R.W.E., and Hales, A.L., 1968. The travel times of P waves to 30° in the Central United States and upper mantle structure, Bull. Seism. Soc. Am., 58: 267-289.

Gutenberg, B., 1959. Wave velocities below the Mohorovicic discontinuity, Geophys. J.R. astr. Soc., 4: 348-352.

Gutowski, P.R., and Kanasewich, E.R., 1974. Velocity spectral evidence of upper mantle discontinuities. Geophys. J.R. astr. Soc., 36: 21-32.

Haddon, R.A.W., Husebye, E.S., and King, D.W., 1977. Origins of precursors to P'P'. Phys. Earth Planet. Int., 14: 41-70.

Hajnal, Z., 1980. Cooperative near-vertical incident reflection and refraction seismic surveys across the Superior-Churchill boundary zone in southern Canada: Location, Outline of Objectives field procedures, field parameters, tape formats, and preliminary results. Unpublished report, DSS Contract No: OSU79-00033.

Hajnal, Z., Cumming, G.L., Kanasewich, E.R., Green, A.G., Mair, J.A., Hall, D.H., Mereu, R.F., 1980. Seismic refraction and continuous refletion profiles over the Nelson Front. EOS, Trans. AGU, 61: 291.

Hales, A.L., 1972. The travel times of P seismic waves and their relevance to the upper mantle velocity distribution, Tectonophysics, 13: 447-482.

Hales, A.L., Cleary, J.R., Doyle, H.A., Green, R., and Roberts, J., 1968. P-wave station anomalies and the structure of the upper mantle, J. Geopys. Res., 73: 3885-3896.

Hales, A.L., and Sacks, I.S., 1958. Evidence for an intermediate layer from crustal structures studies in the eastern Transvaal, Geophys., J., 2: 15.

Helmberger, D., and Wiggins, R.A., 1971. Upper mantle structure of midwestern United States, J. Geophy. Res., 76: 3229-3245.

Herrin, E., Arnold, E.P., Bolt, B.A., Clawson, C.E., Engdahl, E.R., Freedman, H.W., Gordon, D.W., Hales, A.L., Lobdell, J.L., Nuttli, O., Romney, C., Taggart, J., and Tucker, W., 1968. Seismological tables for P phases, Bull. Seism. Soc. Am., 58: 1193-1241.

Hodgson, J.H., 1953. A seismic survey in the Canadian Shield, I: refraction studies based on rockbursts at Kirkland Lake, Ontario, Publ. Dom. Obs., Ottawa, 16: 111-163.

James, D.E., and Steinhart, J.S., 1966. Structure beneath the continents; a critical review of explosion studies 1960-65, in: The Earth beneath the Continents, edited by J.S. Steinhart and T.J. Smith, AGU Monograph, 10: 293-333.

Jackson, P.L., 1970. Seismic ray simulation for a spherical earth, Bull. Seism. Soc. Am., 60: 1021-1025.

Jeffreys, H., 1939. The times of P, S, and SKS and the velocities of P and S, Mon. Not. R. astr. Soc., Geophys. Suppl., 4: 498-533.

Jeffreys, H., and Shimshoni, M., 1966. The use of amplitudes in improving velocity distribution for Europe, Geophys. J.R. astr. Soc., 10: 515-524.

Johnson, L.R., 1967. Array measurement of P velocities in the upper mantle, J. Geophys. Res., 72: 6309-6325.

Johnson, L.R., and Gilbert, F., 1972. Inversion and inference for teleseismic ray data, in: Methods in Computational Physics, edited by B.A. Bolt, 11: 231-266, Academic, New York.

Jordan, T.H., and Lynn, W.S., 1974. A velocity anomaly in the lower mantle. J.Geophys. Res., 79: 2679-2685.

Julian, B.R., and Anderson, D.L., 1968. Travel times, apparent velocities and amplitudes of body waves, Bull. Seism. Soc. Am., 58: 339-366.

Julian, B.R., and Gubbins, D., 1977. Three-dimensional seismic ray tracing. J. Geophys., 43: 95-113.

Jurkevics, A., and Wiggins, R., 1980. Body-wave inversion using travel time and amplitude data. Geophys. J.R. astr. Soc., 63:75-93.

Kaila, K.L., Krishna, V.G., Chaudhury, K.R., and Narain, H., 1978. Structure of the Kashmir Himalaya from deep seismic soundings, J. Geol. Soc. India, 19: 1-20.

Kaila, K.L., Krishna, V.G., Narain, H., 1969. Upper mantle velocity structure in the Hindukush region from travel-time studies of deep earthquakes using a new analytical method, Bull. Seism. Soc. Am., 59: 1949-1967.

Kaila, K.L., Reddy, P.R., and Narain, H., 1968. P-wave travel times from shallow earthquakes recorded in India and inferred upper mantle structure. Bull.

Seism. Soc. Ame., 58: 1879-1897.

Kanamori, H., 1967. Upper mantle structure from apparent velocities of P waves recorded at Wakayama micro-earthquake observatory, Bull. Earthquake Res. Inst. Tokyo, 45: 657-678.

Kanasewich, E.R., Hemmings, C.D., and Alpaslan, T., 1973. Nth root stack nonlinear multichannel filter, Geophysics, 38: 327-338.

Katz, S., 1955. Seismic study of crustal structure in Pennsylvania and New York, Bull. Seism. Soc. Am., 45: 303-325.

Keen, C.E., and Barrett, D.L., 1971. A measurement of seismic anisotropy in the northeast Pacific, Can. J. Earth Sci., 8: 1056-1064.

Kelly, E.J., 1964. Limited network processing of seismic signals, M.I.T. Group report 44.

Kelly, E.J., 1968. A study of two short-period discriminants, Lincoln Laboratory, M.I.T. Technical Note 1968-8.

Kelly, K.R., Ward, R.W., Treitel, S., and Alford, R.M., 1976. Synthetic seismograms: A finite-difference approach, Geophysics, 41: 2-27.

Kennett, B.L.N., 1976. A comparison of travel-time inversions, Geophys. J.R. astr. Soc., 44: 517-536.

Kennett, B.L.N., and Orcutt, J.A., 1976. A comparison of travel time inversions for marine refraction profiles. J.Geophys. Res., 81: 4061-4070.

King, D.W., and Calcagnile, G., 1976. P wave velocities in the upper mantle beneath Fennoscandia and western Russia, Geophys. J.R. astr. Soc., 46: 407-432.

King, D.W., Haddon, R.A.W., and Husebye, E.S., 1975. Precursors to PP, Phys. Earth Planet. Inter., 10: 103-127.

King, D.W., Mereu, R.F., and Muirhead, K.J., 1973. The measurement of apparent velocity and azimuth using adaptive processing techniques on data from the Warramunga seismic array, Geophys. J.R. astr. Soc., 35: 137-167.

Lambert, D.G., Alexander, S.S., Von Seggern, D.H., and Galat, G.A., 1969. The Long Shot experiment-volume II: Comprehensive analysis,

Seismic Data Laboratory Report No. 234.

Lehmann, I., 1964. On the travel times of P as determined from Nuclear explosions, Bull. Seism. Soc. Am., 54: 123-139.

Lehmann, I., 1967. On the travel times of P as obtained from the nuclear explosions Bilby and Shoal, Phys. Earth Planet. Int., 1: 14-23.

Lewis, B.T.R., and Meyer, R.P., 1968. A seismic investigation of the upper mantle to the west of Lake Superior, Bull. Seism. Soc. Am., 58: 565-596.

Lilwall, R.C., and Douglas, A., 1970. Estimation of P wave travel times using the joint epicentre method, Geophys. J.R. astr. Soc., 19: 165-181.

Lukk, A.A., and Nersesov, I.L., 1965. Structure of the upper mantle as shown by observations of earthquakes of intermediate focal depth, Doklady Akad. Nauk SSSR. (Eng. trans.), 162: 14-16.

Mair, J.A., and Lyons, J.A., 1976. Seismic reflection techniques for crustal structure studies, Geophysics, 41: 1272-1290.

Manchee, E.B., and Somers, H., 1966. The Yellowknife seismological array. Publ. Dom. Obs. 32, No.2: 69-84.

Manghnani, M.H., Ramananantoandro, R., and Clark, S.P.,Jr., 1974. Compressional and shear-wave velocities in granulites facies rocks and eclogites to 10 Kbar, J. Geophys. Res., 79: 5427-5446.

Masse, R.P., and Alexander, S.S., 1974. Compression velocity distribution beneath Scandinavia and Western Russia, Geophys. J.R. astr. Soc., 39:587-602.

Masse, R.P., Landisman, M., and Jenkins, J.B., 1972. An investigation of the upper mantle compressional velocity distribution beneath the basin and range province. Geophys. J.R. astr. Soc., 30: 19-36.

McMechan, G.A., and Wiggins, R.A., 1972. Depth limits in body wave inversions. Geophys. J.R. astr. Soc., 28: 459-473.

Mereu, R.F., Majumdar, S.B., and White, R.E., 1977. Moho topography under the highest ranges of the Canadian Rockies, Can. J. Earth Sci., 14:

196-208.

Mereu, R.F., and Ojo, S.B., 1980. Seismic wave propagation through a crust with random lateral and vertical inhomogeneities, EOS, Trans. AGU, 61: 300-301 (abstract).

Mereu, R.F., and Ojo, S.B., 1980. The scattering of seismic waves through a crust and upper mantle with random lateral inhomogeneities, Phys. Earth Planet. Int., (in press).

Mereu, R.F., and Ram, A., 1975. A computer program package for the analysis of array data using adaptive processing methods, in Exploitation of Seismograph Networks, edited by K.G., Beauchamp: 327-339. NATO Advanced Study Institute Series, Series E, No.11.

Mereu, R.F., Simpson, D.W., and King, D.W., 1974. Q and its effect on the observation of upper mantle travel time branches, Earth Planet. Sci. Letters, 21: 439-477.

Morris, G.B., Raitt, R.W., and Shor, G.G., Jr., 1969. Velocity anisotropy and delay-time maps of the mantle near Hawaii, J. Geophys. Res., 74: 4300-4316.

Mowat, W.M.H., and Burch, R.F., 1974. Handbook for the stations which provide seismograms to the Blacknest seismological centre, United Kingdom, AWRE report no. 44/47/29, January.

Muirhead, K.J., 1968. Eliminating false alarms when detecting seismic events automatically, Nature, 217: 533-534.

Muirhead, K.J., and Ram Datt, 1976. The Nth root process applied to seismic array data, Geophys. J.R. astr. Soc., 47: 197-210.

Nguye-Hai, 1963. Propagation des ondes longitidinales dans le noyau terrestre. Annals de Geophys., 19: 285-346.

Niazi, M., and Anderson, D.L., 1965. Upper mantle structure of western North America from apparent velocities of P waves, J. Geophys. Res., 70: 4633-4640.

Nikolajev, A.V., and Tregub, F.S., 1970. A statistical model of the earth's crust: method and results, Tectonophysics, 10: 573-578.

Nur, A., and Simmons, G., 1969. The effect of saturation on

velocity in low porosity rocks, Earth Planet. Sci. Letters, 7: 183-193.

Ojo, S.B., and Mereu, R.F., 1980. Evidence for differences in oceanic and continental upper mantle structure from array signal coherence measurements, EOS, Trans. AGU, 61: 301 (abstract).

Otsuka, M., 1966. Azimuth and slowness anomalies of seismic waves measured on the Central California seismographic array: Part 1. Observations, Bull. Seism. Soc. Am., 56: 223-239.

Parkiser, L.C., and Robinson, R., 1966. Composition of continental crust as estimated from seismic observations, in: The Earth beneath the Continents, edited by J.S. Steinhart and T.J. Smith, AGU Monograph, 10: 620-626.

Pereyra, V., Lee, W.H.K., and Keller, H.B., 1980. Solving two-point seismic-ray tracing problems in a heterogeneous medium, Part 1: A general adaptive finite difference method, Bull. Seism. Soc. Am., 70: 79-99.

Powell, C., 1975. Evidence for mantle heterogeneity from two large seismic arrays, Nature, 254: 40-42.

Press, F., 1959. Some implications on mantle and crustal structure from G. Waves and Love waves, J. Geophys. Res., 64: 565-568.

Press, F., 1960. Crustal structure in the California-Nevada region, J. Geophys. Res., 65: 1039-1051.

Ram, A., 1976. The identification and interpretation of upper mantle travel time branches from slowness measurements made on data recorded at the Gauribidanur (India) and Yellowknife (Canada) seismic arrays, Ph.D. Thesis, University of Western Ontario, Canada.

Ram, A., and Mereu, R.F., 1975. A comparison of adaptive processing techniques with Nth root beam forming methods, Geophys. J.R. astr. Soc., 42: 653-670.

Ram, A., and Mereu, R.F., 1977. Lateral variations in the upper mantle structure around India as obtained from the Gauribidanur seismic array data, Geophys. J.R. astr. Soc., 49: 87-114.

Ram, A., Mereu, R.F. and Weichert, D.H., 1978. The identification and interpretation of upper mantle travel-time branches from measurements of $dt/d\Delta$

made on data recorded at the Yellowknife seismic array, Can. J. Earth Sci., 15: 227-236.

Ram Datt, 1981. Seismic velocity structure using array data, Phys. Earth Planet. Int., 24: 33-52.

Ringwood, A.E., 1962. A model for the upper mantle, J. Geophys. Res., 67: 857-867.

Ringwood, A.E., 1967. The pyroxene-garnet transformation in the earth's mantle, Earth Planet. Sci. Letters, 2: 255-263.

Ringwood, A.E., and Green, D.H., 1966. Petrological nature of the stable continental crust, in: The Earth beneath the continents, edited by J.S. Steinhart and T.J. Smith, AGU Monograph, 10: 611-619.

Robinson, E.A., 1967a. Multichannel time series analysis with digital computer programs, in Time Series Analysis: San Francisco, Holden-Day, Inc.

Robinson, E.A., 1967b. Statistical communication and detection with special reference to digital data processing of random and seismic signals, Griffin and Co., London.

Romanowicz, B.A., 1979. Seismic structure of the upper mantle beneath the United States by three-dimensional inversion of body wave arrival times. Geophys. J.R. astr. Soc., 57: 479-506.

Sengupta, M.K., and Julian, B., 1976. P wave travel times from deep earthquakes, Bull. Seism. Soc. Am., 66: 1555-1579.

Simpson, D.W., 1973. P wave velocity structure of the upper mantle in the Australian region, Ph.D. Thesis, Australian National University, Canberra, Australia.

Simpson, D.W., 1980. Seismicity, Tectonics and topography of the Hindukush, Pamirs, Karakorum and Tadjik depression, EOS Trans. AGU (abstract), 61: 1031.

Simpson, D.W., Mereu, R.F., and King, D.W., 1974. An array study of P wave velocities in the upper mantle transition zone beneath northeastern Australia, Bull. Seism. Soc. Am., 64: 1757-1788.

Singh, D.D., Rastogi, B.K., and Gupta, H.K., 1979. Spectral analysis of body waves for earthquakes in the Himalaya and nearby regions and their source Parameters, Phys. Earth Planet. Int., 18: 143-152.

Smithson, S.B., Brewer, J.A., Kaufman, S., Oliver, J.E., and Hurich, C.A., 1979. Structure of the Laramide Wind River Uplift, Wyoming from COCORP deep reflection data and from gravity data, J. Geophys. Res., 84: 5955-5972.

Smithson, S.B., and Decker, E.R., 1974. A continental crustal model and its geothermal implications. Earth Planet. Sci. Letters, 22: 215-225.

Steinhart, J.S., and Woollard, G.P., 1961. Seismic evidence concerning continental crustal structure, in: Explosion Studies of Continental Structure, edited by J.S. Steinhart and R.P. Meyer, Carnegie Institute of Washington Publ. 622: 344-383.

Takeuchi, H.F., Press, F., and Kabayashi, N., 1959. Rayleigh wave evidence for the low-velocity zone in the mantle, Bull. Seism. Soc. Am., 49: 355-364.

Tandon, A.N., 1967. Upper mantle seismic wave velocities in the Hindukush region, Indian J. Met. Geophys., 18: 385-390.

Telford, W.M., Geldart, L.P., Sheriff, R.E., and Keys, D.A., 1976. Applied Geophysics, Cambridge University Press, Cambridge.

Toksoz, M.N., and Anderson, D.L., 1966. Phase velocity of long period surface waves and structure of the mantle, 1. great circle love and Rayleigh wave data, J. Geophys. Res., 71: 1649-1658.

Toksoz, M.N., Chinnery, M.A., and Anderson, D.L., 1967. Inhomogeneities in the earth's mantle. Geophys. J.R. astr. Soc., 13: 31-59.

Vinnik, L.P., Lukk, A.A., and Nersesov, I.L., 1977. Nature of the intermediate seismic zone in the mantle of Pamirs-Hindukush, Tectonophysics, 38: T9-T14.

Weichert, D.H., 1972. Anomalous azimuths of P: evidence for lateral variations in the deep mantle. Earth Planet. Sci. Letters, 17: 181-188.

Weichert, D.H., 1975. The role of medium aperture arrays: The Yellowknife system, in: Exploitation of Seismography Networks, edited by K.G. Beauchamp: 167-195, NATO Advanced Study Institute Series, Series E. No.11.

Weichert, D.H., and Whitham, K., 1969. Calibration of the Yellowknife seismic array with first zone explosions, Geophys, J.R. astr. Soc., 18:

461-476.

Wiggins, R.A., and Helmberger, D.V., 1973. Upper mantle structure of the western United States, J. Geophys, Res,, 78: 1870-1880.

Woollard, G.P., 1959. Crustal structure from gravity and seismic measurements, J. Geophys. Res., 64: 1521-1544.

Wright, C., 1972. Array studies of seismic waves arriving between P and PP in the distance range 90° to 115°, Bull. Seism. Soc. Am., 62: 385-400.

Wright, C., 1975. The origin of short-period precursors to PKP, Bull. Seism. Soc. Am., 65: 765-786.

Wright, C., and Muirhead, K.J., 1969. Longitudinal waves from the Novaya Zemlya nuclear explosion of October 27 1966, recorded at the Warramunga seismic array, J. Geophys. Res., 74: 2034-2047.

VITA

NAME:	Samuel Bakare Ojo
PLACE OF BIRTH:	Ijagba, Nigeria
YEAR OF BIRTH:	December 14, 1947
POST-SECONDARY EDUCATION AND DEGREES:	Ahmadu Bello University, Zaria, Nigeria 1968-1971 B.Sc. (Hons) Physics. Ahmadu Bello University, Zaria, Nigeria 1972-1974 M.Sc. Physics University of Western Ontario London, Ontario Ph.D. Geophysics
HONOURS AND AWARDS:	Ahmadu Bello University Postgraduate Scholarship 1972-1974
RELATED WORK EXPERIENCE:	Lecturer II King's College, Lagos, Nigeria 1971-1972 Lecturer II Ahmadu Bello University Zaria, Nigeria 1974-1977 Lecturer I Ahmadu Bello University Zaria, Nigeria 1977-present (study leave) Teaching Assistant University of Western Ontario 1978-1981 Participated in Long-range refraction experiments in Manitoba, Saskatchewan and British Columbia, Canada Summer, 1979 and 1980 Extensive experience in regional gravity surveys

PUBLICATIONS:

(1) S.B. Ojo, 1974. Gravity investigations in the Middle Niger Basin area, Nigeria, M.Sc. thesis, Ahmadu Bello University, Zaria.

(2) S.B. Ojo and D.E. Ajakaiye, 1976. Preliminary interpretation of gravity measurements in the Middle Niger Basin area, Nigeria, In: The Geology of Nigeria, edited by C.A. Kogbe, Elizabethan Publ. Co., Lagos: 295-307.

(3) R.F. Mereu and S.B. Ojo, 1980. The scattering of seismic waves through a crust and upper mantle with random lateral inhomogeneities, Physics of the Earth and Planetary Interiors, (in press).

PAPERS PRESENTED AT SCIENTIFIC MEETINGS:

S.B. Ojo and R.F. Mereu, 1979. Array signal coherence and its relationship to the scattering of P waves in the crust and upper mantle, The VI-th annual meeting of the Canadian Geophysical Union, Fredericton, New Brunswick, Canada.

R.F. Mereu and S.B. Ojo, 1979. The scattering of seismic waves through a crust and upper mantle with random lateral inhomogeneities, The XVII-th IUGG, IASPEI meeting, Canberra, Australia.

S.B. Ojo and R.F. Mereu, 1980. Evidence for differences in oceanic and continental upper mantle structure from array signal coherence measurements, Spring annual meeting of the American Geophysical Union, Toronto, Ontario, Canada.

R.F. Mereu and S.B. Ojo, 1980. Seismic wave propagation through a crust with random lateral and vertical inhomogeneities, Spring annual meeting of the American Geophysical Union, Toronto, Ontario, Canada.